INSTITUT POLYTECHNIQUE DE PARIS

NNT : 2026IPPAX011

Thèse de doctorat

# Controlling pattern formation via magnetic field at the surface of magneto-active elastomer structures

Thèse de doctorat de l'Institut Polytechnique de Paris
préparée à l'École Polytechnique

École doctorale n°626 École doctorale de l'Institut Polytechnique de Paris (EDIPP)
Spécialité de doctorat : Mécanique des fluides et des solides, acoustique

Thèse présentée et soutenue à Palaiseau, le 23 mars 2026, par

**VIGNESH SELVAM**

Composition du Jury :

| | |
|---|---|
| Benoît ROMAN<br>Directeur de recherche CNRS, Université Paris Cité (PMMH) | Président |
| Christelle COMBESCURE<br>Maître de Conférences HDR, Académie Militaire de Saint-Cyr Coëtquidan & Université Bretagne Sud (IRDL) | Rapporteure |
| Frédéric DEMOLY<br>Professeur des Universités, Université de Technologie de Belfort-Montbéliard (ICB) | Rapporteur |
| Joël MARTHELOT<br>Chargé de recherche CNRS, Aix Marseille Université (IUSTI) | Examinateur |
| Laurence BODELOT<br>Professeure, Institut Polytechnique de Paris (LMS) | Directrice de thèse |
| Konstantinos DANAS<br>Directeur de recherche CNRS, Institut Polytechnique de Paris (LMS) | Co-directeur de thèse |

# Contents

**Abstract** iv

**Résumé** vi

**Acknowledgements** viii

**General introduction** 1

**1 State of the art** 4
- 1.1 Magnetorheological elastomers (MREs) . . . 5
- 1.2 Magneto-elastic instabilities . . . 10
- 1.3 Fabrication aspects . . . 15
- 1.4 Modeling of MREs and instabilities . . . 22
- 1.5 Scope and organization of the thesis . . . 23

**2 Active mixing-assisted direct ink writing** 28
- 2.1 Material selection . . . 29
- 2.2 Rheological characterization . . . 31
- 2.3 3D printer setup . . . 39
- 2.4 Print parameter selection . . . 43
- 2.5 Interdependency of print parameters and extension to multi-layer printing . 56
- 2.6 Concluding remarks . . . 62

**3 Numerical modeling and validation** 64
- 3.1 Material characterization . . . 65
- 3.2 Numerical modeling and implementation . . . 73
- 3.3 Numerical validation against the 2D model . . . 90
- 3.4 Numerical validation against experimental 3D surface profiles . . . 95
- 3.5 Concluding remarks . . . 101

**4 Surface-morphing of heterogeneous film/substrate systems** 104
- 4.1 Effect of overall topology . . . 105
- 4.2 Effect of geometrical parameters . . . 119
- 4.3 Effect of material property contrast . . . 133
- 4.4 Concluding remarks . . . 136

**Conclusion and perspectives** 138

**A Mixer length selection** 143

**B Rheological validation** 145

B.1 Constitutive equations . . . . . 145
B.2 Simplified analytical rheometer model . . . . . 147

**C Material characterization of molded and printed samples 149**
C.1 Fabrication of dogbone specimens and mechanical testing . . . . . 149
C.2 Effect of Thivex on the tensile response . . . . . 151
C.3 Effect of particle content on tensile response . . . . . 152
C.4 Comparison of molded and printed specimens . . . . . 153
C.5 Effect of the heated bed and printing orientation . . . . . 155

**D Stereo digital image correlation (stereo-DIC) 157**

**E 3D magnetic profile contour maps 164**

**Bibliography 167**

# Abstract

Magnetorheological elastomers (MREs) are smart composite materials composed of magnetizable particles embedded in an elastomeric matrix. They respond readily and reversibly to applied magnetic fields through magneto-induced deformations or surface instabilities driven by coupled magneto-mechanical stresses and magnetic interactions. In layered MRE film–substrate systems, such instabilities can be triggered by mechanical, magnetic, or combined loading, leading to surface morphologies ranging from periodic wrinkling to more complex crinkling patterns. Despite extensive experimental and numerical efforts, these phenomena have so far been mostly limited to uniform films, resulting in 2.5D patterns with restricted tunability. However, achieving fully three-dimensional surface morphologies in uniform films requires large magnetic fields, while instability is often confined to narrow ranges of mechanical loading. This work aims to overcome these limitations by enabling controllable, targeted three-dimensional surface patterns through the introduction of heterogeneous magneto-mechanical properties in MRE films, made possible by advanced fabrication techniques.

To achieve these objectives, an active mixing method for MRE inks is developed and implemented in a direct ink writing process using a dynamic helical mixer. This represents the first application of active mixing to MREs. This integrated approach provides a reliable and repeatable route to print heterogeneous MRE films with well-controlled geometry, uniformity, and rheological properties. Particular attention is also paid to optimizing the printing process and understanding the relationship between manufacturing parameters and the final properties of the resulting structures. The influence of parameters such as extrusion speed, nozzle geometry, mixing speed, and the rheological properties of inks on print quality and geometric fidelity is analyzed. These aspects are essential to ensure the reproducibility and accuracy of introduced heterogeneities. Concurrently, a three-dimensional numerical model is established to accurately capture surface pattern evolution under magnetic fields. This model employs a framework capable of reproducing magnetization, magnetostriction, and mechanical behavior across a broad spectrum of magnetic fields. Material properties are identified experimentally, and three-dimensional surface profiles are measured using stereo digital image correlation, enabling validation of the numerical model.

Using this integrated experimental and numerical approach, this study systematically investigates surface pattern evolution in heterogeneous MRE film–substrate systems. Fur-

thermore, the numerical model allows the exploration of configurations that are difficult to access experimentally, thereby providing a predictive tool for the design of new EMR architectures. This complementarity between experimentation and simulation strengthens the robustness of the proposed approach. The influence of film heterogeneity on the onset and transformation of surface patterns is examined, revealing new strategies for controlling complex three-dimensional morphologies via magnetic fields. Overall, the findings demonstrate that the combination of heterogeneous film design, additive manufacturing, and advanced modeling substantially expands the range of achievable shape transformations in MRE-based systems, thereby enabling new opportunities for adaptive surfaces and reconfigurable soft devices.

# Résumé

Les élastomères magnétorhéologiques (EMR) sont des matériaux composites intelligents, constitués de particules magnétisables incorporées dans une matrice élastomère. Ils réagissent rapidement et de manière réversible aux champs magnétiques appliqués, par des déformations magnéto-induites ou des instabilités de surface provoquées par des contraintes magnéto-mécaniques couplées et des interactions magnétiques. Dans les systèmes de film EMR-substrat, ces instabilités peuvent être déclenchées par des charges mécaniques, magnétiques ou combinées, conduisant à des morphologies de surface allant d'ondulations périodiques à des motifs de plissement plus complexes. Malgré d'importants efforts expérimentaux et numériques, ces phénomènes ont jusqu'à présent été principalement limités aux films uniformes, donnant lieu à des motifs 2,5D avec une capacité d'ajustement restreinte. Cependant, l'obtention de morphologies de surface entièrement tridimensionnelles dans des films uniformes nécessite des champs magnétiques importants, tandis que l'instabilité est souvent confinée à des plages étroites de charges mécaniques. Ce travail vise à surmonter ces limites en permettant l'obtention de motifs de surface tridimensionnels contrôlables et ciblés grâce à l'introduction de propriétés magnéto-mécaniques hétérogènes dans les films EMR, rendue possible par des techniques de fabrication avancées.

Pour atteindre ces objectifs, une méthode de mélange actif pour les encres EMR est développée et mise en œuvre dans un processus de "direct ink writing" à l'aide d'un mélangeur hélicoïdal dynamique. Il s'agit de la première application de mélange actif aux EMR. Cette approche intégrée offre une façon fiable et reproductible d'imprimer des films EMR hétérogènes présentant une géométrie, une uniformité et des propriétés rhéologiques bien contrôlées. Une attention particulière est également portée à l'optimisation du procédé d'impression et à la compréhension du lien entre les paramètres de fabrication et les propriétés finales des structures obtenues. L'influence de paramètres tels que la vitesse d'extrusion, la géométrie de la buse, la vitesse de mélange et les propriétés rhéologiques des encres sur la qualité d'impression et la fidélité géométrique est analysée. Ces aspects sont essentiels pour garantir la reproductibilité et la précision des hétérogénéités introduites. Parallèlement, un modèle numérique tridimensionnel est établi pour capturer avec précision l'évolution des motifs de surface sous l'effet de champs magnétiques. Ce modèle utilise un cadre capable de reproduire la magnétisation, la magnétostriction et le comportement mécanique sur un large spectre de champs magnétiques. Les propriétés des matériaux sont identifiées expérimentalement et les profils de surface tridimensionnels sont mesurés par corrélation stéréo d'images numériques, ce qui permet de valider le

modèle numérique.

Grâce à cette approche expérimentale et numérique intégrée, ce travail examine de manière systématique l'évolution des motifs de surface dans les systèmes film EMR hétérogène-substrat. Par ailleurs, le modèle numérique permet d'explorer des configurations difficilement accessibles expérimentalement, offrant ainsi un outil prédictif pour la conception de nouvelles architectures EMR. Cette complémentarité entre expérimentation et simulation renforce la robustesse de l'approche proposée. L'influence de l'hétérogénéité du film sur l'apparition et la transformation des motifs de surface est examinée, révélant de nouvelles stratégies pour contrôler des morphologies tridimensionnelles complexes à l'aide de champs magnétiques. Dans l'ensemble, les résultats démontrent que la combinaison d'une conception de film hétérogène, de fabrication additive et d'une modélisation avancée élargit considérablement la gamme des transformations de forme réalisables dans les systèmes basés sur les EMR, ouvrant ainsi de nouvelles perspectives pour les surfaces adaptatives et les dispositifs souples reconfigurables.

# Acknowledgements

This thesis was conducted at the *Laboratoire de Mécanique des Solides (LMS)* as part of the doctoral program of Ecole Polytechnique and funded by the l'Agence nationale de la recherche (ANR).

First and foremost, I am immensely grateful to my thesis advisor, Professor Laurence Bodelot. It has been an honor and a privilege to work alongside her, and I am grateful for the knowledge and skills I have gained under her mentorship. I would also like to extend my sincere thanks to my thesis co-advisor, Professor Kostas Danas. His exceptional guidance and constructive feedback have significantly helped the development and quality of this work. I would also like to thank Professor Christelle Combescure and Professor Frederic Demoly for taking the time to read and comment on my thesis manuscript. My gratitude is also extended to the members of my thesis committee, Professor Joel Marthelot and Benoit Roman, for accepting to serve on my thesis committee.

I would also like to thank the staff and everyone at LMS for supporting me and providing a warm, helpful environment. In particular, I would like to thank Alexandra Joly, Anna Johnsson, and Valérie Jamet for their support with the administrative process. Furthermore, I am grateful for all the technical support that was provided by Abdelfattah Halim. I would also like to thank Matthieu Roy, Hakim Gharbi, and Simon Hallais for their great technical contributions during the experimental work. Moreover, I would like to thank my colleagues at LMS for their support and the wonderful, memorable times we shared together.

I would like to extend my deepest gratitude to Mr. Philippe Rolland for his immense support over the past three years and for welcoming me into his family. And my heartfelt thanks to my parents, Selvam and Sasikala, and my brothers, Venkatesh and Bala Govind, for their unconditional love, encouragement, and support throughout this endeavor. Their constant belief in my abilities has been a driving force behind my accomplishments. I am forever grateful for their sacrifices and support in performing my studies abroad.

# General introduction

Magneto-responsive soft materials are a promising class of functional systems capable of undergoing large, reversible deformations under external magnetic fields. Magnetorheological elastomers (MREs) are made by dispersing magnetizable particles in a flexible elastomer matrix. They are of special interest because they combine mechanical flexibility with fast, reversible actuation that can be precisely controlled by a magnetic field. Because of these features, MREs are useful in areas such as vibration control, soft robotics, adaptive surfaces, and tactile interfaces.

A distinctive feature of MREs is their strong magnetoelastic coupling, meaning that an applied magnetic field can generate internal stresses, modify stiffness, and induce large deformations. In thin MRE film/substrate systems, combined magneto-mechanical coupling can lead to the spontaneous formation of surface instabilities such as wrinkles, folds and localized crinkling patterns, similar to those observed in mechanically-driven systems. These surface deformations can be controlled by the applied magnetic field and evolve into pronounced surface morphologies, enabling dynamic, tunable pattern formation.

From a fundamental standpoint, magnetically-induced instabilities in soft materials represent a complex problem involving large deformations, interactions between magnetic fields and material, and bifurcation phenomena. From an applied perspective, they offer a route toward low-energy, fast and reversible surface actuation. In particular, surface morphing driven purely by magnetic fields is very promising for haptic and tactile devices, where it is important to rapidly switch surface textures on and off using realistically attainable magnetic fields.

Despite significant progress in recent years, the design of MRE systems that exhibit controllable, three-dimensional surface morphologies under magnetic loading alone remains challenging. These difficulties arise from both limitations in material fabrication and the complexity of predicting and controlling instability phenomena. Addressing these challenges requires a combined effort involving experimental fabrication, magnetic and mechanical characterization, testing strategy, and advanced numerical modeling.

## Motivation and research gap

Early studies on MRE film/substrate systems demonstrated that homogeneous MRE films subjected to magnetic loading typically develop surface patterns that are effectively two-and-a-half-dimensional, since they are extruded in a single direction, thereby reflecting the underlying material uniformity and geometric symmetry. While these systems provided important insight into magnetoelastic instability mechanisms, the resulting surface morphologies remain fundamentally limited in complexity.

Subsequent investigations revealed that introducing heterogeneity into the film, for example, through spatial variations in geometry, can lead to truly three-dimensional surface patterns. This observation highlights heterogeneity as a key design parameter for accessing more complex instability modes. However, traditional fabrication techniques, such as molding, offer limited control over material heterogeneity at the length scales relevant to instability pattern formation.

Additive manufacturing, particularly extrusion-based techniques, offers a potential way for fabricating heterogeneous MRE films. Nevertheless, printing soft magneto-active materials introduces its own challenges. In particular, commonly-used silicone matrices for MREs are often two-component systems with short pot lives, leading to continuous curing and rheological evolution after mixing. This evolution complicates extrusion-based printing, especially for particle-filled inks, as small changes in rheology can strongly affect flow stability and print fidelity.

Direct ink writing (DIW) has emerged as a promising technique for printing soft elastomers, provided that suitable rheological conditions are satisfied. While the use of rheological modifiers alleviates several limitations associated with the extrusion of material, the pot-life constraint of two-part silicones remains a major challenge. Current approaches to address this issue, such as feedback-controlled extrusion or chemical modification of the ink, either significantly increase process complexity or risk altering the material properties.

Alongside fabrication challenges, modeling magnetoelastic instabilities also presents substantial numerical difficulties. Surface pattern formation is highly sensitive to imperfections, boundary conditions and loading paths, making robust numerical frameworks essential. While two-dimensional models have provided valuable insight into instability onset and critical modes, they are insufficient for capturing fully three-dimensional surface patterns and complex material heterogeneities. Extending numerical models to three dimensions introduces additional challenges, including the treatment of the surrounding magnetic field and the increased computational cost associated with large-scale

simulations. Moreover, quantitative comparison between experiments and full-field three-dimensional simulations remains absent in the literature for heterogeneous MRE film-substrate systems. This gap restricts the ability to reliably predict surface morphologies and critical magnetic fields, which are essential for design-oriented applications.

Together, these observations reveal a clear research gap. There is a need for (i) fabrication strategies that enable controlled fabrication of heterogeneous MRE films without compromising pattern quality, (ii) experimental measurement approaches capable of accessing the full three-dimensional surface profile of the deformed geometry during magnetically-induced instabilities, and (iii) three-dimensional numerical models capable of predicting instability onset and post-bifurcation behavior under purely magnetic loading. Bridging this gap is essential for improving the fundamental understanding of magnetoelastic instabilities and enabling their practical exploitation in adaptive and haptic surfaces.

## Objectives of the thesis

The main objective of this thesis is to develop and study magnetorheological elastomer film-substrate systems that exhibit controllable, three-dimensional surface instabilities driven by magnetic fields, with particular emphasis on the role of geometry, material heterogeneity, and magnetic loading in governing three-dimensional instability modes and surface morphologies.

To achieve this goal, the specific objectives of the thesis are as follows:

- to develop a modified direct ink writing approach suitable for fabricating heterogeneous MRE films with improved control over material extrusion and print quality;
- to experimentally investigate the onset and evolution of magnetically induced surface instabilities in MRE film/substrate systems;
- to establish a full-field three-dimensional numerical framework capable of capturing instability initiation and post-bifurcation surface morphologies under magnetic loading
- to compare experimental observations with numerical predictions and identify key parameters governing instability modes and critical magnetic fields, and to analyze instability modes and post-bifurcation surface patterns through combined experimental measurements and numerical simulations.

Through this combined experimental and numerical investigation, the thesis aims to provide new insight into the design of magneto-active soft systems with enhanced three-dimensional patterning capabilities, while laying the foundation for future applications requiring rapid and energy-efficient surface actuation.

# Chapter 1
# State of the art

This chapter provides an overview of the classification and applications of magnetorheological elastomers (MREs), as well as of the experimental techniques and modeling approaches dedicated to these so-called "smart materials". Firstly, a brief description of the types of magnetic materials used for fabricating MREs is presented along with their respective applications. Secondly, the principles of magneto-elastic buckling instabilities are addressed, focusing on the formation of instabilities. Following this, the chapter outlines some conventional fabrication methodologies, emphasizing additive manufacturing of polymers in the context of MREs. It also introduces the fundamentals of flow rheology and the instruments and methods used for characterizing the rheological behavior of MREs. Next, different fundamental constitutive models of MREs at finite strains are reviewed, highlighting their key components and their treatment of the magneto-mechanical couplings. Finally, the scope of the present work is exposed, and the manuscript's organization is detailed as a guide for the following chapters.

**Contents:**


1.1 Magnetorheological elastomers (MREs) . . . 5
1.1.1 MREs among smart materials . . . 5
1.1.2 Classification of MREs . . . 6
1.1.3 Applications of MREs . . . 8
1.2 Magneto-elastic instabilities . . . 10
1.2.1 An overview of instabilities . . . 10
1.2.2 Magnetically-triggered instabilities . . . 11
1.2.3 Instabilities in film/substrate systems . . . 12
1.3 Fabrication aspects . . . 15
1.3.1 Fabrication of film/substrate systems . . . 15
1.3.2 Molding and other classical manufacturing techniques to fabricate MREs . . . 15
1.3.3 Additive manufacturing of MREs . . . 17
1.3.4 Rheology and rheometry . . . 19
1.4 Modeling of MREs and instabilities . . . 22
1.4.1 Modeling approaches in MREs . . . 22
1.4.2 Numerical treatment of instabilities . . . 23
1.5 Scope and organization of the thesis . . . 23

## 1.1 Magnetorheological elastomers (MREs)

### 1.1.1 MREs among smart materials

As discussed in the general introduction, since this study's motivation lies in tailored instability patterns formed by magneto-mechanical couplings in MREs, a comprehensive review of these materials is essential. MREs are a class of "smart" or "active" materials (Takagi 1990) that respond to an applied magnetic field in a reversible, pre-determined manner. Other smart materials include electroactive polymers, shape memory alloys, and piezoelectric ceramics, which respond to external stimuli such as electric fields, temperature, stress, etc (Bahl et al. 2020). Among these smart materials, the rapid response, the large deformations attained, and the precise control of these deformations by changing the magnetic field make MREs of special interest in modern technology (Li et al. 2013; Kang et al. 2020; Dhiman et al. 2024).

Early research on magneto-active materials primarily concentrated on magnetorheological fluids (MRFs), which usually contain micron-sized iron particles dispersed in a fluid medium (Rabinow 1948). In the presence of a magnetic field, the particles start to form aggregated chains parallel to the external field, effectively increasing the viscosity of the mixture (Ginder et al. 1996; Ginder 1998) or even changing its nature from Newtonian to non-Newtonian (Li et al. 2019). Due to these field-dependent material characteristics, MRFs are exploited in various vibration and damping control devices (Ginder 1998; Carlson and Spencer 2021). The main disadvantages of MRFs are the fact that the active fluid needs to be enclosed in a sealed container as well as the sedimentation of the suspended particles over time (Carlson and Jolly 2000), although the latter can be mitigated by adding surfactants like silica gel and stearates (Winslow 1949; Shtarkman 1991).

A more effective solution to these problems is to use a magnetorheological elastomer (MRE). In MREs, the magnetic particles are initially mixed into the fluid-like elastomer matrix but then remain locked in place within the cross-linked network of the cured elastomer. Hence, MREs are essentially elastomeric solids filled with magnetizable, mechanically stiff particles (Rigbi and Jilken 1983; Jolly et al. 1996; Ginder et al. 1999), as shown in Figure 1.1. When the magnetic particles get magnetized by an external magnetic field, each particle in the elastomer becomes a magnetic dipole and interacts with the other particles, thereby transmitting internal stresses within the composite. This interaction results in an increased material stiffness in a confined medium, and is known as the magnetorheological effect (or MR effect). The extent of the MR effect depends on the particles' volume fraction, size, and magnetic properties (i.e., relative permeability, magnetic saturation), as well as on the matrix's stiffness. In response to the external magnetic field, MREs can also exhibit large displacements due to the compass effect, and/or sizable strains if the matrix is soft enough due to a strong magneto-elastic coupling (Gin-

der et al. 2000; Danas et al. 2012; Bodelot et al. 2018). This latter magnetically-induced macroscopic deformation of MREs in a uniform magnetic field is (abusively) termed "magnetostriction"[1]. In all cases, the MRE swiftly retrieves its original state after the magnetic field is removed.

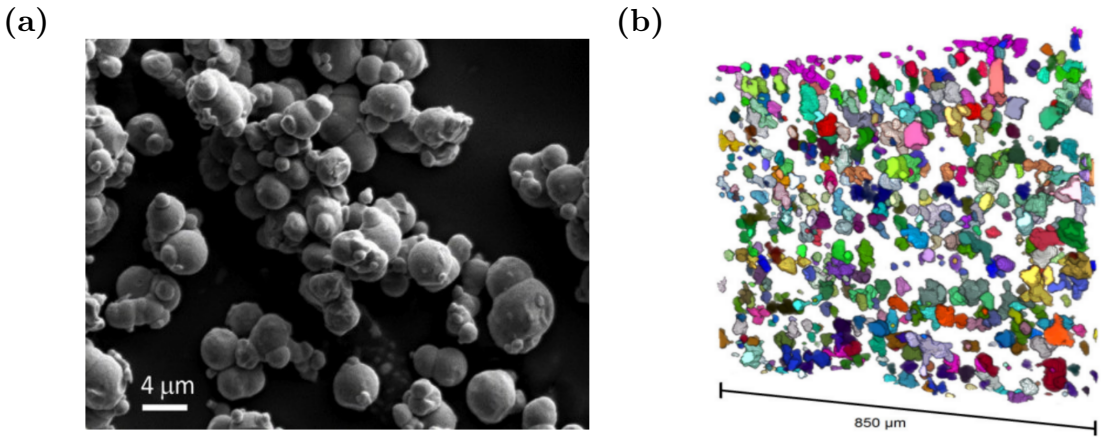


Figure 1.1: (a) Scanning electron microscope (SEM) image of carbonyl iron powder (CIP) particles in RTV 3325 silicone polymer matrix (Perales-Martínez et al. 2017). (b) 3D-reconstructed tomography data of particle microstructure in polydimethylsiloxane DMS-V25 polymer matrix (Schümann et al. 2017).

### 1.1.2 Classification of MREs

Different types of magnetic filler particles are reported in the literature, starting from highly magnetostrictive particles such as Terfenol-D (Duenas and Carman 2000) and NiMnGa (Chiu et al. 2023), to more common ferromagnetic materials like nickel, cobalt and iron alloys (Rigbi and Jilken 1983; Ausanio et al. 2011; Soledad Antonel et al. 2011). Among them, the most prominent type of particles used for fabricating MREs is carbonyl iron powder (CIP) (Gorodkin et al. 2009), due to its high saturation magnetization, high susceptibility, and low coercivity (soft-magnetic material) (Kusakawa and Otani 1964). Although these soft-magnetic materials can undergo strong magnetization in the direction of the applied magnetic field, they cannot retain the magnetization once the applied external field is removed (Jolly et al. 1996; Ginder et al. 1999; Gong et al. 2005). On the other hand, ferromagnetic particles of high-coercivity (hard-magnetic material) such as neodymium-iron-boron (NdFeB) possess the ability, once they have been magnetically saturated, to retain a certain amount of magnetization (remanent magnetization) after the applied magnetic field is removed (Deng et al. 2015). The particles' magnetic response depends on their chemical composition and underlying microstructure, and typical magnetization responses of the commercially available CIP and NdFeB particles are compared in Figure 1.2.

[1]In its proper definition, magnetostriction is an intrinsic property of a material that exhibits a change in volume and thus in shape when a magnetic field is applied. Note, however, that the largest magnetostriction, reported for Terfenol-D, is only in the order of 0.2%, whereas magnetically-induced macroscopic deformation in MREs can reach several % (Bodelot et al. 2018).

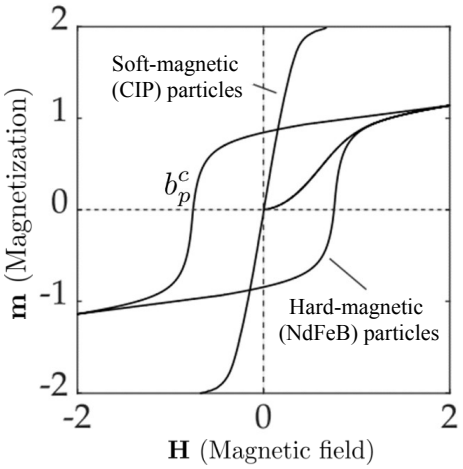


Figure 1.2: Comparison between soft- (CIP) and hard-magnetic (NdFeB) particles magnetization responses, adapted from Sugawa et al. (2013) and Deng et al. (2015).

Furthermore, based on the final orientation and arrangement of the magnetic particles within the matrix, MREs are classified as isotropic and anisotropic (Rudykh and Bertoldi 2013; Li et al. 2014) (see Figure 1.3). When the mixture is cured in the absence of a magnetic field, the particles stay distributed randomly and homogeneously, resulting in isotropic MREs (Lokander and Stenberg 2003; Sun et al. 2008; Boczkowska and Awietj 2012). In contrast, when a magnetic field is applied during the curing process, it aligns the particles in the direction of the magnetic flux, resulting in magnetic particles forming chains that remain locked in place during curing. Such MREs are known as anisotropic MREs (Wang et al. 2006; Li et al. 2014; Bodelot et al. 2018; Borin et al. 2019). More complex orientations of the particle chains can also be achieved using multi-axial magnetic fields during the fabrication process (Martin et al. 2004; Kim et al. 2018). Note that the number of particles that can be added to the matrix is limited by the maximum packing fraction, above which the viscosity of the mixture tends to infinity (Zhou et al. 1995), which makes the MRE difficult to process.

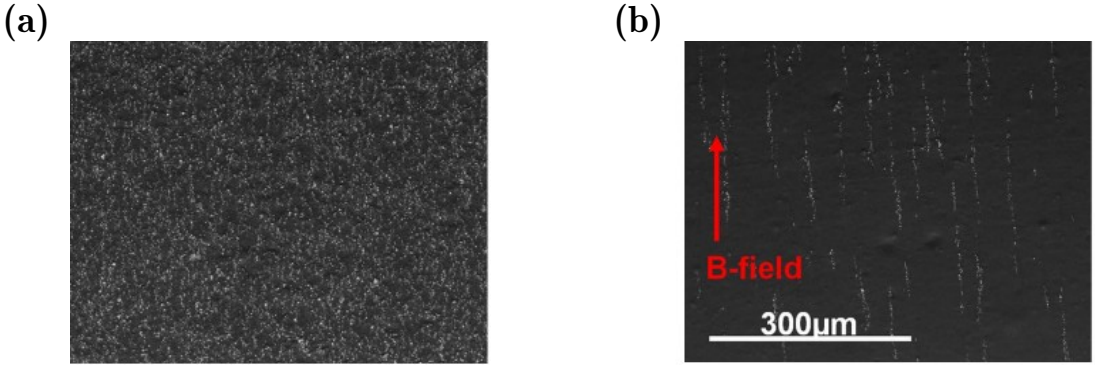


Figure 1.3: Scanning electron microscope (SEM) images of (a) an isotropic MRE exhibiting randomly distributed particles (30% CIP volume fraction in a silicone matrix) and (b) an anisotropic MRE exhibiting particle chains alignment (3.5% CIP volume fraction in a silicone matrix) (Pössinger et al. 2014).

### 1.1.3 Applications of MREs

Applications of MREs are based on two primary dominant features:

1. The alteration of their mechanical properties in the presence of the magnetic field (magnetorheological (MR) effect).

2. The modification of their geometrical configuration in the presence of the magnetic field (either due to the compass effect or due to "magnetostriction").

The MR effect in MREs has been primarily exploited in applications such as tunable dampers (Ginder et al. 1999; Li et al. 2014) and adaptive vibration absorbers (Ginder et al. 2000; Kim et al. 2011b; Liu and Xu 2019). The "magnetostriction" effect allows the material to exhibit large overall deformations in response to an applied external magnetic field, but is rarely used in practical applications as it requires rather high fields (Danas et al. 2012; Bodelot et al. 2018; Moreno-Mateos et al. 2022). In contrast, changes in geometrical configuration linked to the compass effect require much lower magnetic fields and thus have inspired several advanced applications, such as actuators (Kim et al. 2011a; Cao et al. 2021), soft robots (Kim et al. 2019; Xie et al. 2019; Xu et al. 2019), and evolving surface roughness for droplet or fluid manipulation (Shao et al. 2022; Zhou et al. 2022; Jing et al. 2023). MREs used for various applications are summarized in Figure 1.4.

Note that, among these applications, $s$-MREs[2] are primarily used for applications that leverage the MR effect or "magnetostriction". However, some applications have harnessed the compass effect by employing $s$-MREs in a varying/dynamic magnetic field gradient (Shao et al. 2022). In contrast, $h$-MREs[3] rely on the compass effect and can express more complex morphological shape changes under a uniform magnetic field due to their programmable nature (Kim et al. 2018; Ren et al. 2019; Bastola and Hossain 2021). A significant amount of research is also performed to harness the out-of-plane deformation of MREs for use in haptic or tactile devices (Vidal-Verdu and Hafez 2007; Alkhalaf et al. 2020; Christie et al. 2023). For instance, controlled patterns can be displayed on a surface by an MRE-based system to achieve a rapid (in the order of milliseconds) and reversible surface morphing. The present thesis focuses on such an application by harnessing the instability patterns formed at the surface of heterogeneous MRE film/substrate systems.

[2]Soft-magnetic MRE ($s$-MRE) describes an MRE fabricated using non-dissipative soft-magnetic particles

[3]Hard-magnetic MRE ($h$-MRE) describes an MRE fabricated using dissipative hard-magnetic particles

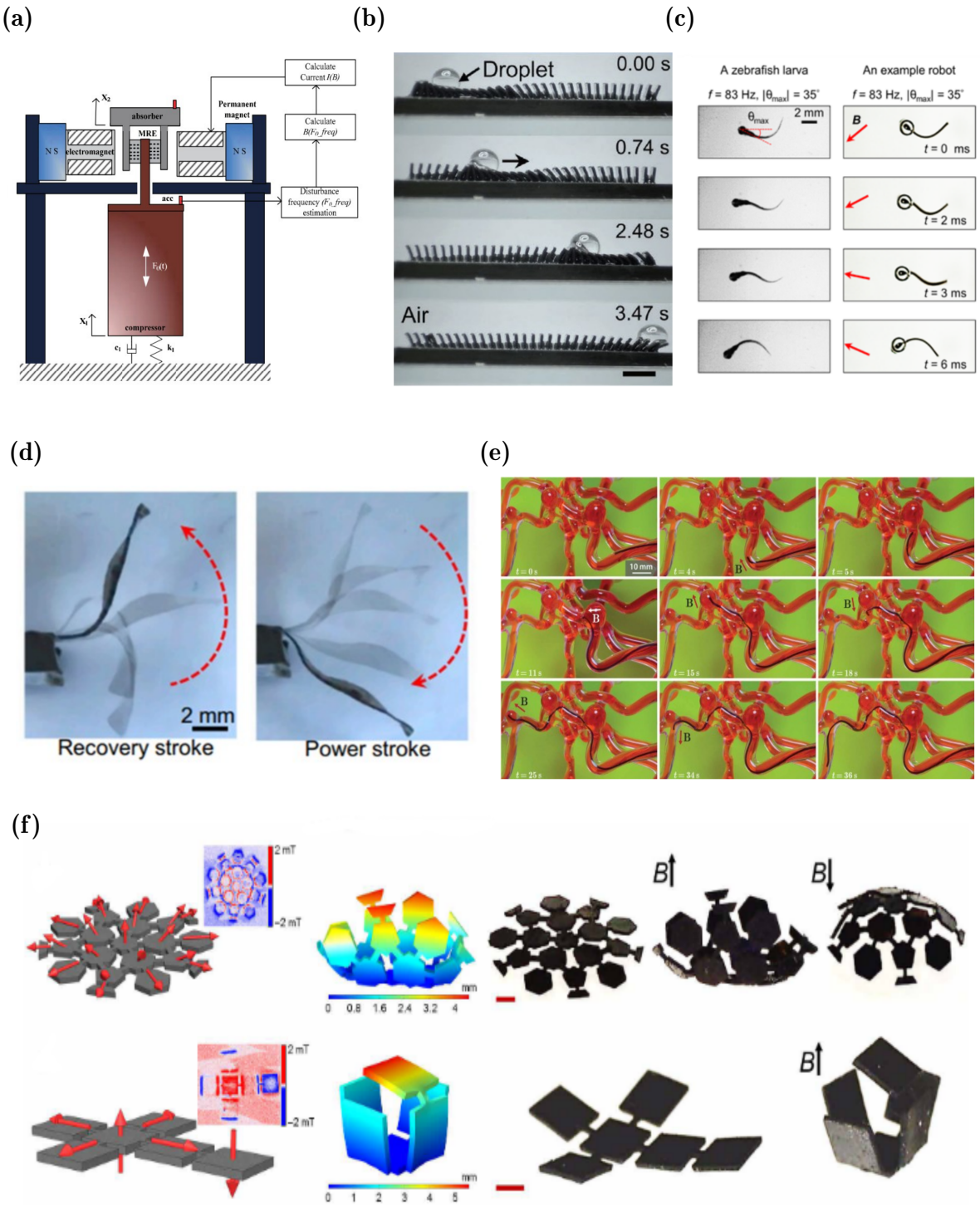


Figure 1.4: (a) An adaptive *s*-MRE-based tunable vibration absorber using a hybrid magnetic design (Li et al. 2014). (b) Multi-substance transport using lubricated slippery magnetic responsive microplate array developed using *s*-MRE (Shao et al. 2022). (c) A zebrafish larva-inspired *h*-MRE swimming microrobot controlled by an oscillating magnetic field (Wang et al. 2021a). (d) An *h*-MRE-based propelling system under external magnetic field. (e) An *h*-MRE-based soft robot navigating through a model of the cerebrovascular network (Kim et al. 2019). (f) Finite element simulations and experimental shape changes of *h*-MRE-based meta-structures upon magnetic loading (Alapan et al. 2020).

## 1.2 Magneto-elastic instabilities

### 1.2.1 An overview of instabilities

The buckling of elastic beams (also known as Euler buckling) under compressive axial loading is a classical instability problem in the field of elasticity. Elastic slender beams can indeed undergo large deformations as they experience a sudden lateral deformation under a critical compressive load. The critical load at which the beam buckles was first derived by Euler (1744) (see also (Euler 1759)), and later, the theory was further refined by Lagrange (1867). Since then, numerous studies have investigated the buckling phenomenon in various structures, including cylindrical shells (Timoshenko and Gere 2012), flat plates (Shanley 1947), and sandwich structures (Allen and Feng 1998).

Further research explored the buckling instabilities that occur in soft materials, specifically elastic rubber under compression and thin films under tension due to the transverse Poisson effect (Wang et al. 2022). Biot (1963) was the first to study this phenomenon using an elastomeric/rubber-like material under purely mechanical uniaxial compressive loading. He used a linear perturbation analysis of a semi-infinite neo-Hookean material that formulates an incremental boundary value problem with the flat state as a reference. The onset of wrinkles corresponds to the existence of a non-trivial solution to the incremental boundary value problem, which is an eigenvalue problem. Following this, Gent and Cho (1999) and Hohlfeld and Mahadevan (2011) showed that smooth wrinkles further develop into sharp, localized creases at specific critical compressive strains. In parallel, studies on tension-induced film instability, beginning in the early twenty-first century, revealed that a stretched sheet with clamped boundaries could experience compression within boundary layers, which leads to wrinkling in the sheet when a critical tensile load is reached. Cerda et al. (2002) demonstrated this by using a thin polyethylene sheet that was clamped and strained in the plane, resulting in wrinkling due to lateral deformation. This non-intuitive behavior arises because the clamped boundaries prevent the sheet from contracting laterally in their vicinity, creating a local biaxial state of stress at the center (Cerda and Mahadevan 2003).

Similarly, the most common buckling instabilities inducing surface patterns can also be observed in a thin, stiff film resting on a soft substrate, which will be explored in detail in subsection 1.2.3. These instabilities can form under different loading conditions, such as compression, swelling, and differential growth (Vandeparre et al. 2010). When the magnitude of the load reaches a specific critical value, the system loses stability, and its total energy is minimized, resulting in buckling instabilities. These instabilities are commonly observed in various biological systems found in nature, including buckling of cells (Ghosh et al. 2006), brain development (Richman et al. 1975), fingerprint formation (Kücken and Newell 2004), and formation of the gut inner layers (Hannezo et al. 2011).

Although instabilities were initially considered to be a mode of failure (e.g., buckling of cylindrical pipes (Chater and Hutchinson 1984) and of composite materials (Allen and Feng 1998; Hu et al. 2004)), due to their unique nature, they are now exploited for various applications such as flexible electronics (Hamers 2001; Khang et al. 2006; Kim et al. 2008), tunable optical devices (Koo et al. 2010; Lee et al. 2010), microfluidics (Chan et al. 2008; Khare et al. 2009), microlens arrays (Chan and Crosby 2006; Chandra et al. 2007) and tunable surface wettability (Chung et al. 2007; Ohzono and Monobe 2010). A lot of theoretical studies have been performed in recent years to further develop the understanding of instabilities with non-linear material properties (Li and Batra 2007; Goriely et al. 2008; Song et al. 2008; Li et al. 2010).

### 1.2.2 Magnetically-triggered instabilities

As previously discussed, instabilities are generally triggered by mechanical loads (which can be forces applied directly or forces resulting from, e.g., swelling) on structures such as slender beams, thin shells, or bi-layer systems. However, when such structures are made of magnetic materials and a magnetic field is applied, the slender object tries to rotate to align with the applied magnetic field due to the compass effect. However, if this rotation is constrained by the boundary conditions, instabilities can arise. Numerous studies have demonstrated this phenomenon, which is referred to as magneto-elastic buckling (Wallerstein and Peach 1972; Miya et al. 1978; Miya et al. 1980; Peach et al. 1988). Investigation into this theory dates back to 1968, when Moon and Pao (1968) studied the problem of magneto-elastic buckling of a thin metallic ferromagnetic plate subjected to a transverse magnetic field. They determined the critical buckling point of a magneto-elastic thin plate constrained in a transversely applied magnetic field, and their results were compared to experiments. Subsequently, much theoretical research has been done on the magneto-elastic buckling of MREs (Popelar 1972; Kankanala and Triantafyllidis 2008; Otténio et al. 2008; Rudykh and Bertoldi 2013). In later research, Huang et al. (2015) conducted buckling experiments using paramagnetic particle chains embedded in a soft polymer gel. In this study, the observed instability was due to the embedded particle chains rather than to the behavior of the entire body (Figure 1.5a) . In a recent study, Chen et al. (2023) investigated the buckling response of a composite system comprising a magnetoactive layer embedded within an inactive elastomeric matrix (see Figure 1.5b). They treated the stability using numerical analysis and a developed computational model based on experimental data. Their numerical model was verified against experiments, demonstrating its capability to predict the onset of magneto-mechanical instability and the post-buckling behavior of the MRE. In a recent study, Abbasi et al. (2024) introduced an innovative concept of a reversibly switchable braille dot for refreshable braille displays. This design utilizes bistable magnetic shells that can be snapped into place under an external magnetic field during the writing phase, while remaining stable against fingertip

pressure when being read (see Figure 1.5c). The bistable shell is created by sandwiching a circular $h$-MRE plate between two radially pre-stretched boundary annuli. Once the pre-stretch is released, it causes the plate to buckle into a shell shape. However, the complexity of the problem limits such a study to simpler MRE geometries, such as slender beams, thin plates, shells, and MRE blocks.

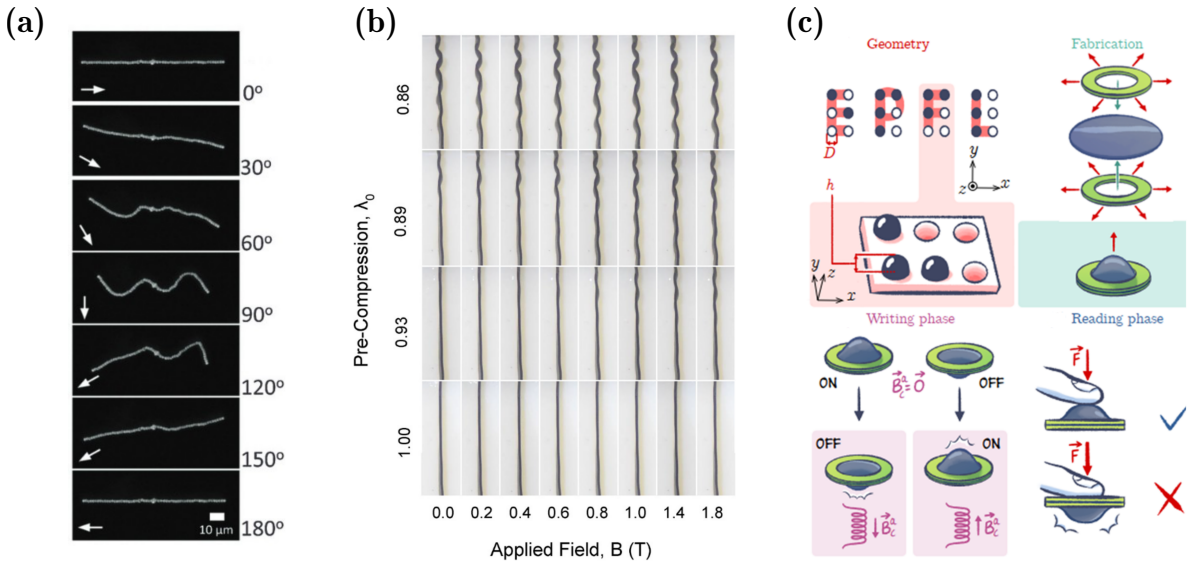


Figure 1.5: (a) Evolution of morphologies of magnetic chains in a soft gel with a magnetic field of increasing orientation (Huang et al. 2015). (b) Image array of a single-layer MRE laminate showing how pre-compression and magnetic field affect the amplitude of the wrinkles (Chen et al. 2023). (c) Tactile word formed from Braille cells, with each dot a bistable shell fabricated from a pre-stretched $h$-MRE disk. An external magnetic field programs dots as ON (bump) or OFF (dimple), which are read by a finger applying force (Abbasi et al. 2024).

### 1.2.3 Instabilities in film/substrate systems

As mentioned in subsection 1.2.1, surface instabilities are widely studied in bi-layer or film/substrate systems, as they are very common structures found in nature (Li et al. 2012). A bi-layer system consists of a thin elastic film bonded to a soft substrate (e.g., PDMS). It can undergo buckling instability due to a mismatch in the equilibrium states of the layers when a load is applied, leading to the formation of various morphological patterns on different lengthscales and allowing the system to reach a new equilibrium state. The resulting critical buckling mode is determined by the contrast in thickness and stiffness of the two layers (Jin et al. 2015). Bowden et al. (1998) was the first to investigate the instability patterns formed on the surface of a system consisting of mechanically stiff films resting on a passive compliant substrate. The stability of such systems is unique and stable until the load exceeds a critical value, after which the film bifurcates into a geometric mode influenced by the viscoelastic nature of the substrate. Some of the most commonly seen modes of mechanical surface instabilities in such systems are wrinkle, crease, delaminated-buckle, fold, period-double, and ridge, as illustrated in Figure 1.6. These types of instabilities primarily arise from unidirectional compressive loading.

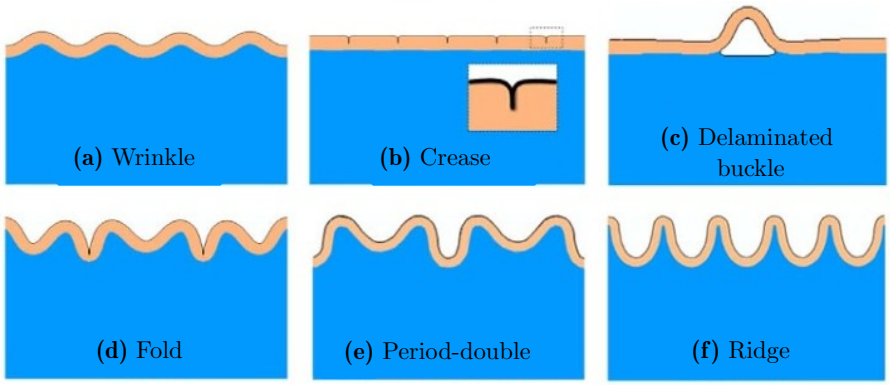


Figure 1.6: Schematics of different types of mechanical surface instabilities: (a) wrinkle, (b) crease, (c) delaminated-buckle, (d) fold, (e) period-double, and (f) ridge (Wang and Zhao 2015).

By applying more complex compressive loadings and altering material properties, these systems have demonstrated the capability to go further into secondary instability phenomena, going beyond simple wrinkling to complex surface patterns such as checkered board, hexagonal, triangular, herringbone and zig-zag patterns as illustrated in Figure 1.7 (Chen and Hutchinson 2004; Audoly and Boudaoud 2008a; Audoly and Boudaoud 2008b; Audoly and Boudaoud 2008c; Breid and Crosby 2011; Zang et al. 2012). The simultaneous occurrence of different modes has also been observed and analyzed, which is triggered by (equi-)biaxial in-plane compression, leading to intriguing two-dimensional patterns, such as segmented labyrinths and localized ridges (Cai et al. 2011; Cao et al. 2014).

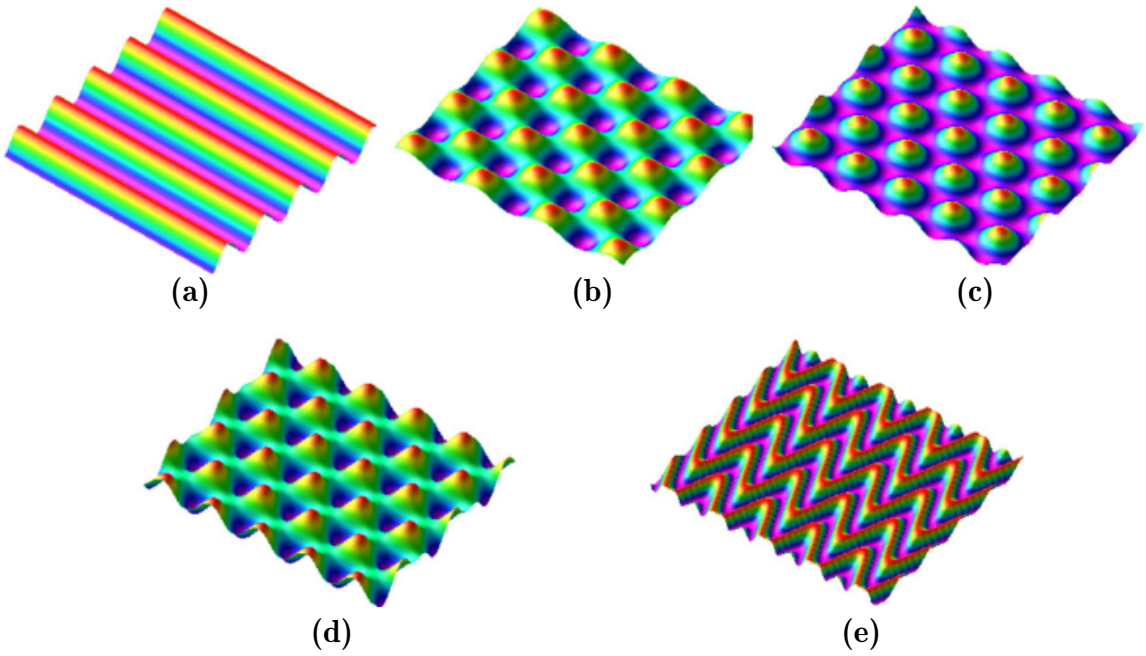


Figure 1.7: Schematic diagrams of the buckling patterns: (a) one-dimensional mode, (b) square checkerboard mode, (c) hexagonal mode, (d) equilateral triangular mode, and (e) herringbone mode under equi-biaxial compression (Zhang et al. 2014).

Effectively controlling such surface instability patterns formed by film/substrate systems requires coupled multi-physical stimuli like thermal expansion (Huck et al. 2000) and differential growth/swelling (Chan et al. 2008). Motivated by these investigations, Danas and Triantafyllidis (2014) theoretically analyzed the bifurcation response of an infinite MRE layer perfectly bonded to a non-magnetic soft substrate, subjected to a transverse magnetic field and lateral in-plane compression. The proposed model successfully estimated the onset of a bifurcation at different substrate-to-film shear moduli ratios ($G_s/G_f$) and pre-compressions. This was later experimentally verified using an MRE film/substrate system (Psarra et al. 2017), and it was successfully demonstrated that the magnetic field required to destabilize the system can be reduced by applying a mechanical field, specifically uniaxial pre-compression (see Figure 1.8). This study primarily focused on analyzing the evolution of "1D" wrinkle patterns (i.e., 1D patterns extruded along the depth) as a function of applied pre-compression and magnetic fields. Subsequent work addressed the evolution of wrinkles into more complex geometries, such as crinkles (Psarra et al. 2019). The study was then expanded numerically to include a wider range of materials and loading conditions using modified theoretical and numerical models (Rambausek et al. 2022). Additionally, the effects of biaxial pre-compression on the critical magnetic field were studied in comparison to those resulting from uniaxial pre-compression.

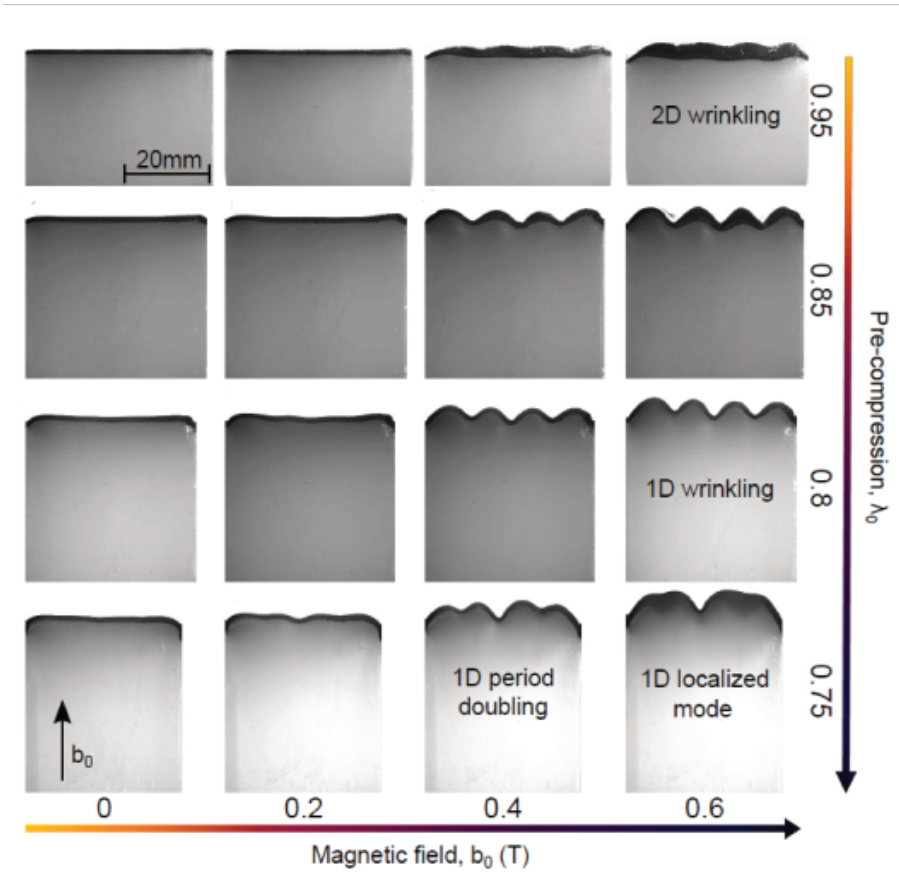


Figure 1.8: Optical images of the morphological pattern evolution of an MRE film/substrate system under magneto-mechanical loading conditions (Psarra et al. 2017).

## 1.3 Fabrication aspects

### 1.3.1 Fabrication of film/substrate systems

As discussed in subsection 1.2.3, stiff, thin films on soft substrates are one way to induce instability patterns. Numerous experimental strategies have been employed to obtain the patterns in a controlled environment, as illustrated in Figure 1.9a. Bowden et al. (1998) was the first to investigate this material system by depositing a thin layer of Au (50 nm) by e-beam evaporation onto an expanded polydimethylsiloxane (PDMS) substrate, using a 5 nm layer of Ti as an adhesion promoter. When the PDMS (initially expanded by heat) cools, the resulting compressive stress on the gold film leads to ordered wrinkling patterns (Huck et al. 2000). Jiang et al. (2007) studied the wavelength and amplitude of similar instability patterns using Si wafers on expanded PDMS. This was performed by covalently bonding thin-crystal Si ribbons onto the PDMS surface using chemical contact (Figure 1.9b). In another study, Chan et al. (2008) investigated the wrinkling patterns that occur when a photocurable nBA monomer is deposited onto a film of poly(n-butyl acrylate) PnBA polymer. This deposition causes the polymer to swell, and since the PnBA film is fixed to a rigid substrate, the lateral expansion of the polymer film is confined. Thus compressive forces are formed within the film, causing surface wrinkling (Figure 1.9c). Yin et al. (2014) used chemical oxidation to develop wrinkled morphologies on aqueous-phase-synthesized PDMS microspheres by mixing the microspheres in a $H_2SO_4/HNO_3/H_2O$ solution. This forms a stiff oxidized $SiO_x$ layer, thereby yielding a film/substrate system, and the differential growth/shrinkage leads to the development of wrinkled topologies (Figure 1.9d). A similar approach to creating a film/substrate system using chemical oxidation was explored by various authors (Efimenko et al. 2005; Zhao et al. 2015). Finally, Psarra et al. (2017) used a conventional molding technique to fabricate an MRE film onto a soft silicone substrate, using RTV Ecoflex™ 00-10 and 00-50 for the soft substrate and stiff film, respectively. The combined curing of the film and substrate yielded a well-bonded film/substrate system.

### 1.3.2 Molding and other classical manufacturing techniques to fabricate MREs

Since the main objective of the thesis is to effectively control the instability patterns formed on MRE film/substrate systems, it is essential to now review fabrication processes of MREs in detail. The traditional method for creating MREs involves mixing a polymer matrix with magnetic particles, degassing the mixture to eliminate air bubbles, and then curing the blend under mild temperature to accelerate the polymerization of the matrix (Pelteret and Steinmann 2019; Kang et al. 2020). Additionally, various additives can be added during mixing to enhance the mechanical properties of the matrix (Aziz et al. 2017; Poojary et al. 2018; Khairi et al. 2022). Furthermore, the particles can be pre-treated to increase the mechanical bonding between particles and matrix (Jiang et al. 2008; Fang

et al. 2010; Pössinger et al. 2014). Finally, as discussed before, depending on whether curing is performed in the presence of a magnetic field or not, anisotropic and isotropic MRE are achieved, respectively, as summarized in Figure 1.10.

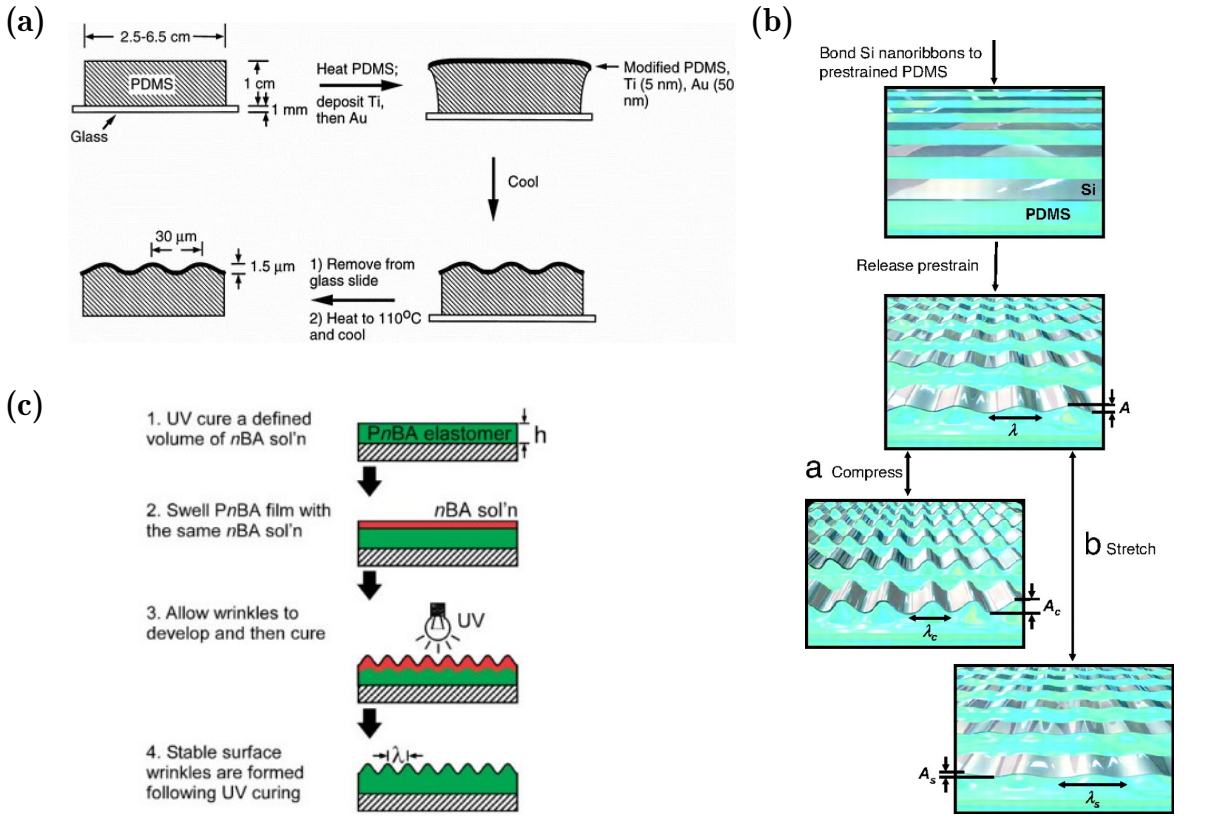


Figure 1.9: Different strategies to fabricate film/substrate systems. (a) Deposition of a thin layer of Au on a PDMS substrate using e-beam evaporation (Bowden et al. 1998). (b) Covalently bonded thin-crystal Si ribbons onto PDMS (Jiang et al. 2007). (c) Deposition of photocurable nBA monomer onto a film of PnBA polymer (Chan et al. 2008). (d) Chemical oxidation of PDMS microspheres using aqueous solution to form stiff oxidized layers (Yin et al. 2014).

Moreover, many studies also report other conventional manufacturing techniques, such as casting, to fabricate magnetorheological polymers with a thermoplastic matrix (Razzaq et al. 2012; Soto et al. 2018; Yarali et al. 2022). This technique requires a solvent, like poly(ethylene glycol) (PEG) or ethylene glycol (EG), to separate the polymeric chains. Once the solvent is poured into the mold with the polymer, it is removed using a vacuum oven (Wang et al. 2021b). The solvent evaporation from the polymer matrix causes

shrinkage, leading to dimensional changes. This issue is addressed by using a hot press (compression molding) once the solvent is evaporated. However, this process can lead to micro-cracks in the polymer matrix (Calvo-Correas et al. 2020). Additionally, methods like spin coating, spray deposition, and UV polymerization are also reported to fabricate MREs (Bratek-Skicki 2021; Yarali et al. 2022).

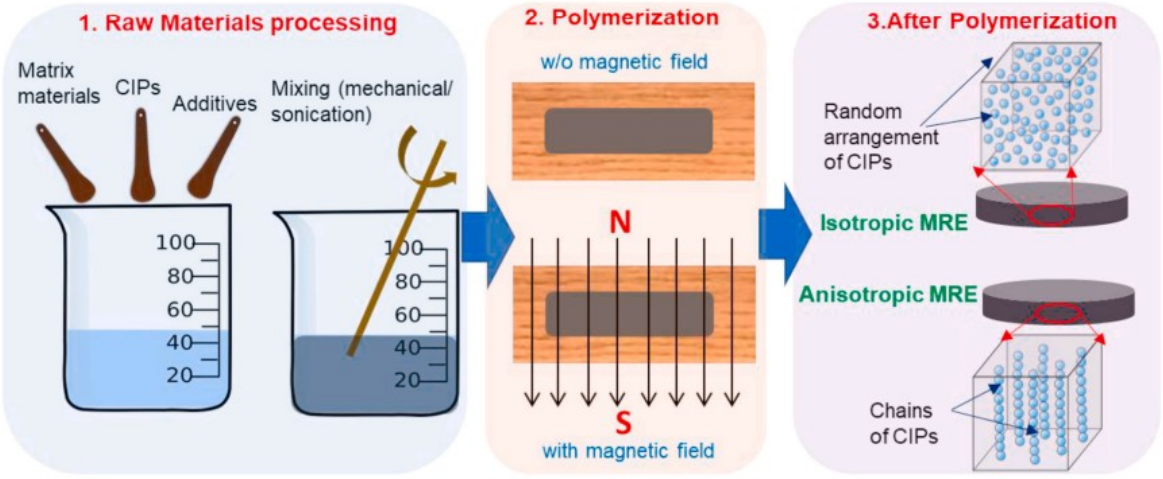


Figure 1.10: MRE fabrication methodology by a molding technique. Isotropic magneto-mechanical behavior is achieved if the curing is done without magnetic field, and anisotropic behavior is achieved when a magnetic field is applied during curing (Bastola et al. 2020).

### 1.3.3 Additive manufacturing of MREs

Additive manufacturing (AM), commonly called 3D printing, has gained significant popularity over the last decades due to its cost-effectiveness and reduced fabrication time in most cases (Falahati et al. 2020; Yarali et al. 2022). AM techniques have also become popular since they allow the creation of geometrically complex multi-material parts (Bandyopadhyay and Heer 2018) as well as the fabrication of more advanced structures, such as architected structures, by reducing fabrication complications (Meza et al. 2014; Xia et al. 2022). When AM is used to print smart materials that can respond to external stimuli, it reaches a higher functionality and performance. This advanced printing strategy is known as 4D printing, where the new dimension relates to the ability of the material to modify its properties with respect to time, thanks to external stimuli (Tibbits 2014; Quanjin et al. 2020).

Some well-known 3D printing techniques used for printing MREs (Figure 1.11) are fused deposition modeling (FDM) (Qi et al. 2019; Zhang et al. 2019), vat photopolymerization-based techniques (Lantean et al. 2019; Liu et al. 2022), inkjet printing (De Pedro et al. 2014; Song et al. 2014; Kolchanov et al. 2019), and direct ink writing (DIW) (Bastola et al. 2018; Kim et al. 2019; Guan et al. 2022; Te et al. 2022).

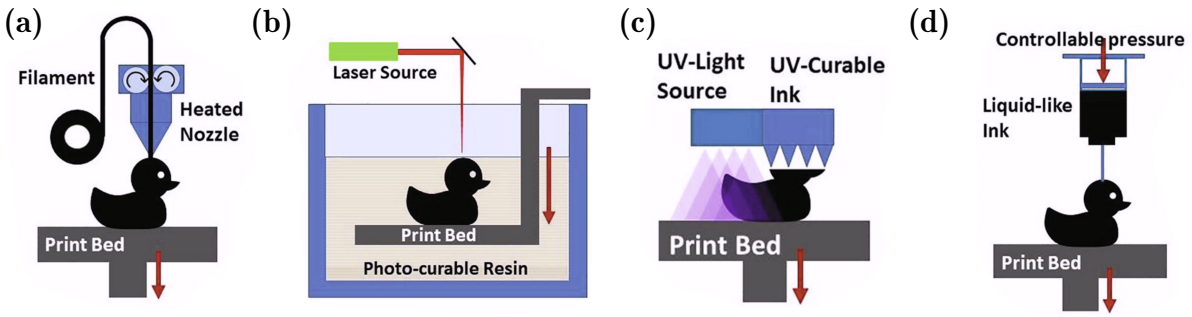


Figure 1.11: Schematic representation of well-known 3D printing techniques. (a) Fused deposition modeling (FDM) in which a filament is heated and extruded through a nozzle, depositing material layer by layer to form the 3D object. (b) Vat photopolymerization, here stereolithography (SLA), in which a liquid photopolymer resin is selectively cured by a UV laser or light source, solidifying the resin layer by layer. (c) Inkjet printing in which droplets of materials are precisely deposited onto a substrate, where they solidify or are cured layer by layer to build the structure. (d) Direct ink writing (DIW) in which a viscoelastic ink is extruded through a nozzle and directly deposited, with the shape maintained by the material's rheological properties and subsequent curing. (Falahati et al. 2020).

Fused deposition modeling (FDM), also known as fused filament fabrication (FFF), is an extrusion-based additive manufacturing technique particularly suitable for processing stiff thermoplastic polymers such as (poly)lactic acid (PLA), acrylonitrile butadiene styrene (ABS), thermoplastic polyurethane (TPU), polycarbonate (PC), and polyamides/nylons due to its ability to extrude high-viscosity materials (Lee et al. 2017). In this methodology, the thermoplastic filament is fed into a heated nozzle, melted, and extruded onto a heated print bed (Wickramasinghe et al. 2020). To print magneto-responsive polymer using FDM, the thermoplastic polymer (e.g., PLA) is first dissolved in a solvent to add magnetic particles to the solution. Then, the mixture is fed into an extruder to produce a magnetic filament suitable for the FDM printing process (Zhao et al. 2019). However, FDM is generally unsuitable for soft or elastomeric polymers due to both filament feeding and extrusion difficulties.

In vat photopolymerization-based methods, such as stereolithography (SLA) or digital light processing (DLP), a photo-reactive resin is polymerized layer by layer using a focused light (Nagarajan et al. 2020). Although this methodology can fabricate very fine parts, the resulting prints often show poor mechanical properties (Falahati et al. 2020). For fabricating MREs, magnetic nanoparticles are mixed within a photopolymer resin. However, filler-reinforced resins can have higher viscosity and high filler content can hinder light penetration and cure depth due to increased light absorption and scattering (Lantean et al. 2022). Consequently, this method is unconventional for printing polymers with opaque inclusions, particularly at higher particle volume fraction, which is considered in the present thesis.

The inkjet 3D printing technique deposits continuous ink droplets through a micro-sized nozzle, which are then polymerized using heat or UV light (Derby 2010; Bastola et al. 2023). It is primarily used for low-viscosity inks. As a result, factors like surface tension, density, and droplet shape play important roles in this technique (Sirringhaus and Shimoda 2003). Due to the micron size of the nozzle, this printing strategy is susceptible to clogging when used with magnetic particles. Additionally, adding particles increases the viscosity of the ink (De Pedro et al. 2014; Alamán et al. 2016), making it difficult to print MREs with this printing strategy.

Direct ink writing (DIW) is also an extrusion-based 3D printing method, where shear-thinning viscoelastic inks are extruded under shear stress and deposited on a heated bed to create 3D geometries (Lewis 2006; Yuk and Zhao 2018). DIW is the most popular 3D printing technique to fabricate MREs due to its ease of use and ability to print multi-materials at multiple scales with little restriction on particle content (Zhang et al. 2021). In DIW printing, various rheological properties (e.g., shear-thinning/thixotropy) and the shape fidelity ability of the ink should be investigated. Additionally, various print parameters such as print speed and die swelling ratio[4], extrusion rate and print height need to be optimized for a successful DIW printing process (Kim et al. 2019). For printing MREs using DIW, the magnetic particles are mixed in the polymeric matrix to form an active ink. The most popular polymeric matrix used for DIW printing includes heat-curable silicone-based polymers, hydrogels (e.g., polyethylene glycol (PEG), poly(ethylene glycol) diacrylate (PEGDA), and acrylamide (AAm)) (Chen et al. 2019; Podstawczyk et al. 2020; Tang et al. 2021). It is thus the most suitable method for printing very soft polymers, as it was derived from a robocasting printing technique that was previously developed to print particles containing slurry (Cesarano and Calvert 2000).

### 1.3.4 Rheology and rheometry

For an ink to be suitable for DIW, a specific rheological behavior is required: the ink should exhibit non-Newtonian shear-thinning properties, i.e., the viscosity of the material should decrease with the shear rate (Freundlich and Bircumshaw 1926; Myers et al. 1959; Hoffman and Myers 1960). As a consequence, when the material is extruded (Figure 1.12), the viscosity of the material decreases, permitting easy extrusion through the nozzle. Once deposited, it regains its viscosity and maintains its shape[5] (Rocha et al. 2020). To enable this for a Newtonian polymer, authors usually use inks that either contain rheological modifiers/additives such as non-silica powder to enhance the printability of the material or combine different elastomeric matrices, such as mixing soft and hard silicones, to achieve the required mechanical and printable properties (Kim et al. 2018; Zhou et al. 2019).

[4]Die-swelling is a phenomenon caused by the viscoelastic nature of the ink where the extruded filament's diameter is greater than the nozzle diameter.

[5]Depending on the material's properties, the time it takes to regain its viscosity varies.

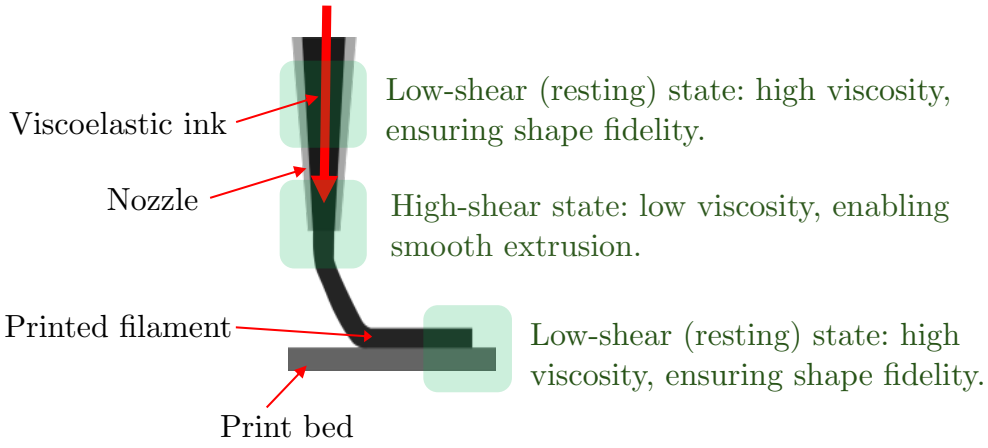


Figure 1.12: Schematic of the direct ink writing (DIW) process. When pressure is applied, the ink transitions from a low-shear, resting state to a high-shear state with low viscosity, enabling smooth extrusion through the nozzle. Once the ink is deposited onto the print bed, it returns to a low-shear, high-viscosity state, preserving the shape of the printed filament.

Rheometry refers to the methods/tests used to assess the rheological properties of materials and confirm whether the ink possesses the rheology required for DIW. More precisely, it provides a characterization of the viscous response of the material and, in turn, of its viscosity-shear rate dependency. Rheological tests are conducted using various setups to measure how fluids behave under diverse applied stresses. Different rheometer geometries are employed to evaluate the flow behavior of fluids, depending on the material type and specific measurement requirements. Standard configurations include capillary rheometers, which force the sample through a narrow die to determine shear viscosity at high shear rates, and Couette (concentric cylinder) rheometers, where fluid is sheared in the annular gap between two coaxial cylinders (Mezger 2020). Another common approach involves performing rotational and oscillatory tests with either a parallel-plate or cone-plate measuring system. In this method, the fluid is placed between two surfaces and sheared at different rates, and the resulting behavior of the fluid is measured (Mezger 2020).

The rheological characteristics of a DIW ink are commonly assessed by rotational rheological analysis. The corresponding analysis involves conducting a steady-shear flow sweep to determine the apparent viscosity ($\eta$) of the ink over a range of shear rates ($\dot{\gamma}$). Indeed, a DIW ink undergoes a wide range of shear rates during the printing process, ranging from approximately 0.01 $s^{-1}$ while at rest inside the syringe to shear rates exceeding 100 $s^{-1}$ during the extrusion process (see Figure 1.12). Therefore, it is essential to study how viscosity varies from very low to very high shear rates (Duty et al. 2018). During the rheological analysis, if the apparent viscosity increases at increased shear rates, the fluid is classified as shear thickening, making the extrusion challenging as the behavior will lead to nozzle clogging and will not facilitate flow extrusion through the nozzle (Wagner

and Brady 2009). However, if the apparent viscosity decreases at increased shear rates (indicating the sought shear-thinning behavior), extrusion of highly viscous inks will be possible at moderate shear rates. As illustrated in Figure 1.13a, the viscosity-shear rate curve for a shear-thinning fluid can be divided into three distinct regions (Chhabra and Richardson 2011). The first region is the zero shear viscosity region, where viscosity is measured at very low shear rates. In this region, the viscosity remains high and relatively constant. The second is the power-law region, characterized by a reduction in viscosity as the shear rate increases, which demonstrates shear-thinning behavior. Finally, the third region is the infinite shear viscosity region, where the viscosity approaches a low, constant value at very high shear rates. Shear-thinning behavior is thus essential for printing high-viscosity inks, and high viscosities at low shear rates help the extruded filament retain its geometry upon deposition (Chen et al. 2018).

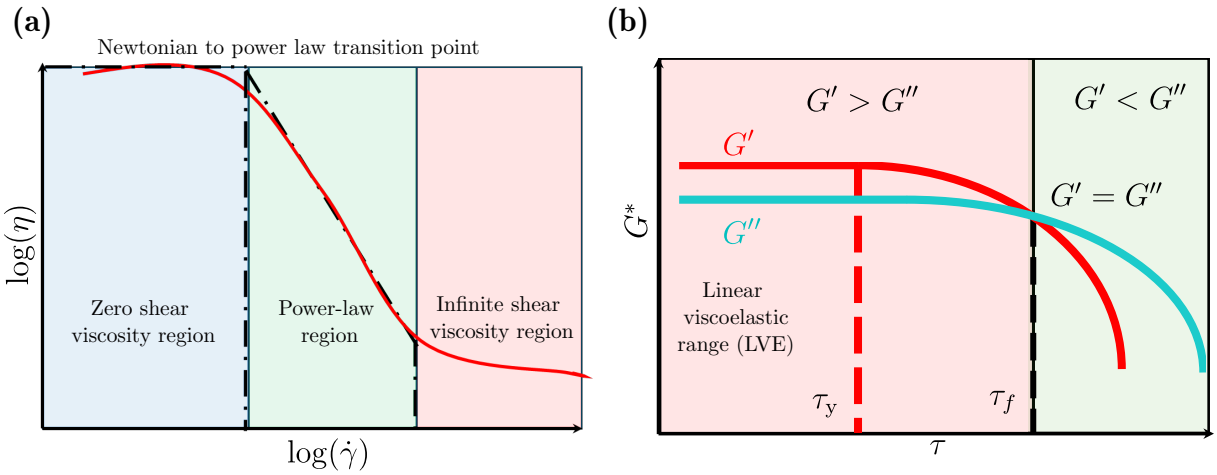


Figure 1.13: (a) A representative steady-shear flow sweep plot where the material exhibits non-Newtonian shear-thinning behavior. (b) A representative oscillatory strain sweep plotted against shear stress shows the transition of the fluid from solid/gel-like to liquid-like behavior. The red region indicates solid-like behavior, where $G' > G''$. In contrast, the green region represents liquid-like behavior, where $G' < G''$ once the stress reaches the flow stress $\tau_f$ of the material.

Additionally, oscillatory rheological analysis can also be performed to determine the ink's yield stress and viscoelastic properties. In an oscillatory amplitude sweep (see Figure 1.13b), an ink's complex modulus ($G^*$) is measured versus an increasing oscillatory amplitude of strain or stress ($\tau$) at a fixed frequency. In the linear viscoelastic (LVE) region, both the storage modulus ($G'$) and the loss modulus ($G''$) stay relatively constant with respect to applied stress. This means that the material maintains its internal structure when subjected to small amounts of stress. However, once the yield stress ($\tau_y$) is reached, there is a noticeable drop in the modulus, indicating that the material is starting to break down structurally. This test also reveals the crossover point or flow point ($\tau_f$), which is the stress level at which the storage modulus ($G'$) equals the loss modulus ($G''$). This measurement helps further characterize the behavior of the ink, whether as a liquid, gel, or solid, by determining which of the shear modulus or loss modulus is greater (Chhabra and Richardson 2011; Mezger 2020).

## 1.4 Modeling of MREs and instabilities

### 1.4.1 Modeling approaches in MREs

The growing interest in magnetorheological elastomers (MREs) over the past few decades has led to significant theoretical advances in understanding their strong non-linear magneto-elastic coupling behavior. The development of a mathematical foundation for coupled magneto-elastic behavior dates back to the 1960s–1970s (Truesdell and Toupin 1960; Brown 1966; Maugin and Eringen 1972a; Maugin and Eringen 1972b; Pao and Hutter 1975; Kovetz 2000). Building on this groundwork, Dorfmann and Ogden (2003) and Kankanala (2004) were the first to propose a magneto-mechanical variational formulation for nearly incompressible elastomeric matrices, using both Eulerian and Lagrangian approaches. Further developments of variational formulations in finite strains were presented in Dorfmann and Ogden (2004), Dorfmann and Ogden (2005), Kankanala and Triantafyllidis (2008), and Steigmann (2010), while Danas et al. (2012) extended the framework to anisotropic MREs. These approaches are typically classified as phenomenological models, as their constitutive equations are based on macroscopic experimental data.

In parallel, multi-scale homogenization approaches were developed, in which the magneto-mechanical problem is solved on a representative microscale domain and subsequently homogenized to obtain macroscopic responses (Ponte Castañeda and Galipeau 2011; Javili et al. 2013; Galipeau and Ponte Castañeda 2013; Kalina et al. 2016; Lefèvre et al. 2017; Danas 2017). The main advantage of such approaches is that they provide direct insight into the microscopic mechanisms driving magneto-elastic couplings. However, their major drawback is the heavy computational cost, especially when applied to large domains. Building on this idea, Keip and Rambausek (2016) and Keip and Rambausek (2017) introduced a two-scale finite element approach that simultaneously resolves the microstructural and macroscopic boundary value problems, enabling the study of size and shape effects.

More recently, a class of microstructurally guided phenomenological models has been proposed to reduce computational cost while retaining microstructural fidelity. These models combine homogenization principles with phenomenological formulations, offering a balance between accuracy and efficiency (Lefèvre et al. 2019; Mukherjee 2020). Across all these approaches, two main modeling formulations are commonly used: the **F**–**H** and the **F**–**B** formulations. Here, **F** denotes the deformation gradient, while **H** and **B** represent the magnetic field and magnetic induction, respectively. The distinction lies in the choice of the independent magnetic variable. The **F**–**H** formulation is scalar-potential based and computationally advantageous, as it reduces the nodal degrees of freedom. The **F**–**B** formulation is vector-potential based and computationally more demanding, but offers distinct advantages for certain classes of problems. This latter **F**–**B** version is particularly useful in boundary value problems such as instability analyses (see further

explanation in subsection 1.4.2) or device-level problems where magnetic poles and coils must be modeled (Dorn et al. 2021).

### 1.4.2 Numerical treatment of instabilities

The analysis of instabilities using finite element techniques also presents inherent challenges due to the complexity of the problem. Capturing local deformation instabilities of certain modes proves difficult due to their highly unstable nature (Audoly and Boudaoud 2008a). Traditionally, addressing these challenges in the context of purely mechanical problems involved employing multi-step processes, including separate pre- and post-instability analyses (Mei et al. 2011; Cao and Hutchinson 2012b). However, these methods are complex, computationally intensive, and often necessitate incorporating the wave or pattern into the model, thus influencing the subsequent formation of instabilities (Huck et al. 2000; Cao and Hutchinson 2012a). Later on, some authors adopted the "embedded imperfection" approach, in which perturbed elastic properties are assigned to specific elements at the film/substrate interface (Nikravesh and Shen 2022). Despite its simplicity in implementation for numerical problems, this approach lacks correlation with actual experimental results, and it remains difficult to determine the effects of imperfections on the stability modes. Finally, in the context of a coupled magneto-mechanical problem pertaining to a thin stiff magnetic film bonded to a soft non-magnetic substrate, works by Psarra et al. (2017) and Psarra et al. (2019) demonstrated that imperfections arise naturally from the non-uniformity of the magnetic field within the film, leading to numerical bifurcation without the need for user-defined geometrical imperfections. Moreover, in this case, using the **F**–**B** version of the model provides an additional benefit since it runs further without loss of convergence compared to the **F**–**H** version. This feature is crucial for instability studies, where capturing post-bifurcation behavior requires simulations to remain stable over an extended deformation range.

## 1.5 Scope and organization of the thesis

The instabilities formed in MRE film/substrate systems fabricated by the molding technique in Psarra et al. (2017) and Psarra et al. (2019) remained limited to so-called 2.5D patterns, i.e., 1D profiles extruded in one direction (see Figure 1.14a). This is mainly because of the uniformity of the film as a result of the molding fabrication process. Following this work, in order to break the uniformity of the MRE film and obtain 3D morphological patterns, Brusa Da Costa Linn et al. (2022) fabricated a heterogenous MRE film/substrate system in which four thin magneto-active discs were bonded to a non-magnetic thick, soft substrate and produced truly three-dimensional surface patterns upon applying a magnetic field (see Figure 1.14b). In this methodology, the discs and the layer surrounding the discs were printed using the liquid additive manufacturing (LAM) printing technique. MRE or pure silicone inks were prepared and subsequently extruded

from a syringe. Although this method simplifies the printing process without resorting to additional rheological modifiers, it has some limitations, including (1) the inability of the printed ink to maintain its shape due to its Newtonian nature, (2) unwanted extrusion caused by gravity, and (3) continuous rheological evolution of the printed ink since the mixing of the silicone two-part components was done prior to filling the syringe. Hence, an objective of this thesis is to address these limitations.

**(a)** Homogenous MRE film/substrate system

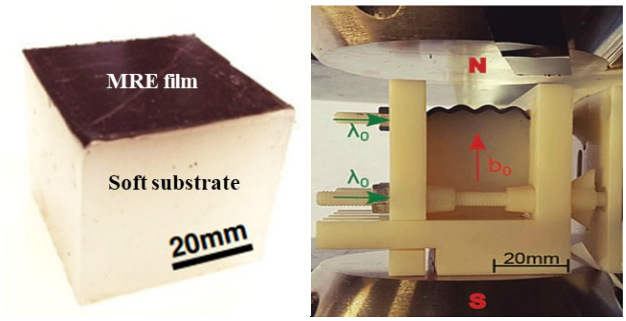


**(b)** Heterogenous MRE film/substrate system

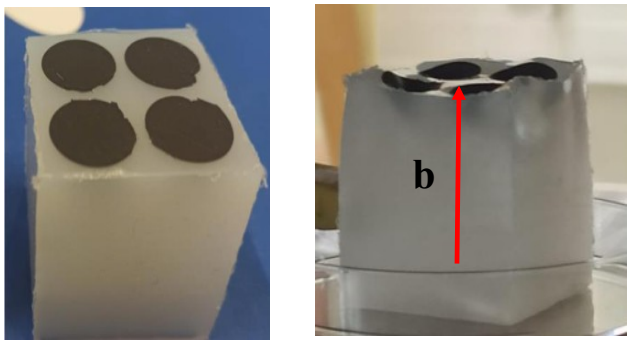


Figure 1.14: (a) Homogeneous MRE film/substrate system leading to 2.5D patterns under magnetic field (Psarra et al. 2017). (b) Heterogeneous MRE film/substrate system leading to 3D morphological patterns under magnetic field (Brusa Da Costa Linn et al. 2022).

As mentioned in subsection 1.3.3, direct ink writing (DIW) appears the most appropriate for the printing of silicones, provided they exhibit shear-thinning properties. This readily solves points (1) and (2) of the above-mentioned limitations encountered with LAM. However, point (3) still remains to be treated: in order to print soft polymers using the DIW technique successfully, the polymer filament should be continuously extruded, which requires a stable printing ink. Unfortunately, the most common soft polymer matrix for formulating MRE inks is a two-component heat-curing silicone that has a limited pot life[6] once the two components are mixed since the polymerization reaction starts upon mixing (Perrinet et al. 2020). Due to the continuous curing and rheological evolution of viscoelastic inks after preparation, print parameters such as input pressure and printing speed must be adjusted over time, which increases the complexity of the process. These effects are even more pronounced in the presence of particles, leading to abrupt changes

[6]Pot life: period for which two mutually reactive chemicals remain usable/workable when mixed before they begin to cure or harden.

in flow behavior and shortening the total printable time (Brusa Da Costa Linn et al. 2022). To address this challenge, a pressure-controlled extrusion system coupled with computational feedback was proposed by Lopez-Donaire et al. (2023), enabling real-time adjustment of printing conditions to compensate for curing-induced changes during deposition. Nevertheless, beyond remaining limited by the pot life of the blend, this method relies heavily on precise temperature regulation and is therefore not straightforward to implement. Alternatively, other studies have sought to extend the printable window by incorporating curing retardants into epoxy-based inks (Te et al. 2022), but this addition may have unpredictable effects on the performance of the elastomers (Zhou et al. 2019).

Recently, active mixing has been introduced into the DIW process as a strategy to homogenize complex fluids at the microscale during extrusion. This approach was first demonstrated by Ober et al. (2015) for thermally conductive inks. Their setup (Figure 1.15a) utilizes a dual-inlet, impeller-driven nozzle that effectively mixes multiple fluid streams directly at the extrusion point with high temporal precision. Building on this concept, Li et al. (2021) developed an active mixing method for ceramics (Figure 1.15b), where two ceramic inks are delivered into a confined chamber equipped with a rotating blade, allowing for the fabrication of continuous compositional gradients. More recently, Duncan et al. (2023) reported a system for viscoelastic inks (Figure 1.15c), in which two ink streams are continuously blended in a compact screw-impeller chamber before extrusion.

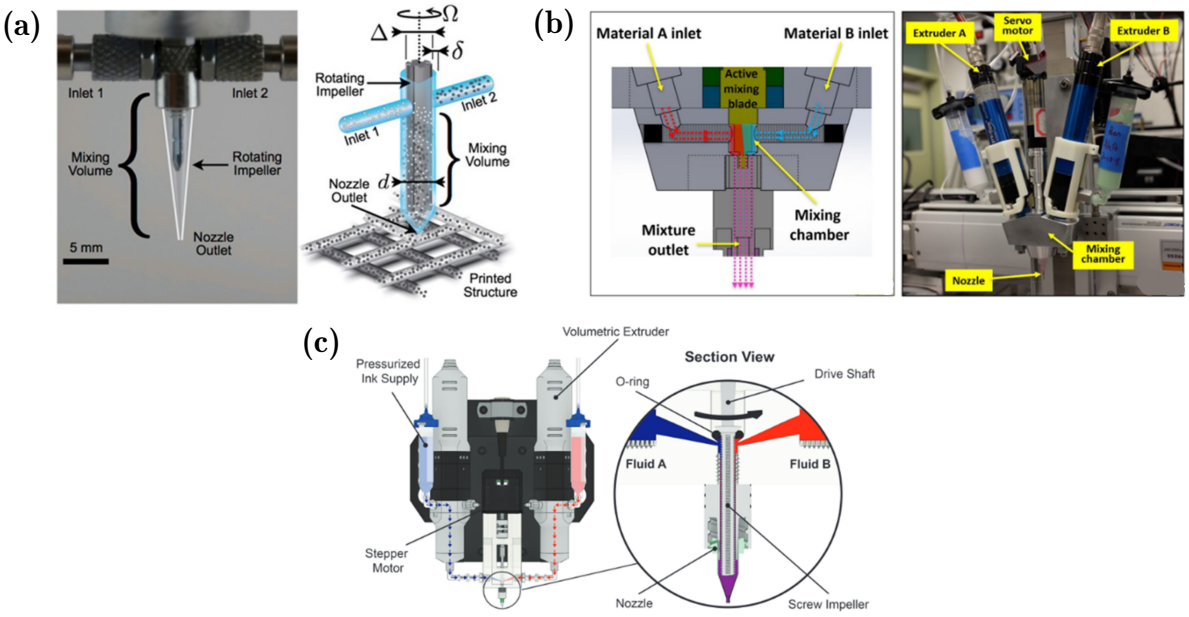


Figure 1.15: Active mixing DIW setups. (a) Dual-inlet impeller nozzle for microscale mixing (Ober et al. 2015). (b) Dual-extruder with active mixing blade for graded ceramics (Li et al. 2021). (c) Screw-impeller equipped extruder for continuous ink blending (Duncan et al. 2023).

Despite targeting different material classes, these systems share two defining characteristics: they rely on screw or blade mixers operating at high speeds for effective blending, and they confine mixing to very small volumes, which makes the process sensitive to flow

fluctuations and complicates the achievement of uniform mixing conditions. In chapter 2 of this thesis, we extend the concept of active mixing to MRE inks by employing a helical mixer integrated into the DIW process. To the best of our knowledge, active mixing strategies have not yet been reported for MREs, making this study the first to explore their potential for improving homogenization and print quality in this class of smart materials. The helical mixer provides the advantage of achieving efficient mixing at lower rotational speeds, and in our design it is complemented with a larger mixing chamber to increase residence time, thereby reducing sensitivity to flow fluctuations and improving uniformity.

As discussed in section 1.4, previous work in our group led to the development of a two-dimensional numerical model to study the profiles of instabilities formed over the homogeneous MRE film/substrate system shown in Figure 1.14a (Psarra et al. 2017), in particular with the $\mathbf{F} - \mathbf{B}$ formulation, where the constitutive equations are expressed directly in terms of the magnetic vector potential rather than the scalar potential. However, since the present investigation focuses on truly three-dimensional surface instabilities with more complex patterns, a full-field three-dimensional numerical framework is needed. The primary challenge of extending the model to 3D in chapter 3 of this thesis is the significantly larger computational domain required to represent the surrounding air, which increases the cost of the simulations. For the analysis of instabilities, we employ the material model presented by Mukherjee (2020) for isotropic MREs, which has proven to be highly versatile for analyzing instabilities, as demonstrated by Rambausek et al. (2022). It belongs to the class of homogenization-guided phenomenological models for isotropic MREs. These models are constructed through an appropriate choice of energy functions, and in such a way that they recover three main features of the homogenization model: (i) the exact effective magnetization response at both small and very large magnetic fields (i.e., at magnetization saturation), (ii) the exact magnetostriction response at small-to-moderate magnetic fields for all mechanical pre-loads, and (iii) a purely mechanical response that coincides exactly with that of the homogenization model. This extended version of the model is also straightforward to implement in a finite element user material/element subroutine, making it especially suited for the present 3D simulations. Additionally, different forms of Coulomb gauge regularization were considered and tested to make sure the magnetic vector potential remains unique without changing the actual magnetic field. This step greatly improves the numerical stability of the simulations, which is especially important in the 3D instability problem at hand. Since the formation of surface patterns is highly sensitive to small numerical perturbations, enforcing the right gauge condition helps eliminate unstable modes and ensures that the model captures only the true physical bifurcation behavior, leading to more reliable predictions of the critical fields and resulting morphological patterns. Aside from this numerical contribution, chapter 3 also presents the tests conducted to identify the properties of the materials at hand as well as the stereo

digital image correlation setup devised to measure the 3D profiles of heterogeneous MRE film/substrate systems under magnetic field for the purpose of validating the numerical predictions.

With these experimental and numerical tools in place, chapter 4 explores the surface-morphing behavior of heterogeneous film/substrate systems. The chapter examines how different MRE film designs and geometries influence the onset and evolution of instabilities. It then extends the analysis to full-field numerical studies, which provide detailed insight into the associated instability modes, and concludes with a systematic investigation of how topology, geometry and material contrast govern the resulting post-bifurcation surface morphologies.

Finally, a summary of the key results of this thesis is provided, and possible perspectives of future research inspired by the presented work are discussed.

# Chapter 2
# Active mixing-assisted direct ink writing

In this chapter, direct ink writing (DIW) with active mixing is introduced for the first time for magnetorheological elastomer (MRE) inks made of silicones having a short pot life, with the purpose of fabricating MRE heterogeneous films. This method keeps particle mixing steady and efficient during extrusion, which leads to filaments with even particle distribution. The chapter starts with an overview of the materials used in the ink formulation. It then provides a detailed rheological analysis, covering both static and dynamic tests to examine how inks flow at different particle contents. The setup of the 3D printer is described next, with attention to how the ink is formulated. The chapter also presents a systematic framework for choosing print parameters, such as mixer speed, nozzle shape, height ratio, printing speed, and extruder speed. Finally, the chapter discusses the combined effects of these print parameters and the quality of the obtained prints when multilayer printing is considered.

**Contents:**


2.1 Material selection . . . 29
2.1.1 Silicones and particles . . . 29
2.1.2 Selection of a rheology modifier . . . 30
2.1.3 Estimation of particle volume fraction . . . 30
2.2 Rheological characterization . . . 31
2.2.1 Static rheological analysis . . . 32
2.2.2 Dynamic rheological analysis . . . 35
2.3 3D printer setup . . . 39
2.3.1 General overview . . . 39
2.3.2 Ink preparation . . . 41
2.4 Print parameter selection . . . 43
2.4.1 Determination of the dynamic mixer speed $V_M$ . . . 45
2.4.2 Determination of nozzle geometry . . . 50
2.4.3 Determination of printing height $H$ and printing speed $V$ . . . 53
2.4.4 Determination of extruder speed $V_E$ . . . 55
2.5 Interdependency of print parameters and extension to multi-layer printing . . . 56
2.5.1 Combined effect of printing speed $V$, nozzle diameter $D$ and extruder speed $V_E$ . . . 57
2.5.2 Summary of print parameters . . . 58
2.5.3 Multi-layer printing . . . 60
2.6 Concluding remarks . . . 62

## 2.1 Material selection

### 2.1.1 Silicones and particles

To study the instabilities formed on the MRE film/substrate systems in the presence of a magnetic field, the employed silicones should be very soft to undergo large deformations in response to the field. For this study, we selected Ecoflex™ 00-10 as the substrate material and a stiffer Ecoflex™ 00-50 as the film material, obtained from Smooth-On Inc., USA, based on prior works (Psarra et al. 2017; Brusa Da Costa Linn et al. 2022). The material specifications of both elastomers are given in Table 2.1. A key reason for selecting this specific material configuration is its proven ability to produce a wrinkling instability due to the stiffness contrast. Both materials are incompressible and isotropic hyperelastic when fully cured.

| Properties | Substrate (Ecoflex™ 00-10) | Film (Ecoflex™ 00-50) |
|---|---|---|
| Shore hardness | 00-10 | 00-50 |
| Elongation at break (%) | 800 | 980 |
| Density $[kg/m^3]$ | 1.040 | 1.070 |
| Mixed viscosity [cps] | 4000 | 8000 |

Table 2.1: Material properties of the silicones used in this study (manufacturer's data).

Ecoflex™ elastomers are available as two-part, room-temperature-vulcanizing (RTV) silicones that cure through a platinum-catalyzed reaction. The two parts (part A contains the silicone elastomer and part B the platinum-based catalyst) must be mixed in a 1:1 ratio to initiate the curing process. Both the Ecoflex™ silicones have a limited pot life[1] of approximately 18 min. The addition of particles increases the mixed viscosity of the blend, and the heat generated during the mixing and degassing warms up the mixture, resulting in an expedited curing. However, the particles should be mixed thoroughly and the blend should be degassed (to eliminate entrapped air bubbles) for a sufficiently long period in order to achieve good dispersion and incompressibility[2], respectively. Hence, using the MRE ink with the two parts already mixed leaves very limited time for the actual printing process. This time constraint is addressed in this work by using an active mixing system that enables mixing the two parts during the printing process. This effectively extends the available print time through a continuous mixing and extrusion process, as will be detailed in section 2.3.

The magnetic filler used in this study is the carbonyl iron powder (CIP) SM procured from BASF, Germany. This powder consists of spherical particles with a median diameter of 3.5 $\mu m$ and contains mostly 99.8% Fe, with trace amounts of C, N, and O. The particles are considered magnetically soft (referred to as *s*-MRE in the study), defined by their low

[1]Pot life: period for which two mutually reactive chemicals remain usable/workable when mixed before they begin to cure or harden.

[2]Mixing and degassing times depend on the volume fraction of the particles added.

coercivity and magnetic saturation ($\mu_0 m_p^s = 2.5\ T$) (Haynes 2016). Consequently, it does not retain magnetization once the magnetic field is removed. The bulk density of the particles according to the manufacturer is between 1500 and 2500 $kg/m^3$ in powder form. However, this density becomes irrelevant when the particles are added to the viscous elastomer. Therefore, the density of the particles when inside the MRE is commonly considered to be that of the solid iron metal, i.e., 7874 $kg/m^3$ (Schubert 2014) or slightly lower than that of iron to account for the exact particle chemistry (Gorodkin et al. 2009).

### 2.1.2 Selection of a rheology modifier

As exposed in section 1.5, direct extrusion of MREs (via liquid additive manufacturing) possesses some limitations, including: (1) the inability of the printed ink to maintain its shape due to its Newtonian nature, (2) unwanted extrusion caused by gravity. Hence, to overcome these two limitations and render MREs amenable to direct ink writing (DIW), a liquid thixotropic agent called THIVEX® is used to transform the Newtonian polymer into a non-Newtonian material with shear-thinning and yield behaviors. In previous works of the literature, printable inks were often developed either by introducing additives like nanosilica particles to enhance the rheological properties of the material (Yuk and Zhao 2018; Zhou et al. 2019) or by combining different elastomeric matrices (Skylar-Scott et al. 2019; Yuk et al. 2020). However, if the addition of secondary phases or rheology-modifying agents improves printability, it also inevitably alters the final material properties. In our approach, we avoid the use of secondary fillers, since we aim to dedicate the entire "filler capacity" of the matrix to the incorporation of CIP, ensuring that the magnetic functionality is maximized without compromising the intended performance.

### 2.1.3 Estimation of particle volume fraction

During the fabrication process, the various material compounds are measured in different masses, namely $m_{CIP}$ for the mass of CIP particles, $m_A$ for silicone part A, $m_B$ for silicone part B, and $m_T$ for the mass of THIVEX®. The ratio of particles to silicone in this study is expressed in terms of parts per hundred rubber ($phr$)[3]. For the present formulation, 1 wt% of THIVEX® relative to the silicone mass (selection based on the rheological analysis discussed in subsection 2.2.1) is added, i.e., $m_T = 0.01\,(m_A + m_B)$. From this, the corresponding volume fraction $c$ of the particles can be estimated[4] using the CIP density ($\rho_{CIP}$), silicone elastomer density ($\rho_{sil}$), and THIVEX® density ($\rho_T \approx 1000\ kg/m^3$ based on manufacturer's data) as follows:

$$c \approx \frac{\frac{m_{CIP}}{\rho_{CIP}}}{\frac{m_{CIP}}{\rho_{CIP}} + \frac{(m_A+m_B)}{\rho_{sil}} + \frac{m_T}{\rho_T}} \approx \frac{\frac{phr}{100\,\rho_{CIP}}}{\frac{phr}{100\,\rho_{CIP}} + \frac{1}{\rho_{sil}} + \frac{0.01}{\rho_T}}. \tag{2.1}$$

[3] $phr$ is defined as the mass of filler per hundred mass of raw polymer: $phr = m_{CIP}/(m_A + m_B) \times 100$.
[4] It is assumed that the silicone matrix mass and volume in liquid and cured form are conserved.

In compact form, this expression can be written as:

$$c \approx \left[1 + \frac{100}{phr}\,\rho_{CIP}\left(\frac{1}{\rho_{sil}} + \frac{0.01}{\rho_T}\right)\right]^{-1}. \tag{2.2}$$

In this work, MRE inks with concentrations of 70, 140 and 210 *phr* are investigated. Ecoflex™ 00-50 silicone elastomer is used to formulate the MRE ink, resulting in corresponding volume fractions of 8.5, 15.6 and 21.7 %. To evaluate the effectiveness of this formulation strategy and to better understand how the additives influence the material's rheology, the next section investigates the flow behavior of different ink formulations.

## 2.2 Rheological characterization

Herein, the effects of both THIVEX® and CIP particles on the flow behavior of Ecoflex™ 00-50 silicone[5] are studied to determine shear-thinning and yield stress properties through steady-state and dynamic rheological tests, respectively, aiming to meet the rheological requirements for DIW. The rheological properties of the inks are measured using a rheometer (Anton Paar MCR 502) equipped with a parallel-plate measuring system of diameter 50 mm and with a gap of 0.5 mm. As sketched in Figure 2.1a, the inks are prepared by weighing all components according to the desired volume fraction estimate. The constituents are then thoroughly mixed for 5 min using a rotating drill at 1100 rpm to achieve a homogeneous dispersion of the particles. To eliminate any trapped air bubbles that might influence the rheological properties, the mixture is degassed under vacuum for 5 min. All the rheological analyses are performed within the pot life of the polymer to avoid the effects of curing. Finally, all the tests are conducted at a standard room temperature of 25°C and repeated three times.

Once prepared, each sample is loaded within the rheometer plates following precise recommendations for such a test (Kukla et al. 2018). As a matter of fact, care should be taken to avoid overfilling, which can cause sample overflow or edge effects, as well as under-filling, which may lead to poor surface contact and uneven shear (see corresponding sketches in Figure 2.1b). Perfect loading involves placing a volume slightly greater than the intended gap on the lower plate, then bringing the upper plate into contact and removing any surplus material, thereby ensuring that the measurement gap is fully occupied without voids. Additionally, applying uniform, gentle pressure when lowering the upper plate helps distribute the sample evenly while minimizing air entrapment.

[5]For fluids with suspension, the flow properties depend on many parameters like particle size, particle distribution, particle shape, particle concentration, and the properties of the suspending medium (And and De Kee 2001).

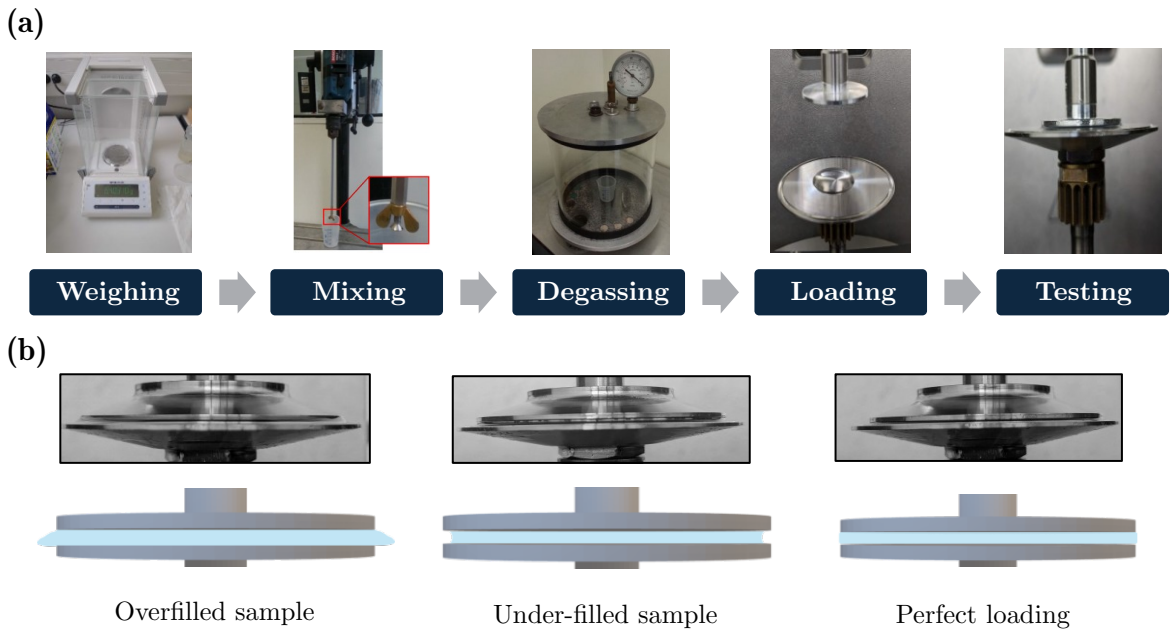


Figure 2.1: (a) Ink preparation process, including weighing, thorough mixing of components, and degassing to eliminate entrapped air, followed by loading into the rheometer and testing using a parallel-plate measuring system. (b) Overfilling and under-filling of the sample in a parallel plate rheometer, and perfect loading involving trimming the excess material after the upper plate is lowered to ensure proper gap filling so as to avoid edge effects.

### 2.2.1 Static rheological analysis

In the static rheological analysis, the apparent viscosity $\eta$ of different inks is measured by applying a controlled steady shear rate $\dot{\gamma}$. For a parallel plate rheometer with plate radius $R$ and gap $h$, if the upper plate rotates at an angular velocity $\Omega$ and the torque $M$ is measured, the steady shear parameters are obtained as follows (Morrison 2001):

$$\text{Shear rate at the rim:} \quad \dot{\gamma}_R = \frac{\Omega R}{h}. \tag{2.3}$$

$$\text{Shear stress at the rim:} \quad \tau_R = \frac{2M}{\pi R^3}. \tag{2.4}$$

$$\text{Viscosity:} \quad \eta = \frac{\tau_R}{\dot{\gamma}_R} = \frac{2M}{\pi R^3} \cdot \frac{h}{\Omega R} = \frac{2Mh}{\pi R^4 \Omega}. \tag{2.5}$$

Representing the apparent viscosity $\eta$ as a function of shear rate $\dot{\gamma}$ provides information on the flow behavior of the inks. In the present case, the inks are subjected to a steady shear rate sweep within a shear rate range of 0.01–1000 $s^{-1}$ in order to characterize the flow behavior across values that are representative of what is encountered in the DIW extrusion process. However, when measuring at shear rates $\dot{\gamma} < 1\ s^{-1}$, it is important to ensure that the measuring point duration is long enough. Otherwise, start-up effects or time-dependent transition effects are obtained. As a rule of thumb, the measuring point duration should be selected to be at least as long as the value of the reciprocal shear rate $(1/\dot{\gamma})$ (Mezger 2020). Additionally, all the experiments are conducted by starting at a

higher shear rate and moving towards a lower shear rate (down-sweep test). This approach is taken to minimize the torque effects caused by the surface tension of the fluid during the relative rotation of the plates (Johnston and Ewoldt 2013). Indeed, at low shear rates the torque measured by the rheometer can be very small. Furthermore, in soft low-viscosity fluids like silicones, surface tension at the air-fluid interface can introduce extra resistance, and this effect can mask the actual torque generated by the fluid flow, thereby giving inaccurate viscosity readings. To minimize this error, the experiments begin at a high shear rate, where torque is large and surface tension effects are negligible, and then decrease in steps to lower shear rates. This method allows the instrument to stabilize the fluid flow beforehand, consequently reducing the artificial torque contributions from surface tension. Rheometer parameters used for this study are given in Table 2.2.

| Method | Measuring system | Plate diameter (mm) | Gap height (mm) | Shear rate range ($s^{-1}$) | Temperature (°C) |
|---|---|---|---|---|---|
| Rotational | Parallel plate | 50 | 0.5 | 0.01–1000 | 25 |

Table 2.2: Rheometer parameters for rotational tests.

With these considerations, the rheological response of the base Ecoflex™ 00-50 silicone polymer is first characterized prior to examining the modified inks, so as to establish a reference for other ink formulations containing additives. In Figure 2.2a, the apparent viscosity is plotted as a function of shear rate and compares the Ecoflex™ 00-50 silicone flow behavior without and with 1 wt% THIVEX®. The base Ecoflex™ 00-50 polymer exhibits Newtonian behavior, with viscosity remaining nearly constant across the tested shear rates. When 1 wt% of THIVEX® is added, the zero-shear viscosity (viscosity at a very low shear rate) of the mix increases by about three orders of magnitude. Hence, by adding THIVEX®, the silicone clearly transitions from a purely Newtonian to a non-Newtonian shear-thinning behavior marked by a significant drop in viscosity when the shear rate increases. This shear-thinning effect of the THIVEX® will be crucial in reducing the base Ecoflex™ 00-50 silicone's low-viscosity free-flowing nature and in preventing distortions of printed patterns. Additionally, note that for a non-Newtonian shear-thinning fluid, a hysteresis loop forms during rheological tests when conducted from lower to higher shear rates (up-sweep test) and higher to lower shear rates (down-sweep test) due to the ink's viscoelastic nature, as indeed observed in Figure 2.2b. However, since our goal is to perform a comparison study between different inks with varying rheological properties, we only focus on the down-sweep curves in what follows, since this method helps minimize the surface tension-related error discussed earlier.

Next, we set out to identify the optimal amount of THIVEX® to be added to the base Ecoflex™ 00-50 silicone. The effects of different wt% of THIVEX® on the flow characteristics of Ecoflex™ 00-50 silicone are reported in Figure 2.3, in terms of the variation of apparent viscosity with shear rate. The viscosity of the Ecoflex™ 00-50 silicone mixture increases until 2 wt% of THIVEX® and then gradually drops. Further increase of

THIVEX® content actually slightly hinders the zero-shear viscosity of the ink. Since there is no significant increase in viscosity between 1 and 2 wt%, 1 wt% of THIVEX® is selected for the subsequent fabrication of MREs.

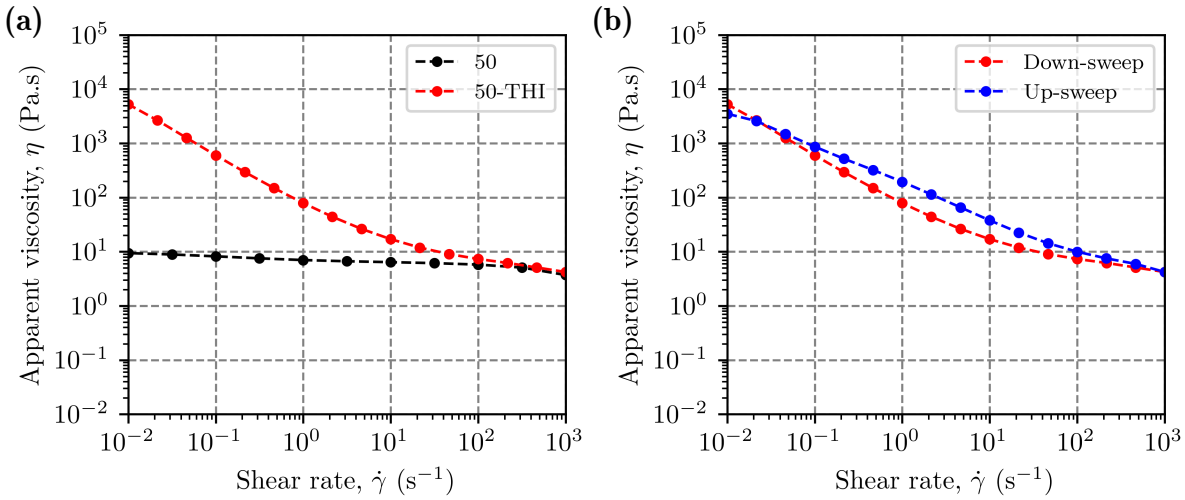


Figure 2.2: (a) Viscosity response of base Ecoflex™ 00-50 silicone without and with 1 wt% THIVEX®. (b) Rheological hysteresis loop of Ecoflex™ 00-50 silicone mixed with 1 wt% THIVEX® formed between shear rate down-sweep and up-sweep tests.

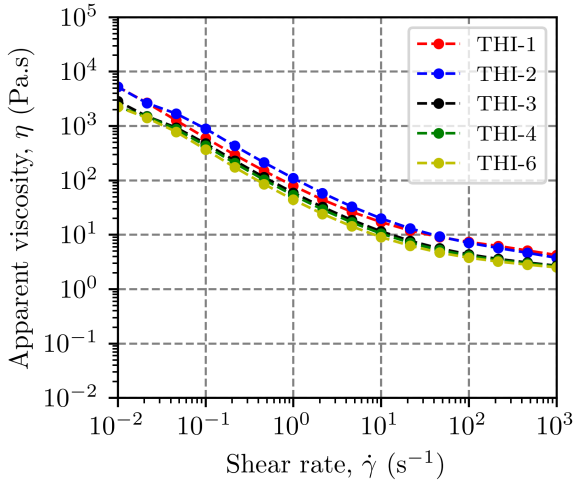


Figure 2.3: Viscosity response of Ecoflex™ 00-50 silicone mixed with varying wt% of THIVEX®.

In Figure 2.4a, the same rheological test is performed on Ecoflex™ 00-50 base silicone with different concentrations of CIP particles (70, 140 and 210 *phr*). The addition of CIP also induces a shear-thinning response, as the apparent viscosity decreases with increasing shear rate. However, the zero-shear viscosity in this case remains relatively low compared to a mixture containing THIVEX® (Figure 2.3). Even at the highest particle loading of 210 *phr*, the viscosity at low shear-rates remains below that of Ecoflex™ 00-50 with only 1 wt% of THIVEX®. In contrast, as evidenced in Figure 2.4b, the incorporation of 1 wt% of THIVEX® in combination with CIP significantly increases the zero-shear viscosity of the ink, as it now reaches $10^4$ Pa.s and beyond. This effect is further highlighted in Figure 2.4c, which reports the zero-shear viscosity of the MRE ink with and without

1 wt% of THIVEX® for different *phr* values. This suggests that while CIP particles raise the overall viscosity and contribute to shear-thinning behavior, THIVEX® primarily controls the low-shear rheology by creating much stronger resistance to flow at rest. This modified rheology is crucial for DIW applications in order for the ink to maintain its shape fidelity after extrusion and ensure good printing resolution (Lewis 2006; Rocha et al. 2020).

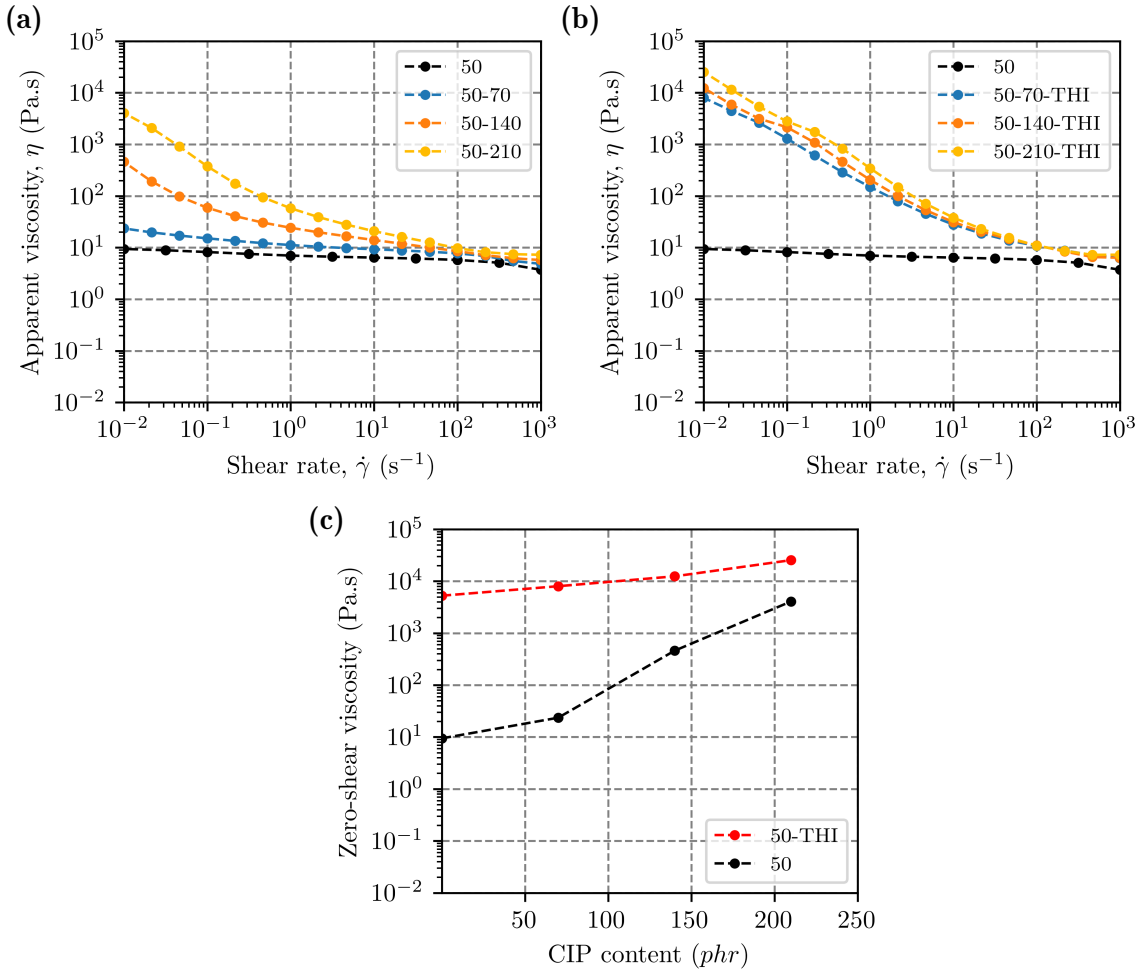


Figure 2.4: Effect of additives on the flow behavior of Ecoflex™ 00-50. (a) Base Ecoflex™ 00-50 silicone without and with different contents (70, 140 and 210 *phr*) of carbonyl iron powder (CIP). (b) Base Ecoflex™ 00-50 silicone with both 1 wt% THIVEX® and different contents (70, 140 and 210 *phr*) of CIP. (c) Zero-shear viscosity of Ecoflex™ 00-50 silicone with 1 wt% and without THIVEX® for different contents of CIP.

### 2.2.2 Dynamic rheological analysis

Additionally, to investigate the yielding behavior resulting from the viscoelastic nature of the materials, dynamic oscillatory rheological tests are performed. In these tests, the rheometer imposes a small-amplitude sinusoidal shear strain $\gamma(t)$ with time $t$, and the corresponding stress response $\tau(t)$ is measured. After transient effects have decayed, the stress signal becomes sinusoidal with the same angular frequency $\omega$ but is shifted in phase by an angle $\delta$ relative to the applied strain. If the time origin is chosen such that $t = 0$

corresponds to the maximum strain, the strain and stress are expressed as (Ferry 1948; Ferry and Myers 1961):

$$\gamma(t) = \gamma_0 \sin(\omega t), \tag{2.6}$$

$$\tau(t) = \tau_0 \sin(\omega t + \delta), \tag{2.7}$$

where $\gamma_0$ and $\tau_0$ are the amplitudes of the shear strain and shear stress, respectively.

It is convenient to transfer the strain and stress functions into the frequency domain as their complex quantities using the algebraic operations used in harmonic systems:

$$\gamma^* = \gamma_0 \exp(i\omega t), \tag{2.8}$$

$$\tau^* = \tau_0 \exp(i(\omega t + \delta)). \tag{2.9}$$

The ratio of complex stress to complex strain then defines the complex shear modulus $G^*$, which can be decomposed into storage and loss components:

$$G^* = \frac{\tau^*}{\gamma^*} = \frac{\tau_0}{\gamma_0}\cos(\delta) + i\frac{\tau_0}{\gamma_0}\sin(\delta), \tag{2.10}$$

$$G' = \frac{\tau_0}{\gamma_0}\cos(\delta) \quad \text{(storage modulus)}, \tag{2.11}$$

$$G'' = \frac{\tau_0}{\gamma_0}\sin(\delta) \quad \text{(loss modulus)}, \tag{2.12}$$

$$\tan(\delta) = \frac{G''}{G'} \quad \text{(damping factor)}. \tag{2.13}$$

The storage modulus $G'$ measures the elastic energy stored and recovered during each deformation cycle. This modulus represents the reversible component of the material's mechanical response. In contrast, the loss modulus $G''$ quantifies the energy that is dissipated as heat due to molecular rearrangements. The damping factor $\tan(\delta)$ indicates the relative contributions of the viscous and elastic behaviors. When $\tan(\delta) = 1$, the ink reaches the yield stress point, marking the transition between the solid-like and liquid-like states. For $\tan(\delta) < 1$, the applied shear stress is below the yield stress, and the ink remains in a solid-like state. Conversely, when $\tan(\delta) > 1$, the applied shear stress exceeds the yield stress, and the ink exhibits shear-thinning behavior characteristic of the liquid-like phase. While steady shear tests characterize how the material flows under constant deformation rates, dynamic oscillatory measurements provide insight into the viscoelastic nature of the ink under cyclic loading, offering a more complete picture of the material's rheological behavior.

| Method | Measuring system | Plate diameter (mm) | Gap height (mm) | Stress range (Pa) | Oscillation frequency (Hz) | Temperature (°C) |
|---|---|---|---|---|---|---|
| Oscillatory | Parallel plate | 50 | 0.5 | 1–1000 | 1 | 25 |

Table 2.3: Rheometer parameters for oscillatory tests.

To measure the storage and loss moduli, shear stress sweep tests are conducted at a constant frequency of 1 Hz and within a stress range of 1–1000 Pa, as listed in Table 2.3. Figure 2.5a shows the storage $G'$ and loss $G''$ moduli in relation to shear stress $\tau$ for the base Ecoflex™ 00-50 silicone without and with 1 wt% THIVEX®. For Ecoflex™ 00-50 silicone without THIVEX®, $G'$ is less than $G''$ for the entire shear stress regime, which means that the ink exhibits a flowable liquid-like phase unsuitable for printing (Rocha et al. 2020; Zheng et al. 2023). For Ecoflex™ 00-50 silicone with 1 wt% THIVEX®, the storage modulus $G'$ is larger than the loss modulus $G''$ before reaching the flow stress $\tau_f$, which shows that the ink exhibits a stable solid-like phase. The yield stress $\tau_y$, identified when the storage modulus starts to decrease, marks the onset of the solid-to-liquid transition. When the applied shear stress exceeds $\tau_y$, both $G'$ and $G''$ sharply decrease, and once it reaches $\tau_f$, $G'$ becomes smaller than $G''$, signifying a transition to liquid-like flow behavior. Figure 2.5b shows the storage $G'$ and loss $G''$ moduli of MRE inks containing different CIP particle contents (70, 140 and 210 *phr*): in all cases, $G'' > G'$ across the full shear stress regime. This indicates a dominant viscous response and liquid-like behavior, demonstrating again that CIP particles alone are insufficient to impart the solid-like behavior or the yield stress required for DIW 3D printing. Finally, Figure 2.5c shows the storage $G'$ and loss $G''$ moduli of MRE inks formulated with both THIVEX® and different CIP particle contents. Below the flow stress $\tau_f$, $G'$ remains substantially higher than $G''$, confirming a solid-like phase. An increasing CIP content increases the overall magnitude of $G'$ thereby shifting the flow stress $\tau_f$ to higher values. However, for all three *phr* levels, the inks yield at approximately the same stress point. Beyond the flow stress $\tau_f$, $G''$ becomes higher than $G'$, denoting a transition to liquid-like flow.

In summary, this rheological characterization highlights the importance of considering both static and dynamic measurements: the static rotational tests reveal that increasing CIP content enhances the overall viscoelastic response and may promote shear-thinning behavior during flow, whereas the dynamic oscillatory measurements clearly show that the yielding transition itself is governed by the presence of 1 wt% THIVEX®. Together, these complementary tests confirm that the response of MRE inks modified with 1 wt% THIVEX® provides the necessary rheological profile for successful DIW, characterized by a transition from a solid-like phase to a liquid-like flow after the flow stress is reached.

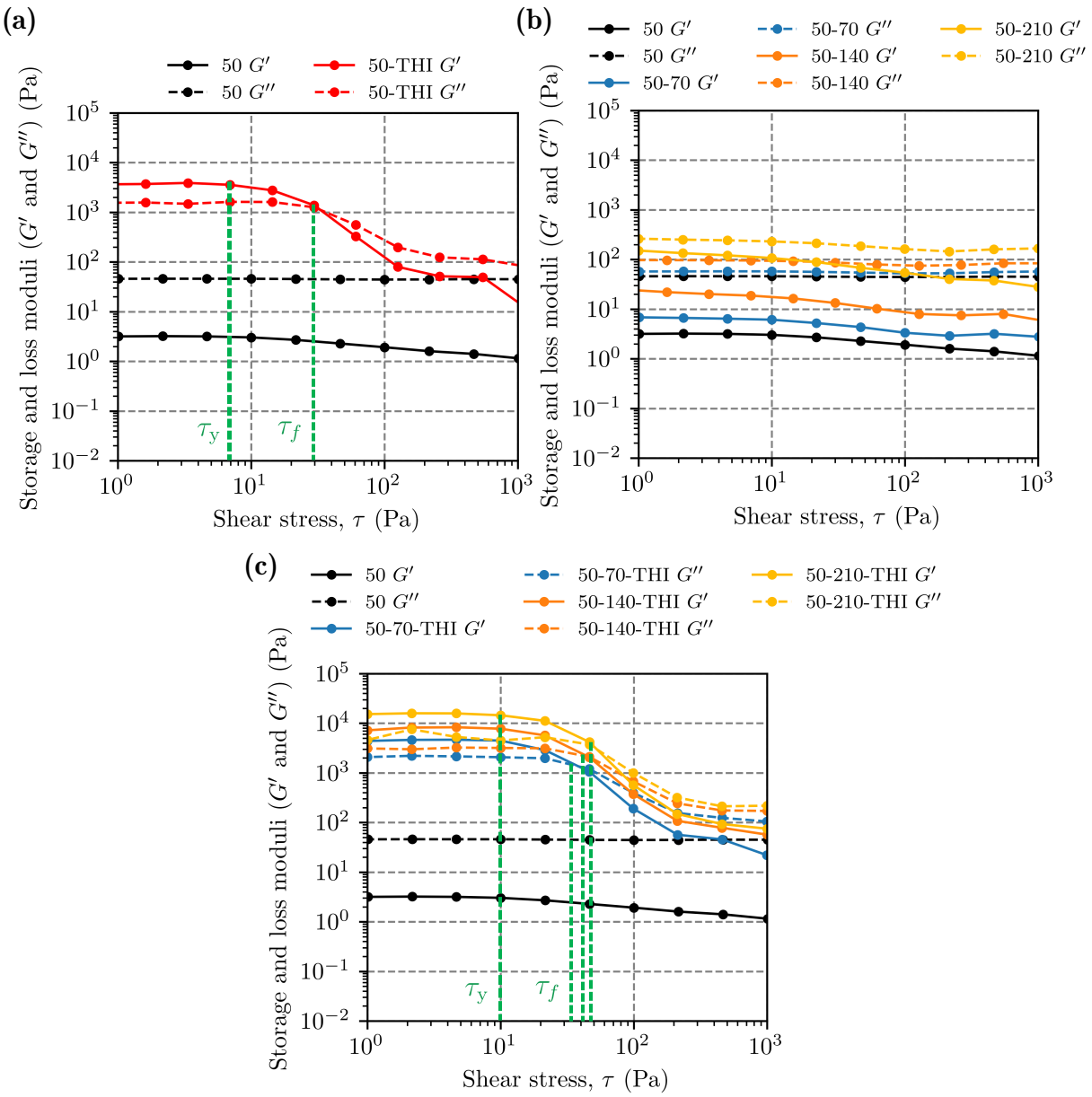


Figure 2.5: (a) Effect of THIVEX®: $G'$ and $G''$ as a function of shear stress for Ecoflex™ 00-50 silicone without (black) and with 1 wt% THIVEX® (red). (b) Effect of CIP particles only: $G'$ and $G''$ as a function of shear stress for CIP-only inks of 70, 140 and 210 *phr*. The response of pure Ecoflex™ 00-50 is indicated in black. (c) Effect of both THIVEX® and CIP particles: $G'$ and $G''$ as a function of shear stress for inks with 1 wt% THIVEX® and different CIP contents (70, 140 and 210 *phr*). The response of pure Ecoflex™ 00-50 is indicated in black.

## 2.3 3D printer setup

### 2.3.1 General overview

As discussed in section 1.5, a critical challenge in DIW of soft polymers is due to the continuous curing and thus time-dependent rheological evolution of viscoelastic inks during the printing process. MRE inks formulated with silicone elastomer matrices start the crosslinking process once mixed with curing agents. This ongoing reaction alters the ink's rheology during printing, leading to many issues like nozzle clogging, inconsistent extrusion rates, and difficulties in maintaining uniform deposition across extended print durations. In addition, these changes in properties are even more abrupt in the presence of particles.

To address this challenge, we employ a 3D printer equipped with an active mixing head, referred to as the dynamic mixing head (DMH). This system, provided by Hyrel 3D (Norcross, GA, USA), enables both real-time mixing and extrusion during the printing process. In this study, the DMH is used to extend the workable print time by continuously blending the two silicone components (containing the required additives) directly before deposition. The head receives material input from two independent syringe extruders, actively blends the components within the mixing tube, and subsequently extrudes the ink through the selected nozzle as shown in Figure 2.6. Mixing strategies for multi-material 3D printing have traditionally relied on passive mixers that operate without moving parts and rely on flow (Hardin et al. 2015; Hassan and Selvaganapathy 2022) and impeller geometry to redistribute fluids (Zhou et al. 2019). While effective in specific regimes, their mixing efficiency is strongly dependent on flow rate, geometry, and fluid viscosity. As a result, static mixers are typically suited for low-viscosity fluids or systems where diffusion dominates. In contrast, yielding viscoelastic materials, such as MRE inks, require continuous mixing to achieve homogeneity. At the macroscale, active mixers provide a powerful alternative through chaotic advection generated by impeller motion (Ober et al. 2015; Teves et al. 2024). They enable rapid, real-time homogenization of highly viscous and particle-filled fluids. This capability is thus particularly advantageous in DIW of MRE inks, where achieving both homogeneous particle distribution and consistent extrusion flow is critical for print fidelity.

The printing system is based on a Hyrel System 30M (Hyrel 3D, Norcross, GA, USA), adapted to accommodate the DMH. Two SDS-60 XT (Hyrel 3D, Norcross, GA, USA) syringe screw extruders, each controlled by a stepper motor, are mounted on the printer to supply compounds containing additives as well as Ecoflex™ 00-50 silicone base (part A) and curing agent (part B) separately, ensuring precise control of mixing ratios, as shown in Figure 2.6. To accommodate the syringe screw extruders, a custom mounting bracket is designed to support its additional weight and ensure alignment with the DMH.

In addition, rigid tubing and couplings are used to provide stable material transfer from the syringes to the DMH without leakage or backflow. These modifications enable the printer to manage time-sensitive, viscoelastic inks by preventing premature curing within the nozzle, stabilizing the flow during extended print runs, and enhancing the uniformity of the deposited structures. The DMH is further equipped with a pneumatically controlled valve (minimum 60 psi) that regulates the flow inside the DMH (see Figure 2.6). This valve allows the flow to be opened or closed independently of the syringe extruders, thereby preventing spontaneous extrusion due to back pressure from the syringes when the system is idle. The valve is electronically connected to one of the syringe extruders, enabling its actuation through G-code commands for precise synchronization during printing.

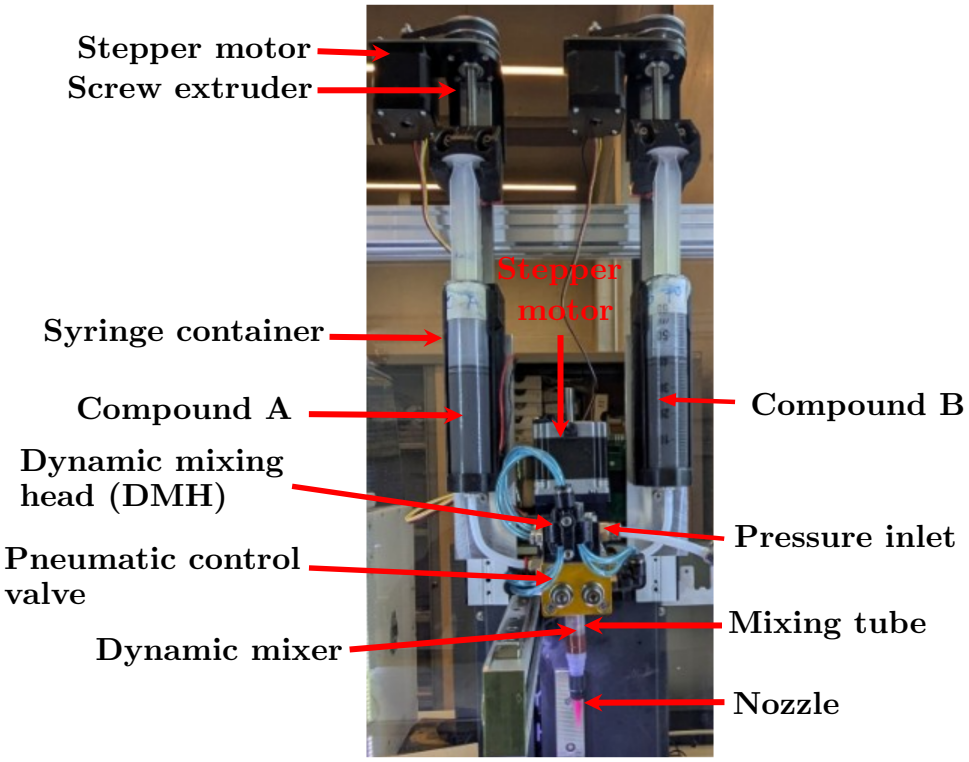


Figure 2.6: DIW 3D printer setup equipped with a dynamic mixing head (DMH).

The printer uses a motorized Cartesian system, in which the nozzle moves along the X and Y axes, while the Z-axis is controlled through the vertical translation of the print bed. To define and manage motion paths, we utilize Slic3r, an open-source slicing software, to generate G-code files that dictate the nozzle's movements. Specifically for DIW, the CAD models of the desired printed structures are sliced into sequential deposition layers along Z and each layer hatched into sequential nozzle passes in the (X-Y) plane, which directly determines the extrusion paths of the printed filaments. Key printing parameters, such as printing speed and extruder speeds, are integrated into the G-code using specific commands. The Repetrel software is then used to perform the printing operations. This includes executing custom G-code commands that facilitate synchronized extrusion through extruder cloning, allowing both extruders to operate simultaneously. To optimize

the system for dual-material handling through the DMH, the G-code generated by the slicer is further modified to ensure smooth coordination between the two syringe extrusion processes and the control valve. This modification guarantees that the flow rates of both extruders remain consistent throughout the printing operation. The printer also incorporates a heated bed with a temperature range up to 90°C, which is particularly used for geometries involving multiple layers in order to improve structural integrity during printing (see further discussion on this subject in subsection 2.5.3).

### 2.3.2 Ink preparation

The preparation of the MRE inks is a critical step since the final print quality, curing behavior and reproducibility of mechanical properties strongly depend on how homogeneously the components are prepared and mixed with the additives. In our experience, even slight variations in the mixing order or timing can result in poor particle dispersion or inconsistencies in filament extrusion. Therefore, it is essential to adopt a careful and reproducible protocol for this process.

To prepare the MRE inks for the dual-extruder DMH system, two ink compounds are created by thoroughly mixing equal amounts of Ecoflex™ 00-50 silicone elastomer part A or part B with CIP at three different concentrations: 70, 140 and 210 *phr*. Additionally, 1 wt% THIVEX® is addded as a rheology modifier, as described in detail in section 2.2, where 1 wt% is calculated with respect to the total polymer weight (part A + part B).

The common preparation steps for both compounds are as follows:

1. Ecoflex™ 00-50 silicone parts A and B are weighed in a 1:1 ratio and each combined with an equal weight of CIP depending on the loading concentration. The mixture is homogenized using a mechanical mixer at 1100 rpm for 10 min.
2. The mixture is then degassed in a vacuum chamber for 7 min to remove entrapped air.
3. Subsequently, 1 wt% THIVEX® is added to each compound. The mixtures are gently mixed at a reduced speed of 500 rpm for 5 min to improve particle dispersion while avoiding the introduction of new air bubbles.
4. A secondary degassing is performed for 10 min. Secondary degassing is necessary, as the addition of THIVEX® significantly increases viscosity, and degassing with both particles and THIVEX® added at the same time is difficult with the vacuum chamber.
5. The prepared mixtures are carefully transferred into separate 60 cc syringes, ensuring no air pockets are introduced during filling. The syringes are finally mounted onto the two SDS-60 XT extruders that independently supply the materials to the DMH, as illustrated in both Figure 2.6 and Figure 2.7.

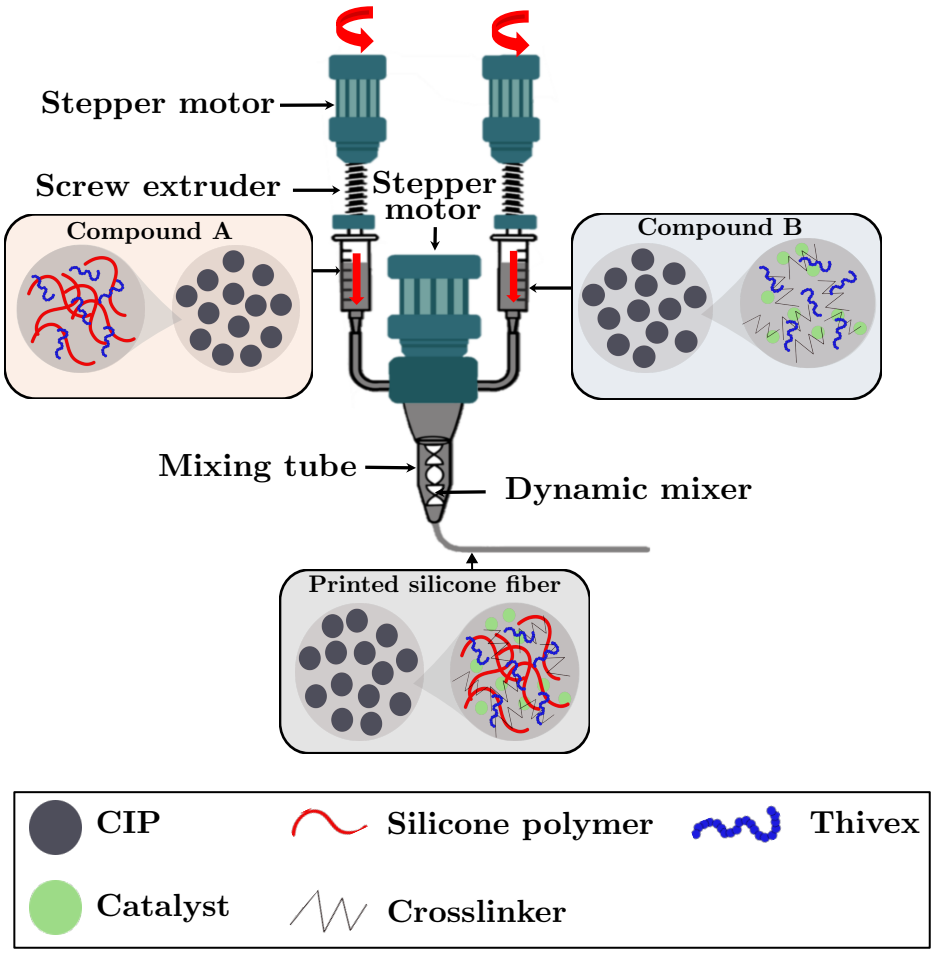


Figure 2.7: Schematic of the dual-syringe DMH system: the two compounds are fed from separate syringes, mixed in a 1:1 ratio within the mixing tube, and extruded as a uniform MRE ink filament.

At the entrance of the mixing tube (see Figure 2.7), the two compounds are delivered in a 1:1 ratio. The active mixer then blends the two compounds containing the polymer base, crosslinker/catalyst, THIVEX® and CIP in real time, ensuring that the inks are bubble-free. As the two compounds created with THIVEX® and CIP have already formed a well-homogenized mixture through the detailed preparation process, the active mixer can blend them together more easily and efficiently. Curing is initiated by the reaction of part A with part B, while the CIP particles remain evenly distributed throughout the polymer network just before extrusion. Importantly, by carefully selecting the mixer length (see details in Appendix A), the time spent by the MRE ink in the mixing tube remains within the defined pot life of the ink. This ensures that the ink is continuously extruded as a fiber in a consistently-mixed state, providing stable processing conditions and reproducible filament formation.

## 2.4 Print parameter selection

The extrusion and deposition of filaments in the DIW process is governed by a set of coupled extrusion and deposition parameters, as summarized in Figure 2.8. The extrusion parameters include the dynamic mixer speed $V_M$ as well as the nozzle diameter $D$, the extrusion speed $C$ (governed by the extruder speed $V_E$ through the stepper motor input $V_R$) and the die swell ratio $\alpha$, that together control the flow rate and filament dimensions at the nozzle exit. The deposition parameters consist of the nozzle height $H$ (and its dimensionless form $H^* = H/D$), the printing speed $V$ and the final filament diameter $d$, which is determined by the interplay between extrusion and deposition dynamics.

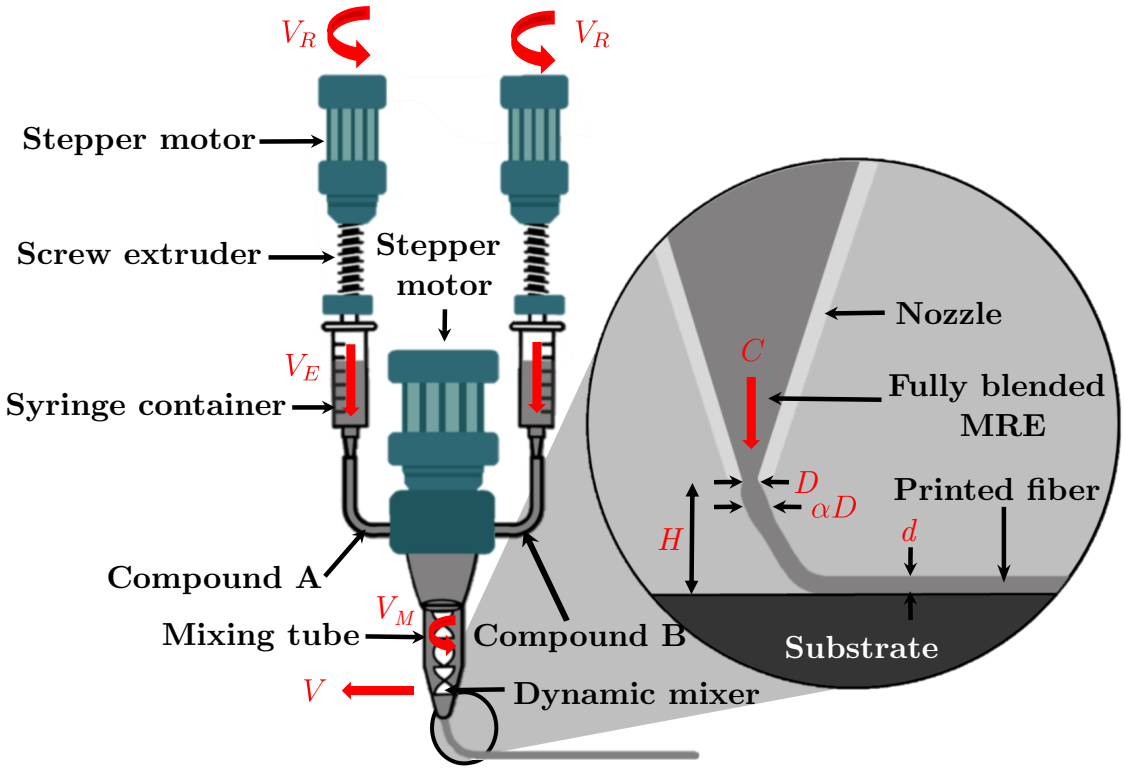


Figure 2.8: Schematic of extrusion and deposition parameters in active-mixing assisted DIW: extrusion parameters include mixer speed $V_M$, nozzle diameter $D$, extrusion speed $C$ (governed by the extruder speed $V_E$ through the stepper motor input $V_R$) and die-swell ratio $\alpha$, while deposition parameters include nozzle height $H$, print speed $V$ and printed filament diameter $d$.

First, the dynamic mixer speed $V_M$ regulates the blending of the two ink compounds inside the mixing tube. The nozzle diameter $D$ defines the initial cross-section of the extruded filament (equal to the outlet diameter of the nozzle). In addition, the extrusion speed $C$ represents the velocity at which material exits the nozzle under the action of the screw extruder. The nozzle height $H$ controls the vertical distance between the nozzle exit and the substrate, which strongly influences filament flattening and interlayer adhesion. The print speed $V$ corresponds to the lateral motion of the nozzle across the substrate, whereas the final filament diameter $d$ is determined by the interplay between extrusion and deposition dynamics. Indeed, due to the viscoelastic nature of the ink, die swelling

occurs at the nozzle exit, thus giving a swollen filament diameter (Sun et al. 1996):

$$d = \alpha D, \tag{2.14}$$

where $\alpha$ is the die-swell ratio.

By applying the principle of volume conservation, the volumetric flow rate can be expressed as:

$$Q = \frac{\pi\ (\alpha D)^2\ C}{4}, \tag{2.15}$$

indicating that $d$ is controlled by extrusion speed $C$, with additional dependence on die-swelling. The dimensionless ratio of nozzle height to diameter is given by $H^*$, which is another important factor that governs filament stretching and bonding to the substrate (Yuk and Zhao 2018):

$$H^* = \frac{H}{D}. \tag{2.16}$$

The nozzle diameter $D$ is fixed by the chosen printing hardware and the desired print resolution, while the other quantities are directly controlled in the printer setup. The G-code independently controls the dynamic mixer speed $V_M$, the nozzle height $H$ and the print speed $V$. The extrusion speed $C$ is determined by the extruder speed $V_E$, which refers to the linear displacement of the screw. This displacement is governed by the extrusion rate $V_R$ of the stepper motor driving the screw. This conversion is given by:

$$V_E = \frac{1}{16576}\, V_R, \tag{2.17}$$

where $V_R$ is the motor input in pulses.s$^{-1}$ and the factor (16576 pulses/mm) arises from the motor specification (16576 pulses per revolution) combined with the screw pitch (1 mm per revolution).

In summary, the relationships between the parameters indicate that the active mixing-assisted DIW process is influenced by the simultaneous control of several factors: mixer speed ($V_M$), nozzle diameter ($D$), extrusion speed ($C$) linked to extruder speed ($V_E$), nozzle height ($H$) and print speed ($V$). Coordinating these parameters allows for precise control over filament diameter, deposition fidelity, and interlayer adhesion during the printing process. Additionally, the quality of the printed output is heavily reliant on these parameters. Therefore, a systematic approach should be employed to determine, for each factor, the values that ensure reliable extrusion and accurate fabrication with MRE inks.

### 2.4.1 Determination of the dynamic mixer speed $V_M$

Before delving into other parameters, the efficiency of the active mixer is addressed since it is paramount for ensuring the uniformity of the multi-component silicone-based ink before it even reaches the nozzle. Indeed, if the two MRE ink compounds are not mixed adequately, it can lead to incomplete curing and result in printing defects. Thus, accurately determining the appropriate mixer rotational speed (rpm) range is essential for achieving high print quality. To tackle this, two complementary approaches are used. First, an experimental methodology is developed using transparent pigmented silicone inks (blue and yellow) as surrogates. This approach allows for direct visualization of mixing quality through colorimetric analysis, making it possible to identify the threshold rpm for homogeneous mixing of the two Ecoflex™ 00-50 silicone components in a straightforward manner. Second, since optical methods are not applicable to MRE inks due to their opaque black appearance, a theoretical model is employed. By coupling these two methods, a strong framework is established to determine the necessary active mixer speed range for achieving consistent homogeneity in MRE inks.

#### 2.4.1.1 Experimental estimate of the dynamic mixer speed $V_M$

To determine the active mixer speed required for complete mixing of the two ink compounds dispensed from separate extruders, a mixing efficiency study is conducted using blue and yellow pigment inks blended with Ecoflex™ 00-50 silicone polymer, part A and part B, respectively, each containing 1 wt% Thivex®(Figure 2.9a). The inks are subsequently mixed at various rotational speeds (rpm), controlled by the number of pulses sent to the motor. At various speeds, the change in mixing behavior can be clearly seen in the dynamic chamber (Figure 2.9b), where the initially distinct yellow and blue inks gradually merge into a uniform green tone as the rotational speed increases.

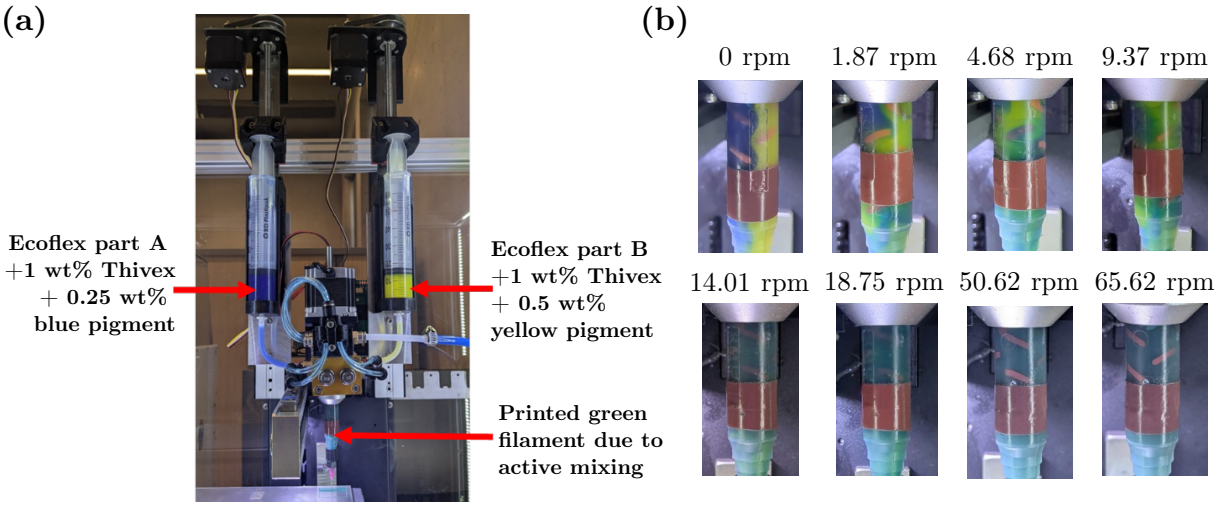


Figure 2.9: (a) Active-mixing 3D printer setup showing Ecoflex™ 00-50 part A (blue pigmented) and part B (yellow pigmented) inks (with 1 wt% Thivex®) dispensed into the dynamic mixing chamber. (b) Dynamic mixing chamber at different rotational speeds (rpm).

To further assess the mixing quality at each speed, a sample measuring 40 x 40 x 0.6 mm is printed[6] (Figure 2.10a). The printed samples reveal that as the mixing speed increases, the print appearance transitions from a distinct yellow-blue separation to a uniform green tone. At speeds exceeding 50.62 rpm, the printed samples display a visually homogeneous green coloration, indicating the effective and complete mixing of the two Ecoflex™ 00-50 silicone ink compounds.

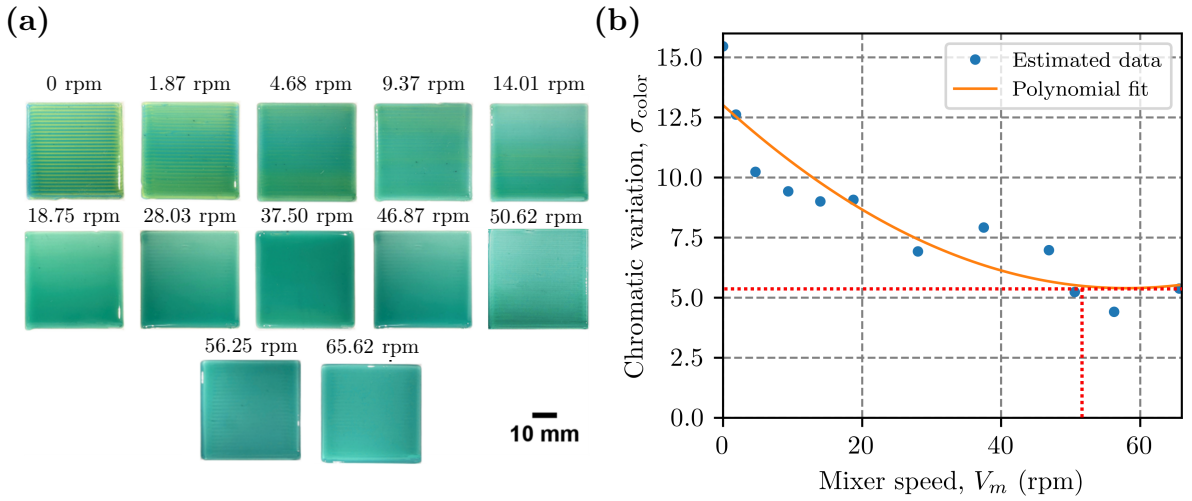


Figure 2.10: Experimental determination of active mixing efficiency. (a) Squares printed by mixing blue and yellow Ecoflex™ 00-50 silicone inks with 1 wt% Thivex at various mixer speeds show complete homogenization into green at speeds above 50.62 rpm. (b) Chromatic variation analysis confirms mixing efficiency increases with speed and plateaus beyond 50.62 rpm.

To quantitatively study the variation in mixing across different mixer speeds, a colorimetric analysis is performed using Python image libraries. The raw images of the printed squares are cropped so that only the printed part is visible for the analysis. The images are then loaded in RGB format using the OpenCV library, normalized to the [0,1] range, and converted to the CIELAB color space using the scikit-image library. In the CIELAB space, luminance is separated from the chromatic components a* and b*, in which a* represents the green-red axis and b* represents the blue-yellow axis, respectively (Sharma et al. 2005; Tan et al. 2025). The mean $(\mu_{a*}, \mu_{b*})$ and standard deviation $(\sigma_{a*}, \sigma_{b*})$ of the a* and b* channels are computed across all the pixels $(N)$, allowing for the estimation of the overall chromatic variation, denoted as $\sigma_{color}$:

$$\sigma_{a*} = \sqrt{\frac{1}{N}\sum_{i=1}^{N}(a_i^* - \mu_{a*})^2}, \quad \sigma_{b*} = \sqrt{\frac{1}{N}\sum_{i=1}^{N}(b_i^* - \mu_{b*})^2}, \tag{2.18}$$

$$\sigma_{\text{color}} = \sqrt{\sigma_{a*}^2 + \sigma_{b*}^2}. \tag{2.19}$$

[6]The print parameters are: $V_E = 0.0065$ mm s$^{-1}$, $V = 10$ mm s$^{-1}$, $D = 0.6$ mm and $H^* = 1$.

The chromatic variation $\sigma_{color}$ is plotted as a function of mixer speed in Figure 2.10b. To illustrate the general trend, a second-order polynomial fit is applied to the data. The results indicate that chromatic variation decreases with increasing mixer speed, eventually reaching a plateau after a speed of 50.62 rpm. This shows that increasing the mixer speed increases the color homogeneity (indicating proper mixing of the two ink compounds) from a specific minimum threshold value. Beyond this point, further increases in speed result in minimal changes in chromatic variation.

However, there is also an upper limit to the mixer speed: at very high rotational speeds and prolonged mixing times, microbubbles are observed in the printed samples as shown in Figure 2.11. This occurrence is attributed to cavitation, a process where vapor bubbles form and collapse due to rapid pressure changes in the fluid medium during high-shear mixing. Based on the previous results of chromatic uniformity and visual inspection of bubble formation, the optimal mixing range for the active mixer is identified to lie between 50.62 and 65.62 rpm (corresponding to 2500 and 3500 pulses, respectively). Thus, to account for possible variations in the ink, the intermediate value of 56.25 rpm is retained to ensure full mixing of the two Ecoflex™ 00-50 silicone ink compounds while preventing bubble formation.

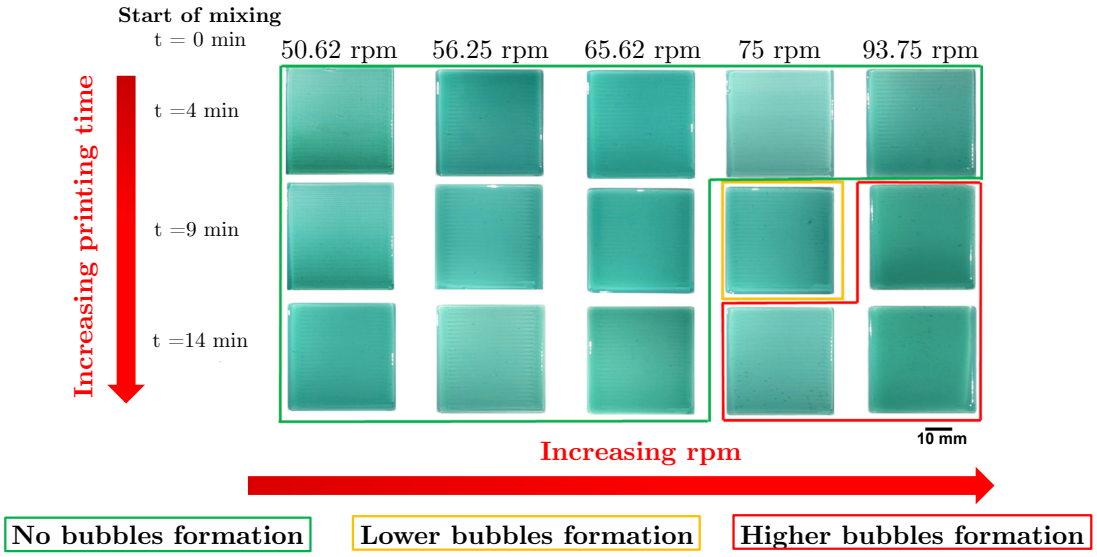


Figure 2.11: Squares printed at different mixer speeds (50.62–93.75 rpm) after the ink had spent 4, 9 and 14 min in the mixer. Low to moderate speeds ($\leq$ 65.62 rpm) yield bubble-free prints, while higher speeds ($\geq$ 75 rpm) and longer mixing times cause bubble formation.

#### 2.4.1.2 Theoretical estimate of the dynamic mixer speed $V_M$

The experimental approach to determine the mixer rpm cannot be directly applied to MRE inks due to their opaque black color caused by the high concentration of carbonyl iron particles (CIP). The lack of color contrast unfortunately makes it impossible to quantify mixing efficiency via optical or colorimetric methods. Therefore, a theoretical

framework is used (Golobic et al. 2019) in what follows to estimate the minimum dynamic mixer speed required for complete mixing in the case of MRE inks.

The theoretical criterion for complete mixing is defined by the ratio of residence time to mixing time:

$$\frac{t_{\text{res}}}{t_{\text{mix}}} \geq 1, \tag{2.20}$$

where $t_{\text{res}}$ is the average residence time of the ink inside the mixing tube, and $t_{\text{mix}}$ is the characteristic mixing time determined by impeller shear and Reynolds number.

Residence time is calculated from the ratio of the mixing tube volume ($V_{mt}$) to the volumetric flow rate ($Q$):

$$t_{\text{res}} = \frac{V_{mt}}{Q}. \tag{2.21}$$

The mixing tube has a length of 38.5 mm and a diameter of 14.5 mm (see details in Appendix A), yielding a volume $V_{mt} = 6357.50$ mm$^3$, and the flow rate is calculated using Eq. (2.15).[7]

Mixing time is given by (Golobic et al. 2019):

$$t_{\text{mix}} \propto \frac{1}{Re \cdot V_m}, \tag{2.22}$$

where $V_m$ is the mixer rotational speed (rpm), and $Re$ is the Reynolds number inside the mixing tube given by:

$$Re = \frac{\rho\, u_m\, L}{\eta(\dot{\gamma})}. \tag{2.23}$$

Here, $\rho$ is the effective density of the MRE ink (increasing with CIP content), $u_m$ is the average linear velocity, $L$ is the characteristic gap between impeller and tube wall ranging between 2.5–12.5 mm (see Figure A.1a), and $\eta(\dot{\gamma})$ is the apparent viscosity of the ink.

The apparent viscosity $\eta(\dot{\gamma})$ is obtained by fitting the rheological data from the rotational rheometer (subsection 2.2.1) to the Casson-Papanastasiou model:

$$\eta = \left[\sqrt{\mu_p} + \sqrt{\frac{\tau_y}{\dot{\gamma}}}\left(1 - \exp(-\sqrt{m_p\,\dot{\gamma}})\right)\right]^2, \tag{2.24}$$

[7] At a printing speed $V = 10$ mm s$^{-1}$, the flow rate $Q$ for the 70, 140 and 210 *phr* MRE inks are 7.17, 8.12 and 9.07 mm$^3$ s$^{-1}$, respectively, corresponding to residence times $t_{\text{res}}$ of 887, 783 and 700 s ($\sim$ 15, 13 and 12 min). Since the residence time is inversely proportional to the volumetric flow rate, increasing the extruder speed (or print speed) and thus the volumetric flow rate reduces the residence time, and conversely.

where $\mu_p$ is the plastic viscosity, $\tau_y$ is the yield stress, $m_p$ is the Papanastasiou regularization parameter (stress growth exponent), and $\dot{\gamma}$ is the applied shear rate.

This model is selected because it incorporates two critical rheological features of viscoelastic MRE inks:

- **Yield stress behavior:** a finite stress must be exceeded before flow begins, reflecting the resistance of the particle-filled silicone to deformation.
- **Shear-thinning behavior:** the viscosity decreases with increasing shear rate, which is characteristic of viscoelastic particle suspensions such as MRE inks.

The exponential term introduced by Papanastasiou regularizes the discontinuity of the classical Bingham or Casson yield-stress models at $\dot{\gamma} = 0$, ensuring smooth numerical implementation for both rheometer fitting and computational modeling (Pham and Mitsoulis 1994). Using Python-based nonlinear regression (SciPy's `curve_fit` function), the model is fitted to experimental viscosity–shear rate curves of Ecoflex™ 00-50 with 1 wt% Thivex®and different CIP concentrations (70, 140 and 210 *phr*) in order to get the model parameters $(\mu_p, \tau_y, m_p)$. In Figure 2.12a, representative fits are shown to capture the measured shear-thinning trends across shear rates. The fitted $\eta(\dot{\gamma})$ values are then directly used in the Reynolds number calculation for the mixing analysis, thereby linking the experimentally-measured rheology of MRE inks to the theoretical estimation of the minimum mixer rpm required for homogeneous mixing of MRE inks.

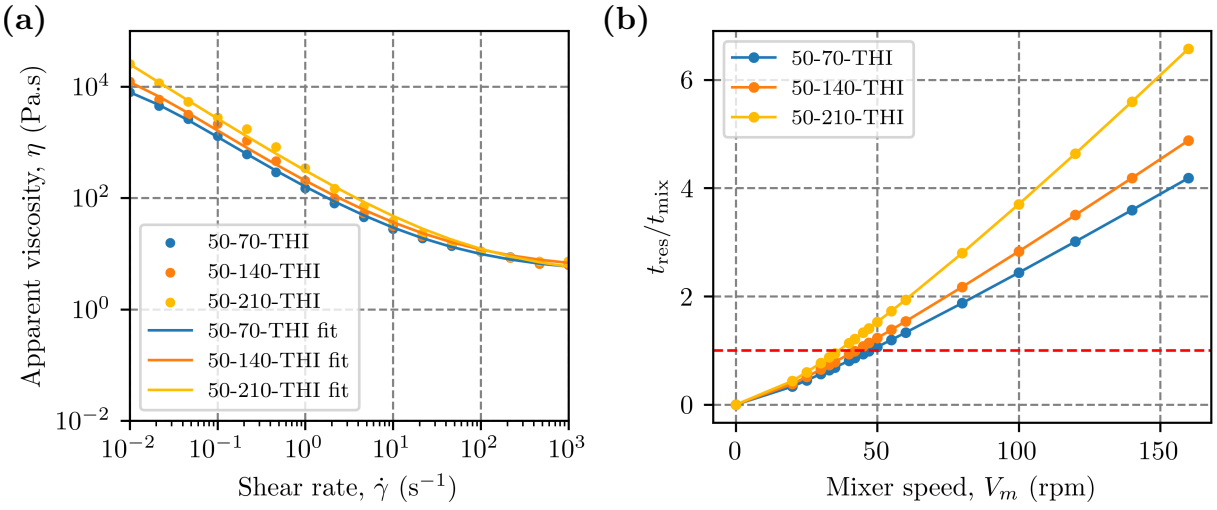


Figure 2.12: (a) Apparent viscosity $\eta$ of MRE inks with CIP contents of 70, 140 and 210 *phr* as a function of shear rate measured using a rotational rheometer (dots) and fitted curves (lines) using the Casson-Papanastasiou model. (b) Theoretical estimation of mixing efficiency expressed as the ratio of residence time to mixing time ($t_{res}/t_{mix}$), plotted against mixer rotational speed ($V_m$) for the three CIP concentrations. The red dashed horizontal line indicates the complete-mixing criterion ($t_{res}/t_{mix} = 1$).

Based on the relationships defined in Eq. (2.20)-Eq. (2.23), as the CIP content increases, the density $\rho$ also increases, which increases the Reynolds number $Re$ and reduces the required mixing speed $V_m$ at which $t_{\text{res}}/t_{\text{mix}} = 1$. Similarly, increasing the characteristic length $L$ also raises the Reynolds number, thereby decreasing the necessary mixing speed. With a characteristic length of $L = 2.5$ mm, the theoretical model predicts that the minimum mixer speed at which $t_{\text{res}}/t_{\text{mix}} = 1$ is approximately 47 rpm for 70 *phr*, 45 rpm for 140 *phr*, and 40 rpm for 210 *phr* as shown in Figure 2.12b.

It must be emphasized that the use of this theoretical model introduces uncertainties related to the effective Reynolds number in highly shear-thinning regimes, and to the simplified assumption that shear imparted by the impeller is equivalent to that in parallel-plate rheometry. As such, the model should not be considered an exact predictor of the required mixer speed but rather a reference framework for estimating the minimum rpm at which complete mixing is expected.

When compared to experimental results obtained with transparent pigmented Ecoflex™ 00-50 silicone inks, the theoretical predictions fall within the same range, which supports the use of the model as a guideline. Due to the uncertainties mentioned earlier, an operating speed of 56.25 rpm (3000 pulses per second) has been chosen. This speed serves as an upper limit that ensures complete mixing for all the inks used in this study, and it will be applied for all subsequent MRE printing.

### 2.4.2 Determination of nozzle geometry

The nozzle geometry plays a critical role in determining the extrusion behavior of MRE inks. Given their high viscosity, yield stress and particle content, the nozzle must provide sufficient shear for flow initiation while maintaining continuous extrusion without stalling the extruder motor.

Two nozzle types are considered:

- *Converging conical nozzle*: axisymmetric taper from inlet to outlet over an axial length of $L_{con} = 12.5$ mm.
- *Cylindrical capillary nozzle*: straight nozzle of lengths $L_{cyl} = 12.7$ mm and $L_{cyl} = 6.35$ mm, giving $L_{cyl}/D$ ratios of 21.2 and 10.6, respectively.

Both experimental and numerical investigations are performed to identify which nozzle geometry offers the most stable extrusion behavior and the most suitable flow characteristics for MRE inks.

#### 2.4.2.1 Experimental analysis of nozzle geometry

Direct extrusion trials[8] are first conducted using the base Ecoflex™ 00-50 silicone and the 210 *phr* MRE ink (both containing 1 wt% THIVEX®). These experiments aim to determine the influence of nozzle geometry and diameter on extrusion behavior.

Figure 2.13 summarizes the outcomes for the considered nozzle geometries and diameters ranging from 0.4 to 1.6 mm. Green, orange, and red markers respectively indicate successful continuous extrusion, extrusion with discontinuities, and no extrusion across the tested extrusion speed range. For all tested configurations, the base silicone extrudes continuously, except for the 12.7 mm-length cylindrical nozzle with a 0.4 mm diameter, where the motor eventually stalls. According to later numerical results (Figure 2.15b), this corresponds to the most critical case in terms of required inlet pressure.

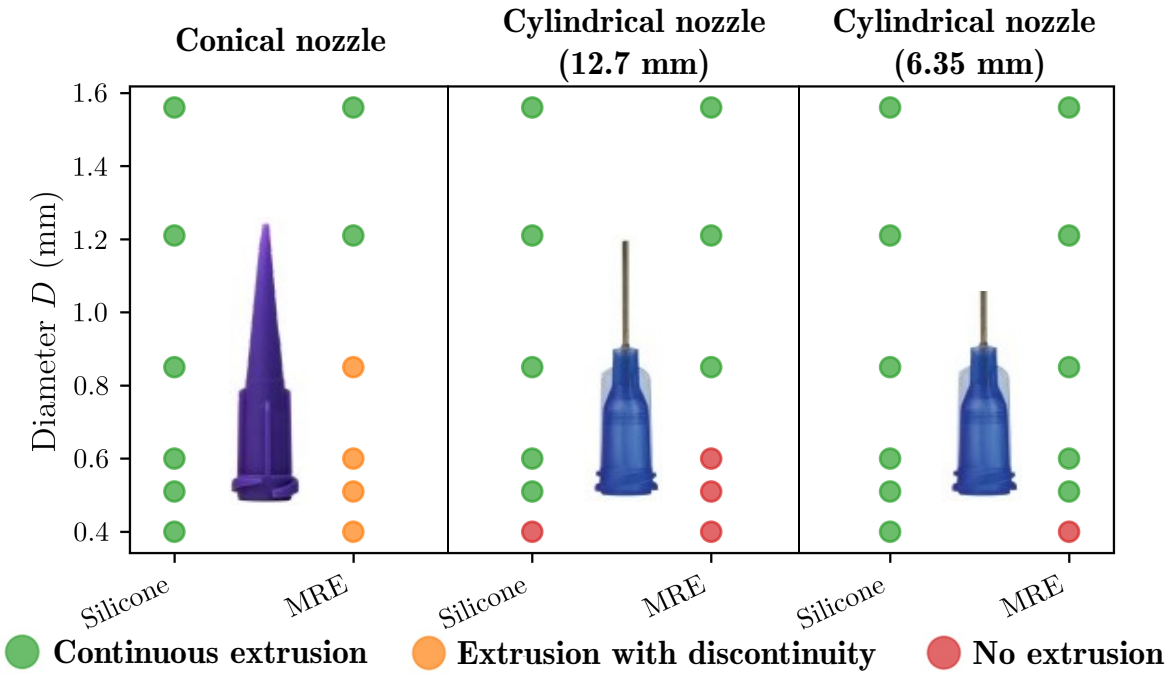


Figure 2.13: Extrusion trials of base Ecoflex™ 00-50 silicone and 210 *phr* MRE ink (both with 1 wt% THIVEX®) using different nozzle geometries and diameters. (Left) Conical nozzle, (middle) cylindrical nozzle with 12.7 mm needle length, (right) cylindrical nozzle with 6.35 mm needle length.

For the MRE ink, conical nozzles ensure stable extrusion only for larger diameters, while discontinuities appear below $D = 0.85$ mm. Long cylindrical nozzles ($L_{cyl} = 12.7$ mm) fail to extrude below $D = 0.6$ mm due to excessive torque and pressure buildup that cause the extruder motor to stall. Short cylindrical nozzles ($L_{cyl} = 6.35$ mm) enable stable extrusion at diameters as small as $D = 0.51$ mm, representing the minimum reliable printing configuration.

[8] In each case, $V_M = 56.25$ rpm, $D = H$ (see next section), and $V_E$ spans $[0.1,1]\times10^{-2}$ mm s$^{-1}$.

Hence, the optimal configuration is chosen as a 6.35 mm-length cylindrical nozzle with a 0.6 mm outlet diameter. Although extrusion is technically achievable with a 0.51 mm diameter, the slightly larger 0.6 mm diameter is preferred to operate sufficiently far from motor overload and to accommodate possible variations in the ink, such as the presence of filler aggregates.

#### 2.4.2.2 Numerical nozzle simulations

To complement the experimental findings and gain insight into the internal flow characteristics of the nozzle types, numerical simulations are performed in COMSOL MULTIPHYSICS (Polymer Flow Module). The same nozzle geometries, conical and cylindrical, with an outlet diameter of $D = 0.6$ mm are analyzed numerically. The 210 *phr* MRE ink is modeled using the Casson–Papanastasiou relation with parameters obtained from rheometer data fitting (Figure 2.12a). The flow is assumed steady, laminar and incompressible, with no-slip boundary conditions at the walls. A volumetric flow rate of $Q = 9.07$ mm$^3$ s$^{-1}$ is applied at the inlet and zero gauge pressure at the outlet. Along the walls, a boundary-layer mesh resolves near-wall shear-rate peaks in both nozzle types. The velocity and shear-rate distributions obtained from the simulations are shown in Figure 2.14.

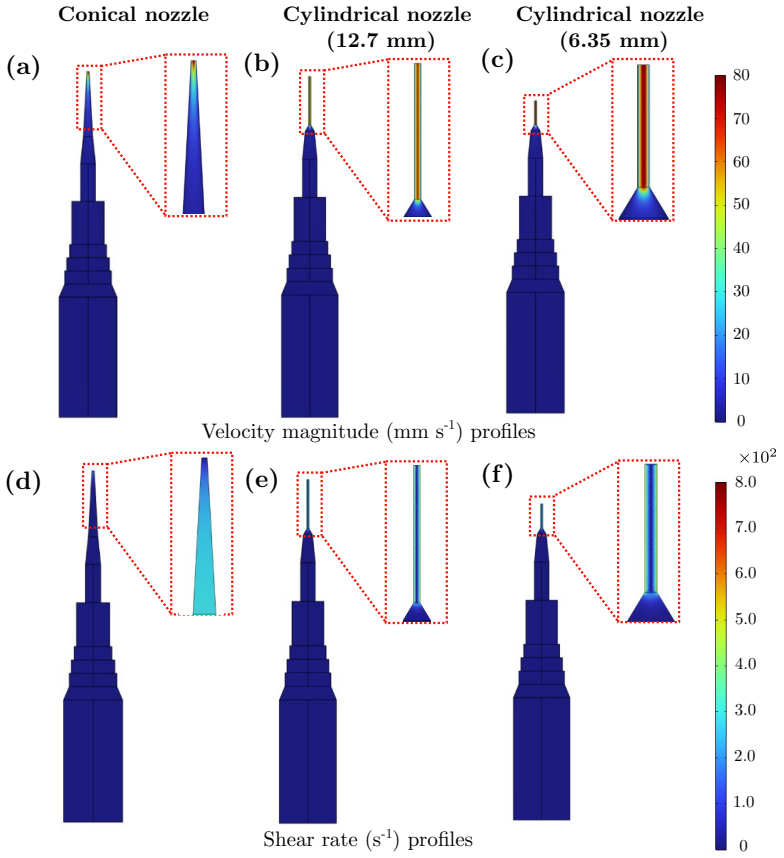


Figure 2.14: Top: velocity magnitude profiles for (a) the conical nozzle and (b–c) cylindrical nozzles of respective lengths 12.7 mm and 6.35 mm. Bottom: shear-rate profiles for (d) the conical nozzle and (e–f) cylindrical nozzles of respective lengths 12.7 mm and 6.35 mm. Inlet flow rate $Q = 9.07$ mm$^3$ s$^{-1}$.

The conical nozzle shows a gradual acceleration that peaks sharply at the tip (Figure 2.14a). In comparison, cylindrical nozzles have almost uniform velocity along their length (Figure 2.14b–c). The shear-rate distribution follows a similar trend in both nozzle geometries. The conical nozzle has low shear along most of its length but a sharp spike at the exit (Figure 2.14d), which can cause rheological changes and flow instability. Cylindrical nozzles, on the other hand, keep steady wall shear rates (Figure 2.14e–f) that support smooth and stable extrusion.

Figure 2.15a shows the wall shear rate along the nozzle axis. The conical nozzle has low shear along most of its length, with a sharp increase near the tip. In contrast, the cylindrical nozzles have higher and more uniform wall shear rate. Figure 2.15b presents the pressure needed for different flow rates. The conical nozzle requires the lowest inlet pressure, but this results in less stable extrusion. Cylindrical nozzles, especially the longer 12.7 mm type, need higher inlet pressures but provide more continuous flow. The shorter 6.35 mm cylindrical nozzle offers the best balance between stable extrusion and the required pressure, which aligns with the experimental results.

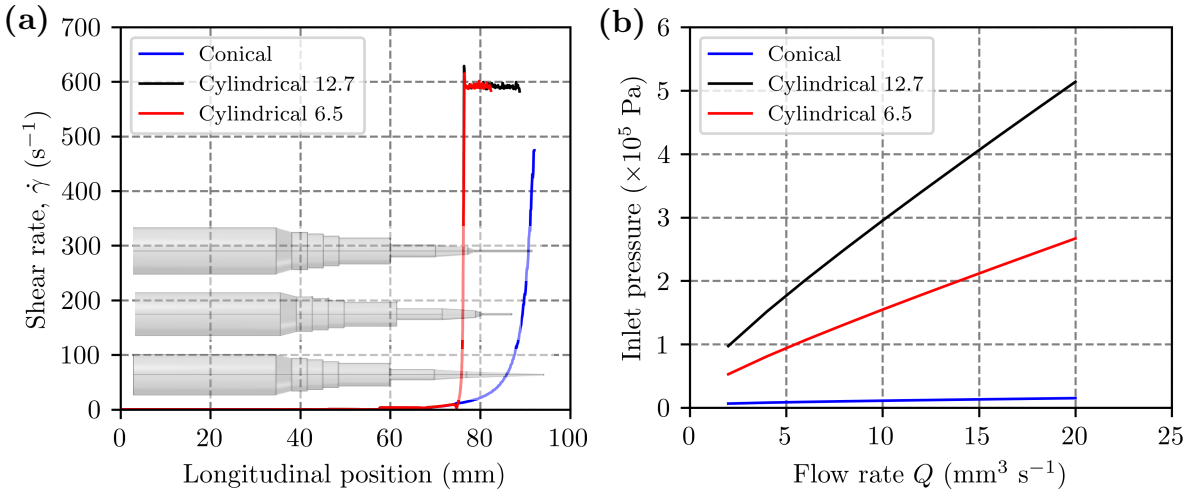


Figure 2.15: (a) Wall shear rate along nozzle length for the considered nozzle geometries. (b) Variation of inlet pressure with flow rate for the same geometries.

### 2.4.3 Determination of printing height $H$ and printing speed $V$

The selection of the printing height $H$ and the printing speed $V$ is crucial to obtain stable and reproducible filaments during the printing process. The geometry of the printed features imposes practical constraints on the choice of these parameters.

First, the effect of the layer height $H$ is considered through the ratio of height to nozzle diameter, $H^* = H/D$. Here, $H^* = 1$ is selected as the standard condition for the printing height in order to produce printed layers having the same thickness than the extruded filament (as will be seen in subsection 2.4.4, we will also target equi-dimensional filament). At a given printing speed, $H^*$ governs filament geometry. Literature reports have shown

that if the printing speed $V$ is adjusted so that $H^* = 1$ yields straight and uniform filaments, increasing $H^*$ often results in curved or distorted filaments (Yuk and Zhao 2018)[9]. This trend is confirmed by our experiments: when $V$ is such that $H^* = 1$ yields straight filaments throughout deposition (Figure 2.16a), enforcing $H^* = 2$ leads to filaments exhibiting noticeable waviness, as shown in Figure 2.16b.

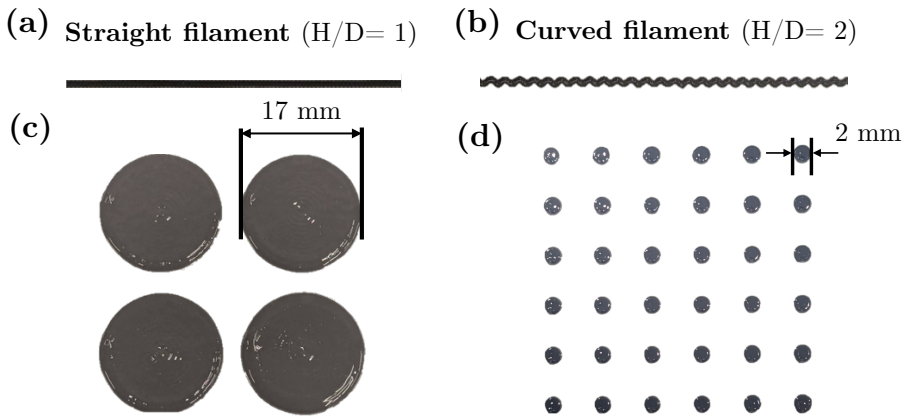


Figure 2.16: Determination of printing height $H$ and printing speed $V$. (a) Straight filaments at $H^* = 1$ and (b) curved filaments at $H^* = 2$. (c) Large 17 mm-diameter discs printed with $V = 10$ mm s$^{-1}$ and (d) small 2 mm-diameter discs printed with $V = 5$ mm s$^{-1}$.

Next, the printing speed $V$ is examined. When printing at high speeds, such as $V = 15$ mm s$^{-1}$, the extrusion rate cannot keep up with the required flow due to torque limitations of the extruder motors, and the material deposition becomes discontinuous and irregular. It also becomes challenging to accurately produce small geometries like discs with a radius of 1 mm, as the print head struggles to follow tight curves precisely at such velocities. The printing speed is thus reduced to lower values that allow the ink to be deposited consistently within the torque capability of the extruders. Patterns of centimetric size can be printed successfully at $V = 10$ mm s$^{-1}$ (Figure 2.16c), while millimetric features appear to be printed successfully at $V = 5$ mm s$^{-1}$ (Figure 2.16d). Hence, printing speeds of 5 and 10 mm s$^{-1}$ are selected for subsequent experiments, as they provide a good balance between deposition stability for small features and process efficiency, respectively. In particular, at a printing speed of $V = 10$ mm s$^{-1}$, the time spent by the ink in the mixer remains below pot life (see further details in subsection 2.4.4), thereby offering extended printing times. Reducing the printing speed to $V = 5$ mm s$^{-1}$ for fine details will however reduce the available printing times. Even though this speed will not be used to produce the centimetric heterogeneous patterns studied in this thesis, it is still considered to enable finer printing in the future but will require further assessment of the available printing times.

[9]The parameters $H$ and $V$ are interdependent, meaning increasing the printing speed can compensate for filament waviness at higher $H^*$, and thus they should ideally be optimized together.

### 2.4.4 Determination of extruder speed $V_E$

The extrusion speed $C$ plays a central role in regulating the volumetric supply of ink through the nozzle and, consequently, in the quality and geometry of the deposited filament. The extrusion speed $C$ (directly governed by the extruder speed $V_E$ through the stepper motor input $V_R$) is determined by mass conservation between the inlet and outlet flows. In this setup, $V_E$ represents the plunger speed corresponding to the volumetric flow rate of one syringe, so that the overall inlet flow rate coming from both syringes into the mixer is $Q = 2\ A_S V_E$, where $A_S$ is the cross-sectional area of a single syringe. Enforcing mass conservation at the nozzle exit yields:

$$C = \frac{Q}{A_N} = \frac{8 A_S V_E}{\pi D^2}, \tag{2.25}$$

where $A_N$ is the nozzle cross-sectional area and $D$ the nozzle diameter. Thus, the outflow velocity $C$ is directly proportional to a single extruder speed $V_E$, linking plunger actuation to the resulting extrusion. To systematically evaluate the influence of $V_E$, we first print a "snake" structure (Figure 2.17a) incrementing $V_E$ at each horizontal line while keeping the nozzle diameter $D$ and printing speed $V$ constant, with $H^* = 1$, using the 70 *phr* MRE ink. As shown in Figure 2.17a, when $V_E$ is too low, the material feed becomes insufficient, leading to discontinuous filaments and poor print quality. Conversely, when $V_E$ is too high, excess material accumulates, resulting in thickening filaments.

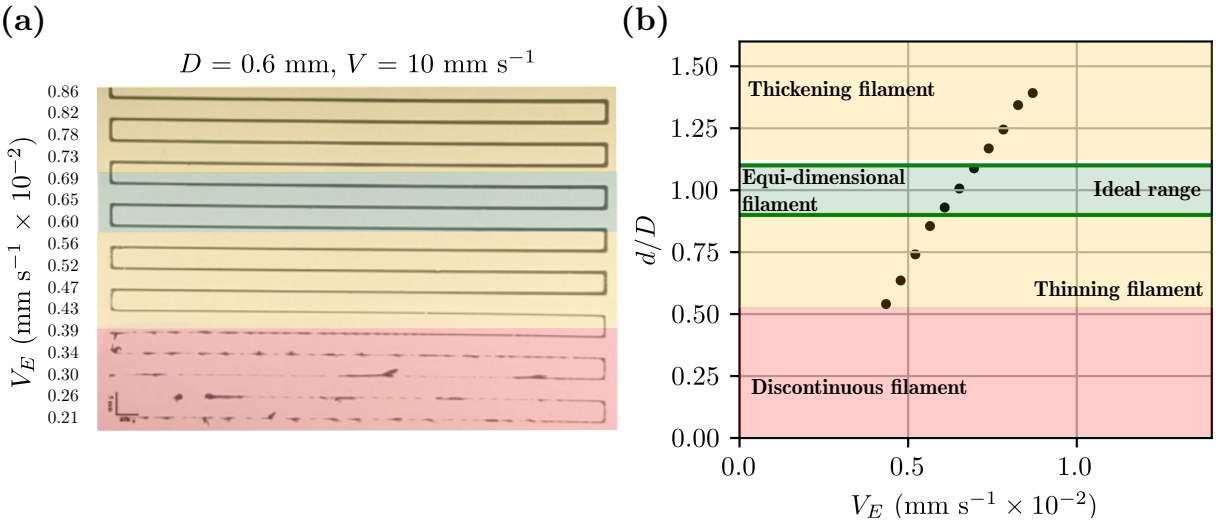


Figure 2.17: Effect of extruder speed $V_E$ on the quality and geometry of the deposited filament, for $D = 0.6$ mm, $V = 10$ mm s$^{-1}$ and $H^* = 1$ with the 70 *phr* MRE ink. (a) Printed "snake" structure at varying $V_E$, showing discontinuous filaments at low $V_E$ and over-extrusion at high $V_E$. (b) Ratio of filament to nozzle diameter ($d/D$) as a function of $V_E$, highlighting in green the equi-dimensional regime where $d/D \approx 1$ and stable deposition is achieved.

To quantitatively identify the optimal operating regime, the ratio of the deposited filament diameter $d$ to the nozzle diameter $D$ is plotted against $V_E$ (Figure 2.17b). Between the two extremes (discontinuous and thickening filament) lies an equi-dimensional regime where

$d/D \approx 1 \pm 0.1$, which corresponds to uniform and continuous filament deposition. Based on this study, the extruder speed is selected as $V_E = 0.0065$ mm s$^{-1}$, which ensures equi-dimensional filament deposition under the selected conditions ($D = 0.6$ mm, $V = 10$ mm s$^{-1}$ and $H^* = 1$). A thinner filament diameter corresponding to a finer printing resolution of nearly 500 $\mu m$ could be obtained but the equi-dimensional regime is favored to accommodate potential variations in the extrusion speed linked to possible variations in the ink such as the presence of filler aggregates. Note that the optimal $V_E$ value will vary if either the printing speed $V$ or the nozzle diameter $D$ is changed.

To study the influence of the ink particle content on filament formation, the same test is conducted for 140 and 210 *phr* MRE inks (Figure 2.18). As shown, for the same extruder speed $V_E$, the $d/D$ ratio decreases with increasing *phr*. This indicates that increasing *phr* reduces the printed filament diameter $d$, because of higher particle loading and flow resistance. Consequently, the optimal conditions for achieving an equi-dimensional regime ($d/D \approx 1$) shift with variations in particle content, requiring slightly higher extruder speeds to ensure uniform and continuous deposition of filaments as *phr* increases.

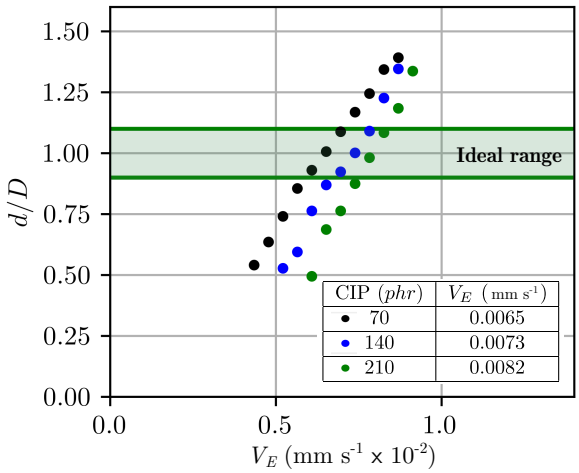


Figure 2.18: Effect of the extruder speed $V_E$ on filament diameter for different ink particle contents (70, 140 and 210 *phr*) at $D = 0.6$ mm, $V = 10$ mm s$^{-1}$ and $H^* = 1$.

## 2.5 Interdependency of print parameters and extension to multi-layer printing

In DIW, the quality and geometry of the deposited filament is influenced by the combined effects of the nozzle diameter $D$, printing speed $V$ and extruder speed $V_E$. These parameters determine the volumetric flow rate through the nozzle, which in turn affects the stability of the filament and the resulting filament diameter $d$. While in the previous section, printing speed $V$ and nozzle diameter $D$ were deliberately fixed before adjusting the other parameters, we examine in what follows how varying printing speed and nozzle diameters impact filament diameter $d$ to identify conditions that produce equi-dimensional

filaments ($d/D \approx 1$). Since the objective is only to study the interdependency of certain print parameters, all tests are performed using the 70 *phr* MRE ink.

### 2.5.1 Combined effect of printing speed $V$, nozzle diameter $D$ and extruder speed $V_E$

First, at varying printing speed $V$, filaments are printed at constant extruder speed $V_E = 0.0065$ mm s$^{-1}$ and nozzle diameter $D = 0.6$ mm, with the layer height fixed such that $H^* = 1$. As shown in Figure 2.19a, at low printing speeds, excess material accumulates, producing thick filaments with $d/D > 1$. At high printing speeds, however, the deposited filament becomes thinner ($d/D < 1$) and may even break due to insufficient material feed.

To quantify this effect, the ratio $d/D$ is plotted as a function of $V$ (Figure 2.19b), showing here a non-linear relationship. Between the extremes lies the narrow equi-dimensional regime where $d/D \approx 1$, corresponding to stable and continuous deposition. This regime is consistent with the optimal printing conditions identified from the extruder speed variation test, with $V = 10$ mm s$^{-1}$ providing reliable equi-dimensional filaments under the selected conditions.

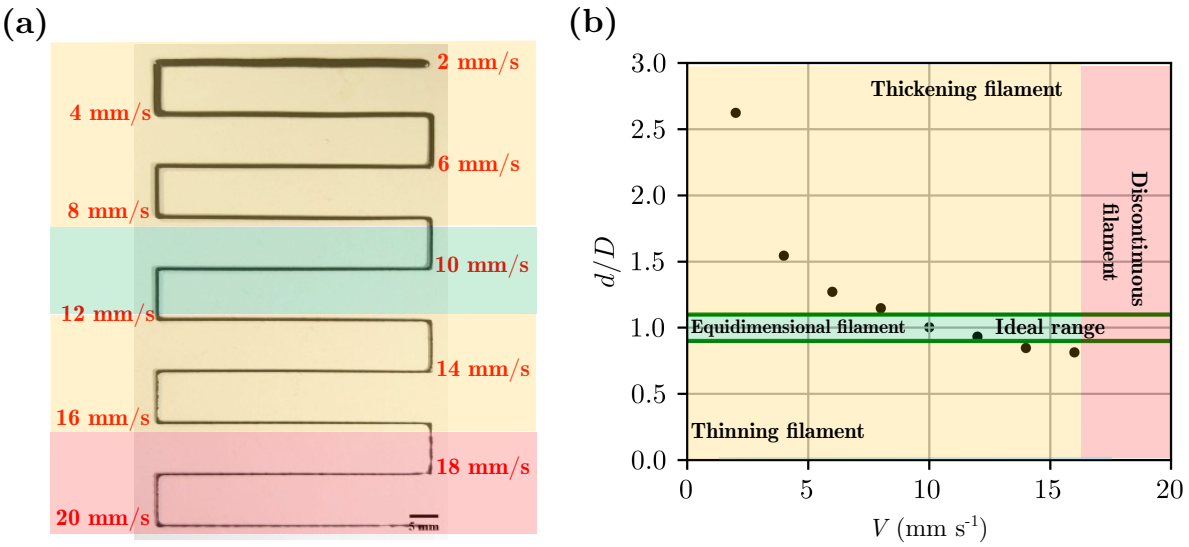


Figure 2.19: Effect of printing speed $V$ at $V_E = 0.0065$ mm s$^{-1}$, $D = 0.6$ mm and $H^* = 1$. (a) Continuous filaments printed at different $V$, showing over-extrusion at low speeds and thinning/breaking at high speeds. (b) Ratio of filament to nozzle diameter ($d/D$) as a function of printing speed $V$, highlighting in green the narrow equi-dimensional regime ($d/D \approx 1$) where stable deposition occurs.

Next, the combined influence of nozzle diameter $D$, extruder speed $V_E$, and printing speed $V$ on filament formation is summarized in Figure 2.20.

Figure 2.20a shows how $d/D$ changes with extruder speed $V_E$ for different nozzle diameters and printing speeds. At low $V_E$, discontinuous filaments are observed even at moderate printing speeds due to insufficient material delivery. As $V_E$ increases, the system reaches

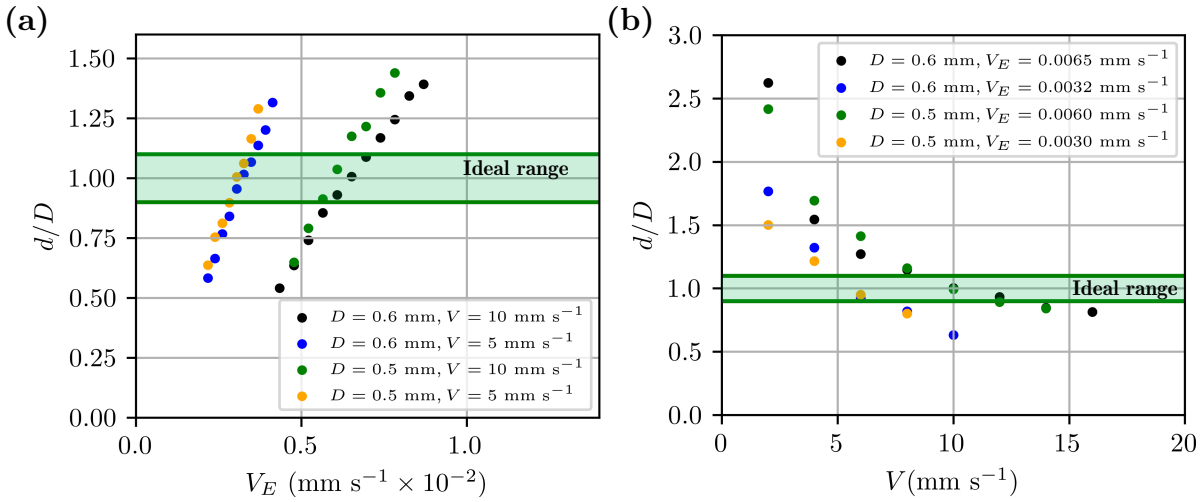


Figure 2.20: Combined effects of nozzle diameter $D$, printing speed $V$ and extruder speed $V_E$ on filament to nozzle diameter ratio $d/D$. (a) $d/D$ as a function of extruder speed $V_E$ for different combinations of nozzle diameters and printing speeds, showing the influence of $D$ and $V$ on the necessary $V_E$ required to reach equi-dimensional deposition. (b) $d/D$ as a function of printing speed $V$ for different combinations of nozzle diameters and extrusion speeds, highlighting the greater tolerance of larger nozzles to high-speed printing compared to smaller nozzles.

the equi-dimensional regime ($d/D \approx 1$). It can also be seen that the nozzle diameter $D$ influences both the maximum filament diameter and the maximum extruder speed achievable since the diameter sets the shear rate inside the nozzle. Smaller nozzles create more shear, which boosts elastic recovery at the nozzle exit and causes more die-swelling, leading to a larger extruded filament diameter ($\alpha D$). Additionally, because the volumetric flow rate depends on the nozzle's cross-sectional area, smaller nozzles reduce the total flow rate and thus lower the maximum extruder speed.

Complementary results are shown in Figure 2.20b, where $d/D$ is plotted against the printing speed $V$ for different combinations of nozzle diameters and extruder speeds. Here, larger nozzles can sustain higher printing speeds while maintaining equi-dimensional filaments, whereas smaller nozzles are more sensitive to under-extrusion and filament discontinuities at elevated speeds. Together, these results highlight how $D$, $V$, and $V_E$ must be co-optimized to achieve stable filament deposition.

### 2.5.2 Summary of print parameters

The experimentally-determined operating parameters for different printing speeds, extruder speeds and CIP contents (*phr*) are summarized in Table 2.4. For the larger nozzle ($D = 0.6$ mm), at a printing speed of $V = 10$ mm s$^{-1}$, stable deposition is achieved with an extruder speed of $V_E = 0.0065$ mm s$^{-1}$ for the 70 *phr* MRE ink formulation. Reducing the printing speed to $V = 5$ mm s$^{-1}$ results in a proportional reduction of the extruder speed to $V_E = 0.0032$ mm s$^{-1}$, demonstrating that $V_E$ approximately doubles as the printing speed increases from 5 to 10 mm s$^{-1}$ due to conservation of flow rate. For higher

CIP loadings, slightly higher extruder speeds are required to maintain equi-dimensional filaments due to the increased viscosity of the ink. At a printing speed of $V = 10$ mm s$^{-1}$, extruder speed of $V_E = 0.0073$ mm s$^{-1}$ and 0.0082 mm s$^{-1}$ is obtained for 140 *phr* and 210 *phr*, respectively. These results highlight that the effect of particle content is secondary compared to printing speed, but must still be accounted for when calibrating extrusion parameters. Relative extruder speed at $V = 5$ mm s$^{-1}$ can be calculated for 140 *phr* and 210 *phr* using flow conservation. For the smaller nozzle ($D = 0.5$ mm), similar trends were observed with a slightly reduced extruder speed $V_E$, but in this study $D = 0.6$ mm is used to avoid blockages of the nozzle. In all cases, the operating window is determined by the balance between material deposition and translation speed of the nozzle.

| **Parameter** | **Particle content** | **Value** |
|---|---|---|
| Dynamic mixer speed ($V_m$) | – | 56.25 rpm |
| Nozzle geometry | – | Cylindrical, 6.35 mm needle height |
| Nozzle diameter ($D$) | – | 0.6 mm |
| Printing speed ($V$) & Extruder speed ($V_E$) | Ecoflex™ 00-50 | $V = 10$ mm s$^{-1}$, $V_E = 0.0060$ mm s$^{-1}$<br>$V = 5$ mm s$^{-1}$, $V_E = 0.0030$ mm s$^{-1}$ |
| | 70 *phr* | $V = 10$ mm s$^{-1}$, $V_E = 0.0065$ mm s$^{-1}$<br>$V = 5$ mm s$^{-1}$, $V_E = 0.0032$ mm s$^{-1}$ |
| | 140 *phr* | $V = 10$ mm s$^{-1}$, $V_E = 0.0073$ mm s$^{-1}$<br>$V = 5$ mm s$^{-1}$, $V_E = 0.0036$ mm s$^{-1}$ |
| | 210 *phr* | $V = 10$ mm s$^{-1}$, $V_E = 0.0082$ mm s$^{-1}$<br>$V = 5$ mm s$^{-1}$, $V_E = 0.0041$ mm s$^{-1}$ |
| Height ratio ($H^*$) | – | 1 |

Table 2.4: Final selected printing parameters.

The active-mixing DIW printing parameters have been established with the purpose of printing heterogeneous thin films. In this case, the heat bed is not activated because the modified rheology allows the deposited filament to hold its shape (up to three layers for 210 *phr* ink).

Furthermore, for all the geometries considered, a rectilinear infill pattern is used. In each case, the outer boundary is first printed following the prescribed geometric shape, and the interior is subsequently filled using a uniform rectilinear hatching pattern. For the strip topology, the hatching lines are oriented perpendicular to the strip length, whereas for disc and disc–annulus geometries, the infill direction is fixed along a single global Cartesian axis. This strategy ensures a homogeneous infill for all geometries, independent of the specimen shape. Note, however, that in DIW with soft polymer inks, the orientation of the hatching path has little effect on the final material behavior. Unlike FDM printing, where filament orientation has a strong impact on anisotropy and mechanical performance, the

soft DIW materials relax and level out after being deposited. This means that orientation-dependent effects are minimal, as will be discussed further in Appendix C. Hence, while the hatching pattern shapes the internal path layout, it has little mechanical impact in this DIW context.

Finally, continuous-printing experiments are performed by printing back-and-forth lines using Ecoflex™ 00-50 base silicone ink and the 210 *phr* MRE ink at a print speed of 10 mm $s^{-1}$ with the selected process parameters. It is observed that the 00-50 silicone ink can be printed continuously for nearly 126 min, that is more than 2 h and 7 times the pot life, whereas the 210 *phr* MRE ink remains stable for approximately 45 min before curing-related effects become noticeable through filament irregularities. Note that the printing time could be further extended by increasing the printing speed (and thus lowering the residence time) if geometries with larger footprint are considered. In both above-mentioned cases, the printed line diameters are examined to quantify extrusion diameter stability. The 00-50 silicone ink produces a mean filament diameter of 0.75 mm with a standard deviation of 0.16 mm, while the 210 *phr* MRE ink yields a mean diameter of 0.68 mm with a standard deviation of 0.087 mm.

### 2.5.3 Multi-layer printing

Even though our primary goal is to print one- to three-layer heterogeneous patterns, the printer can also be used to deposit a large number of layers. This capability allows for the fabrication of more intricate three-dimensional MRE designs, showcasing the versatility of this setup for practical uses.

First, 2.5D structures in the form of dogbone specimens with nominal thickness 3 mm are considered (for mechanical characterization purposes, see section 3.1 and Appendix C) following the geometry shown in Figure 2.21a. In the case of samples printed in a cross-hatching configuration with five layers (see Appendix C for more details), the specimen printed without heated bed (Figure 2.21b) shows larger geometrical deviations compared to the CAD design than the specimen printed with a heated bed set at 60°C (Figure 2.21c).

However, the quick curing triggered by the use of the heated bed can disrupt the even spreading of filaments, resulting in voids between layers, as observed in Figure 2.21c and illustrated in Figure 2.21d. Alternatively, when printing without a heated bed, the filaments have more time to blend and flow, which decreases the likelihood of void formation and improves layer filling (Figure 2.21b). Yet, the absence of heat can slow down the curing process, and negatively affect the vertical alignment of layers, causing deformations and greater variations from the intended shapes (Jang et al. 2021).

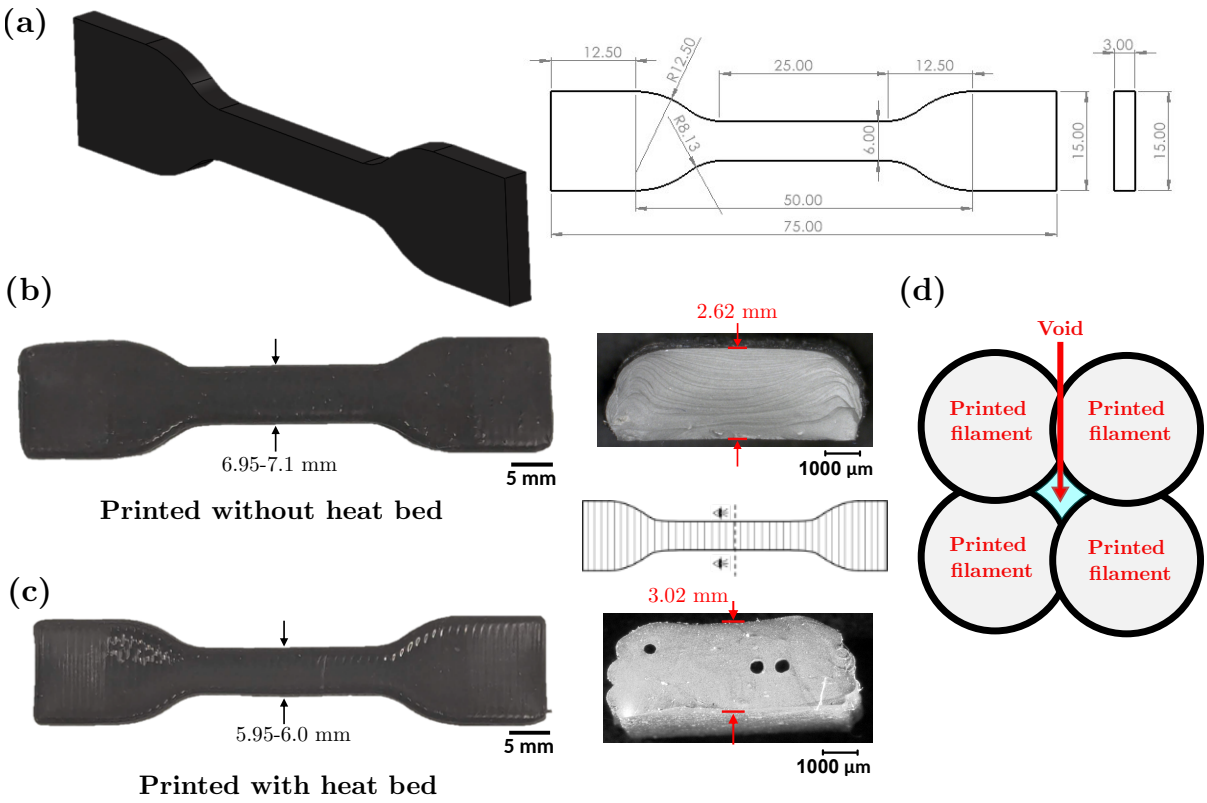


Figure 2.21: Dogbone specimens with 70 *phr* MRE ink. (a) CAD geometry and dimensions (in mm) of the specimens. (b) Specimen printed without a heated bed, showing deviations from the CAD design but no voids. (c) Specimen printed with a heated bed, showing improved shape retention but with voids between layers. (d) Illustration highlighting void formation between deposited layers.

The vertical alignment of layers, and thus the role of heat, is even more critical when considering 3D objects. As shown in Figure 2.22a-b, complex 3D structures such as a pyramid and an hourglass with 10° overhang are successfully printed with the 70 *phr* MRE ink when the heated bed is set to 60°C. By using a heated bed, the curing of the filament occurs more quickly, which enhances layer adhesion and helps maintain the shape of the printed object even after adding numerous layers. Consequently, this reduces discrepancies between the designed and printed geometries, leading to better dimensional accuracy in the final product.

In contrast, Figure 2.22c-d illustrates the printing outcomes for the same pyramid and hourglass structures using 70 *phr* MRE ink and 210 *phr* MRE ink, respectively, without a heated bed. Without heat, the prints are unable to support themselves after a few layers, resulting in significant deformation in the 70 *phr* ink due to insufficient curing and weak interlayer bonding. The 210 *phr* MRE ink shows somewhat better structural stability, as the higher filler content increases viscosity and stiffness. However, even in this case, the prints do not maintain their intended geometry as effectively as those fabricated with the heated bed. These comparisons highlight the essential role of heating in achieving reliable

3D-printed structures with polymers.

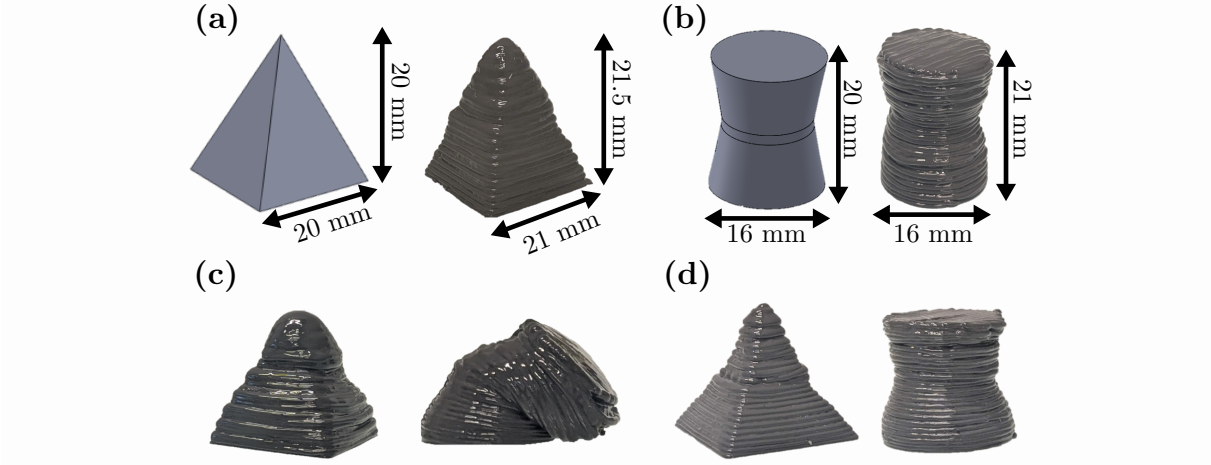


Figure 2.22: Printing of complex 3D structures. (a) Pyramid structure printed using 70 *phr* MRE ink with heated bed. (b) Hourglass structure with 10° overhang printed using 70 *phr* MRE ink with heated bed. (c) Pyramid and hourglass structures printed using 70 *phr* MRE ink without a heated bed. (d) Pyramid and hourglass structures printed using 210 *phr* MRE ink without a heated bed.

These observations also reveal an important trade-off: while using a heated bed improves shape accuracy and stability across layers, it can lead to increased porosity. In contrast, printing without heat helps reduce voids but sacrifices overall geometric precision. Since the objective of this study is to print thin films of only one to three layers, we choose to perform the printing without heat.

## 2.6 Concluding remarks

In this chapter, direct ink writing with active mixing has been proposed and calibrated to print MRE inks with different particle contents. First, rotational and oscillatory rheometry tests were carried out to study the effects of a liquid thixotropic agent (THIVEX®) and CIP particles on the behavior of Ecoflex™ 00-50. It was shown that 1 wt% THIVEX® was enough to change Ecoflex™ 00-50 from a Newtonian fluid to a shear-thinning, yield-stress material. Static tests demonstrated that both CIP and THIVEX® encourage shear-thinning, but that THIVEX® mainly controls the zero-shear, shape-holding behavior. Dynamic tests confirmed that THIVEX® mostly determines the yield behavior and solid-like plateau, while CIP increases apparent viscosity and changes the flow stress.

A transparent pigmented silicone system was used to calibrate experimentally the dynamic mixer speed by analyzing color changes. This approach set a lower limit for complete mixing and showed that going faster could cause bubbles from cavitation. A theoretical framework was then employed to estimate the minimum mixer speed for opaque MRE inks. The predicted rpm range matched experimental results and supported using 56.25 rpm for all MRE formulations.

Extrusion tests with conical and cylindrical nozzles showed that a short cylindrical nozzle ($L_{cyl}$ = 6.35 mm) worked best for highly-filled MRE inks. A 0.6 mm outlet diameter was chosen to balance print resolution, reliable extrusion, and lower risk of motor stalling or clogging. Numerical simulations explained the experimental findings by showing that conical nozzles experience sharp increases in shear rate at their tip while cylindrical nozzles have a more even wall shear rate throughout their length, thereby promoting stable extrusion.

The relationship between nozzle diameter $D$, printing speed $V$ and extruder speed $V_E$ was assessed experimentally using straight-line tests and the extruder speed $V_E$ was calibrated for each CIP content (70, 140 and 210 *phr*) to keep the filaments equi-dimensional and obtain stable, continuous filament deposition.

Multi-layer printing tests showed a trade-off between shape accuracy and porosity. Using a heated bed improves dimensional accuracy and overhang stability but causes more voids between layers. In contrast, printing without heat reduces porosity but sacrifices some geometric precision. Because this work focuses on thin films, printing without a heated bed was chosen as the best approach.

Furthermore, the continuous-printing studies provided a practical estimate of the achievable print windows for the inks used in this work. The Ecoflex™ 00-50 silicone exhibited a stable printing window of approximately 126 min (7 times the pot life), while the 210 *phr* MRE ink remained printable for about 45 min under the selected process conditions. It is worth noting that studies reporting the use of curing retardants such as SLO-JO in DIW were only able to extend the working time of two-part silicones up to 2.7 times the pot life (Calais et al. 2022) while such additives can alter the mechanical properties of the cured polymer. Thus the active-mixing-assisted DIW proposed in this work can be considered in itself as a significant improvement to the state-of-the art of soft material printing.

In summary, the active-mixing-assisted DIW platform, together with the optimized MRE ink and tuned process settings, offers a reliable and repeatable way to print heterogeneous MRE films with controlled geometry, uniformity and rheology. The development of this chapter thus lay the foundations to study instabilities in heterogeneous MRE films/substrate systems, both experimentally and numerically, in the next chapters.

# Chapter 3
# Numerical modeling and validation

This chapter presents a comprehensive investigation of the magneto-mechanical response of magnetorheological elastomer (MRE) heterogeneous layers deposited on soft silicone substrates through experimental and numerical approaches. The first section details the material characterization conducted to access the mechanical properties of pure silicone and silicone-based MREs. The second section outlines the development and implementation of the numerical modeling framework using the finite element method. The homogenized phenomenological model based on the **F**-**B** constitutive law is introduced for isotropic soft MREs. An alternative formulation to the Coulomb gauge is examined, and its impact on numerical accuracy and stability is assessed. The discretization strategy, mesh design, and boundary conditions used in the simulations are also described. Finally, experimental and numerical results are compared to quantitatively validate the numerical predictions and the observed morphological patterns in various MRE film and substrate systems.

**Contents:**


3.1 Material characterization . . . 65
3.1.1 Mechanical behavior of elastomers . . . 65
3.1.2 Pure silicone substrate . . . 67
3.1.3 Magnetorheological elastomer film . . . 69
3.2 Numerical modeling and implementation . . . 73
3.2.1 Kinematics and balance laws . . . 73
3.2.2 Variational formulation . . . 76
3.2.3 Constitutive model for isotropic soft MREs . . . 78
3.2.4 3D boundary value problem (BVP) . . . 84
3.3 Numerical validation against the 2D model . . . 90
3.4 Numerical validation against experimental 3D surface profiles . . . 95
3.4.1 Sample fabrication . . . 95
3.4.2 Measurements of 3D morphological patterns . . . 96
3.4.3 Numerical model . . . 97
3.4.4 Comparison between experiments and numerics . . . 98
3.5 Concluding remarks . . . 101

## 3.1 Material characterization

In film–substrate systems with a magnetorheological elastomer (MRE) layer, the difference in shear moduli between the film and the substrate plays a decisive role in the onset of magnetically-induced surface instabilities. For the numerical model development presented in later sections, it is thus necessary to obtain reliable mechanical properties of the MRE film/substrate system. In particular, the shear moduli of both the substrate and film directly enter the constitutive laws that govern the bifurcation analysis and the prediction of surface instabilities. Since the critical strain for buckling is strongly dependent on $G_s/G_f$, a careful material characterization is required before any meaningful numerical predictions can be made.

### 3.1.1 Mechanical behavior of elastomers

Elastomers behave in a nonlinear manner, with viscoelastic characteristics and a nearly incompressible nature. These behaviors stem from the structure of their polymer chains and the way these chains are interconnected through a process called crosslinking. Elastomers are indeed made up of long, flexible chains that are bonded together by covalent links (crosslinks) introduced during the curing or vulcanization process (Gent 2011). This crosslinking prevents the chains from sliding past each other irreversibly, allowing them to bounce back to their original shape after being deformed, which is what gives elastomers their elasticity (Treloar 1975).

To quantitatively describe the stress–strain behavior of elastomers, the framework of hyperelasticity is typically employed. In this framework, the stress that a material experiences at a given point is only dependent on its current deformation state and can be calculated from a function that defines its strain energy (Ogden 1997). However, in reality, elastomers rarely fit this perfect hyperelastic model. Their behavior is often accompanied by energy loss mechanisms such as hysteresis, stress softening (also known as the Mullins effect), and residual deformation, especially noticeable during repeated loading and unloading cycles (see Figure 3.1).

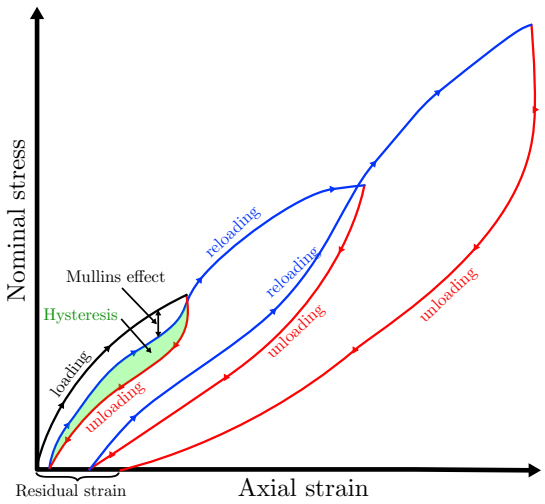


Figure 3.1: Illustration of the typical stress-strain response of a filled elastomer with inelastic effects under cyclic loading conditions, adapted from Dargazany et al. (2014).

When elastomers are subjected to repeated cyclic tests, they show a hysteretic stress–strain response, as illustrated in Figure 3.1. This means that there is a loop formed between the loading and unloading curves, and the area enclosed by the loop indicates the energy dissipated during the deformation process. After unloading, the remaining extension at zero load indicates residual strain. During the first unloading–reloading cycle, a noticeable drop in stress occurs compared to the initial loading, corresponding to the Mullins effect or stress softening (Mullins 1969). This happens because, under strain, microstructural changes occur in the polymer network. These include weak bond breaking, rearrangement of the polymer chains, and local damage within the network. After several cycles at the same maximum strain, the material typically stabilizes, showing reproducible minor hysteresis loops (Bauman 2008).

The extent of hysteresis and softening experienced by the elastomer heavily depends on its composition. For instance, in filled elastomers reinforced with materials like carbon black, silica or magnetic particles, the energy dissipation during deformation is significantly higher than in unfilled rubbers (Houwink 1956). The fillers interact with the polymer in complex ways, leading to mechanisms like the rupture of filler networks, slippage at filler interfaces, and disentanglement of polymer segments. Typically, the higher the concentration of these fillers, the more pronounced the effects are (Diani et al. 2009). In addition to this, residual deformation, or permanent set, occurs and is responsible for the irreversible strain remaining after unloading (Mullins 1949). This arises due to molecular reorganizations when the material is stretched, like bonds breaking or new crosslinks forming, as well as the anisotropy caused by the presence of fillers. Although some of this residual strain can gradually recover over time due to viscoelastic relaxation, a permanent portion usually persists, particularly in filled systems.

MREs, since they incorporate magnetic particles like carbonyl iron into a soft silicone or rubber matrix, display these viscoelastic and hysteretic behaviors influenced by the interactions between the magnetic particles and the polymer matrix (Bellan and Bossis 2012). The way the particles are distributed, their sizes, and their alignment can greatly affect how the material responds mechanically by changing its microstructure during deformation and impacting internal stresses. Additionally, when exposed to magnetic fields, MREs exhibit a unique magneto-mechanical coupling, which causes the matrix to stiffen and alters both the energy dissipation and the Mullins softening behavior (Bodelot et al. 2018).

In this work, compression and tension are the main loading modes that reflect the mechanical loading of the substrate and the MRE film, respectively, during the magnetically-induced instability. Uniaxial compression tests are conducted on cubic samples of the substrate material to determine its shear modulus, as direct tensile testing is also not well suited for such soft compliant silicones. In parallel, uniaxial tensile tests are performed on dogbone samples of the MRE to characterize its mechanical response and identify the relevant material parameters. These experiments provide direct insights into the hyperelastic and viscoelastic properties of the MRE at hand, including the degree of hysteresis, Mullins softening, and residual deformation. Together, these tests aim at providing the constitutive parameters required for the finite element model so that the simulations reflect the mechanical behavior of both the substrate and film materials.

### 3.1.2 Pure silicone substrate

#### 3.1.2.1 Mechanical tests

The test specimen considered in this study is fabricated using a molding process to produce a cubic sample of dimensions $20 \times 20 \times 20$ mm$^3$. The material used is Ecoflex™ 00-10 (Smooth-On Inc.), a soft platinum-cured silicone elastomer characterized by a very low modulus and a high flexibility. The two components (parts A and B) are mixed in a 1:1 ratio by weight and manually stirred thoroughly for 2 min to ensure homogeneity, followed by a 5 min degassing step to eliminate entrapped air. The resulting mixture is then poured into a 3D-printed mold without introducing any air bubbles, subjected to thermal curing at 70 °C for 2 h, and subsequently left at room temperature for 2 h to ensure complete crosslinking before testing.

The quasi-static uniaxial compression test is performed using a custom-built compression device equipped with a linear displacement motor (DRLM42G-04B2M-K, Oriental Motors). The system consists of a fixed bottom plate and a movable top plate attached to the actuator, as shown in Figure 3.2a. The top plate is driven at a constant speed of 0.02 mm s$^{-1}$, corresponding to a nominal strain rate of approximately $10^{-3}$ s$^{-1}$, while a total displacement of 10 mm is applied to the specimen. All tests are carried out under ambient laboratory conditions.

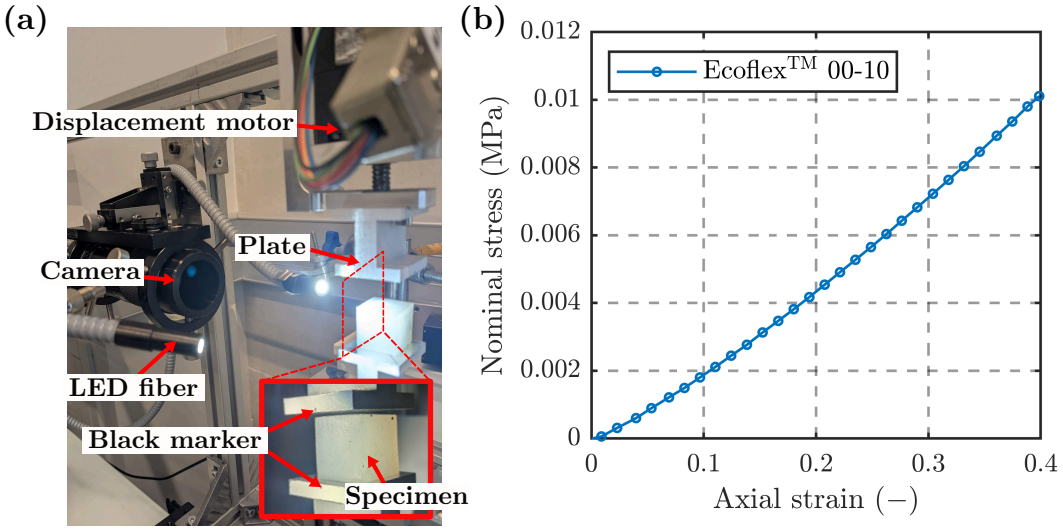


Figure 3.2: (a) Plate compression setup used for the mechanical characterization of the Ecoflex™ 00-10 silicone substrate. Black markers are applied on the plates for optical extensometry measurements, using a high-resolution camera and LED illumination. (b) Nominal stress-strain response obtained on a cube of the probed material.

Two black markers are applied on the plate faces to enable precise tracking of the applied axial displacement via non-contact video extensometry. For this purpose, a 5 megapixel camera (GO-5100M-USB, Jai) equipped with a telecentric lens (FXL-0305-VT-165, Seiwa Optical) is employed and illumination is supplied by a coaxial LED fiber light source (intraLED 5, Volpi). The compressive force transmitted through the specimen is simultaneously measured using a force sensor (LCAE-10KG, Omega Engineering). The synchronized displacement and force data are subsequently processed to compute the nominal stress–strain curve plotted in Figure 3.2b.

#### 3.1.2.2 Constitutive model fitting

The experimental stress–strain data obtained from the quasi-static compression test is used to identify the mechanical parameters of the substrate. Since the substrate is an unfilled elastomer exhibiting negligible hysteresis and rate dependence under the tested conditions, a hyperelastic constitutive model is sufficient to describe its response.

The Neo-Hookean constitutive law, derived from the statistical thermodynamics of crosslinked polymer chains, is often used as a first approximation for such materials. Initially, crosslinked polymers (such as elastomers and thermosets) behave in a Neo-Hookean manner because their polymeric chains can move relative to one another when subjected to stress. As the applied load increases, the polymer material undergoes significant molecular rearrangements, resulting in a steep rise in the incremental elastic modulus. This nonlinear stiffening cannot be captured by the Neo-Hookean model alone, motivating the use of the more general Lopez–Pamies model (Lopez-Pamies 2010), which also belongs to the class of incompressible isotropic stored-energy functions.

The strain energy density for the incompressible Neo-Hookean model is given by:

$$W(\mathbf{F}) = \begin{cases} \dfrac{G_s}{2}\,(I_1 - 3), & \text{if } J = 1, \\ +\infty, & \text{otherwise.} \end{cases} \tag{3.1}$$

where $G_s$ is the shear modulus of the substrate and $I_1$ is the first invariant of the modified right Cauchy–Green tensor.

In contrast, the Lopez-Pamies (LP) model introduces a nonlinear dependence on the first invariant $I_1$ through a sum of power-law terms, allowing for a more accurate description of material stiffening at large strains. The incompressible form of the equation is given by:

$$W_{\mathrm{LP}}(\mathbf{F}) = \begin{cases} \displaystyle\sum_{i=1}^{2} \frac{3^{1-a_i}}{2a_i}\, G_s^i \big(I_1^{a_i} - 3^{a_i}\big), \; a_i \in \mathbb{R}\ (i = 1, 2) & J = 1, \\ +\infty, & \text{otherwise,} \end{cases} \tag{3.2}$$

where $a$ is a real number.

Both models are fitted to the experimental nominal stress–strain data using a nonlinear least-squares data-fit in MATLAB. As shown in Figure 3.3, the Neo-Hookean model provides a reasonable approximation for small to moderate strains, yielding a best-fit shear modulus of $G_s = 0.0051$ MPa. However, deviations become noticeable at larger strains due to the model's inability to account for nonlinear stiffening. The Lopez–Pamies model with $m = 1$ and fitted parameters $G_s = 0.0058$ MPa and $a = 0.05$, accurately reproduces the entire experimental curve, including the high-strain regime. The obtained shear modulus value is consistent with literature data for Ecoflex™ 00-10, which reports a comparable modulus of approximately 0.0055 MPa

(Liao et al. 2020). This agreement confirms the validity of both the experimental procedure and the adopted constitutive model.

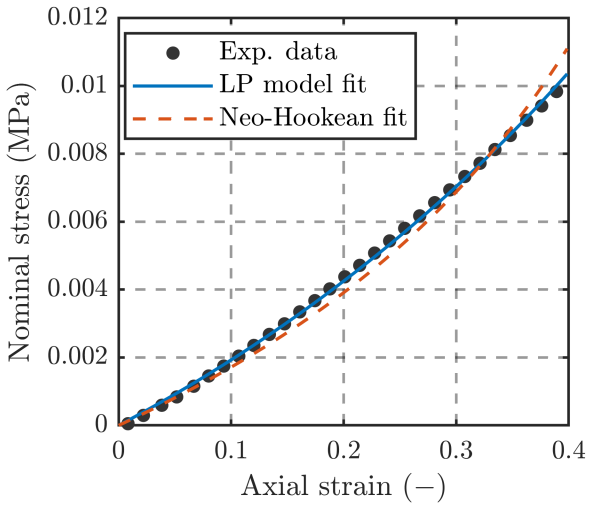


Figure 3.3: Experimental and fitted nominal stress–strain response for Ecoflex™ 00-10 under quasi-static compression, showing the comparison between the Neo-Hookean model ($G_s$ = 0.0051 MPa) and the Lopez–Pamies model ($G_s = 0.0058$ MPa, $a = 0.05$).

### 3.1.3 Magnetorheological elastomer film

#### 3.1.3.1 Mechanical tests

Dogbone specimens of MRE are prepared using the active-mixing direct ink writing (DIW) methodology discussed in chapter 2 and the processing parameters reported in Table 2.4. A printing speed of $V = 10$ mm s$^{-1}$ is employed and the corresponding extruder speed $V_E$ is adjusted for each particle content (70, 140 and 210 *phr*) according to the calibration summarized in Table 2.4. Furthermore, the samples used for the identification of the mechanical parameters are printed without the heated bed as they are most representative of the heterogeneous film used in the instability experiments (see Appendix C for further details on the characterization of molded samples, and of samples printed without and with a heated bed, as well as with various hatching strategies).

Cyclic uniaxial tensile tests are performed using an Instron-5967 machine equipped with a 50 N load cell (see Figure 3.4a). The experiments are conducted under displacement control at a rate of 0.25 mm s$^{-1}$, corresponding to a nominal strain rate of $5 \times 10^{-3}$ s$^{-1}$, and the unloading phase stops when the load reaches zero. Three specimen per case are tested and each specimen undergoes 10 consecutive loading–unloading cycles to capture both the Mullins effect and the stabilized stress–strain behavior. The longitudinal and transverse stretches of the specimen are tracked through the displacement of white markers applied on the specimen gage area by means of optical extensometry, using a high-resolution camera equipped with a telecentric lens and illumination from a coaxial LED fiber light source (similarly to subsection 3.1.2). To reduce high-frequency noise in the force-stretches synchronized signals, a Savitzky-Golay digital filter ($2^{nd}$-degree polynomial, 51-point window) is applied to process the measured raw data, before computing the nominal stress–strain curve (see also Appendix C regarding the measurement

of the samples' cross-sectional area). The upload parts of the stabilized $10^{\text{th}}$ cycle top curve of samples with different particle contents are reported in Figure 3.4b, where the dotted line corresponds to the mean response, and the shaded region represents the variable range that includes the results of all three specimens tested for the specific type.

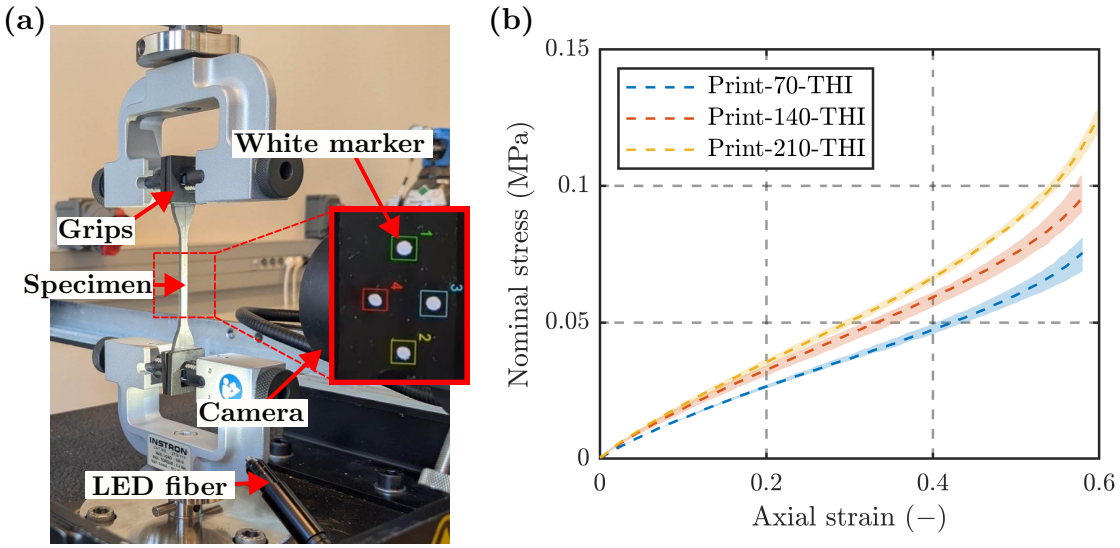


Figure 3.4: (a) Tensile setup used for the mechanical characterization of the Ecoflex™ 00-50 printed silicone. White markers are applied in the gage area of the samples for optical extensometry measurements, using a high-resolution camera and LED illumination. (b) Nominal stress-strain response of samples with different CIP particle contents (70, 140 and 210 *phr*).

### 3.1.3.2 Constitutive model fitting

The mechanical response of MREs is governed by a soft polymer matrix containing large volume fractions of rigid CIP particles. Because these inclusions do not deform under the mechanical loading conditions, the stress carried by the composite cannot be described by the polymeric matrix shear modulus $G_m$ alone. Instead, an effective shear modulus $G(c)$, dependent on the particle volume fraction $c$, must be used within the hyperelastic formulation.

The polymer matrix is modeled using the incompressible Lopez-Pamies (2010) strain-energy density, in the same form as for the polymer substrate:

$$W_{\text{LP}}(\mathbf{F}) = \begin{cases} \displaystyle\sum_{i=1}^{2} \frac{3^{1-a_i}}{2a_i} G_m \left(I_1^{a_i} - 3^{a_i}\right), \; a_i \in \mathbb{R} \; (i = 1, 2) & J = 1, \\ +\infty, & \text{otherwise}, \end{cases} \tag{3.3}$$

where $G_m$ is replaced by a homogenized modulus $G(c)$ to account for the presence of rigid particles.

To model the effective response of the matrix with the rigid inclusions and also to capture the full range of particle concentrations studied, an explicit homogenization model proposed by Lefèvre

and Lopez-Pamies (2022) (LLP) is used in this study, that reads:

$$G_{\mathrm{LLP}} = \frac{G_m}{\left[\left(1+\alpha(\beta+(c/p_n)^2)(c/p_n)^2\right)\left(1-\frac{c}{p_n}\right)\right]^{5p_n/2}}, \tag{3.4}$$

where $p_n$ is the percolation threshold and $\alpha, \beta \in \mathbb{R}$ are fitting parameters. This expression reduces to the classical Krieger and Dougherty (1959) (KD) relation, when $\alpha = \beta = 0$, such that:

$$G_{\mathrm{KD}} = \frac{G_m}{(1-c/p_n)^{5p_n/2}}. \tag{3.5}$$

A standard requirement for any valid homogenization model is that it agrees with the Hashin and Shtrikman (1961) (HS) lower bound:

$$G_{\mathrm{HS}} = \frac{2+3c}{2(1-c)}\, G_m. \tag{3.6}$$

In the dilute limit, this expands as $G_{\mathrm{HS}}/G_m = 1 + \frac{5}{2}c + O(c^2)$, which gives a universal slope of 5/2 for composites with rigid inclusions (Einstein 1905). All constitutive parameters used in Eq. (3.3) and Eq. (3.4) are fitted using the nominal stress–strain response of the highly filled 210 *phr* MRE specimen (see Figure 3.5). The percolation threshold parameter is fixed to $p_n = 1$ to reflect the polydisperse particle microstructure, while the remaining parameters are identified from the 210 *phr* data. These calibrated parameters are then used to predict the responses of the 70 and 140 *phr* specimens. As shown in Figure 3.5, the model captures both the nonlinear stiffening at high particle contents, and provides accurate predictions at lower particle loadings.

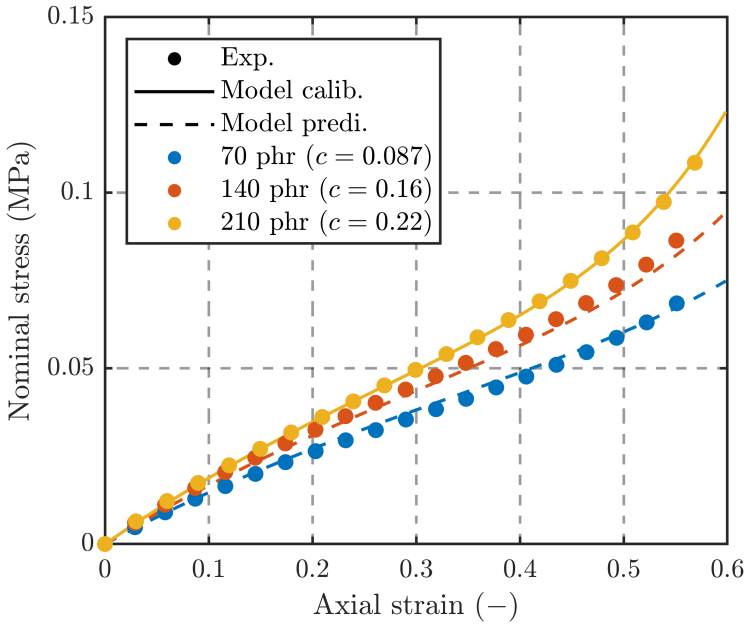


Figure 3.5: Experimental and fitted nominal stress-strain response of the MRE specimens under uniaxial tension. All constitutive parameters of the Lopez-Pamies model and Lefèvre-Lopez-Pamies homogenization law are calibrated using the 210 *phr* ($c = 0.22$) experimental data, and the same parameter set is then used to predict the responses of the 70 and 140 *phr* specimens ($c = 0.087$ and 0.16, respectively).

The calibrated parameter values of the LLP model are shown in Table 3.1. Note that here, two terms are needed to capture the stiffening at higher strain.

| $G_1$ (MPa) | $G_2$ (MPa) | $a_1$ | $a_2$ | $\alpha$ | $\beta$ | $p_n$ |
|---|---|---|---|---|---|---|
| 0.0017 | 0.045 | 7.98 | 0.68 | −0.0036 | 6.07 | 1 |

Table 3.1: Calibrated mechanical and homogenization parameters of the LLP model.

A comparison of $G/G_m$ computed from the Lefèvre and Lopez-Pamies (LLP) model with the Hashin and Shtrikman (HS) and Krieger and Dougherty (KD) predictions is provided in Figure 3.6, confirming that the fitted parameters remain well above the HS lower bound for all $c$ and therefore satisfy the micromechanical admissibility conditions.

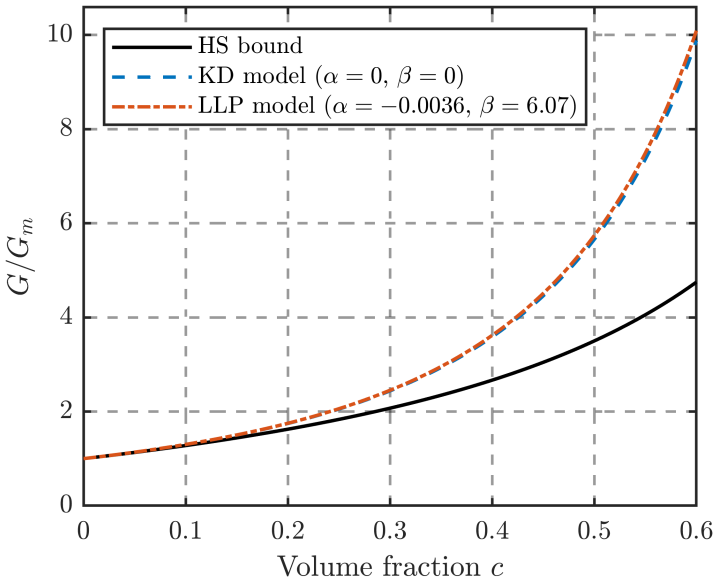


Figure 3.6: Effective shear modulus ratio $G/G_m$ as a function of particle volume fraction $c$ predicted by the Hashin-Shtrikman bound, the Krieger-Dougherty model, and the Lefèvre-Lopez-Pamies model with the calibrated parameters.

To allow for a weakly compressible response while preserving the same deviatoric structure, we can use an ad-hoc compressible extension of the incompressible phenomenological model that relaxes the constraint of strict incompressibility without modifying the essential features of the formulation in the nearly incompressible limit, corresponding to large values of the bulk modulus. This becomes very useful when incorporating in the finite-element solver. The resulting compressible Lopez-Pamies energy reads:

$$W_{\mathrm{LP}}(\bar{I}_1, J) = \sum_{i=1}^{2} \left[ \frac{3^{1-a_i}}{2a_i} G_m^i \left( \bar{I}_1^{a_i} - 3^{a_i} \right) - \frac{G_m^i}{s} \ln J \right] + \frac{G'_m}{2\,s^2} \left( J^2 - 1 \right)^2, \tag{3.7}$$

with:

$$\begin{aligned} I_1 = \mathrm{tr}(\mathbf{C}), \qquad J = \det \mathbf{F}, \qquad \bar{I}_1 = 3 + \frac{I_1 - 3}{s}, \\ s(c, \alpha, \beta, p_n) = \Big( (1 + \alpha(\beta + (c/p_n)^2)(c/p_n)^2)(1 - c/p_n) \Big)^{\frac{5p_n}{2}}, \end{aligned} \tag{3.8}$$

which reduces to a nearly incompressible approximation of the analytical effective mechanical free energy density Eq. (3.2). We typically set the Lamé parameter $G'_m = 500\, G_m$, which ensures a nearly incompressible response delivering $J \approx 1$ as shown in Figure 3.7.

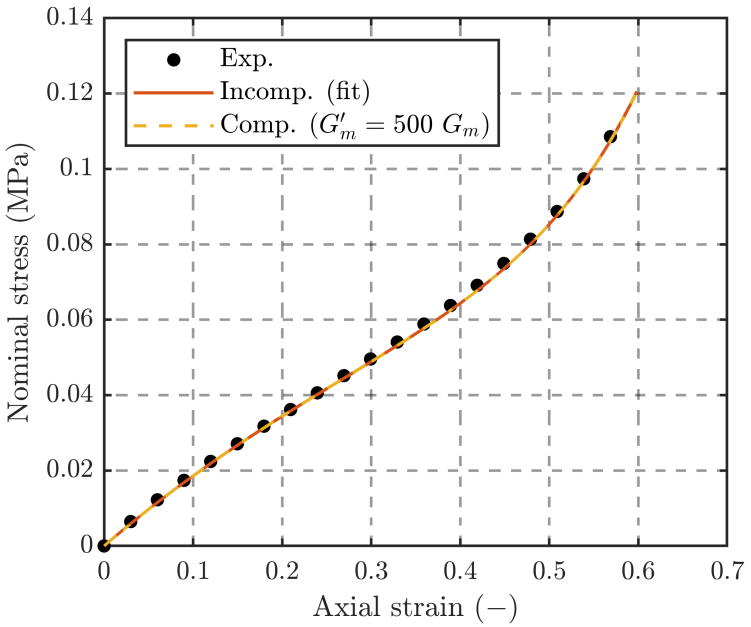


Figure 3.7: Nominal stress as a function of axial strain for a representative uniaxial tension test comparing 210 *phr* ($c = 0.22$) experimental data, incompressible Lopez-Pamies fit, and compressible extension with $G'_m = 500\, G_m$. The compressible model reduces to a nearly incompressible response with $J \approx 1$.

## 3.2 Numerical modeling and implementation

This section introduces the theoretical and numerical framework used to solve the MRE boundary value problem, with the aim to reproduce the magnetically-induced instabilities observed experimentally. We first present the governing kinematics and balance laws in both Eulerian and Lagrangian formulations (subsection 3.2.1), followed by the corresponding variational principle based on the magnetic vector potential $\mathbf{A}$ (subsection 3.2.2) formulated following the approach of Brown (1966). The constitutive behavior of the MRE film, substrate and surrounding air is introduced through the Helmholtz free energy density expressed as a function of the deformation gradient $\mathbf{F}$ and the Lagrangian magnetic induction $\mathbf{B}$ (subsection 3.2.3). An alternative gauge condition and its numerical implications are also discussed. Additionally, the formulation incorporates regularization terms to stabilize the solution under large deformations and magneto-mechanical coupling conditions. Finally, the mesh configuration and boundary conditions used in the finite element simulations are detailed in subsection 3.2.4 along with the small material imperfections introduced to facilitate the numerical treatment of instabilities.

### 3.2.1 Kinematics and balance laws

Although the governing equations for finite strain magnetoelasticity are known (Kankanala 2004; Dorfmann and Ogden 2005; Bustamante et al. 2008; Danas et al. 2012), a brief presentation is given here for completeness. We adopt the usual continuum mechanics conventions: all field

quantities associated with the current configuration are denoted by lowercase letters, while capitals are used for their reference configuration counterparts. Scalars are denoted by script symbols, while bold symbols are used for vectors and tensors.

Consider a 3D magnetoelastic body that occupies a region $\mathcal{V}_0$ (respectively $\mathcal{V}$ in the deformed current configuration) with boundary $\partial\mathcal{V}_0$ and outward normal $\mathbf{N}$ in the undeformed reference configuration as shown in Figure 3.8. A material point of initial position vector $\mathbf{X} \in \mathcal{V}_0$ has a current position vector:

$$\mathbf{x} = \mathbf{x}(\mathbf{X}) = \mathbf{X} + \mathbf{u}(\mathbf{X}), \tag{3.9}$$

where $\mathbf{u}$ is the displacement vector field.

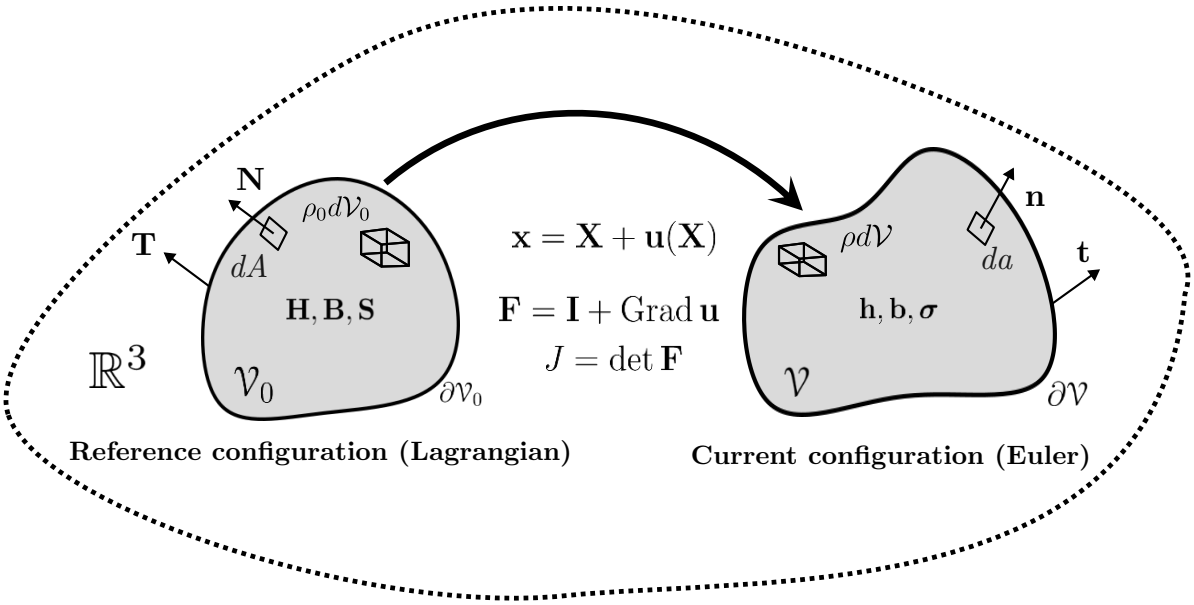


Figure 3.8: Reference configuration $\mathcal{V}_0$ with boundary $\partial\mathcal{V}_0$ and current configuration $\mathcal{V}$ with boundary $\partial\mathcal{V}$, both embedded in the ambient space $\mathbb{R}^3$.

The deformation gradient $\mathbf{F}$ and its determinant $J$ needed to quantify the mechanical strain contribution to the free energy of MREs are defined by:

$$\mathbf{F} \equiv \boldsymbol{\nabla}\mathbf{x} = \mathbf{I} + \boldsymbol{\nabla}\mathbf{u}; \qquad J \equiv \det \mathbf{F} > 0, \quad \forall \mathbf{x} \in \mathcal{V}; \tag{3.10}$$

where $\boldsymbol{\nabla} \equiv \partial/\partial\mathbf{x}$ is the current configuration gradient operator. The reference density of the solid $\rho_0^i$ (for i = f: film, s: substrate, a: air) is related to the current density $\rho^i$ through mass conservation by:

$$\rho_0^i = \rho^i J. \tag{3.11}$$

The mechanical quantities needed for setting the MRE boundary value problem are the total Cauchy stress $\boldsymbol{\sigma}$, the body force $\mathbf{f}$ and the traction $\mathbf{t}$ in the deformed current configuration. They satisfy (Kankanala 2004; Dorfmann and Ogden 2005):

$$\boldsymbol{\nabla} \cdot \boldsymbol{\sigma} + \rho\mathbf{f} = 0, \quad \forall \mathbf{x} \in \mathcal{V}; \qquad \mathbf{n} \cdot [\![\boldsymbol{\sigma}]\!] = \mathbf{t}, \quad \forall \mathbf{x} \in \partial\mathcal{V}; \tag{3.12}$$

where $\boldsymbol{\nabla}\cdot$ is the corresponding divergence operator. The magnetic quantities are the magnetic induction $\mathbf{b}$, the magnetic field intensity $\mathbf{h}$ and the magnetization $\mathbf{m}$, related by:

$$\mathbf{b} = \mu_0(\mathbf{h}+\mathbf{m}), \quad \mathbf{m} \neq 0, \quad \forall \mathbf{x} \in \mathcal{V}; \qquad \mathbf{b} = \mu_0 \mathbf{h}, \quad \mathbf{m} = 0, \quad \forall \mathbf{x} \in \mathbb{R}^3 \setminus \mathcal{V}; \tag{3.13}$$

where $\mu_0$ is the magnetic permeability in vacuum. The fields $\mathbf{b}$ and $\mathbf{h}$ are Eulerian fields that satisfy the following differential equations and boundary/interface conditions in magnetostatics (Dorfmann and Ogden 2003; Kankanala 2004; Bustamante et al. 2008; Danas 2017). From the Gauss's divergence theorem and no magnetic monopole law, one indeed obtains:

$$\boldsymbol{\nabla} \cdot \mathbf{b} = 0, \quad \forall \mathbf{x} \in \mathbb{R}^3; \qquad \mathbf{n} \cdot [\![\mathbf{b}]\!] = 0, \quad \forall \mathbf{x} \in \partial\mathcal{V}; \tag{3.14}$$

where $[\![f]\!] \equiv f^+ - f^-$ is the jump of any field quantity $f$, evaluated at either side of the solid/air interface.

From Stokes theorem and Ampère's circuit law, we can derive the following equations in the absence of external current density:

$$\boldsymbol{\nabla} \times \mathbf{h} = 0, \quad \forall \mathbf{x} \in \mathbb{R}^3; \qquad \mathbf{n} \times [\![\mathbf{h}]\!] = 0, \quad \forall \mathbf{x} \in \partial\mathcal{V}; \tag{3.15}$$

where $\boldsymbol{\nabla}\times$ is the corresponding curl operator. Since the variational formulation used here is based on the Lagrangian description, Eulerian quantities can be pulled back to the reference configuration $\mathcal{V}_0$ from the current configuration $\mathcal{V}$. The relation between the first Piola-Kirchhoff stress $\mathbf{S}$ and the Cauchy stress $\boldsymbol{\sigma}$ is:

$$\mathbf{S} = J\boldsymbol{\sigma} \cdot \mathbf{F}^{-T}. \tag{3.16}$$

The Lagrangian counterparts of $\mathbf{b}$ and $\mathbf{h}$, denoted by $\mathbf{B}$ and $\mathbf{H}$, are:

$$\mathbf{B} = J\mathbf{F}^{-1} \cdot \mathbf{b}, \qquad \mathbf{H} = \mathbf{F}^T \cdot \mathbf{h}. \tag{3.17}$$

In the reference configuration, they satisfy:

$$\boldsymbol{\nabla} \cdot \mathbf{S} + \rho_0^i \mathbf{F} = 0, \quad \forall \mathbf{X} \in \mathcal{V}_0; \qquad \mathbf{N} \cdot [\![\mathbf{S}]\!] = \mathbf{T}, \quad \forall \mathbf{X} \in \partial\mathcal{V}_0; \tag{3.18}$$

$$\boldsymbol{\nabla} \cdot \mathbf{B} = 0, \quad \forall \mathbf{X} \in \mathbb{R}^3; \qquad \mathbf{N} \cdot [\![\mathbf{B}]\!] = 0, \quad \forall \mathbf{X} \in \partial\mathcal{V}_0; \tag{3.19}$$

$$\boldsymbol{\nabla} \times \mathbf{H} = 0, \quad \forall \mathbf{X} \in \mathbb{R}^3; \qquad \mathbf{N} \times [\![\mathbf{H}]\!] = 0, \quad \forall \mathbf{X} \in \partial\mathcal{V}_0. \tag{3.20}$$

As noted in the literature by Dorfmann and Ogden (2005) and Danas et al. (2012), the magnetization $\mathbf{m}$ is inherently an Eulerian variable. Hence its Lagrangian form is not unique, since Eq. (3.13) is not invariant under reference-to-current transformations.

### 3.2.2 Variational formulation

In subsection 3.2.1, we discussed the governing equations and boundary/interface conditions needed to define a finitely strained magnetoelastic solid. We are now at the crucial step of formulating the boundary value problem, which involves describing the material's response. To do so, we need to establish an energy density function for the MRE solid. Unlike the purely mechanical part that is determined by the deformation gradient $\mathbf{F}$, the magnetic aspect allows for the use of different independent variables, leading to different ways of approaching the problem.

As noted by Brown (1966) and later by Kankanala (2004), employing a Lagrangian framework is vital for accurately incorporating Maxwell's stresses in magnetoelastic formulations. The Helmholtz free energy density $W$ of the solid can depend not only on $\mathbf{F}$ but also on either the magnetic field $\mathbf{H}$ or the magnetic induction $\mathbf{B}$. Each choice leads to a unique formulation, each with its benefits in calculations, as indicated by Danas (2017). The $\mathbf{F}$–$\mathbf{H}$ approach appears in several recent studies (Lefèvre et al. 2017; Mukherjee et al. 2021), while the $\mathbf{F}$–$\mathbf{B}$ formulation is more commonly used in the literature (Dorfmann and Ogden 2004; Dorfmann and Ogden 2005; Kankanala 2004; Danas 2017). The $\mathbf{F}$–$\mathbf{H}$ framework uses a scalar magnetic potential, so it only adds one extra degree of freedom and allows for faster numerical calculations (Mukherjee 2020). The $\mathbf{F}$–$\mathbf{B}$ formulation, on the other hand, adds three extra degrees of freedom because of the magnetic vector potential, which increases computational cost. However, this approach is based on a fully-variational principle, making it especially useful for stability and bifurcation analyses. In these cases, instability can be detected directly by checking when the global stiffness matrix loses positive definiteness (Psarra et al. 2017; Psarra et al. 2019; Rambausek and Danas 2021). In practical applications, to model electromagnetic coils directly, the $\mathbf{F}$–$\mathbf{B}$ framework is also often preferred because electric currents are directly related to the magnetic vector potential (Dorn et al. 2021). While it is possible in theory to use a partial Legendre–Fenchel transformation to convert energy densities between the $\mathbf{F}$–$\mathbf{H}$ and $\mathbf{F}$–$\mathbf{B}$ formulations (Bustamante et al. 2008), these transformations are usually not available in closed form because the constitutive relations are highly nonlinear.

In this work, we have chosen to focus on the $\mathbf{F}$–$\mathbf{B}$ formulation since it is especially effective for boundary value problems that involve magneto-mechanical interactions and potential instabilities. Building on the works of Dorfmann and Ogden (2003) and Thomas and Triantafyllidis (2009), we first consider the total potential energy as:

$$\mathcal{P}(\mathbf{u}, \mathbf{A}) = \int_{\mathcal{V}_0} W(\mathbf{F}, \mathbf{B}) \, \mathrm{d}\mathcal{V}_0 - \int_{\partial\mathcal{V}_0} \mathbf{T} \cdot \mathbf{u} \, \mathrm{d}A. \tag{3.21}$$

Here, the first term $W$ is an amended energy function (see Dorfmann and Ogden (2005)) and depends on the material choice, which primarily depends on the deformation gradient $\mathbf{F}$ and Lagrangian magnetic induction $\mathbf{B}$. In this expression, $\mathbf{u}$ and $\mathbf{A}$ serve as independent variables with respect to which the potential energy in Eq. (3.21) is minimized. Additionally, the second term represents the applied traction $\mathbf{T}$. Since the total magnetic field $\mathbf{B}$ and applied magnetic field $\mathbf{b}_0$ are divergence free, according to Eq. (3.19) (i.e., $\boldsymbol{\nabla} \cdot \mathbf{B} = 0$, $\forall \mathbf{X} \in \mathbb{R}^3$), one can express

$\mathbf{B}$ in term of a vector potential $\mathbf{A}$ as:

$$\mathbf{B} = \boldsymbol{\nabla} \times \mathbf{A}. \tag{3.22}$$

Thus, as a next step we will consider variations of $\mathcal{P}$ with respect to these independent variables, i.e.,

$$\delta\mathcal{P}(\mathbf{u}, \mathbf{A}) = \mathcal{P}_{,\mathbf{u}}\, \delta\mathbf{u} + \mathcal{P}_{,\mathbf{A}}\, \delta\mathbf{A}. \tag{3.23}$$

First, it is helpful to define the variations of the following quantities:

$$\delta\mathbf{F} = \delta\mathbf{u}\, \boldsymbol{\nabla}, \qquad \delta\mathbf{B} = \boldsymbol{\nabla} \times \delta\mathbf{A}. \tag{3.24}$$

Then, using Eq. (3.23) together with Eq. (3.24), one gets:

$$\delta\mathcal{P} = \int_{\mathcal{V}_0} \left\{ \frac{\partial W}{\partial \mathbf{F}} : (\delta\mathbf{u}\, \boldsymbol{\nabla}) + \frac{\partial W}{\partial \mathbf{B}} \cdot (\boldsymbol{\nabla} \times \delta\mathbf{A}) \right\} \mathrm{d}\mathcal{V}_0 - \int_{\partial\mathcal{V}_0} \mathbf{T} \cdot \delta\mathbf{u}\, \mathrm{d}A, \tag{3.25}$$

which can be rewritten in terms of $\delta\mathbf{F}$ and $\delta\mathbf{B}$ as:

$$\delta\mathcal{P} = \int_{\mathcal{V}_0} \left\{ \frac{\partial W}{\partial \mathbf{F}} : \delta\mathbf{F} + \frac{\partial W}{\partial \mathbf{B}} \cdot \delta\mathbf{B} \right\} \mathrm{d}\mathcal{V}_0 - \int_{\partial\mathcal{V}_0} \mathbf{T} \cdot \delta\mathbf{u}\, \mathrm{d}A. \tag{3.26}$$

Consequently, using Eq. (3.23) and Eq. (3.26), we get:

$$\delta\mathcal{P} = \frac{\partial \mathcal{P}}{\partial \mathbf{F}} : \delta\mathbf{F} + \frac{\partial \mathcal{P}}{\partial \mathbf{B}} \cdot \delta\mathbf{B}, \tag{3.27}$$

where using standard indicial notation in Cartesian coordinates, we obtain:

$$\frac{\partial \mathcal{P}}{\partial F_{ij}} = \frac{\partial W}{\partial F_{ij}}, \qquad \frac{\partial \mathcal{P}}{\partial B_i} = \frac{\partial W}{\partial B_i}. \tag{3.28}$$

From this expression, the first Piola-Kirchhoff stress and Lagrangian $H$-field are readily identified as follows:

$$S_{ij} = \frac{\partial W}{\partial F_{ij}}, \qquad H_i = \frac{\partial W}{\partial B_i}. \tag{3.29}$$

The Eulerian counterparts of these fields are obtained through the standard push-forward operations (Kankanala 2004; Dorfmann and Ogden 2005):

$$\sigma_{ij} = J^{-1} S_{ik} F_{jk}, \tag{3.30}$$

$$h_i = H_j F^{-1}_{ij}. \tag{3.31}$$

The above equations requires the evaluation of:

$$\frac{\partial W}{\partial F_{ij}} = \sum_{P=1}^{n_{inv}} \frac{\partial W}{\partial I_P} \frac{\partial I_P}{\partial F_{ij}}, \tag{3.32}$$

$$\frac{\partial W}{\partial B_i} = \sum_{P=1}^{n_{inv}} \frac{\partial W}{\partial I_P} \frac{\partial I_P}{\partial B_i}, \tag{3.33}$$

where $I_P$ are the magneto-mechanical invariants that will be discussed in the next section.

Similarly, the second variation of the potential energy, which will be needed later in the numerical solver, is given by:

$$\Delta\delta\mathcal{P} = \{\Delta\mathbf{F}, \Delta\mathbf{B}\} \begin{bmatrix} \dfrac{\partial^2\mathcal{P}}{\partial\mathbf{F}\partial\mathbf{F}} & \dfrac{\partial^2\mathcal{P}}{\partial\mathbf{F}\partial\mathbf{B}} \\ \dfrac{\partial^2\mathcal{P}}{\partial\mathbf{B}\partial\mathbf{F}} & \dfrac{\partial^2\mathcal{P}}{\partial\mathbf{B}\partial\mathbf{B}} \end{bmatrix} \begin{Bmatrix} \delta\mathbf{F} \\ \delta\mathbf{B} \end{Bmatrix}, \tag{3.34}$$

where the second-order derivatives are evaluated by direct derivation of the relations in Eq. (3.28), such that:

$$\frac{\partial^2\mathcal{P}}{\partial F_{ij}\partial F_{kl}} = \frac{\partial^2 W}{\partial F_{ij}\partial F_{kl}}, \tag{3.35}$$

$$\frac{\partial^2\mathcal{P}}{\partial F_{ij}\partial B_{k}} = \frac{\partial^2 W}{\partial F_{ij}\partial B_{k}}, \tag{3.36}$$

$$\frac{\partial^2\mathcal{P}}{\partial B_{i}\partial B_{j}} = \frac{\partial^2 W}{\partial B_{i}\partial B_{j}}. \tag{3.37}$$

The above equations will also need the evaluation of the following quantities:

$$\frac{\partial^2 W}{\partial F_{ij}\partial F_{kl}} = \sum_{P=1}^{n_{inv}}\sum_{Q=1}^{n_{inv}} \frac{\partial^2 W}{\partial I_P\,\partial I_Q} \frac{\partial I_P}{\partial F_{ij}} \frac{\partial I_Q}{\partial F_{kl}} + \sum_{P=1}^{n_{inv}} \frac{\partial W}{\partial I_P} \frac{\partial^2 I_P}{\partial F_{ij}\,\partial F_{kl}}, \tag{3.38}$$

$$\frac{\partial^2 W}{\partial F_{ij}\partial B_{k}} = \sum_{P=1}^{n_{inv}}\sum_{Q=1}^{n_{inv}} \frac{\partial^2 W}{\partial I_P\,\partial I_Q} \frac{\partial I_P}{\partial F_{ij}} \frac{\partial I_Q}{\partial B_{k}} + \sum_{P=1}^{n_{inv}} \frac{\partial W}{\partial I_P} \frac{\partial^2 I_P}{\partial F_{ij}\,\partial B_{k}}, \tag{3.39}$$

$$\frac{\partial^2 W}{\partial B_{i}\partial B_{j}} = \sum_{P=1}^{n_{inv}}\sum_{Q=1}^{n_{inv}} \frac{\partial^2 W}{\partial I_P\,\partial I_Q} \frac{\partial I_P}{\partial B_{i}} \frac{\partial I_Q}{\partial B_{j}} + \sum_{P=1}^{n_{inv}} \frac{\partial W}{\partial I_P} \frac{\partial^2 I_P}{\partial B_{i}\,\partial B_{j}}. \tag{3.40}$$

### 3.2.3 Constitutive model for isotropic soft MREs

Following the theoretical background of Dorfmann and Ogden (2003), Danas (2017), and Mukherjee (2020), the free energy density per unit volume of the whole boundary value problem can be decomposed as:

$$W(\mathbf{F},\mathbf{B}) = \rho_0^i\,\boldsymbol{\Phi}^{\text{mech}}(J,\bar{I}_1) + \rho_0^i\,\boldsymbol{\Phi}^{\text{mag}}(J,I_5) + \rho_0^i\,\boldsymbol{\Phi}^{\text{couple}}(J,I_5,I_6) + \boldsymbol{\Phi}^{\text{freespace}}(J,I_5) + \frac{1}{2\mu_0\,\xi}|\mathbf{A}|^2, \tag{3.41}$$

where the corresponding magneto-mechanical invariants are defined as follows:

$$I_1 = \mathbf{F}:\mathbf{F}\,, \quad J = \det\mathbf{F}\,, \quad I_5 = \mathbf{FB}\cdot\mathbf{FB}\,, \quad I_6 = \mathbf{F}^T\mathbf{FB}\cdot\mathbf{F}^T\mathbf{FB}. \tag{3.42}$$

In Eq. (3.41), for the purely mechanical contribution $\boldsymbol{\Phi}^{\text{mech}}$, we use a hyper-elastic model variant proposed by Lopez-Pamies (2010), which is valid and explicit for any incompressible matrix phase that can be described by an energy density depending on $I_1$ (and $J$ in the quasi-incompressible approximation). In the present study, the iron particles are assumed to be mechanically rigid, so the mechanical energy density of the polymer matrix can be written as:

$$\rho_0^i \, \boldsymbol{\Phi}^{\text{mech}}(\bar{I}_1, J) = \rho_0^i \, \Psi_{\text{mech}}(\bar{I}_1) + \frac{G'_m}{2\,s^2}\left(J^2 - 1\right)^2, \tag{3.43}$$

with:

$$\Psi_{\text{mech}}(\bar{I}_1) = \sum_{i=1}^{2}\left(\frac{3^{1-a_i}}{2a_i}\,G_m^i\left(\bar{I}_1^{a_i} - 3^{a_i}\right) - \frac{G_m^i}{s}\,\ln J\right), \qquad a_i \in \mathbb{R}\ (i = 1, 2), \tag{3.44}$$

where $\bar{I}_1$ denotes a strain-amplified invariant incorporating the effect of rigid particle inclusions through the factor $s$ to incorporate the explicit homogenization model by Lefèvre and Lopez-Pamies (2022) used for the material study in subsubsection 3.1.3.2

$$\bar{I}_1 = 3 + \frac{I_1 - 3}{s}, \tag{3.45}$$

$$s(c, \alpha, \beta, p_n) = \Big((1 + \alpha(\beta + (c/p_n)^2)(c/p_n)^2)(1 - c/p_n)\Big)^{\frac{5p_n}{2}}. \tag{3.46}$$

The function $s(c, \alpha, \beta, p_n)$ controls the degree of strain amplification induced by the rigid particle network, accounting for both the particle volume fraction $c$ and the underlying particle distribution, with $p_n$ representing the percolation threshold. The parameters $(\alpha, \beta)$ are calibrated from incompressible experiments. $G_m$ is the shear modulus, and $G'_m$ is the bulk modulus ensuring quasi-incompressibility of the underlying matrix phase of the MRE and the substrate. It is noted that the proposed compressible part of the model is sufficiently robust for the quasi-incompressible responses across a wide range of volume fractions $c$, and a nearly incompressible response is obtained for values $G'_m \geq 100 G_m$ (Mukherjee 2020). Specifically, we will set $G'_m = 500\ G_m$ for all materials considered in the present study.

It is important to clarify here that in the above material model, the underlying shear modulus $G_m$ is that of the polymeric matrix phase of the MRE. So, it is necessary to use an effective shear modulus $G$ (Eq. (3.4)) to capture the effective response of the Neo-Hookean matrix comprising large volume fractions of rigid particles as discussed in subsubsection 3.1.3.2.

The magnetic contribution $\rho_0^i \boldsymbol{\Phi}^{\text{mag}}$ in Eq. (3.41) is formulated following Mukherjee (2020) and is constructed such that the resulting magnetization response $\mathbf{m}(b)$ follows a hypergeometric saturation behavior. The magnetic contribution to energy density is written as:

$$\rho_0^i \, \boldsymbol{\Phi}^{\text{mag}}(J, I_5) = -\frac{\chi}{2\mu_0(1+\chi)}\,\frac{I_5}{J^2}\,{}_2\mathcal{F}_1\left[\frac{1}{k}, \frac{2}{k}, 1 + \frac{2}{k}; -\left(\frac{\chi}{\mu_0(1+\chi)m^s}\,\frac{\sqrt{I_5}}{J}\right)^k\right]. \tag{3.47}$$

The effective magnetic saturation $m^s$ and the effective magnetic susceptibility $\chi$ of the MRE are

expressed in terms of the magnetic properties of the constituent particles, namely the particle saturation magnetization $m_p^s$ and particle magnetic susceptibility $\chi_p$, as well as their volume fraction $c$. In particular, the effective saturation magnetization is given by:

$$m^s = c\, m_p^s, \tag{3.48}$$

while the effective magnetic susceptibility reads (Mukherjee 2020):

$$\chi = \frac{3c(\mu_p - \mu_0)}{(2+c)\mu_0 + (1-c)\mu_p}. \tag{3.49}$$

Here, $\mu_p$ represents the magnetic permeability of the particle phase, which is related to particle susceptibility $\chi_p$ through:

$$\mu_p = (1+\chi_p)\mu_0. \tag{3.50}$$

The Gaussian hypergeometric function in Eq. (3.47) is given by:

$${}_2\mathcal{F}_1(a,b,c;z) = \sum_{n=0}^{\infty} \frac{(a)_n\,(b)_n}{(c)_n} \frac{z^n}{n!}, \tag{3.51}$$

where $a$, $b$, and $c$ are constant parameters characterizing the function and $z$ denotes its argument. The symbols $(x)_n$ denote the Pochhammer symbol (rising factorial), defined for a generic scalar $x$ as:

$$(x)_0 = 1; \qquad (x)_n = x(x+1)\cdots(x+n-1), \quad (n \geq 1). \tag{3.52}$$

In the present formulation, the Pochhammer symbol appears naturally in the series representation of the hypergeometric function and does not introduce any additional independent variables. Further details regarding the derivation of the magnetic energy density using the hypergeometric function can be found in Mukherjee (2020). In general, there is no closed-form expression for the hypergeometric term. However, in the present context, we only require its first derivative with respect to $\mathbf{B}$, which leads directly to the explicit form of the magnetization. Using the below work-conjugate relation:

$$\mathbf{m} = -\rho_0 \mathbf{F}^{-\mathrm{T}} \frac{\partial(\boldsymbol{\Phi}^{\mathrm{mag}})}{\partial \mathbf{B}} = -\frac{\rho_0}{J} \frac{\partial(\boldsymbol{\Phi}^{\mathrm{mag}})}{\partial \mathbf{b}}, \tag{3.53}$$

the magnetization vector is obtained in closed form as:

$$\mathbf{m} = \frac{\chi\, \mathbf{b}}{\mu_0(1+\chi)\left[1 + \left(\frac{\chi|\mathbf{b}|}{m^s \mu_0 (1+\chi)}\right)^k\right]^{1/k}}. \tag{3.54}$$

In general, magnetization saturation behavior can be modeled in several ways. There are different choices for magnetic energy densities besides the one used in Eq. (3.54). Other approaches include Langevin-type saturation energies, polynomial saturation potentials, or saturation functions that use hyperbolic tangent laws. All of these give closed-form expressions for $\mathbf{m}$, which can be adjusted to fit experimental data (see for example Danas (2017)). For comparison, the Langevin-type (Eq. (3.55)) and hyperbolic tangent law saturation function (Eq. (3.56)) are

presented below:

$$\mathbf{m} = \left( \frac{m^s}{|\mathbf{b}|} \coth \left[ \frac{3\chi|\mathbf{b}|}{\mu_0 m^s} \right] \frac{\mu_0 (m^s)^2}{3\chi|\mathbf{b}|^2} \right) \mathbf{b}, \tag{3.55}$$

$$\mathbf{m} = \frac{m^s}{|\mathbf{b}|} \tanh \left[ \frac{\chi|\mathbf{b}|}{\mu_0 m^s} \right] \mathbf{b}. \tag{3.56}$$

Figure 3.9 shows the $\mathbf{m}$–$\mathbf{b}$ response obtained from the Langevin function, the hyperbolic tangent function, and the hypergeometric function evaluated at different values of the exponent $k$. These curves illustrate how each model captures magnetic saturation through different functional forms. Comparison reveals that the hypergeometric-based saturation law provides a smooth interpolation between the Langevin and tanh functions. Specifically, choosing $k \approx 1.7$ produces a response nearly indistinguishable from the Langevin curve, whereas $k \approx 2.8$ closely reproduces the hyperbolic tangent law. Therefore, the exponent $k$ acts as a flexible calibration parameter governing the sharpness of the transition toward magnetic saturation. Following Mukherjee (2020), a value of $k = 6$ delivers an excellent fit across a broad range of particle volume fractions $c \in [0, 0.3]$ and matrix shear moduli, and is thus adopted in the current study.

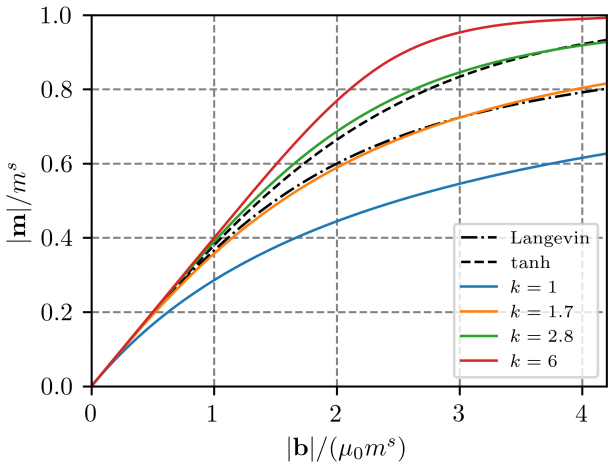


Figure 3.9: Magnetization saturation laws obtained from the hypergeometric magnetic energy function (evaluated for several values of the exponent $k$), together with the classical Langevin and hyperbolic tangent laws (see Danas (2017)).

The magneto-mechanical coupling contribution $\rho_0^i \boldsymbol{\Phi}^{\text{couple}}$ in Eq. (3.41) is introduced following the homogenized implicit formulation proposed by Mukherjee (2020). Within this framework, the coupling energy density consists of two competing contributions associated with the invariants $I_5$ and $I_6$, and is written as:

$$\rho_0^i \boldsymbol{\Phi}^{\text{couple}}(J, I_5, I_6) = \Psi_6(J, I_6) - \Psi_5(J, I_5). \tag{3.57}$$

Each contribution $\Psi_i$ $(i = 5, 6)$ is defined through a nonlinear saturation-type potential of the

form:

$$\Psi_i(J, I_i) = \beta_1 \frac{(1+\chi)(\mu_0 m^s)^2}{2\mu_0 \chi} \ln\left[1 + \sum_{q=1}^{4} \frac{1}{c}\left(\frac{5}{4}\frac{\chi}{1+\chi}\right)^{q+1}\left(\frac{c}{\beta_2(\mu_0 m^s)^2}\frac{I_i}{J^2}\right)^q\right], \qquad i = 5, 6. \tag{3.58}$$

The material parameters $\beta_1$ and $\beta_2$ control the strength of the magneto-mechanical coupling. The parameter $\beta_1$ is defined as:

$$\beta_1 = \frac{16}{25}\frac{\mu_0^2(1+\chi)\big(\nu - (1+\chi)\mu_0\big)}{\nu\,\mu_0\,\chi\big(3(1+\chi)\mu_0 - 2\nu\big)}\,\beta_2, \tag{3.59}$$

where the auxiliary magnetic parameter $\nu$ is given by:

$$\nu = \mu_0 + \frac{3c(10 + 2c + 3c^2)(\mu_p - \mu_0)\mu_0^2}{5\big[(2+c)\mu_0 + (1-c)\mu_p\big]^2} + \frac{3c(1-c)(5+3c)(\mu_p - \mu_0)\mu_0\mu_p}{5\big[(2+c)\mu_0 + (1-c)\mu_p\big]^2}. \tag{3.60}$$

The parameter $\beta_2$ is calibrated from numerical three-dimensional RVE simulations subjected to uniaxial magnetic loading and zero mechanical traction (see Mukherjee (2020) for more details), and is defined as:

$$\beta_2(G_m^*, c) = \begin{cases} \alpha_1(G_m^*) - \alpha_2(G_m^*)\,\mathcal{L}[c\,\alpha_3(G_m^*)]\,, & \text{if } G_m^* \le 0.1, \\ 0.4055 - 0.5\,c\,[1 - 0.67\,\mathcal{L}(15 G_m^*)]\,, & \text{otherwise,} \end{cases} \tag{3.61}$$

where $\mathcal{L}(\cdot)$ denotes the Langevin function:

$$\mathcal{L}(x) = \frac{1}{\tanh(x)} - \frac{1}{x}. \tag{3.62}$$

The functions $\alpha_i(G_m^*)$ are defined as:

$$\alpha_1(G_m^*) = \exp[-0.029\ln(G_m^*) - 0.982]\,, \tag{3.63}$$

$$\alpha_2(G_m^*) = \exp\big[1.78\mathcal{L}\big(-0.32\ln(G_m^*)\big) - 1.78\big]\,, \tag{3.64}$$

$$\alpha_3(G_m^*) = \exp[0.14 - 0.54\ln(G_m^*)]\,, \tag{3.65}$$

and the dimensionless shear modulus $G_m^*$ is defined as:

$$G_m^* = \frac{G_m}{G_m^{\text{ref}}}, \qquad G_m^{\text{ref}} = 1 \text{ MPa}. \tag{3.66}$$

In addition to the material-dependent magnetic contributions, the total potential energy defined in Eq. (3.41) also includes the free-space (vacuum) magnetic energy, which accounts for the energy stored in the magnetic field independently of the presence of magnetizable matter. This contribution is written as:

$$\boldsymbol{\Phi}^{\text{freespace}}(J, I_5) = \frac{I_5}{2\mu_0, J}. \tag{3.67}$$

This term represents the classical magnetic energy density of the field in vacuum and is there-

fore present in all domains, including non-magnetic materials and the surrounding air region. Physically, it describes the energy required to sustain the background magnetic field, irrespective of material magnetization. Its inclusion ensures that the magnetic field is properly defined throughout the entire computational domain and that Maxwell's equations are recovered in regions devoid of magnetic material (Dorfmann and Ogden 2003).

Finally, the last term in Eq. (3.41), that is scaled by the parameter $\xi$, adds a gauge constraint to make sure the magnetic vector potential $\mathbf{A}$ is unique, which is given as:

$$\frac{1}{2\mu_0\,\xi}\int_{\mathcal{V}_0}|\mathbf{A}|^2\,\mathrm{d}\mathcal{V}_0. \tag{3.68}$$

This step is important because only the curl of $\mathbf{A}$ is used to define the magnetic induction $\mathbf{B} = \nabla \times \mathbf{A}$. As a result, the divergence of $\mathbf{A}$ is not set unless we add another condition. In the past, this issue was addressed by applying the Coulomb gauge condition $\nabla \cdot \mathbf{A} = 0$. This condition is enforced with the following penalty functional, as used in classical electromagnetic finite element methods (Coulomb 1981):

$$\int_{\mathcal{V}_0}(\nabla \cdot \mathbf{A})^2\mathrm{d}\mathcal{V}_0. \tag{3.69}$$

Such a constraint guarantees the uniqueness of $\mathbf{A}$ and enforces continuity across material interfaces (e.g., MRE, substrate and air). However, recent studies by Gebhart and Wallmersperger (2024) have shown that an alternative based on the $L^2$–norm of the vector potential:

$$\int_{\mathcal{V}_0}|\mathbf{A}|^2\mathrm{d}\mathcal{V}_0, \tag{3.70}$$

provides improved numerical convergence while preserving the same physical magnetic field as the Coulomb gauge formulation. The $L^2$ approach is also easier to use with standard nodal-based finite element methods. It avoids the problems that come with edge-element formulations that do not work well with displacement continuity in finite-strain mechanics. Dorn et al. (2021) previously used a Coulomb-gauge penalty in a similar magneto-mechanical setting, and in direct comparison both approaches yield indistinguishable solutions for the problems considered here. For these reasons, this work uses the $L^2$ formulation because it is robust and easy to implement. The penalty parameter is selected as:

$$\xi = 10^{-6}. \tag{3.71}$$

This value is small enough to make the vector potential unique, but it does not affect the calculated magnetic fields or cause numerical problems.

The regularization term (Eq. (3.68)) is included in the finite element equations by discretizing the following integral: $\int_{\mathcal{V}_0}|\mathbf{A}|^2\mathrm{d}\mathcal{V}_0$. Only the degrees of freedom for the magnetic vector potential (dofs 4–6 per node) are involved in this term. Since this constraint is a strong penalty, the element matrices are calculated using just one Gauss point (reduced integration). This approach prevents artificial stiffening and keeps the gauge condition effective, while also maintaining good

convergence for the Newton solver.

For the non-magnetic elastic materials, namely the elastomeric substrate, we employ the same constitutive framework as for the magneto-elastic MRE, but with the particle volume fraction set to $c = 0$. This choice immediately leads to $\boldsymbol{\Phi}^{\text{mag}} = \boldsymbol{\Phi}^{\text{couple}} = 0$, such that the response is the same as a purely mechanical Neo-Hookean solid, while the magnetic free space contribution $\boldsymbol{\Phi}^{\text{freespace}}$ remains unchanged. More generally, by choosing suitable values for the reference density $\rho_0^i$ (where $i = \text{f}$ for the MRE film, $i = \text{s}$ for the substrate, and $i = \text{a}$ for the surrounding air), the same total energy functional can be used consistently for all parts of the system. In particular, for the surrounding air, the reference density is chosen such that the mechanical and magneto-mechanical contributions are zero, that is:

$$\rho_0^{\text{a}}\, \boldsymbol{\Phi}^{\text{mech}} = \rho_0^{\text{a}}\, \boldsymbol{\Phi}^{\text{mag}} = \rho_0^{\text{a}}\, \boldsymbol{\Phi}^{\text{couple}} = 0. \tag{3.72}$$

This reflects the lack of mechanical stiffness in free space. As a result, only the vacuum magnetic energy $\boldsymbol{\Phi}^{\text{freespace}}$ contributes in the air domain. This unified approach lets us model the MRE film, the compliant substrate and the surrounding air within a single variational framework, while preserving the correct physical behavior of each part by choosing suitable values for $\rho_0^i$ and the related material parameters.

### 3.2.4 3D boundary value problem (BVP)

#### 3.2.4.1 Numerical implementation, mesh and boundary conditions

All numerical simulations are carried out using Abaqus®. A user-defined element (UEL) is used to implement the magneto-mechanical coupling model described in subsection 3.2.3. The formulation is based on the variational principle introduced in subsection 3.2.2, and the resulting nonlinear system of equations is solved incrementally using a Newton–Raphson scheme.

The 3D BVP consists of a magnetoelastic MRE film perfectly bonded to a compliant elastomeric substrate, both embedded in a surrounding air domain in order to capture the distribution of the magnetic field both inside and outside the solid. Two different air-domain geometries are considered depending on the specimen for convenience in meshing: a cylindrical air domain is employed for cylindrical specimens, whereas a cubic air domain is adopted for cubic specimens (see Figure 3.10a-b). In both cases, the air-domain dimensions are chosen sufficiently large (twice the size of the specimen), in that further enlargement does not affect either the mechanical or magnetic response of the MRE. This ensures independence of the solution with respect to far-field boundary conditions and faithfully represents the experimental magneto-mechanical test setup. The system is not subjected to any mechanical pre-strain.

The entire computational domain, comprising the MRE film, the substrate and the surrounding air, is discretized using a single user-defined finite element. The element is implemented as an eight-node linear hexahedral (brick) element of C3D8 type, with six degrees of freedom per node: three mechanical displacement components $\mathbf{u} = \text{u}_1, \text{u}_2, \text{u}_3$ and three magnetic vector potential

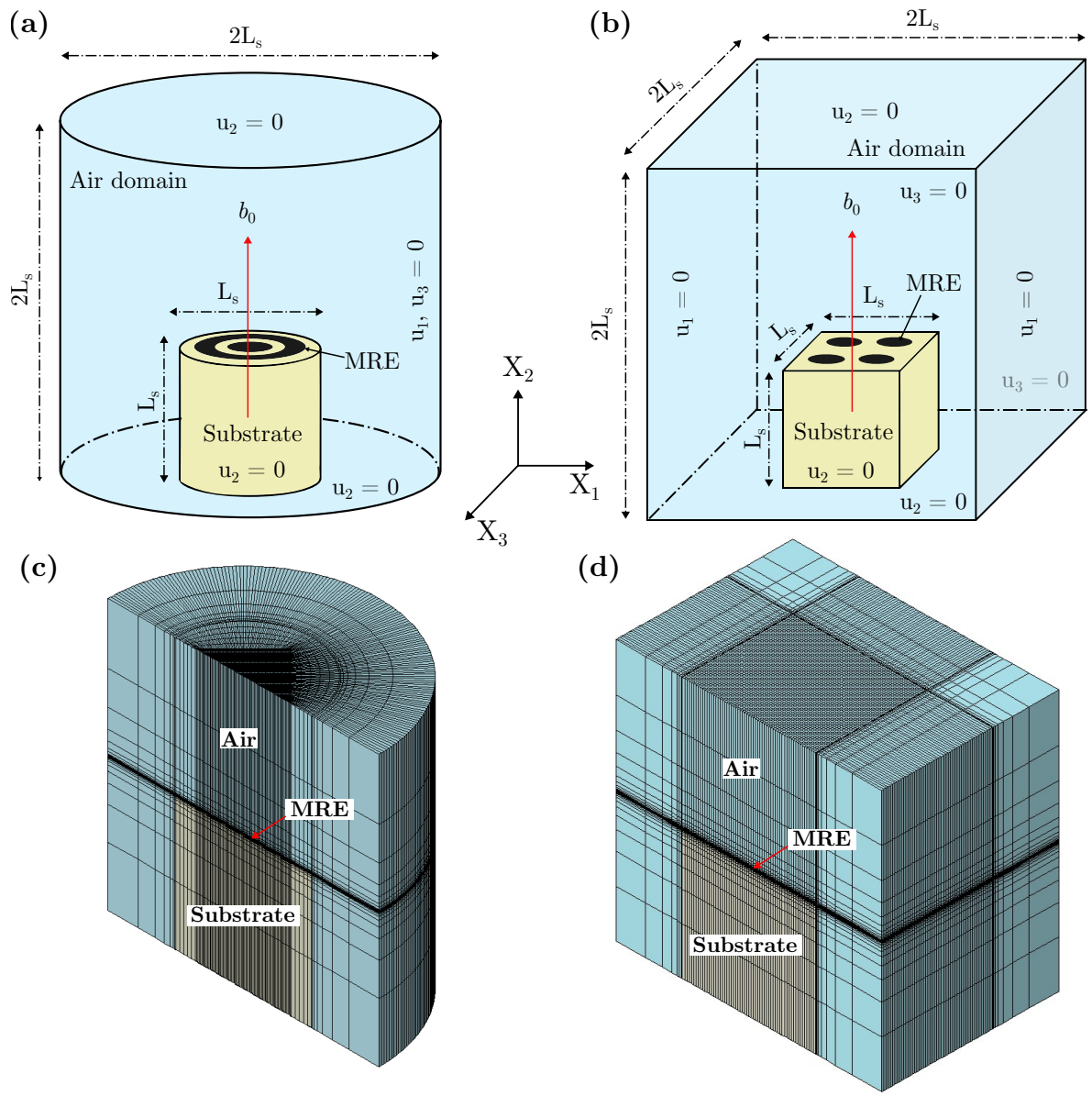


Figure 3.10: (a) Cylindrical specimen embedded in a cylindrical air domain and subjected to a uniform vertical magnetic induction field. (b) Cubic specimen embedded in a cubic air domain with identical magnetic loading. (c) Representative finite element mesh of the cylindrical air-MRE-substrate configuration. (d) Representative finite element mesh of the cubic air-MRE-substrate configuration. In (c) and (d), only half of the mesh is visualized for clarity, while all simulations are performed on the full three-dimensional domain.

components $\mathbf{A} = \mathrm{A}_1, \mathrm{A}_2, \mathrm{A}_3$. For a homogeneous MRE film, a structured mesh consisting of $80 \times 80 \times 10$ linear brick elements is used, which provides enough resolution through the thickness while maintaining computational efficiency. Although the film mesh is kept constant for homogeneous cases, different meshes are used for the heterogeneous films investigated in this study in order to accurately resolve spatial material variations. Consequently, the total number of elements varies depending on the specific heterogeneous configuration considered. The surrounding air domain and the compliant substrate are discretized consistently with the specimen geometry, using cubic structured meshes for both the cylindrical and cubic configurations, with a graded mesh bias that increases element density in the vicinity of the MRE film, as shown in

Figure 3.10c-d, in order to accurately capture the formed instabilities.

Depending on the specimen geometry and air-domain discretization, the resulting finite element model typically has about $10^6$ nodes, corresponding to several million degrees of freedom. In the case of a homogeneous MRE film/substrate system, the whole boundary domain consists of 385,875 elements, corresponding to 2,315,250 DOFs. A standard $2 \times 2 \times 2$ Gauss integration scheme is employed for all mechanical and magneto-mechanical contributions. For the quasi-incompressible MRE and substrate phases, reduced integration is applied for the volumetric penalty term $(J-1)^2$ in Eq. (3.43).

All external surfaces of the solid parts (film and substrate) are traction free. Displacement continuity across the film-substrate interface is automatically satisfied through shared nodal connectivity. Across the solid-air interfaces, the tangential component of the magnetic induction $\mathbf{B}$ is allowed to be discontinuous, while the magnetic vector potential remains continuous. The mechanical and magnetic boundary and interface conditions stated above follow directly from the balance laws and Maxwell equations given in Eq. (3.18)-Eq. (3.20). In particular, traction-free external surfaces of the solid phases are described by the boundary condition $\mathbf{T} = \mathbf{0}$ in the mechanical jump condition $\mathbf{N} \cdot [\![\mathbf{S}]\!] = \mathbf{T}$. Displacement continuity across the film–substrate interface corresponds to the kinematic constraint $[\![\mathbf{u}]\!] = \mathbf{0}$ and is strictly enforced through shared nodal connectivity. The film and substrate are otherwise fully unconstrained mechanically, except for their mutual bonding at the interface.

The loading is purely magnetic and consists of a uniform transverse magnetic induction field prescribed in the reference configuration[1] as:

$$\mathbf{b}_0 = \mathrm{B}_0\, \mathbf{e}_2. \tag{3.73}$$

This magnetic field is generated by prescribing the magnetic vector potential on the outer boundaries of the air domain in the form:

$$\mathbf{A} = \frac{1}{2}\mathrm{B}_0\mathrm{X}_3\, \mathbf{e}_1 - \frac{1}{2}\mathrm{B}_0\mathrm{X}_1\, \mathbf{e}_3, \tag{3.74}$$

where $(\mathrm{X}_1, \mathrm{X}_2, \mathrm{X}_3)$ denote the Cartesian material coordinates. Since the outer air domain is stationary, the Lagrangian and Eulerian magnetic inductions coincide (i.e., $\mathbf{B}_0 = \mathbf{b}_0$ by definition). Taking the curl of Eq. (3.74) yields a uniform magnetic induction field aligned with $\mathbf{e}_2$, consistent with the idealized loading shown in Figure 3.10. On the outer boundaries of the air domain, the magnetic vector potential is prescribed according to Eq. (3.74).

The resulting nonlinear system of equations is solved step by step using a Newton-Raphson scheme. A full simulation, including magnetic loading and the ensuing magneto mechanical response, takes about 25 to 30 hours of wall-clock time on a high performance computing cluster

[1] Although the magnetic loading is prescribed in the reference configuration, the magnetic induction entering the constitutive relations is evaluated in the current configuration through the standard pull-back and push-forward operations associated with the deformation gradient (see Eq. (3.17)).

using 40 CPU cores, with the exact runtime depending on the applied boundary conditions and mesh resolution.

#### 3.2.4.2 Modeling of the surrounding air

The air surrounding the MRE has almost zero mechanical stiffness, while the magnetic fields within it remain finite. In particular, the magnetic induction and magnetic field in air are related by:

$$\mathbf{b} = \mu_0 \mathbf{h}. \tag{3.75}$$

Within the present fully-implicit Lagrangian framework, directly modeling air as a material with vanishing mechanical stiffness leads to severe mesh distortions near the corners of the MRE, which ultimately prevents numerical convergence.

Several strategies have been proposed to address this issue. A common approach is to model air as a very soft hyperelastic solid with a small but finite shear modulus (Rambausek and Keip 2018; Dorn et al. 2021). However, such a treatment may artificially stiffen the system and underestimate the mechanical deformations of MREs, especially under large deflections. An alternative and more accurate strategy is to explicitly constrain the motion of air nodes around the MRE, while keeping zero mechanical stiffness in the air (Psarra et al. 2019; Mukherjee and Danas 2022). This approach is adopted in the present study. To regularize the deformation of the air mesh, each node $j$ belonging to the air domain $\mathcal{V}_0^{\text{Air}}$ is coupled to its nearest node on the MRE–air interface $\partial\mathcal{V}_0^{\text{MRE-Air}}$. The displacement constraint is imposed pointwise as:

$$\mathcal{C}_i^{(j)} \equiv \begin{cases} \mathrm{u}_i^{(j)}\big|_{\mathcal{V}_0^{\text{Air}}} - d_i^{(j)}\, \mathrm{u}_i^{(j^\star)}\big|_{\partial\mathcal{V}_0^{\text{MRE Air}}} = 0, & \text{if } 0 < d_i^{(j)} \leq 1, \\ \mathrm{u}_i^{(j)}\big|_{\mathcal{V}_0^{\text{Air}}} = 0, & \text{otherwise,} \end{cases} \qquad i = 1,2,3. \tag{3.76}$$

where $j^\star$ denotes the nearest node on the MRE–air interface $\partial\mathcal{V}_0^{\text{MRE-Air}}$ to the air node $j$.

The weight function $d_i^{(j)}$, controlling the thickness of the deformable air layer, is defined as:

$$d_i^{(j)} = 1 - \frac{\left|\mathrm{X}_i^{(j)}\big|_{\mathcal{V}_0^{\text{Air}}} - \mathrm{X}_i^{(j^\star)}\big|_{\partial\mathcal{V}_0^{\text{MRE-Air}}}\right|}{R_i}, \qquad i = 1,2,3, \tag{3.77}$$

where $R_i$ denotes the characteristic half-thickness of the deformable air region in the $\mathrm{X}_i$ direction.

The kinematic constraints described above are linear with respect to the nodal displacements and are therefore applied directly using the `*EQUATION` command in Abaqus. This approach enforces the constraints exactly at the discrete level through linear multi-point constraint equations and does not introduce any artificial mechanical stiffness into the surrounding air domain. It has been shown to be equivalent to penalty-based approaches in both two- and three-dimensional settings (Mukherjee 2020). Air nodes located outside this region are treated as undeformable by prescribing zero displacements.

#### 3.2.4.3 Material-level imperfection via random volume fraction fluctuations

To make the numerical instability analysis more robust and to better represent the natural microstructural heterogeneity of MREs, this study adds small imperfections by introducing minor random fluctuations of the local particle volume fraction $c$. These imperfections help break the perfect symmetry found in homogeneous finite-element models and allow for a more realistic selection of instability modes, while also letting the simulations propagate into the post-bifurcation regime. This approach differs from the embedded or geometrical imperfection strategies commonly used in the literature, as discussed in subsection 1.4.2.

The numerical configuration employed to assess the effect of this imperfection is shown in Figure 3.11. As illustrated in Figure 3.11a, the model has a central disc and an annular MRE film (gray area) attached to a non-magnetic elastic substrate (beige area). This specific geometry is chosen because it promotes the development of circumferentially uniform, wave-like instability modes. The associated bifurcation leads to displacement oscillations in the outer annular region of the film, that become particularly evident in the post-bifurcation response through the formation of well-defined waves. Importantly, this configuration also exhibits a high degree of geometric symmetry in all in-plane directions. While such symmetry is advantageous for isolating and analyzing idealized instability patterns, it poses a significant numerical challenge, as the perfectly symmetric problem may struggle to select a unique bifurcation branch in the post-bifurcation regime. As a result, the introduction of controlled imperfections becomes essential to break the artificial symmetry of the numerical model and to enable a stable and physically meaningful continuation of the solution beyond the bifurcation point.

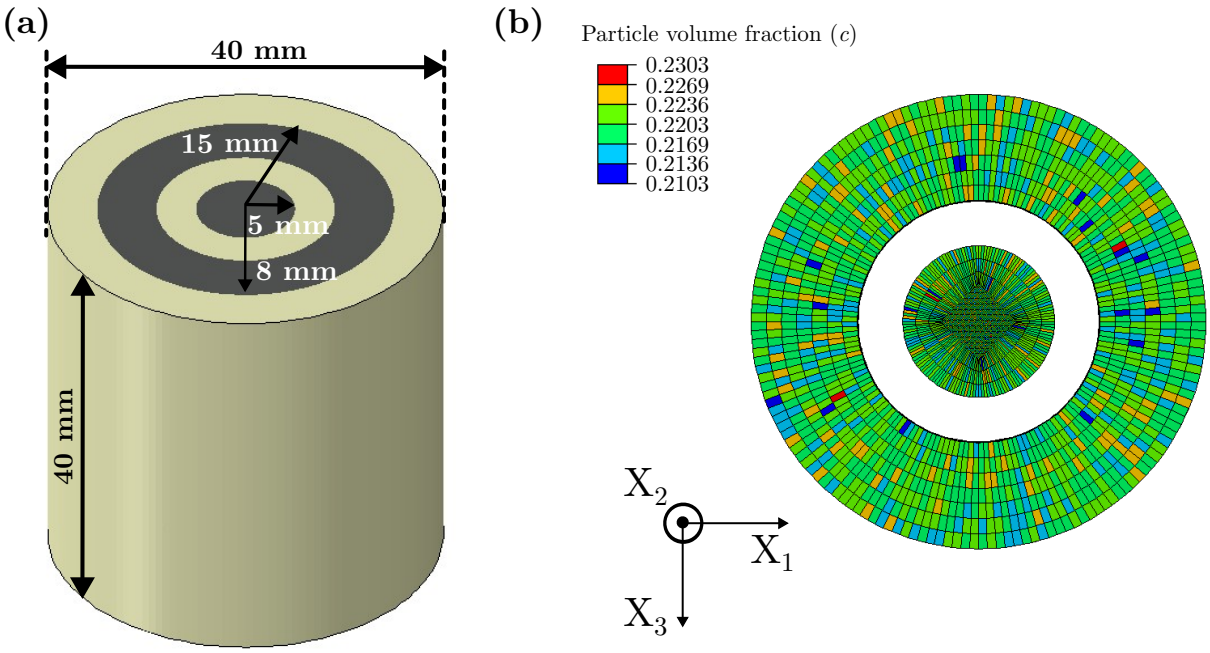


Figure 3.11: (a) Geometry of the numerical model used to investigate the effect of material-level imperfections. The gray region corresponds to the MRE film and the beige region to the non-magnetic substrate. (b) Element-wise spatial distribution of the effective particle volume fraction $c^e$ for an imperfection amplitude $c_{\text{imp}} = 6\%$.

Table 3.2 summarizes the material and geometrical parameters used in these simulations. The MRE film has a thickness $h_f = 0.6$ mm and a 210 *phr* CIP particle content, corresponding to a particle volume fraction of $c = 0.22$. The associated magnetic susceptibility $\chi_f$ and saturation magnetization $\mu_0 m_f^s$ are chosen consistently with experimentally-reported values for highly-filled MREs (Psarra et al. 2019). The substrate is significantly softer than the film, with a shear modulus ratio $G_s/G_f = 0.06$ that lies well below the critical stiffness ratio typically required to trigger wrinkling instabilities in film-substrate systems (Cai et al. 2011). This strong mechanical contrast ensures that the system is well within the instability-prone regime, making it particularly suitable for investigating bifurcation behavior and post-bifurcation responses. The geometry, magnetic loading and boundary conditions are the same as in subsection 3.2.4, so they are not repeated here. The magnetic loading is applied quasi-statically as a uniform magnetic induction field along $X_2$.

| $h_f$ (mm) | $c$ | $G_f$ (MPa) | $G_s$ (MPa) | $G_s/G_f$ | $\chi_P$ | $\mu_0 m_P^s$ (T) |
|---|---|---|---|---|---|---|
| 0.6 | 0.22 | 0.087 | 0.0058 | 0.06 | 30 | 2.5 |

Table 3.2: Geometrical, mechanical and magnetic parameters used in the current study.

In the finite-element model, the imperfection is added by multiplying the particle volume fraction by a scaling factor for each element. For each element $e$, the effective local volume fraction is defined as:

$$c^e = \gamma^e\, c, \qquad \gamma^e \in [\,1 - c_{\text{imp}},\ 1 + c_{\text{imp}}\,], \tag{3.78}$$

where $c_{\text{imp}}$ sets the size of the imperfection. The random factor $\gamma^e$ is chosen from a uniform distribution and given to each element separately. It is created once at the start of the analysis and then kept constant, so the imperfection shows a fixed spatial variation instead of changing with each step. An example of the resulting spatial distribution of the effective particle volume fraction $c^e$ for $c_{\text{imp}} = 6\%$ is shown in Figure 3.11b.

To measure how the imposed material heterogeneity affects the magneto-mechanical response, the vertical displacement component $u_2$ is tracked at five points (P1 to P5) within the MRE film, as shown in Figure 3.12a. The related displacement–magnetic field responses for three different imperfection amplitudes are presented in Figure 3.12b-d. In the absence of material heterogeneity ($c_{\text{imp}} = 0\%$), the solution remains perfectly symmetric and the simulation terminates prematurely at a critical magnetic induction of approximately $b_0 \simeq 0.64$ T, as shown in Figure 3.12b. This premature termination reflects the onset of a bifurcation that cannot be numerically selected in a fully-homogeneous setting. When a small imperfection amplitude of $c_{\text{imp}} = 1\%$ is introduced, the simulation progresses further into the post-critical regime, as shown in Figure 3.12c. However, pronounced oscillations appear in the displacement response as the magnetic field increases. Since the present problem is quasi-static, each value of the applied magnetic induction should correspond to a unique equilibrium configuration; the observed oscillations are therefore non-physical and indicate insufficient symmetry breaking. In contrast, with a larger imperfection amplitude of $c_{\text{imp}} = 6\%$, the oscillations disappear and the displacement–field curves become smooth and clearly separated, as shown in Figure 3.12d. Here, the

material heterogeneity is strong enough to reliably select a bifurcation branch, which leads to stable results over a wider range of magnetic loading. The imperfection is still weak enough that it does not change the overall deformation patterns, but it greatly improves numerical stability after the bifurcation.

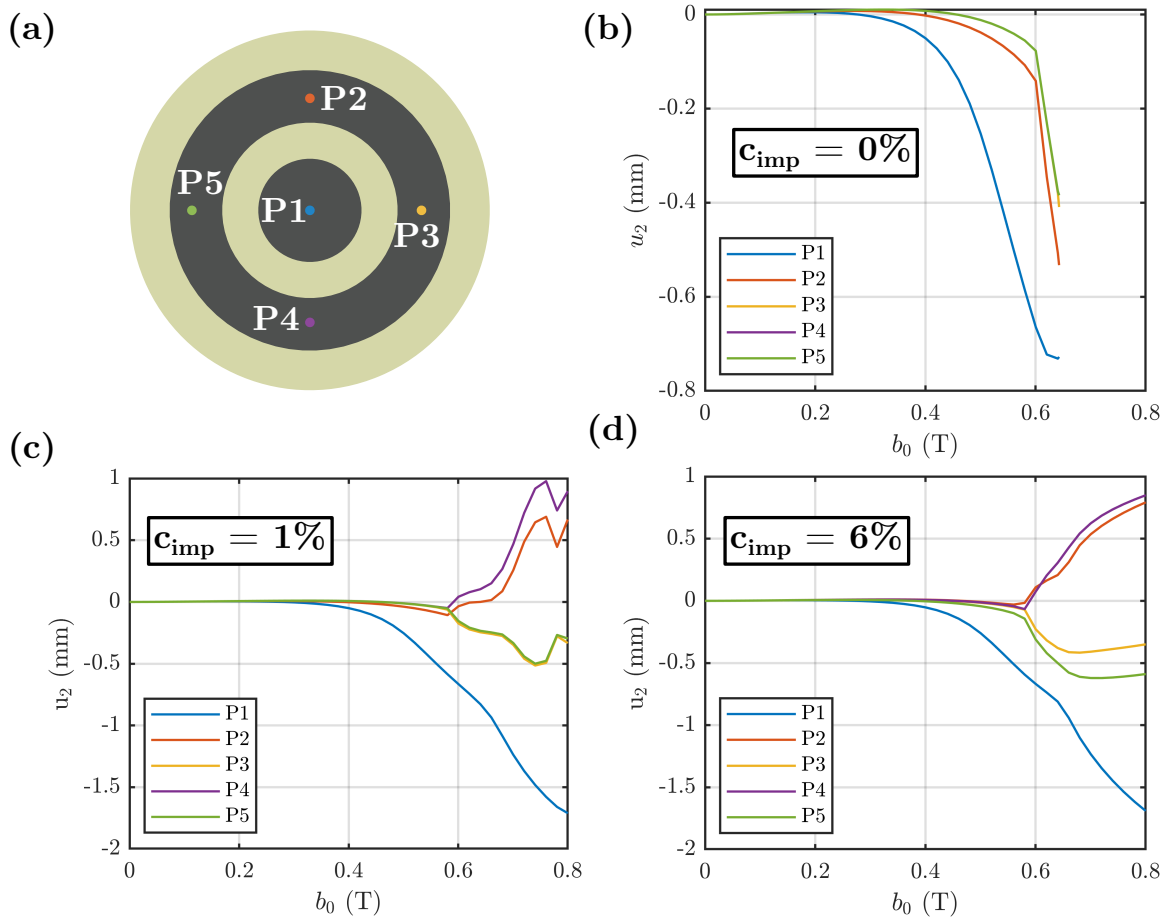


Figure 3.12: (a) Locations of the five monitoring points (P1-P5) within the MRE film. Vertical displacement $u_2$ as a function of the applied magnetic induction $b_0$ (b) for the homogeneous case $c_{\text{imp}} = 0\%$ showing premature termination of the simulation, (c) for an imperfection amplitude $c_{\text{imp}} = 1\%$ where oscillations appear in the displacement field, and (d) for $c_{\text{imp}} = 6\%$ leading to a smooth and stable post-bifurcation response.

Additional simulations performed with an intermediate imperfection amplitude of $c_{\text{imp}} = 2-5\%$ still exhibited noticeable oscillations in the displacement response, indicating that the symmetry breaking was not yet sufficient. Based on these observations, an imperfection amplitude of $c_{\text{imp}} = 6\%$ is adopted in all subsequent numerical simulations presented in this study.

## 3.3 Numerical validation against the 2D model

This section aims to validate the fully-coupled three-dimensional (3D) magneto-mechanical boundary-value problem (BVP) by comparing it to the reduced two-dimensional study by Psarra et al. (2017), which investigates a pre-compressed magneto-active elastomer specimen. The objective is to assess whether the proposed 3D formulation can reliably reproduce both the onset of instability and the post-bifurcation wrinkling behavior predicted by the 2D framework, while

additionally accounting for finite-width effects and out-of-plane kinematics that are inherently absent in 2D models.

The geometry and mechanical pre-loading employed in this validation study are illustrated in Figure 3.13. As shown in Figure 3.13a, the specimen consists of a uniform magneto-active elastic film perfectly bonded to a compliant, non-magnetic substrate. The film thickness is set to $h_f = 0.8$ mm, while the substrate thickness satisfies $h_s/h_f = 49$. The in-plane specimen width is 40 mm, allowing finite-width effects to be captured in the 3D simulations. An initial equi-biaxial pre-compression is imposed by prescribing equal displacements on two opposite lateral faces in both in-plane directions, leading to a nominal stretch $\lambda_0 = 0.85$. The applied displacement corresponds to $u_1 = 3$ mm on each side, while rigid-body motions are eliminated through appropriate symmetry and anchoring constraints. In both the 2D and 3D simulations, the specimen is first subjected to the prescribed pre-compression, after which the magnetic field is applied quasi-statically.

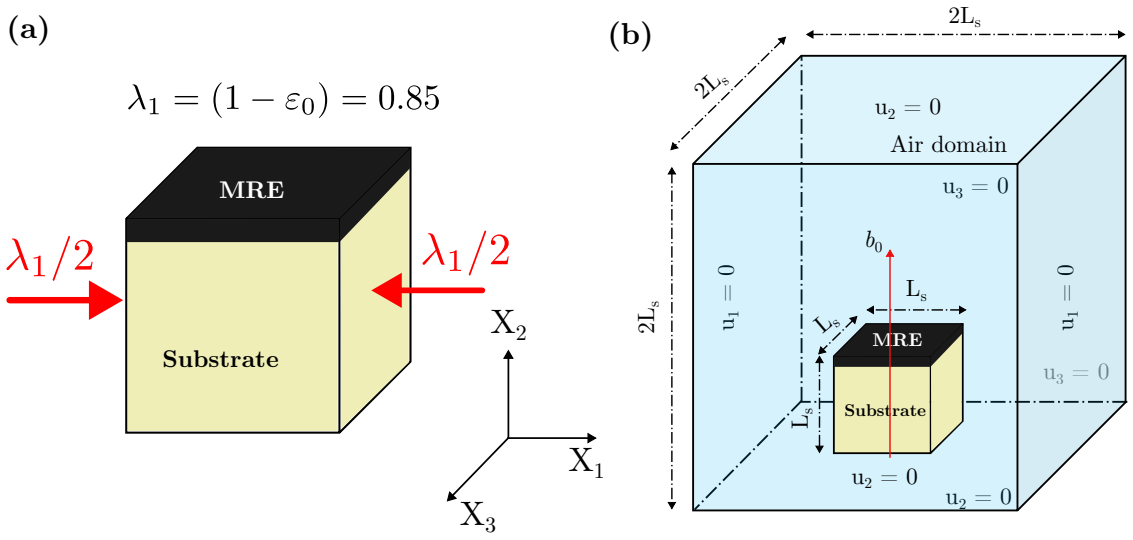


Figure 3.13: (a) Schematic of the specimen subjected to equi-biaxial pre-compression ($\lambda_0 = 0.85$). (b) Complete 3D boundary-value problem, including the surrounding air domain and magnetic boundary conditions used to generate a uniform vertical magnetic field.

The complete magneto-mechanical BVP is shown in Figure 3.13b. The film–substrate system is embedded within a surrounding air domain to correctly capture the Eulerian magnetic field distribution. A uniform vertical magnetic field $b_0$ is generated by prescribing the magnetic vector potential on the outer boundary of the air domain as discussed in subsection 3.2.4. The air domain is sufficiently large to minimize boundary effects and closely replicate the experimental loading conditions. The geometrical and material parameters are chosen to match those reported in Psarra et al. (2017). The magnetically-active film is modeled as an incompressible elastomer containing magnetic particles with a volume fraction $c = 0.2$, whereas the substrate and air are taken to be non-magnetic. The shear moduli are $G_f = 10$ kPa for the film and $G_s = 3$ kPa for the substrate, corresponding to a shear-modulus contrast $G_s/G_f = 0.3$. All parameters are summarized in Table 3.3.

| $h_f$ (mm) | $h_s/h_f$ | $G_s$ (kPa) | $G_s/G_f$ | $c$ | $\chi_f$ | $\mu_0 m_f^s$ (T) |
|---|---|---|---|---|---|---|
| 0.8 | 49 | 3 | 0.3 | 0.2 | 30 | 0.5 |

Table 3.3: Geometrical, mechanical, and magnetic parameters used for numerical validation, following Psarra et al. (2017).

The validation is performed by comparing the evolution of the bifurcation amplitude $A$ as a function of the applied magnetic field $b_0$. The definition of the bifurcation amplitude follows standard experimental and numerical practice and is illustrated in Figure 3.14. The amplitude is extracted from the vertical displacement profile at the free surface according to:

$$A = \frac{A_1 + A_2 + A_3}{3}, \tag{3.79}$$

where $A_1$, $A_2$ and $A_3$ denote the peak-to-valley amplitudes of three consecutive wrinkles. This definition provides a robust scalar measure of post-buckling deformation, even in the presence of slight asymmetries arising from three-dimensional effects or numerical errors. Note that for consistency, both the wrinkle wavelength $\mathcal{L}$ and the bifurcation amplitude $A$ are evaluated along the center plane in the $X_3$ direction, ensuring that the reported values are representative of the bulk response and are not influenced by edge effects.

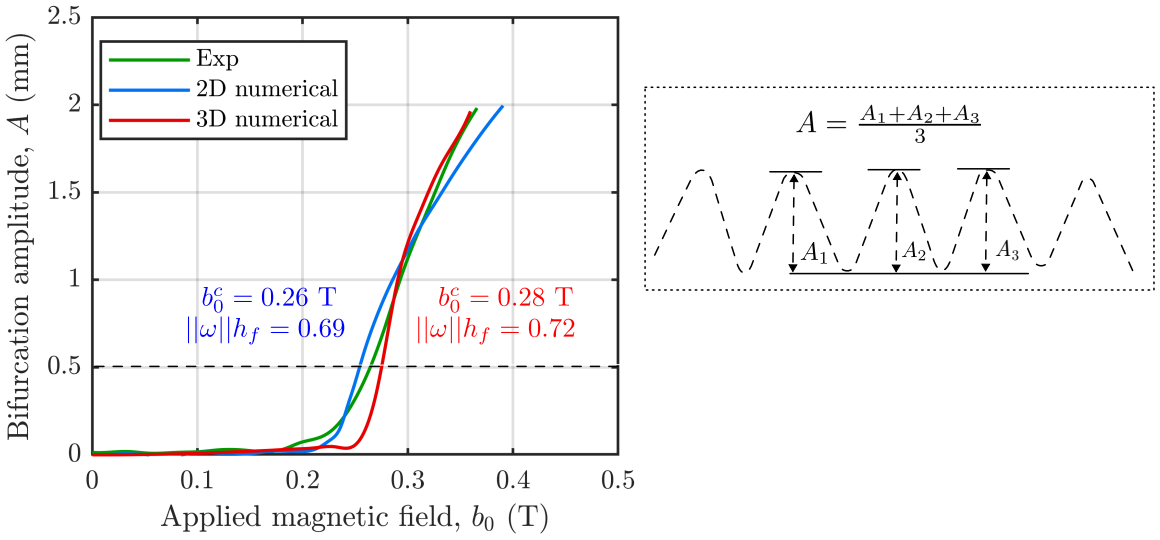


Figure 3.14: Comparison of bifurcation amplitude $A$ as a function of the applied magnetic field $b_0$ obtained from experiments, 2D simulations, and the present 3D model. The inset illustrates the definition of the bifurcation amplitude.

The comparison shown in Figure 3.14 demonstrates good agreement between the two numerical approaches. The transition magnetic field associated with the onset of well-developed wrinkling is identified as $b_0^c \approx 0.26$ T in the 2D model and $b_0^c \approx 0.28$ T in the 3D simulations. These values are obtained by applying a threshold criterion based on the bifurcation amplitude, here taken as $A = 0.5$ mm. This threshold is taken to be of the same order as the film thickness $h_f$ and therefore represents the emergence of a genuine surface instability rather than small-amplitude fluctuations.

It should be emphasized that the reported values of $b_0^c$ correspond to transition fields rather than mathematically sharp bifurcation points. Due to unavoidable imperfections in both experiments and numerical models, the amplitude evolves smoothly with the applied magnetic field. Consequently, a unique bifurcation point cannot be strictly defined for these imperfection-sensitive systems. When expressed in terms of the non-dimensional wavenumber $\|\omega\|h_f$ ($\|\omega\|h_f = \frac{2\pi h_f}{\mathcal{L}}$, where $\mathcal{L}$ is the characteristic surface wavelength of the instability, measured as the spatial period of the wrinkling pattern), the 2D and 3D models predict critical wavelengths that are comparable. The small discrepancy between the two cases can be attributed primarily to strong magnetic field localization near the specimen corners in the fully coupled 3D simulations, as discussed below in detail (Figure 3.15). These localized corner effects slightly perturb the global wavelength selection but do not alter the dominant instability mechanism. Beyond the transition field, small but systematic differences appear in the post-critical evolution of the bifurcation amplitude. These differences primarily originate from the plane-strain assumption inherent to the 2D formulation, which enforces uniform deformation across the specimen width. In contrast, the 3D model allows additional kinematic freedom, enabling deformation to redistribute in both the width and thickness directions. Despite these differences, the overall agreement between the 2D and 3D results remains excellent over the entire loading range considered.

A representative deformed configuration from the 3D simulations is shown in Figure 3.15. The out-of-plane displacement field displayed in Figure 3.15a clearly reveals the formation of a predominantly one-dimensional wrinkling pattern along the free surface. Compared to the strictly periodic pattern observed in the 2D model, the wrinkles in the 3D simulation exhibit a slight curvature along the transverse direction. This curvature arises because the solution lies between configurations with four and five wrinkles across the specimen width. The formation of five wrinkles is consistent with the numerical results reported in Psarra et al. (2019) for a pre-compression level of $\lambda_0 = 0.85$. As discussed in Psarra et al. (2019), numerical simulations predict four wrinkles for larger pre-compression levels ($\lambda_0 = 0.75, 0.8$), while for smaller pre-compression ($\lambda_0 = 0.85, 0.9$) five undulations are obtained, in closer agreement with the theoretical predictions of Cao et al. (2014). This discrepancy is partly due to the fact that, as pre-compression decreases, two-dimensional surface patterns begin to develop in experiments such as the one shown here in the 3D simulation, thereby reducing the direct validity of plane-strain 2D numerical models. A complementary explanation is provided by the theoretical bifurcation analysis of an infinite film-substrate system (Danas and Triantafyllidis 2014), which predicts critical wavenumbers corresponding to patterns lying between four and six wrinkles for the parameters considered. In the present 3D simulation, the resulting wrinkle wavelength remains within the same range as that reported in (Psarra et al. 2019), indicating that the dominant instability mechanism is preserved.

The distribution of the Eulerian magnetic field component $b_2$ is shown in Figure 3.15b. A pronounced concentration of the magnetic field is observed near the film corners, where the film, substrate and air domains meet. These regions correspond to sharp material and geometric transitions and act as numerical singularities in fully coupled magneto-mechanical simulations.

While mesh refinement can mitigate their influence, such singularities cannot be completely eliminated and must be carefully considered when interpreting local field values.

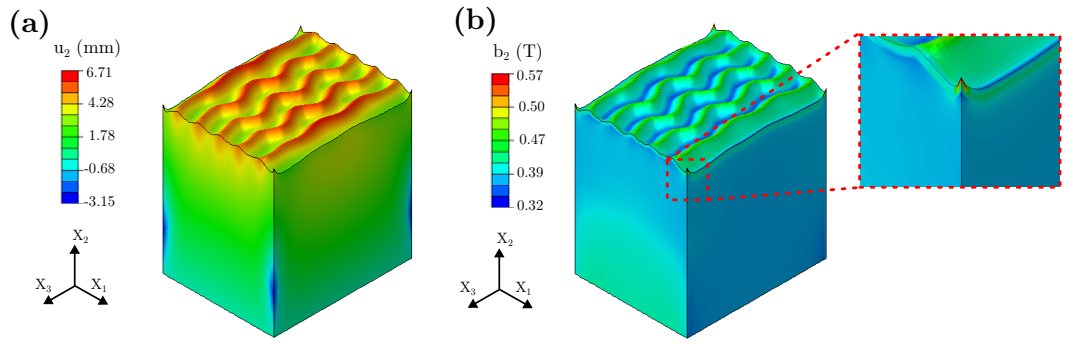


Figure 3.15: Three-dimensional numerical results at $b_0 = 0.4$ T. (a) Out-of-plane displacement field $u_2$ showing the wrinkling pattern. (b) Magnetic induction component $b_2$; the inset highlights the strong localization of the magnetic field near the film corners.

The spatial distributions of the magnetic induction components $(b_1, b_2)$ and magnetization components $(m_1, m_2)$ are shown in Figure 3.16. All contour plots correspond to a cross-section taken at the mid-plane along the $X_3$ direction, ensuring that the reported fields are representative of the bulk response away from edge effects. The magnetic response is dominated by the components $b_2$ and $m_2$, which are aligned with the applied magnetic field $b_0$. The magnetic induction $b_2$ exhibits weak spatial variations with localized amplification near the wrinkle crests, whereas the magnetization component $m_2$ remains almost uniform and strictly positive throughout the magnetic layer. In contrast, the longitudinal and transverse components $b_1$, $b_3$ and $m_1$, $m_3$ display alternating positive and negative regions, reflecting the local redistribution of magnetic fields induced by surface undulations. The in-plane components are however negligible compared to the vertical components for the loading configuration considered.

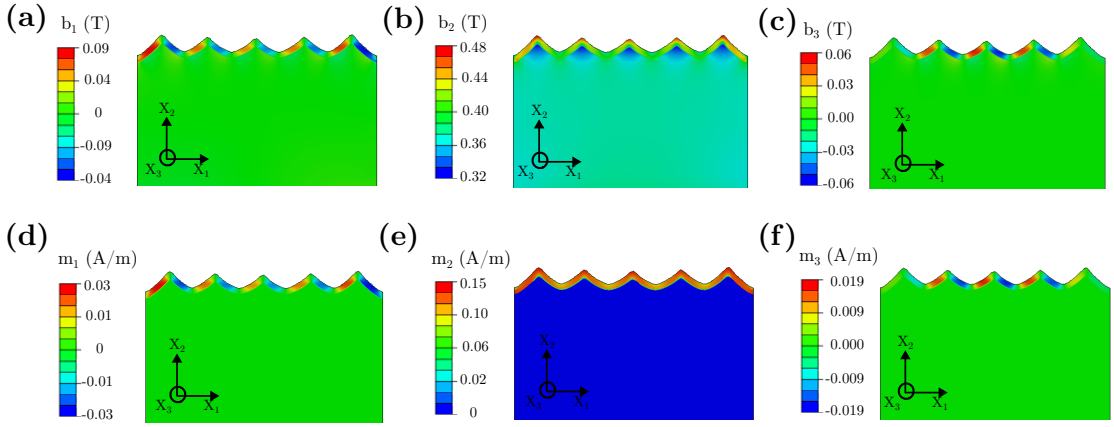


Figure 3.16: Spatial distributions of magnetic induction and magnetization components at $b_0 = 0.4$ T: (a) $b_1$, (b) $b_2$, (c) $b_3$, (d) $m_1$, (e) $m_2$ and (f) $m_3$.

Overall, the results demonstrate that the proposed 3D model reproduces the instability onset, dominant wavelength, and post-bifurcation behavior observed in the 2D framework, while additionally capturing finite-width effects, wrinkle curvature, and three-dimensional magnetic field

heterogeneity. This validation supports the use of the 3D formulation for subsequent studies involving complex geometries, material heterogeneity, and fully three-dimensional instability modes beyond the reach of reduced-dimensional models.

## 3.4 Numerical validation against experimental 3D surface profiles

In this section, the experimentally measured out-of-plane surface displacements of a heterogeneous MRE film/substrate system are compared with results from the fully-coupled 3D magneto-mechanical boundary-value problem (BVP). The validation sample is a cubic block containing four printed MRE discs arranged in a $2 \times 2$ pattern. This topology is intentionally selected because it produces well-defined and repeatable 3D surface profiles while still involving disc-to-disc interactions at higher magnetic loadings, which is further discussed in section 4.1.

### 3.4.1 Sample fabrication

The fabrication steps for the MRE film/substrate block are summarized in Figure 3.17. The process involves two main steps: first, DIW with active mixing is used to print the four-disc MRE layer; second, a thick, soft silicone substrate is poured in a mold directly over the printed pattern to create a single bilayer block.

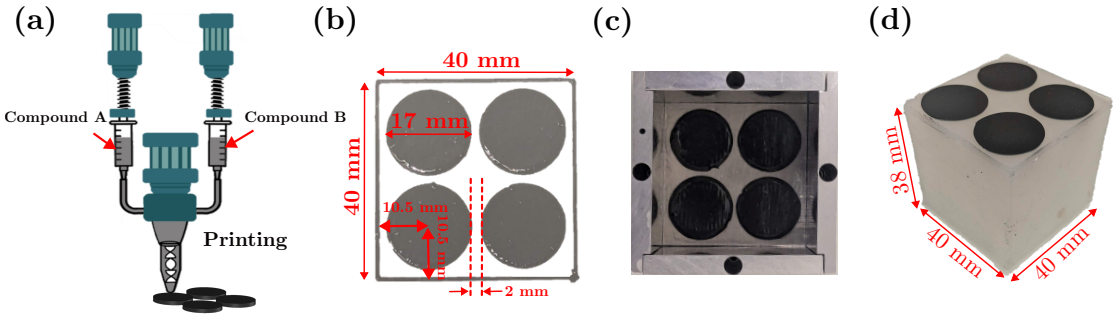


Figure 3.17: Fabrication of the MRE film/substrate block. (a) DIW printing of the 210 *phr* MRE discs using a dynamic mixing head. (b) Topology of the printed film: four discs of diameter 17 mm inside a $40 \times 40$ mm$^2$ footprint. (c) Transfer of the printed pattern (still on the thin PTFE sheet) into the metallic mold. (d) Final cubic block after substrate molding and curing.

The heterogeneous film is made by DIW on a thin PTFE (teflon) sheet, which acts as a temporary carrier for easy transfer of the printed pattern into the mold. For this study, the 210 *phr* ink is used to print the discs at a printing speed of $V = 10\ \mathrm{mm\,s^{-1}}$, with a nozzle diameter of 0.6 mm, and by stacking three layers. The printing parameters are the same as those in Table 2.4.

The pattern consists of four circular discs of diameter 17 mm arranged within a $40 \times 40$ mm$^2$ square footprint (see Figure 3.17b). The overall film thickness is approximately $h_f \simeq 1.8$ mm. After printing, the pattern is kept on the PTFE sheet to avoid distortion or damage during handling. To ensure reliable demolding and prevent unwanted adhesion, a release agent (Ease Release™ 200) is sprayed on both the PTFE sheet before disc printing and the metallic mold

surfaces before casting. The printed pattern is then transferred into the mold along with the PTFE sheet, as shown in Figure 3.17c. In this setup, the printed discs stay fixed in-plane while the substrate casting shapes the final block. The substrate is fabricated from Ecoflex™ 00-10 silicone. The two parts (Part A and Part B) are mixed at a 1:1 weight ratio for 4 min and subsequently degassed in a vacuum chamber for 6 min (same mixing/degassing protocol as used throughout this study for Ecoflex™ 00-10). Immediately after degassing, the Ecoflex™ 00-10 is poured into the mold, directly over the printed discs, until the final cubic geometry is achieved. After molding, the system is cured at 70 °C for 2 h inside an oven, left to rest for an additional 2 h at room temperature, after which the specimen is carefully demolded.

Due to experimental constraints (see subsection 3.4.2 and Appendix D), the total block height is $h = 38$ mm and the four-disc MRE film, of thickness $h_f = 1.8$ mm, is locally embedded at the top surface of the specimen of overall dimensions $40 \times 40 \times 38$ mm$^3$ (Figure 3.17d). The substrate is much thicker than the printed film layer, thereby encouraging a localized surface response from the heterogeneous magnetic layer.

### 3.4.2 Measurements of 3D morphological patterns

The magnetic experiments are conducted within an electromagnet consisting of two water-cooled coils mounted on a C-frame. Each coil contains in its center a truncated conical iron pole 90 mm in diameter, thereby yielding a nearly uniform field across the 82 mm air gap between the two poles (Figure 3.18a). At maximum input current (70 A), the field measured at the center of the air gap is 0.78 T.

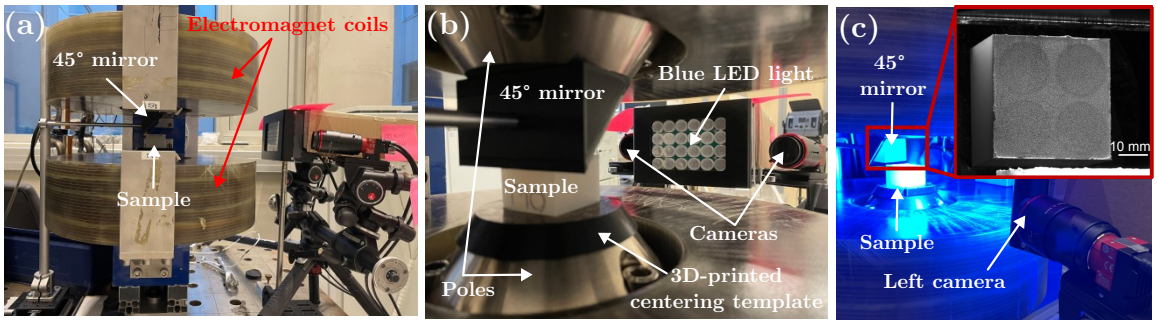


Figure 3.18: (a) Overall view of the electromagnet and stereo-DIC system. (b) View from within the electromagnet showing the sample and the two cameras pointing at the 45° mirror. (c) View from the vantage point of the left camera showing the reflection of the sample illuminated with blue light in the mirror. The inset shows the image of the speckled surface taken by the camera.

The film/substrate system is placed at the center of the lower pole using a 3D-printed centering template (Figure 3.18b). In addition to ensuring accurate positioning, this printed template also provides a mechanical constraint that prevents rigid-body rotation of the specimen during loading. This stabilization is consistent with the boundary condition imposed in the numerical model, where $u_2 = 0$ is applied at the bottom surface, and is essential for enabling the full development of the global deformation mode under higher magnetic fields. The sample height has been reduced to 38 mm for the experiments, compared to the nominal height of 40 mm for the numerical model, to allow for the installation of a mirror and to permit a vertical

movement of the sample's surface without touching the mirror and/or preventing DIC tracking (see Appendix D). Prior to any surface profile measurement, the sample is magnetically pre-cycled 10 times at 2 A.s$^{-1}$ from 0 to 70 A (0.78 T) and back to 0 A.

3D surface profiles are obtained by stereo-digital image correlation (stereo-DIC) using a commercial system provided by Eikosim. The system consists of two high-resolution cameras (Alvium G1-2460 with a 5328×4608 pixel detector) equipped with 50 mm Fujinon objectives. The two cameras are placed outside of the electromagnet, approximately within the mid-plane of the magnet and with an angle of 30° between them. They capture images of the deforming system reflected by a gold-coated mirror placed at a 45° angle to the sample's surface (Figure 3.18c) as it is illuminated by a blue LED light.

In order to perform DIC, the surface of the sample needs to be covered by a speckle pattern exhibiting a wide distribution of gray levels (Jones and Iadicola 2018). Since the system is very soft and submitted to rather large strains and displacements, several routes have been tested to obtain a speckle pattern suitable for DIC that does not crack during the test and does not modify the response of the sample, as detailed in Appendix D. The retained way of obtaining the speckle pattern is as follows: the surface of the sample is first covered with white water-based paint from a spray can by creating a mist of paint above the sample, letting it fall onto the surface and then dry. After 40 passes, the white layer sufficiently covers the surface of the sample. The black speckle is then applied using an elastomeric stamp bearing 100 µm-diameter dots randomly distributed over its surface (Diani et al. 2026). The stamp is mounted onto a roller, rolled over a black inkpad and then onto the sample (see resulting speckle in Figure 3.18c).

During the test, the magnetic field is current-controlled at 0.1 A.s$^{-1}$. Once the target current/field is reached, the sample is left within the static field for 10 s and an image is taken by each camera simultaneously, thereby creating a collection of pairs of images at different fields. These images are post-processed with the Eikosim software in incremental mode, using a 80 pixel mesh and brightness correction, yielding a floor-noise of 6 µm (see Appendix D). The displacement measured at the surface of the sample are then plotted with Paraview.

### 3.4.3 Numerical model

The numerical model considers a heterogeneous MRE film/substrate system of overall size $40 \times 40 \times 40$ mm$^3$, consisting of four circular discs embedded in a soft silicone substrate. Each disc has a diameter of 17 mm and is arranged in a symmetric $2 \times 2$ configuration, with a distance of 2 mm between the disc edges. The magneto-active film has a thickness $h_f = 1.8$ mm and is embedded in the soft substrate.

The three-dimensional magneto-mechanical boundary-value problem is solved using the **F-B** formulation. A surrounding air domain is included to accurately resolve the magnetic field, as described in subsection 3.2.4. A uniform vertical magnetic induction field $b_0$ is applied by setting the magnetic vector potential on the outer boundary of the air domain. The film is

treated as an incompressible magneto-active elastomer with a particle volume fraction $c = 0.22$, corresponding to the 210 *phr* ink used in the experiment. The substrate and air domains are considered non-magnetic. The mechanical properties are chosen based on the experimental results of subsubsection 3.1.3.1 and are listed in Table 3.4. The shear-modulus contrast places the system well within the regime favorable to surface instabilities. All geometric and material parameters are selected to closely match the experimental specimen used for DIC measurements, allowing for direct quantitative comparison of out-of-plane displacements.

| $h_f$ (mm) | $h_s/h_f$ | $G_f$ (MPa) | $G_s$ (MPa) | $G_s/G_f$ | $c$ | $\chi_f$ | $\mu_0 m_f^s$ (T) |
|---|---|---|---|---|---|---|---|
| 1.8 | 20.1 | 0.087 | 0.0058 | 0.06 | 0.22 | 30 | 0.5 |

Table 3.4: Geometrical and mechanical parameters used in the four-disc system numerical model.

### 3.4.4 Comparison between experiments and numerics

In this section, the comparison between experiments and numerical predictions for the heterogeneous four-disc system is presented. Figure 3.19 shows how the out-of-plane displacement $u_2$ at the centers of the four discs (P1 to P4, see Figure 3.19 inset) changes with the applied magnetic field $b_0$, along with the numerical results.

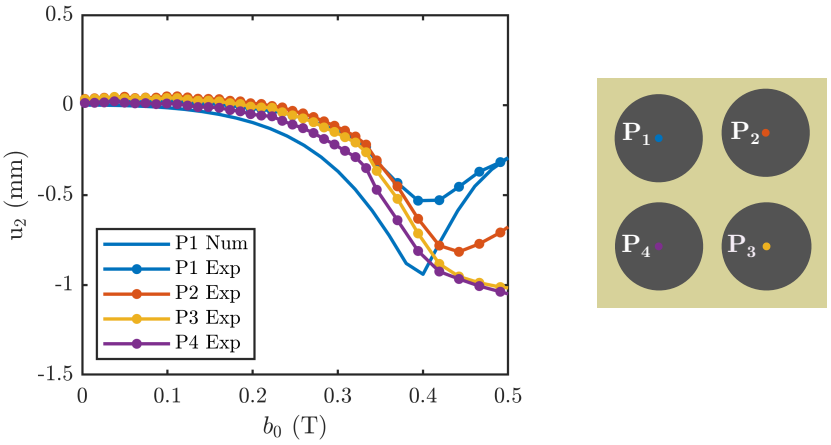


Figure 3.19: Out-of-plane displacement $u_2$ at the centers of the four discs as a function of the applied magnetic field $b_0$. The inset shows the locations of the measurement points.

Both experiments and simulations exhibit a smooth, steady increase in negative displacement with increasing magnetic field, reflecting the gradual development of a downward-dipping instability in the film/substrate system. When $b_0$ reaches about 0.15 T, the displacement amplitude starts to increase more rapidly. This value should be interpreted as a transition field rather than a sharply-defined bifurcation point. In both experiments and simulations, the displacement-field curves remain smooth due to unavoidable imperfections. In experiments, these arise from local magnetic field concentrations near the disc edges, small geometric misalignments, and material differences due to the fabrication process. In the numerical model, even though the geometry and material values are exact, a small volume fraction variation has been incorporated to break the symmetry of the system. As a result, it is not possible to clearly identify a single bifurcation point for this type of problem. When the value exceeds 0.37 T, disc-to-disc interactions become

dominant and the response shifts from localized deformation to a global mode. Under these conditions, the mechanical constraints imposed by the 3D-printed template prevent rigid-body motion, allowing the global deformation pattern to fully develop. Consequently, the experimental response matches the numerical predictions very well, with both showing a consistent global mode shape. Considering the slight underestimation of the extrema ($\sim$ 40 µm, as discussed in Appendix D) caused by the paint layer, the displacement fields are in fair agreement.

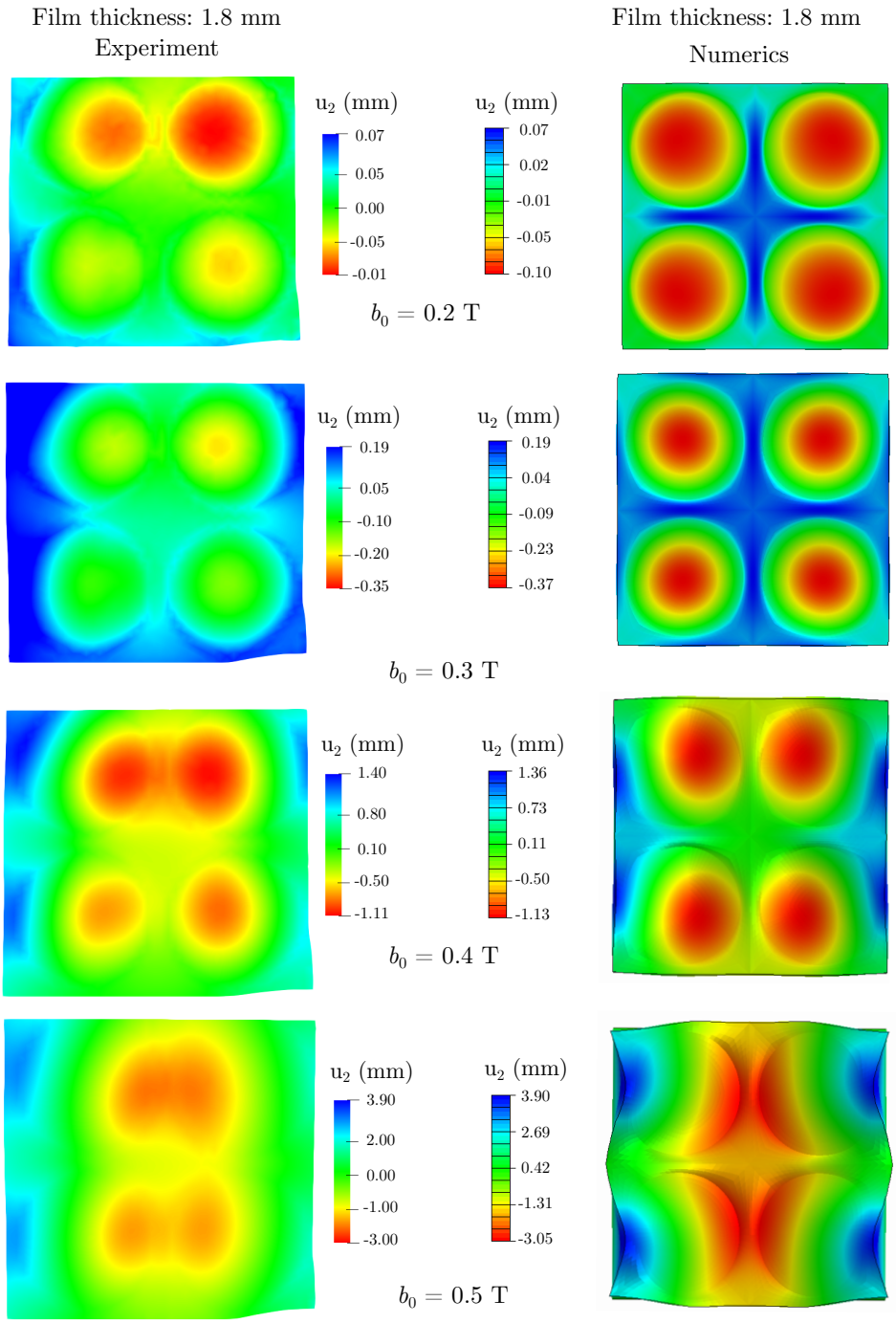


Figure 3.20: Comparison of experimental (DIC) and numerical out-of-plane displacement $u_2$ contours for the heterogeneous four-disc system at increasing magnetic field amplitudes.

Figure 3.19 provides local measurements of the instability response, but it does not capture the spatial structure of the deformation. The out-of-plane displacement contours shown in Fig-

ure 3.20 therefore provide a direct comparison between the experimental (stereo-DIC) and numerical surface profiles at different magnetic field intensities. At low magnetic field ($b_0 = 0.1$ T), both experiments and simulations exhibit similar deformation modes, characterized by a downward displacement at the disc centers and an upward displacement near the disc edges. As the magnetic field increases up to $b_0 = 0.3$ T, the deformation amplitude increases progressively while the overall four-disc symmetry is generally preserved. At higher magnetic field, disc-to-disc interactions begin to emerge. In the numerical simulations, the response remains largely symmetric, as all geometric and material parameters are perfectly defined whereas the experimental sample becomes destabilized before experiencing a global rotation at 0.4 T. Nevertheless, both $u_2$ displacement contours then indicate the onset of a long-wavelength modulation across the specimen, effectively transforming the initially localized four-disc response into a more global deformation mode at 0.5 T.

This transition is also shown by the numerical displacement profiles taken along in-plane directions (see inset) in Figure 3.21. The profiles along the $X_1$ direction (Figure 3.21a) stay mostly centered around each disc, which means the deformation here is controlled by the local response of each domain. In contrast, the profiles along the $X_3$ direction (Figure 3.21b) show a long-wavelength deformation mode gradually appearing as the magnetic field increases. Even though the geometry is symmetric, the long-wavelength mode is linked to a nearly equivalent set of instability modes at higher magnetic fields. In such a regime, the system becomes highly sensitive to small numerical perturbations, which selects a particular orientation of the global mode. In the present simulations, this mode manifests along the $X_3$ direction, without implying a fundamental directional preference of the idealized system. In contrast, the experimental measurements at comparable magnetic fields exhibit a more complex and less clearly organized surface profile due to the imminent overall rotation of the sample. As a result, although the overall deformation amplitude remains comparable, the spatial organization of the surface deformation is less distinct than in the numerical predictions.

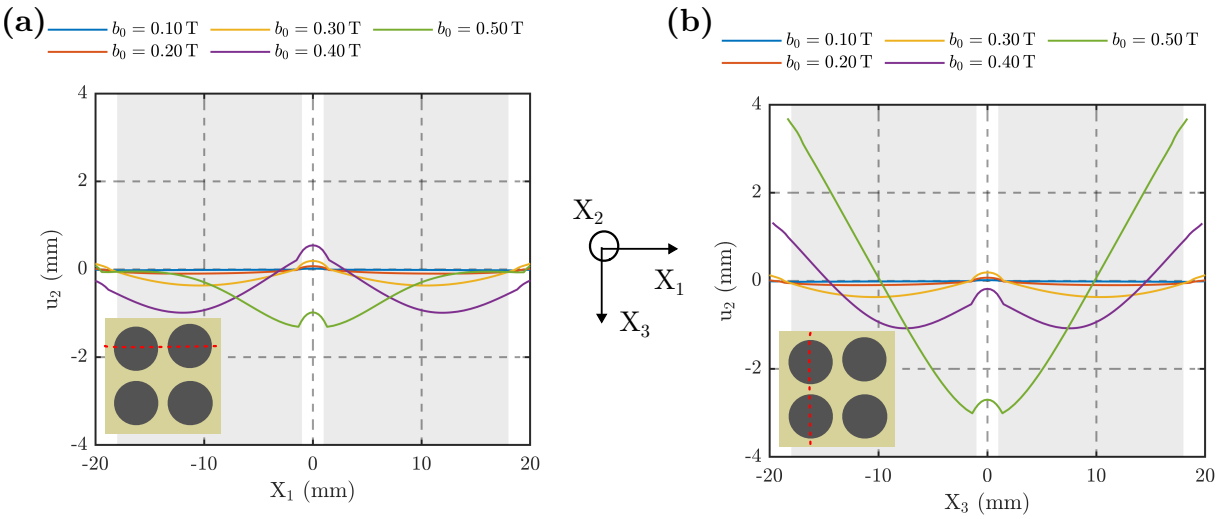


Figure 3.21: Out-of-plane displacement profiles $u_2$ extracted along representative in-plane directions for increasing magnetic field strengths: (a) along the $X_1$ direction and (b) along the $X_3$ direction. The shaded region represents the MRE domain.

The numerical Eulerian magnetic field and magnetization contours in Figure 3.22, measured at the top surface of the film and substrate, help explain the observed deformation patterns. When a vertical magnetic field is applied, the magneto-active layer tends to rotate to align with the field direction, a behavior known as the compass effect. The soft substrate beneath limits this rotation, leading to internal stresses in the film. The presence of disc edges at the boundaries of the MRE domains creates a local concentration of the magnetic field, as shown by the magnetic field and magnetization contours (Figure 3.22a,c,d,f). These areas experience the strongest magnetic torques and tend to move upward first. This initial, localized movement creates a non-uniform magnetic field, which then causes the central region of each disc to move downward as the system tries to rotate the whole magnetic layer. The main magnetic response comes from the vertical components $b_2$ (Figure 3.22b) and $m_2$ (Figure 3.22e), which are nearly uniform inside each disc and much larger than the in-plane components. In contrast, $b_1$, $b_3$, $m_1$, and $m_3$ are concentrated near the disc edges, showing strong magnetic field gradients. These localized magnetic concentrations coincide with regions of increased curvature in the $u_2$ field and are important for initiating the instability and driving the post-bifurcation response.

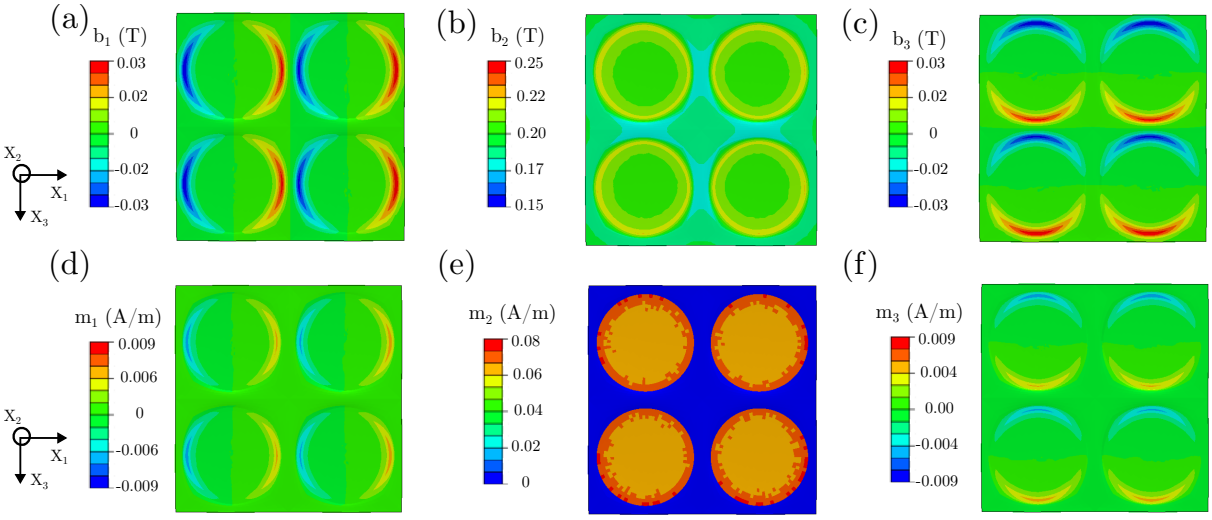


Figure 3.22: Numerical contours of the magnetic Eulerian components $(b_1, b_2, b_3)$ and magnetization components $(m_1, m_2, m_3)$ evaluated on the top surface of the film-substrate system at $b_0 = 0.2$ T.

## 3.5 Concluding remarks

This chapter presented a detailed experimental and numerical framework to study magnetically-induced surface instabilities in heterogeneous MRE film–substrate systems. The work began by reliably identifying material parameters, then developed, implemented and validated a three-dimensional magneto-mechanical model that captures both the onset of instability and post-bifurcation behavior.

The mechanical characterization of the constituent materials was performed to extract material parameters for use with the numerical model. Quasi-static compression tests on the Ecoflex™ 00-10 substrate showed that, while a Neo-Hookean model is sufficient at small strains,

the Lopez–Pamies energy density is required to accurately capture nonlinear stiffening at larger deformations. For the DIW-printed MRE dogbone specimens, cyclic tensile tests revealed the characteristic response of particle-filled elastomers, including nonlinear elasticity, hysteresis and Mullins softening. Since the numerical investigations focus on quasi-static equilibria and pattern formation, constitutive parameters were identified from the stabilized loading response. The mechanical behavior of the MRE films was described using a Lopez–Pamies hyperelastic law combined with an explicit homogenization scheme in which the effective shear modulus depends on the particle volume fraction. The Lefèvre–Lopez–Pamies model, calibrated on the highly filled 210 *phr* material and used predictively for lower particle contents, accurately reproduced the experimental responses while remaining admissible with respect to micromechanical bounds, ensuring physical consistency of the fitted parameters.

Based on this calibrated material model, a unified variational approach was developed using the **F**–**B** framework. The magnetic vector potential was used as an independent variable, making the method fully variational and well suited for studying instability and bifurcation. The total potential energy included mechanical, magnetic, magneto-mechanical and free-space effects, so the MRE film, substrate and air could all be modeled together. Magnetic saturation is captured via a hypergeometric energy density, yielding a closed-form magnetization law. The magneto-mechanical coupling used an implicit homogenization approach that goes beyond linear-susceptibility assumptions. Numerical implementation through a dedicated Abaqus® user-defined element enabled a consistent discretization of displacements and magnetic vector potential within the same finite element mesh and allowed the fully-coupled nonlinear equilibrium problem to be solved with a Newton–Raphson method. Extra care was taken to make the numerical model robust when dealing with large deformations and strong magnetic localization. The air around the sample, which is important for accurate magnetic field and stress calculations, was handled using kinematic constraints that keep the air mesh moving smoothly without introducing artificial stiffness. This approach helped prevent mesh distortion near sharp features and maintained the physical behavior of the free space. A small, physically-based imperfection was also added by randomly varying the particle volume fraction in each element. This breaks the model's artificial symmetry and enables stable calculations after bifurcation. Tests showed that setting the imperfection level to $c_{\text{imp}} = 6\%$ provides a good balance, reliably selecting a bifurcation branch and stopping non-physical oscillations while leaving the overall deformation patterns unchanged. This imperfection method was used for the rest of the thesis.

The three-dimensional model was first tested against a two-dimensional benchmark problem with a pre-compressed magneto-active film bonded to a soft substrate. The 3D simulations matched the critical magnetic field for instability onset and the post-bifurcation amplitude evolution reported in Psarra et al. (2017). The differences between the 2D and 3D results were due to finite-width effects and the additional kinematic freedom in 3D, which were evident in the post-critical response of the instability. Analysis of the magnetic field distributions showed that the response is mainly controlled by the components aligned with the applied field, while out-of-plane magnetic components are negligible for the loading case studied.

A second validation was carried out by directly comparing numerical predictions with experimental three-dimensional surface profiles measured by stereo-DIC on a heterogeneous four-disc MRE film/substrate system. The simulations captured the smooth changes in out-of-plane displacement at the disc centers as the magnetic field increased, as well as the main deformation modes seen in the experiment. At higher magnetic fields, both experiments and simulations showed a shift toward more global deformation patterns driven by interactions between discs, highlighting how sensitive the post-bifurcation regime is to imperfections and magnetic field localization. The numerical magnetic field and magnetization contours explained these patterns. When the local magnetic field concentrates at disc edges, it creates strong torques that initiate upward edge motion, while the substrate constraint converts this into internal stresses that drive downward displacement of disc centers.

In summary, this chapter shows that the fully-coupled three-dimensional **F**–**B** framework, together with well-calibrated material models and robust numerical methods for handling air and imperfections, is a reliable and physically-consistent tool for predicting magnetically induced instabilities in MRE film–substrate systems. The successful validation against both a two-dimensional numerical benchmark and full three-dimensional experiments provides a strong foundation for the next chapter, which will use this framework to study how topology, pattern interactions and material heterogeneity affect the design and control of complex magneto-responsive surfaces.

# Chapter 4
# Surface-morphing of heterogeneous film/substrate systems

This chapter investigates magneto-mechanically-induced surface instabilities in heterogeneous magnetorheological elastomer (MRE) film-substrate systems, with an emphasis on how topology, geometry and material contrast govern the onset of instability and post-bifurcation surface morphologies under an applied magnetic field. The study adopts a combined experimental-numerical approach, where experiments provide direct visualization of instability patterns and their post-critical evolution, while fully coupled three-dimensional finite-element simulations enable systematic parametric analyses. The first section of the chapter examines the effect of the overall topology of the heterogeneous MRE patterns embedded within the film, highlighting how the spatial arrangement and shape of discrete magnetic domains influence the selection of instability modes. The influence of geometrical parameters is then investigated by varying key geometric features such as the thickness, the spatial footprint as well as the spatial distribution of the patterns, and assess their impact on the instability wavelength and localization. Finally, the role of material property contrast between the MRE film and the soft substrate is analyzed to quantify its effect on instability thresholds and post-bifurcation amplitudes.

**Contents:**


4.1 Effect of overall topology . . . 105
4.1.1 Analyzed configurations . . . 105
4.1.2 Regime for thicker films: from local to global instability modes . . . 106
4.1.3 Regime for thinner films: from local to wrinkling instability modes . . . 112
4.1.4 Experimental assessment of the thin-film regime . . . 117
4.2 Effect of geometrical parameters . . . 119
4.2.1 Further insight into the effect of thickness . . . 119
4.2.2 Effect of pattern footprint: annulus width for the cylindrical sample . . . 127
4.2.3 Effect of pattern distribution: number of discs for the cubic sample . . . 129
4.3 Effect of material property contrast . . . 133
4.3.1 Effect of particle content . . . 133
4.3.2 Effect of the substrate softness . . . 135
4.4 Concluding remarks . . . 136

## 4.1 Effect of overall topology

### 4.1.1 Analyzed configurations

The topology of MRE inclusions plays a fundamental role in governing the nature of magneto-mechanically-induced surface instabilities. Beyond material properties and loading conditions, the geometric shape, domain distribution and slenderness of magnetic domains strongly influence how deformation localizes, propagates and interacts across the specimen. In heterogeneous soft systems, topology effectively controls the development of instability and determines whether the response remains localized or evolves into global patterns.

To better understand topological effects, this study uses simple and controlled shapes. By gradually making the shapes more complex, from compact, isolated domains to highly slender features, we can systematically study how topology affects instability onset, mode selection and post-bifurcation behavior. This step-by-step method helps us identify basic deformation mechanisms before examining more complex cases in which different instability modes coexist or interact.

In this context, topology is investigated independently of material contrast and loading variations. All configurations share identical material parameters, boundary conditions and magnetic loadings. Consequently, any observed differences in the deformation patterns can be directly attributed to topological characteristics such as domain shape, aspect ratio and spatial distribution. This strategy provides a clear physical interpretation of how topology governs magneto-mechanical instabilities in heterogeneous MRE systems. Based on this, three representative topologies are considered, as illustrated in Figure 4.1.

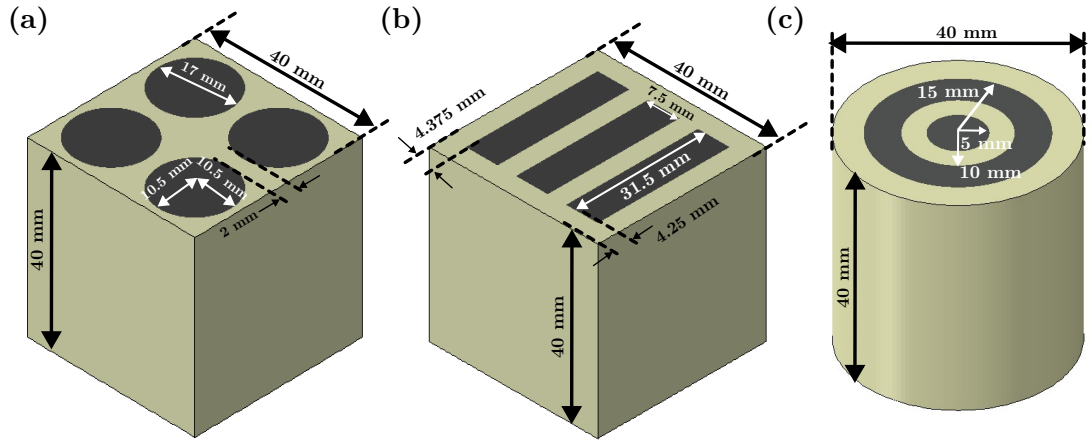


Figure 4.1: Topological configurations considered in the study: (a) cubic specimen with four discrete MRE discs, (b) cubic specimen with three slender MRE strips, and (c) cylindrical specimen combining a central disc and a slender annular MRE region. All specimens have a characteristic dimension of 40 mm in the numerical simulations.

The first configuration, shown in Figure 4.1a, consists of a cubic specimen containing four discrete circular MRE domains arranged symmetrically within a soft silicone matrix. This topology is primarily used as a benchmark configuration, as it has already been examined in detail in

section 3.4. Its simple and compact arrangement provides a convenient reference for comparing the deformation responses of more complex topologies under identical material and loading conditions. The second topology, depicted in Figure 4.1b, is a cubic specimen of the same outer dimensions incorporating three elongated MRE strips. Compared to the first configuration, this geometry introduces magnetic domains with a higher aspect ratio and a pronounced directional layout, offering a distinct spatial organization of the magneto-active regions within the matrix. The final configuration, shown in Figure 4.1c, is a cylindrical specimen with a central MRE disc surrounded by a concentric annular MRE region, with an overall diameter and height of 40 mm. This topology combines a compact magnetic inclusion at the center with a surrounding slender annular domain, thereby incorporating both compact and slender geometric features within a single heterogeneous system, and yielding a layout that fundamentally differs from cubic configurations in terms of magnetic region symmetry and connectivity.

### 4.1.2 Regime for thicker films: from local to global instability modes

Building on the results presented in section 3.4, where the magneto-mechanical response of the cubic four-disc topology was examined at a film thickness of $h_f = 1.8$ mm, this subsection extends the analysis to investigate the effect of topology on surface instabilities for thicker films. Numerical and experimental results are compared for the three configurations shown in Figure 4.1, all evaluated for a film thickness of $h_f = 1.8$ mm. To isolate the influence of topology, all material parameters, boundary conditions and magnetic loading conditions are kept identical across the three configurations and are consistent with those used in section 3.4. Consequently, any differences observed in the deformation patterns can be directly attributed to topological effects.

Figure 4.2 presents the three-dimensional out-of-plane displacement fields $u_2$ predicted numerically for the different topologies at applied magnetic fields of $b_0 = 0.3$ T and 0.5 T. At the moderate magnetic field of $b_0 = 0.3$ T, all three configurations exhibit qualitatively similar deformation patterns characterized by a localized downward displacement within the magneto-active regions. At this stage, the response is primarily governed by the overall topology of the magnetic domains, and the deformation remains confined within each domain.

As the magnetic field is increased to $b_0 = 0.5$ T, the deformation amplitude increases substantially, and a transition toward more global deformation patterns is observed across all topologies. In the cubic specimens, interactions between neighboring magnetic domains become increasingly important, leading to long-wavelength modulations that extend beyond individual inclusions. Similarly, in the cylindrical disc–annulus configuration, the initially localized dip-like response of the central disc progressively couples with the deformation of the surrounding annular region, resulting in a more uniform, specimen-scale deformation mode. This evolution indicates a transition from a heterogeneous, domain-controlled response at lower magnetic fields to a global deformation mode at higher magnetic fields, whose spatial organization is influenced by the overall topology of the system.

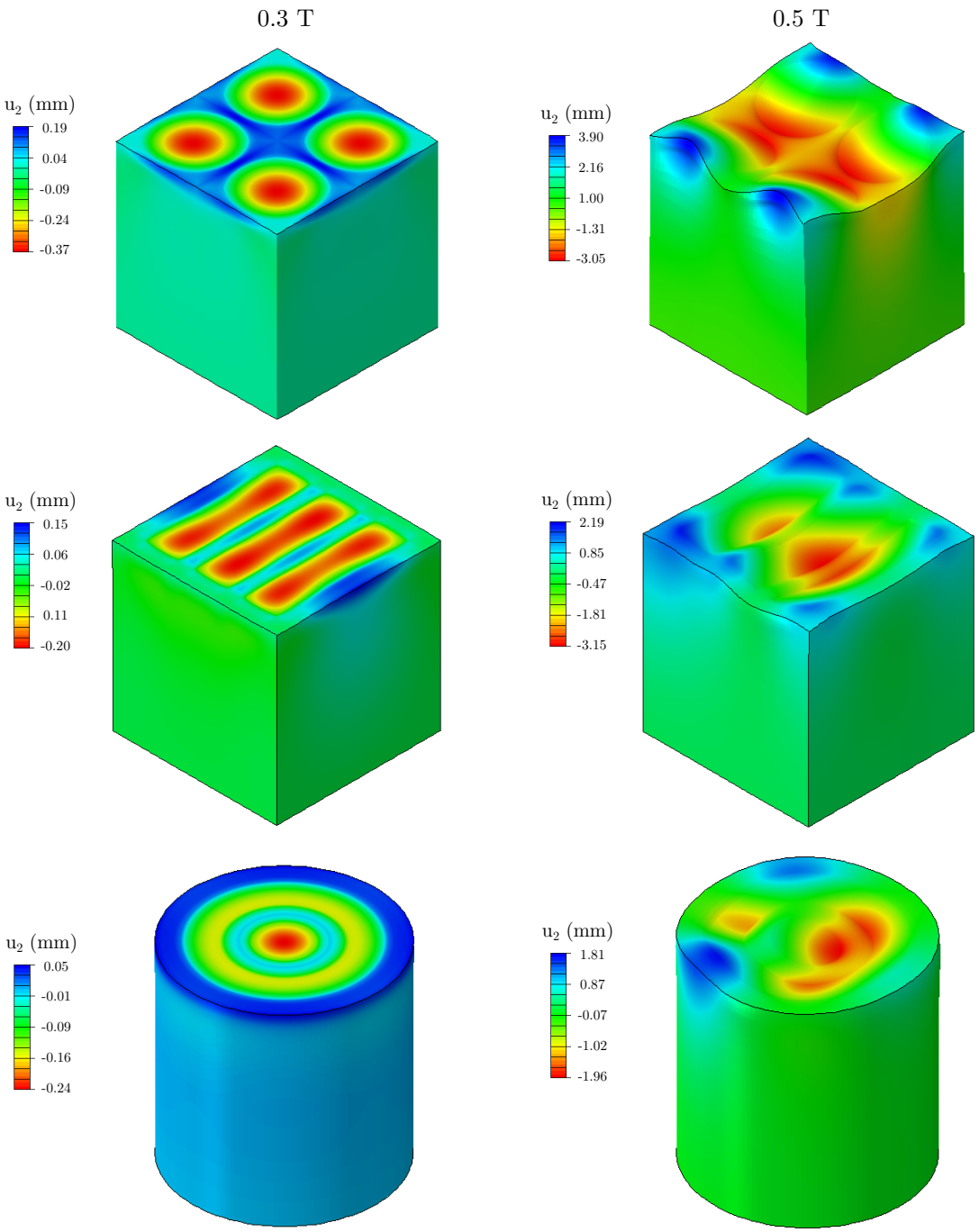


Figure 4.2: Out-of-plane displacement contour profiles $u_2$ for the three topologies at 0.3 T and 0.5 T.

To quantify the evolution of the instability with increasing magnetic field, the out-of-plane displacement $u_2$ is extracted at representative points within the magnetic domains for the cubic three-strip and cylindrical disc-annulus topology similar to the cubic four-disc topology, as shown in Figure 4.3. In all cases, the displacement initially evolves smoothly with increasing $b_0$, reflecting a gradual destabilization rather than a sharply defined bifurcation point. This smooth response is consistent with the presence of unavoidable imperfections in both experiments and numerical models, including magnetic field localization near domain edges and small material or geometric asymmetries.

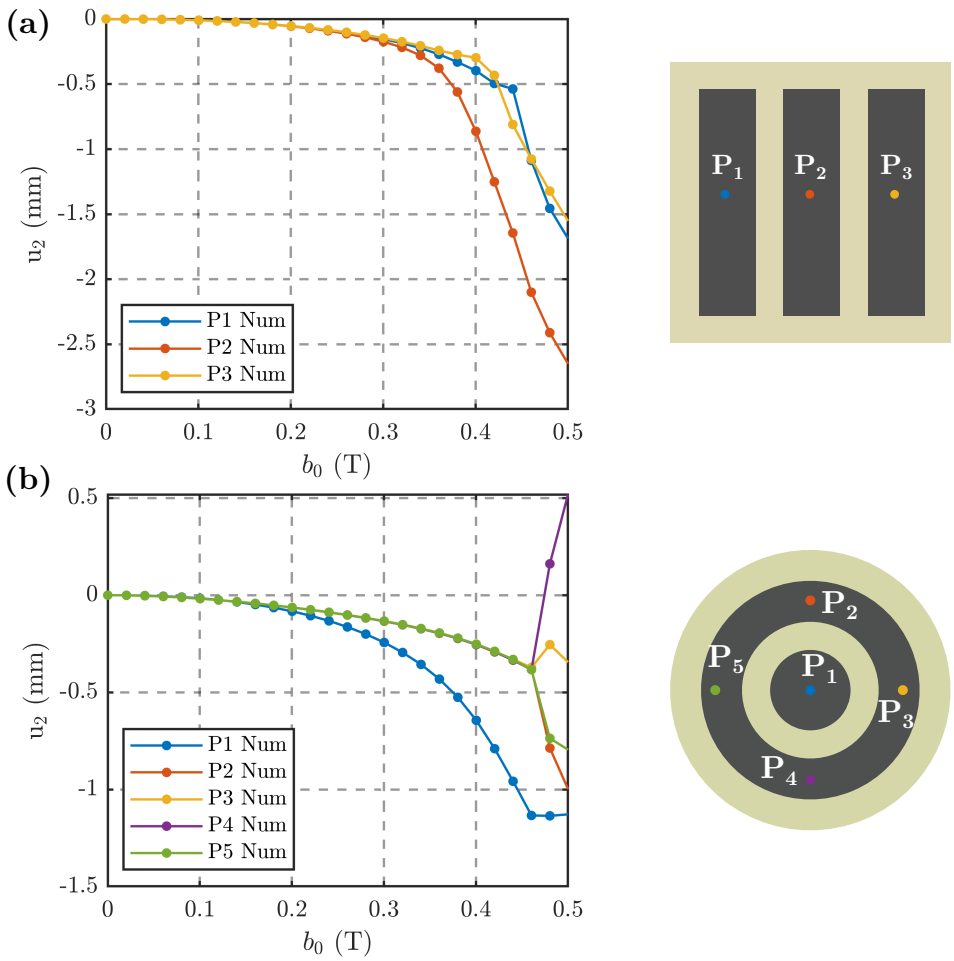


Figure 4.3: Out-of-plane displacement $u_2$ as a function of the applied magnetic field $b_0$. (a) Displacement measured at the centers of the three slender MRE strips (P1-P3), and (b) displacement measured at the center of the circular disc (P1) and at four representative points along the annular MRE region (P2-P5).

For the cubic three-strip topology, the out-of-plane displacement $u_2$ is evaluated at the centers of the three MRE strips, denoted as points P1, P2 and P3, as illustrated in Figure 4.3a. At low magnetic fields, the displacement at all three points evolves gradually and remains nearly identical, indicating a predominantly local response controlled by each individual strip. Beyond a critical magnetic field $b_0 = 0.32$ T, however, the displacement curves begin to diverge and exhibit a more rapid increase in magnitude. This divergence reflects the increasing interaction between neighboring strips, promoted by the anisotropic spatial arrangement of the magnetic domains. Notably, points P1 and P3, which symmetric about the mid-plane, show almost the same deformation across the whole magnetic field range. The central strip, containing P2, moves out of plane more than the others, especially at higher magnetic fields. This greater deformation at P2 happens because it sits between the outer strips, so magnetic forces from both sides add up and have a stronger effect on the overall deformation. At higher magnetic fields, these interactions lead to a deformation response that is no longer governed solely by individual strips but instead reflects the emergence of a global deformation mode spanning the specimen width, with different amplitudes depending on the relative positions of the strips.

In the cylindrical disc–annulus configuration, the out-of-plane displacement $u_2$ is measured at the center of the circular disc (P1) and at four representative points distributed uniformly along the annular MRE region (P2–P5), as shown in Figure 4.3b. Owing to the axisymmetric nature of the annular geometry, the displacement measured at the annular points remains identical nearly over the entire range of applied magnetic field, indicating an initial highly symmetric deformation response. In contrast, the displacement at the central disc exhibits a distinct evolution, with a larger sensitivity to increasing magnetic field. As the magnetic field increases, the response gradually transitions from a localized disc-dominated deformation to a more global film-scale deformation mode ($b_0 = 0.47$ T), in which the disc and annular regions deform in a coupled manner, resulting in a sudden change in the displacement amplitude curves and in the associated reorganization of the deformation into a specimen-scale mode.

For completeness, Figure 4.4 compares the evolution of the out-of-plane displacement $u_2$ as a function of the applied magnetic field $b_0$ for the different topologies, measured at representative points within the magnetic domains.

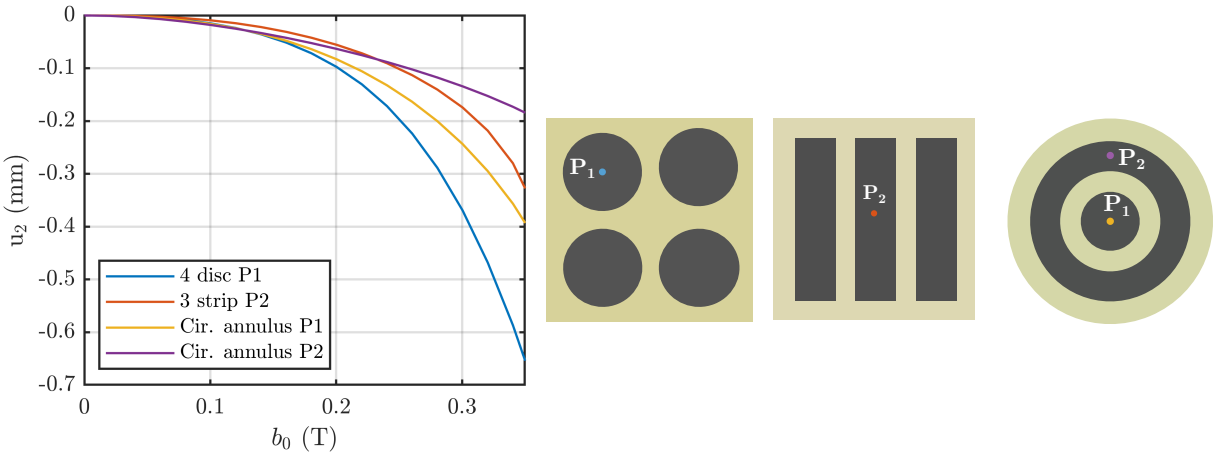


Figure 4.4: Out-of-plane displacement $u_2$ as a function of the applied magnetic field $b_0$ for different geometrical topologies.

This comparison shows the onset of instability across the various topologies and indicates that the critical magnetic field associated with the instability remains very similar for all topologies. This observation suggests that, within the present parameter range, the instability onset is primarily governed by intrinsic material characteristics, such as the particle volume fraction and the film thickness, rather than by the specific topology of the magnetic domains. Despite the comparable onset fields, clear differences emerge in the post-bifurcation response. In the cubic four-disc topology, the out-of-plane displacement $u_2$ increases more rapidly with magnetic field, which can be attributed to the larger disc diameter and the confined symmetry of the discs. In contrast, the disc in the cylindrical disc-annulus configuration exhibits a more gradual response, with the central disc showing a smaller displacement amplitude due to its reduced radius (5 mm) compared to the larger disc radius (8.5 mm) of the cubic four-disc configuration. Finally, owing to the elongated geometry of the strips, the deformation develops more progressively along their length, resulting in a delayed post-bifurcation response compared to the discs.

Additional insight into the spatial organization of the deformation is obtained from the out-of-plane displacement profiles shown in Figure 4.5. These profiles are extracted along representative in-plane directions passing through the magnetic domains, as indicated schematically in each subfigure. At low magnetic fields ($b_0 \leq 0.2$ T), the $u_2$ profiles remain nearly flat across the specimen, with only small localized deviations near the magneto-active regions, indicating that the deformation is primarily governed by the local response of individual domains.

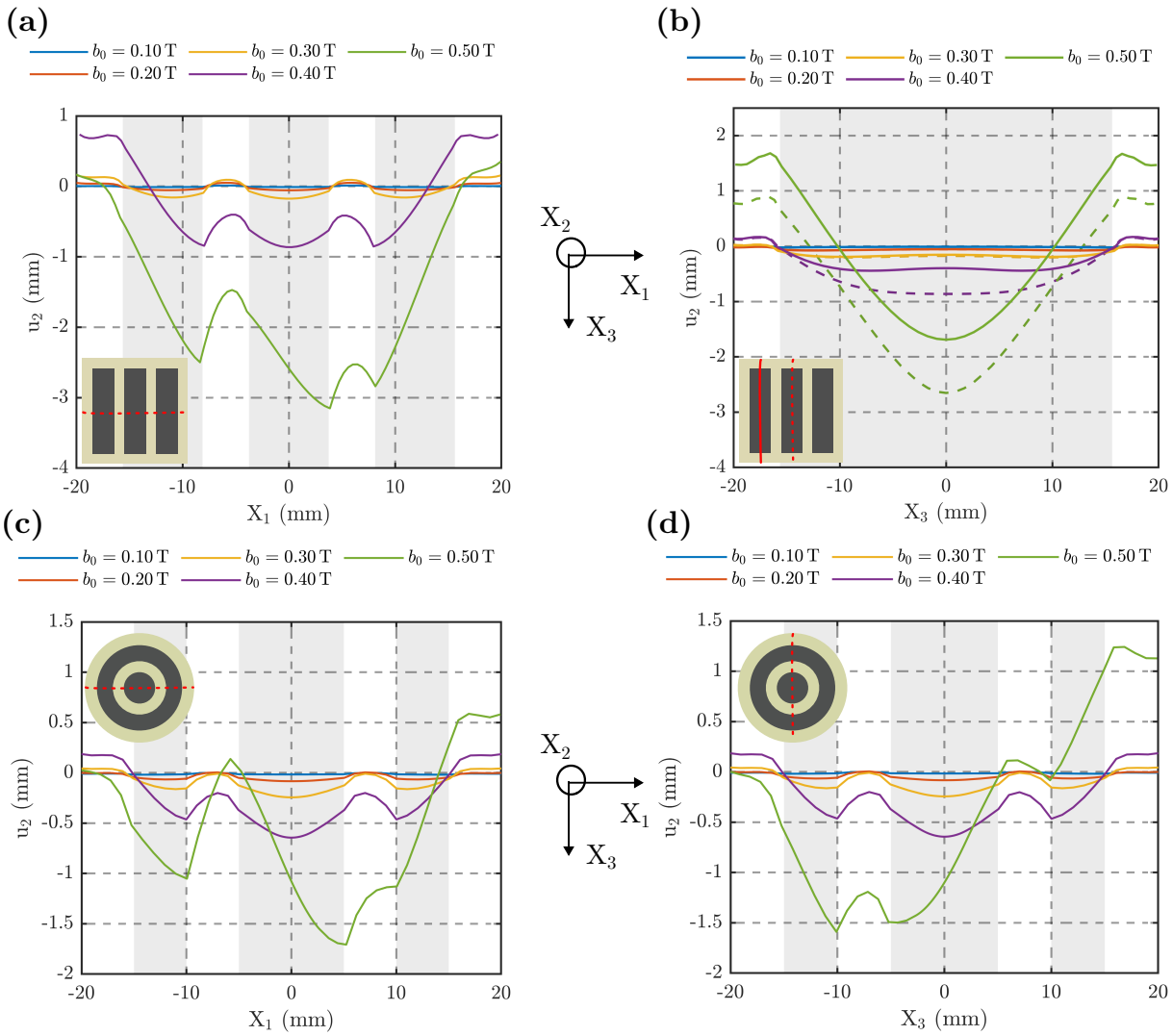


Figure 4.5: Out-of-plane displacement profiles $u_2$ along representative in-plane directions for increasing magnetic fields: (a, b) cubic three-strip topology (solid lines denote measurements taken along the left-most strip, while dashed lines denote measurements taken along the central strip.) and (c, d) cylindrical disc-annulus topology, extracted along $X_1$ and $X_3$ respectively. The shaded region represents the MRE domains.

For the cubic three-strip topology, the displacement profiles along the $X_1$ direction (Figure 4.5a) reveal that, as the magnetic field increases, the deformation becomes increasingly non-uniform across the specimen width. At intermediate magnetic fields ($b_0 \approx 0.3$–$0.4$ T), the initially localized deformation near the individual strips progressively extends over a larger portion of the specimen, leading to the development of smooth, long-wavelength modulations. The characteristic length scale of these modulations is governed by the strip width and spacing, and their amplitude increases continuously with the applied magnetic field. The outer regions of the film

exhibit a pronounced upward displacement relative to the central region. This behavior can be attributed to the freestanding lateral boundaries of the specimen near the edges of the substrate. At these locations, the mechanical constraint provided by the surrounding material is reduced compared to the central region, resulting in a lower resistance to out-of-plane deformation. At high magnetic fields ($b_0 = 0.5$T), the out-of-plane displacement profile no longer follows the symmetry of the MRE pattern, and it appears that each domain tries to fully rotate to align with the vertically-applied magnetic field.

The displacement profiles measured along the $X_3$ direction for the strip geometry (Figure 4.5b) show a smooth, long-wavelength deformation that becomes deeper as the magnetic field increases. The main response is a global bending-like mode, free of localized interactions between neighboring strips. The central strip always dips more than the outer strips. This difference is due to the lateral strips being near the edges of the specimen, which limits the downwards movement of the outer strips compared to the central one.

The displacement profiles for the cylindrical disc–annulus configuration are shown in Figure 4.5c and Figure 4.5d, corresponding to sections taken along the $X_1$ and $X_3$ directions, respectively. Owing to the axisymmetric geometry of the annular magnetic region, the deformation remains initially symmetric with respect to the specimen center, and the profiles extracted along both directions exhibit very similar shapes. Akin to the cubic three-strip topology, at low to intermediate magnetic fields, the deformation is dominated by a localized downward displacement of the central disc, accompanied by a weaker response in the surrounding annular region. As the magnetic field increases, the outer edge of the annular magnetic layer rises more strongly than the inner edge adjacent to the central disc due to the reduced mechanical constraint near the free lateral boundaries of the substrate. At higher magnetic fields, the progressive uplift of the annular region and the downward deformation of the central disc lead to a coupled response in which magnetic domains move closer together. This increased proximity enhances magneto-mechanical interactions between the disc and the annulus, promoting a transition toward a global, specimen-scale deformation mode. Throughout this process, the deformation evolves into a long-wavelength profile characteristic governed by the combined effects of geometry and boundary conditions. The symmetry of the out-of-plane displacement profile is broken during this transition, where it appears again that each domain tries locally to fully rotate to align with the vertically-applied magnetic field.

The numerical Eulerian magnetic field and magnetization contours for the full 3D profiles at 0.3 T, shown in Figure E.1, provide further insight into the deformation mechanisms observed for the different topologies. As in the cubic four-disc case, the application of a vertical magnetic field induces the magneto-active domains to try to rotate and align with the applied field direction. This rotation is constrained by the compliant substrate, giving rise to internal stresses within the MRE layer. For the cubic three-strip topology in Figure E.1a-f , strong magnetic field concentrations develop near the strip edges, as evidenced by the localized extrema in the magnetic field and magnetization components. These regions experience enhanced magnetic torques and act as preferential sites for the initiation of out-of-plane deformation. The vertical magnetic

components $b_2$ and $m_2$ dominate the response within the magnetic strips and remain relatively uniform across their width, while the in-plane components $b_1$, $b_3$, $m_1$, and $m_3$ are mainly localized near the strip boundaries, indicating strong magnetic field gradients associated with the geometric discontinuities. A similar behavior is observed in the cylindrical disc-annulus configuration in Figure E.1g-l. The vertical components $b_2$ and $m_2$ exhibit an almost axisymmetric distribution within the magnetic regions, confirming that the dominant magnetic response is aligned with the applied field. In contrast, the in-plane components are concentrated near the inner and outer edges of the annular region and at the boundary of the central disc. These localized magnetic concentrations coincide with regions of increased curvature in the out-of-plane displacement field $u_2$ and play a key role in triggering the instability and governing the subsequent post-bifurcation deformation. Overall, the magnetic field distributions highlight how geometric features such as edges, slenderness and symmetry control the localization of magnetic forces and, consequently, the observed deformation patterns.

### 4.1.3 Regime for thinner films: from local to wrinkling instability modes

The previous subsection showed that for thicker films ($h_f = 1.8$ mm), the response changes from a localized, domain-controlled deformation at low fields to a more global, specimen-scale instability as the magnetic loading increases. When the film thickness is reduced to $h_f = 0.7$ mm, the deformation is more strongly limited to the magneto-active regions and their immediate surroundings, and additional features associated with wrinkling-type instabilities start to appear. In this thinner-film regime, the deformation remains primarily localized across a wide range of magnetic fields, and the effects of topology become more noticeable, especially for slender magnetic domains.

Figure 4.6 shows the three-dimensional out-of-plane displacement fields $u_2$ calculated for the three topologies at $b_0 = 0.4$ T and 0.7 T. At $b_0 = 0.4$ T, all configurations show a localized downward displacement over the magneto-active regions, similar to the dip-like response seen in thicker films. At $b_0 = 0.7$ T, the deformation modes become more distinct. In the cubic four-disc topology, the response remains mostly localized, and no clear wrinkle pattern forms between the discs, indicating limited interaction across the film surface in this thinner setup. In contrast, slender geometries show wrinkling-type modulations at high fields. The cubic three-strip topology develops undulations linked to the slender magnetic domains, and the cylindrical disc-annulus topology shows a clear circumferential modulation along the annular region.

The film thickness thus plays a crucial role in the observed instability modes. For the thinner film ($h_f = 0.7$ mm), the large thickness ratio between the substrate and the film ($h_s/h_f = 56.142$) strongly constrains the magnetic layer to the compliant substrate, favoring a wrinkling-type instability. By comparison, for the thicker film ($h_f = 1.8$ mm), the smaller thickness ratio ($h_s/h_f = 20.1$) allows stronger interactions between magnetic domains and promotes the development of more global deformation modes. The emergence of the wrinkle patterns is also governed by the topology of the magnetic domains and their spatial distribution. In slender magnetic regions, such as the strips and the annular domain, magnetic stresses are distributed

continuously along an extended direction, allowing local deformations to interact over a larger length scale. Once the magnetic loading exceeds a critical level, this deformation favors the selection of periodic wrinkling modes along the length or circumference of the magnetic region. In contrast, for compact magnetic domains such as in the cubic four-disc topology, the magnetic forces remain strongly localized within each disc, and interactions between neighboring domains are weak in the thin-film configuration. As a result, the deformation remains dominated by local dip-like responses, and the length scale required for the formation of wrinkle patterns is not satisfied.

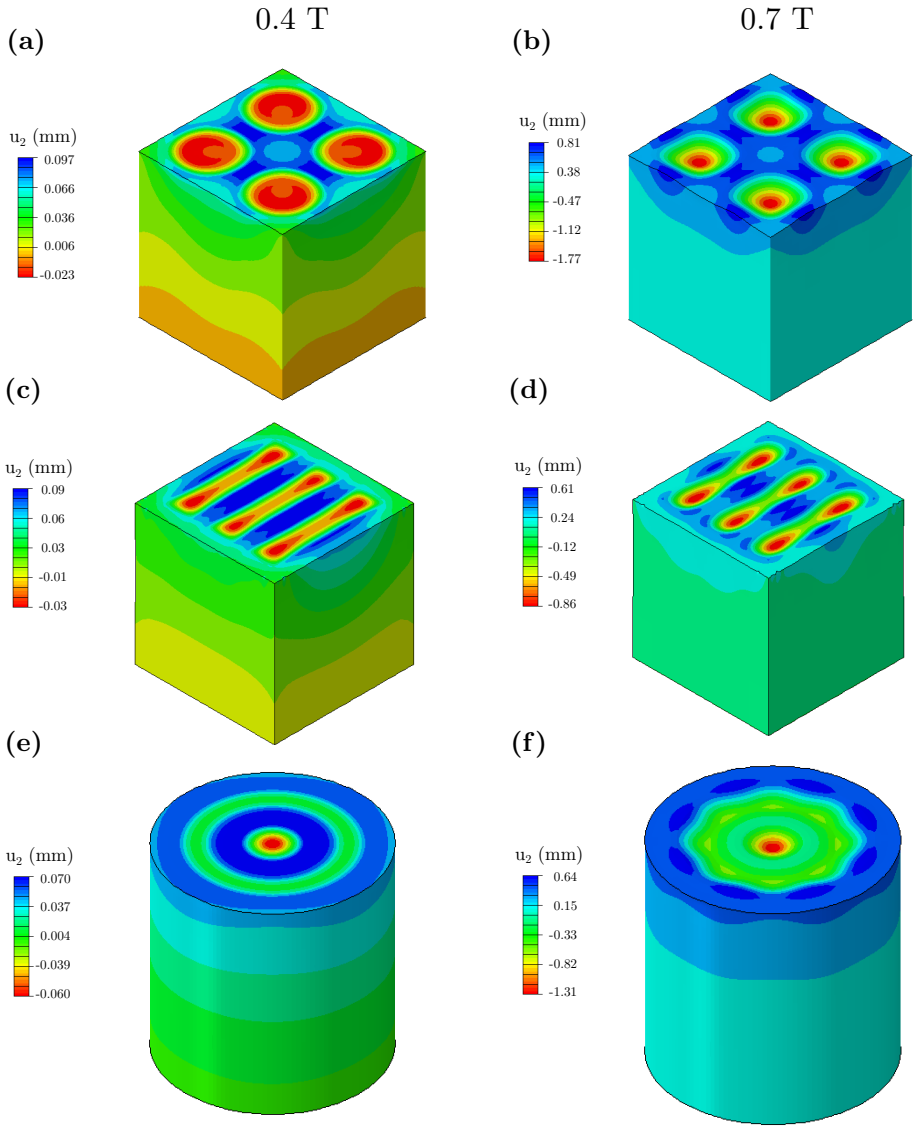


Figure 4.6: Numerical out-of-plane displacement contours $u_2$ for the three topologies at $h_f = 0.7$ mm, shown at $b_0 = 0.4$ T and 0.7 T.

To quantify the evolution of the response with increasing magnetic field, Figure 4.7 shows the out-of-plane displacement $u_2$ extracted at representative points within the magnetic domains for the three topologies. For the cubic four-disc configuration (Figure 4.7a), the response is characterized by a predominantly downward motion at the disc centers, with no indication of an additional wrinkling-driven mode. This behavior is consistent with the contour plots in

Figure 4.6b, where the deformation remains confined to the discs even at high field. For the cubic three-strip topology (Figure 4.7b), the three strip-center curves remain close over the initial loading range, reflecting a localized and nearly uniform dip-like response of each strip. At higher fields, the curves exhibit a change in trend associated with the formation of a localized undulation within the strip. In particular, after an initial downward evolution, the displacement partially recovers as the surface reorganizes into a wrinkling-like profile. In the cylindrical disc-annulus configuration (Figure 4.7c), the response exhibits two distinct destabilization stages. The central disc (P1) destabilizes first, with an increase in downward displacement at lower fields, reflecting the ability of the circular disc to deform easily due to its symmetry, as discussed in subsection 4.1.2. The annular region (P2-P5) remains comparatively weakly deformed throughout the loading, and only at high fields, the response progressively transitions into a wrinkling-type deformation of the annulus, consistent with the emergence of circumferential undulations visible in Figure 4.6f.

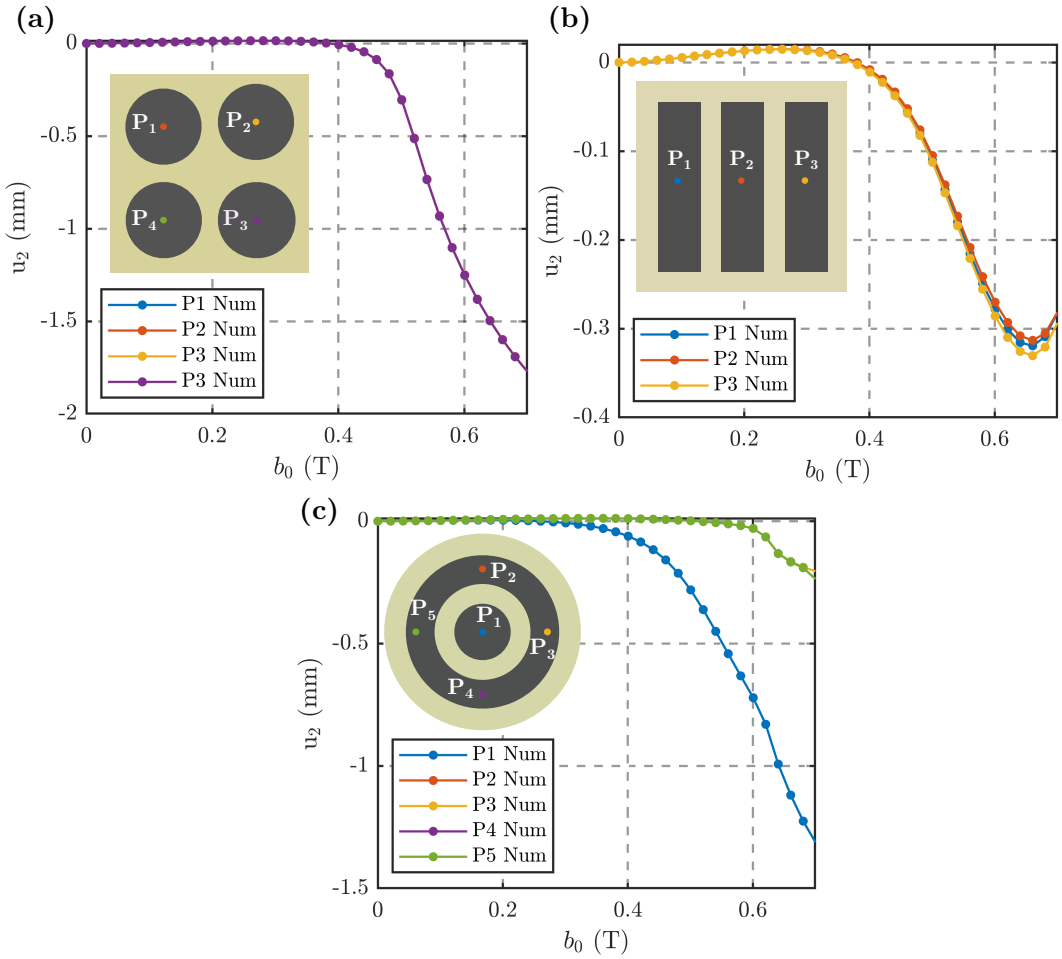


Figure 4.7: Out-of-plane displacement $u_2$ as a function of the applied magnetic field $b_0$ for $h_f = 0.7$ mm. (a) Cubic four-disc topology: displacement at disc centers (P1-P4). (b) Cubic three-strip topology: displacement at strip centers (P1-P3). (c) Cylindrical disc-annulus topology: displacement at the center of the disc (P1) and along the annulus (P2-P5).

Further insight into the deformation behavior is provided by the displacement profiles shown in Figure 4.8, extracted along representative in-plane directions as the applied magnetic field is progressively increased.

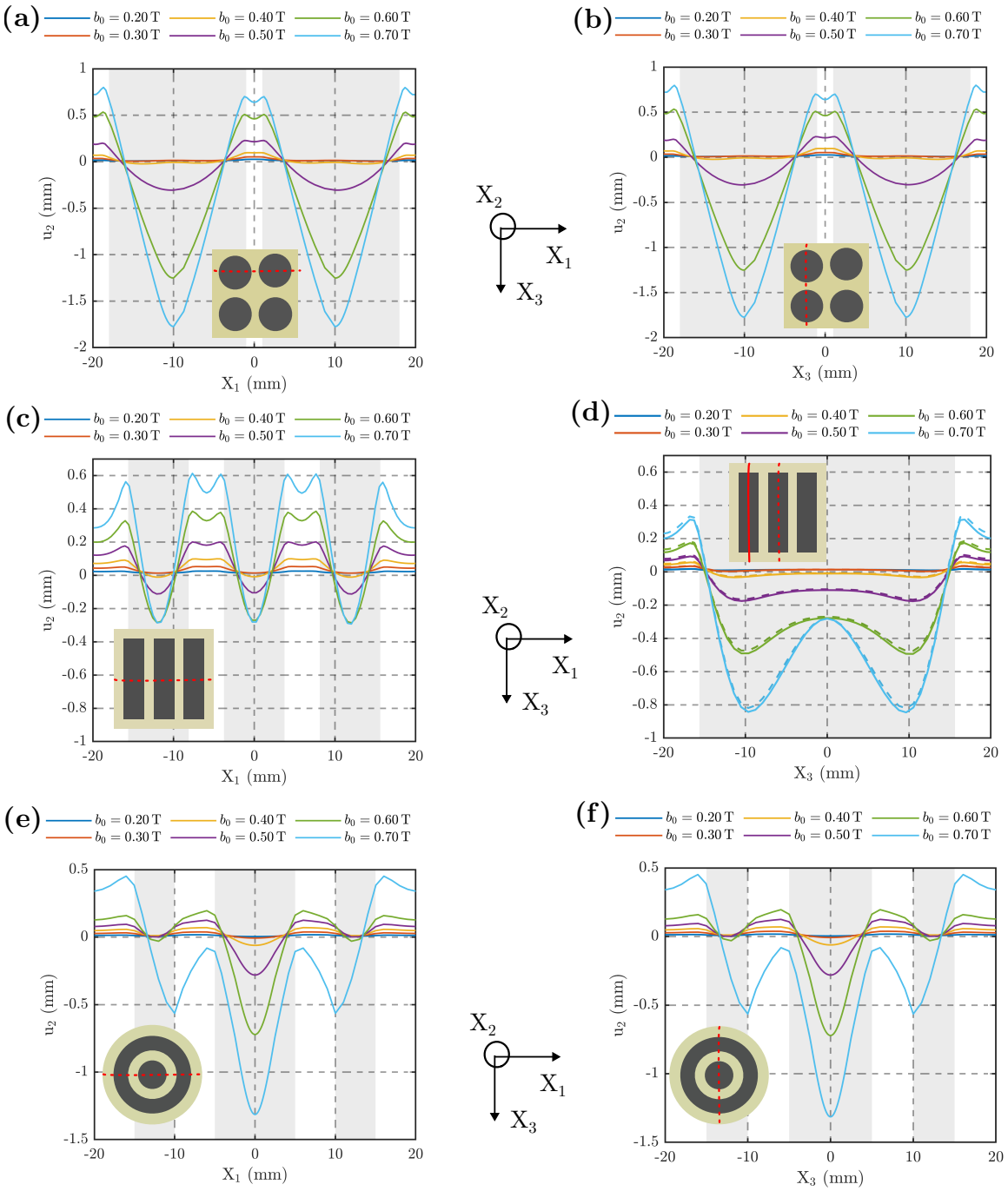


Figure 4.8: Out-of-plane displacement profiles $u_2$ for $h_f = 0.7$ mm extracted along representative in-plane directions for increasing magnetic fields. (a, b) Cubic four-disc topology along $X_1$ and $X_3$. (c, d) Cubic three-strip topology along $X_1$ and $X_3$ (solid lines denote measurements taken along the left-most strip, while dashed lines denote measurements taken along the central strip). (e, f) Cylindrical disc-annulus topology along $X_1$ and $X_3$.

As in the thicker-film regime, the profiles indicate that the specimen edges tend to move upward at high magnetic fields due to the reduced mechanical constraint near the free lateral boundaries. For the cubic four-disc topology (Figure 4.8a,b), the displacement profiles remain symmetric along both the $X_1$ and $X_3$ directions, reflecting the confined and nearly axisymmetric dip-like deformation of each disc, with no clear wrinkle pattern developing between neighboring domains. In the cubic three-strip topology, the $X_1$ profiles (Figure 4.8c) show periodic downward

deformation aligned with the strip locations, while the $X_3$ profiles (Figure 4.8d) reveal a clear wrinkling-type pattern developing along the strip length at high magnetic fields, indicating the onset of a wrinkle instability. In these $X_3$ profiles, solid lines correspond to measurements taken along the left-most strip, whereas dashed lines denote measurements taken along the central strip. Compared to the thicker-film case ($h_f = 1.8$ mm), both the lateral and central strips deform in a similar manner for $h_f = 0.7$ mm, reflecting the absence of significant interaction between neighboring magnetic domains and a deformation response that remains strongly localized. For the cylindrical disc-annulus topology (Figure 4.8e,f), the displacement profiles remain symmetric, following the underlying axisymmetry of the magnetic layout. At higher fields, the response shows the onset of a circumferentially-modulated surface shape localized within the slender annular region. Overall, for all topologies at this reduced film thickness ($h_f = 0.7$ mm), no significant interaction between distinct magneto-active domains is observed within the magnetic field range studied, and the deformation remains strongly localized to the magnetic regions and their immediate surroundings. This reduced interaction explains why none of the topologies exhibit a clear specimen-scale global deformation mode in this regime. In all cases, an initial downward dip is observed at low magnetic fields, while wrinkling-type features become clearly identifiable only at higher magnetic fields for slender geometries, typically around $b_0 \approx 0.65$ T.

To characterize the circumferential wrinkle pattern in the cylindrical disc-annulus topology, Figure 4.9 reports $u_2$ along a circular path located within the annular magnetic region. The sampling curve is parameterized by the arc length $s = R\theta$, where $R$ denotes the radius of the chosen circular path and $\theta$ is the polar angle measured around the cylinder axis. The extracted profiles reveal that, at lower fields, the displacement remains nearly uniform along the circumference, consistent with a primarily dip-like response. As the field approaches $b_0 \approx 0.65$ T, a clear periodic modulation develops and grows in amplitude, indicating the onset of a wrinkling-type instability along the annulus. The resulting wave pattern is well-defined and remains essentially axisymmetric, with the waves organized along the circumference. The wavelength selection and amplitude evolution of these waves are analyzed in more detail in subsection 4.2.1.

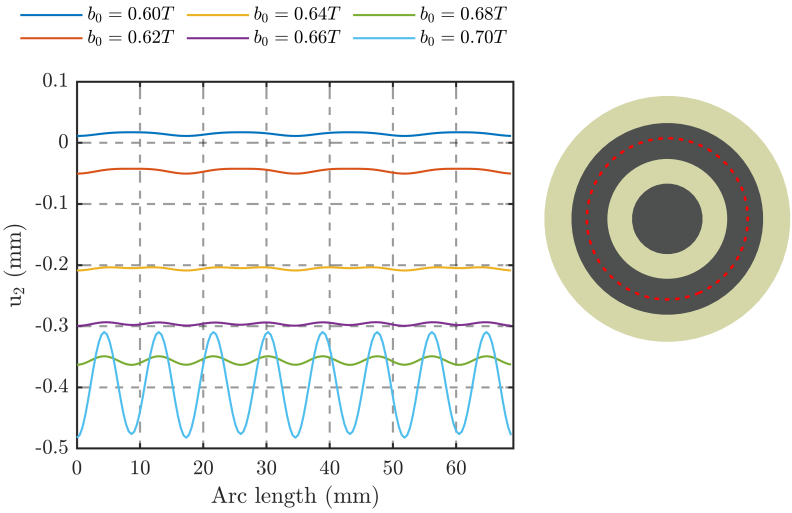


Figure 4.9: Circumferential out-of-plane displacement $u_2$ along a circular path within the annular magnetic region (red dashed circle), plotted versus arc length for increasing magnetic fields.

Finally, the numerical Eulerian magnetic field and magnetization contours at $b_0 = 0.7$ T, reported in Figure E.2, show that the main magnetic response is still controlled by the vertical components $b_2$ and $m_2$, that are fairly uniform inside the magneto-active regions. In contrast, the in-plane components $b_1$, $b_3$, $m_1$, and $m_3$ are strongly focused near the strip edges, disc boundaries, and the inner and outer annulus edges. These edge concentrations exhibit strong magnetic field gradients and higher magnetic torques, matching the regions where the curvature in $u_2$ is largest and where wrinkling-type modulations first appear. Overall, the thinner-film regime keeps the same edge-driven magnetic localization as the thicker-film case, but the reduced thickness makes slender topology more important in selecting localized wrinkling instability modes.

### 4.1.4 Experimental assessment of the thin-film regime

To complement the numerical results of subsection 4.1.3, experiments were performed on printed specimens with $h_f = 0.7$ mm for the cubic three-strip and cylindrical disc-annulus topologies. This thinner-film regime is challenging to validate because the deformation remains highly localized around the magneto-active features and becomes more sensitive to small geometric/material imperfections (printing variability, thickness non-uniformity, local particle distribution). This study aims to examine to which extent the numerical model captures the experimental response in this thin-film regime, focusing on the instability onset and the associated deformation mode.

Figure 4.10a compares the measured out-of-plane displacement $u_2$ as a function of the applied magnetic field $b_0$ for the cubic three-strip topology. The experimental points are extracted at the centers of the three strips (P1-P3), while the numerical curve is plotted for the center of the middle strip (P2). The numerical model is able to predict the experimental instability onset, whereas discrepancies in the post-bifurcation response are attributed to the strong imperfection sensitivity of the thin-film regime.

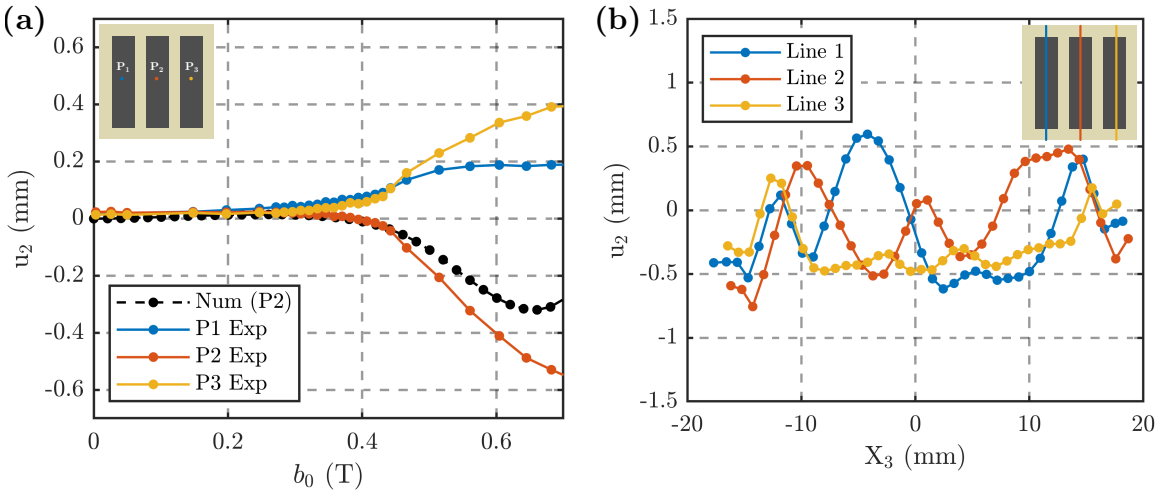


Figure 4.10: Thin-film experimental assessment for the cubic three-strip topology ($h_f = 0.7$ mm). (a) Out-of-plane displacement $u_2$ as a function of the applied magnetic field $b_0$: experiments at the strip centers (P1-P3) compared to the numerical response at the center of the middle strip (P2). (b) Out-of-plane displacement profiles $u_2(X_3)$ extracted along three lines located at the strip centers.

The deformation mode of the instability is further studied by the displacement profiles in Figure 4.10b, where $u_2$ is plotted along the longitudinal direction $X_3$ for three representative lines located at the strip centers. The profiles show the development of wrinkling-type undulations along the slender magnetic regions. The corresponding contour comparison in Figure 4.11 (shown here at $b_0 = 0.7$ T) confirms that the numerical results are able to capture the same qualitative deformation mode as the experiments, where we see localized deformations aligned with the strips, together with a periodic modulation along the strip length.

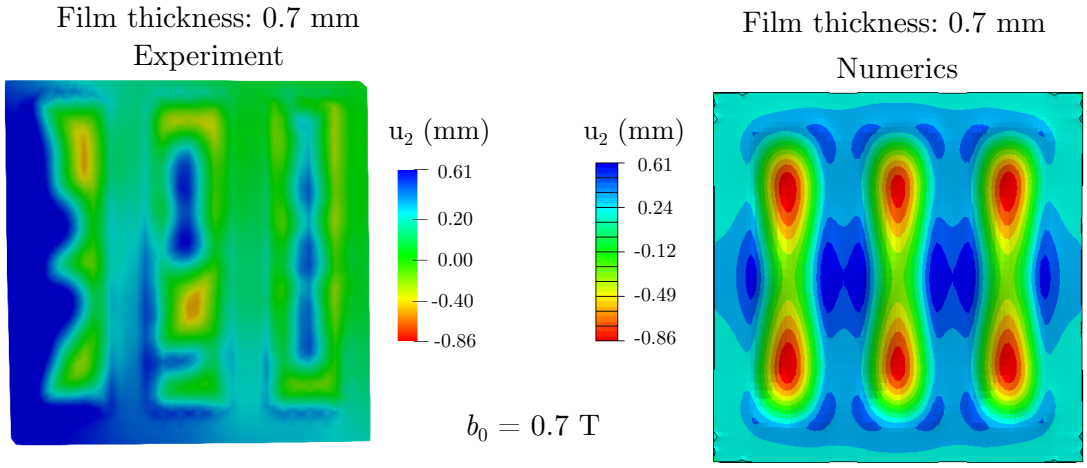


Figure 4.11: Out-of-plane displacement contours $u_2$ for the cubic three-strip topology at $h_f = 0.7$ mm for $b_0 = 0.7$ T: experiment (left) versus corresponding numerical prediction (right).

For the cylindrical annulus-disc topology, Figure 4.12 compares the out-of-plane displacement $u_2$ versus applied magnetic field $b_0$ extracted at the disc center (P1) and at four locations distributed along the annulus (P2-P5), as indicated in the inset.

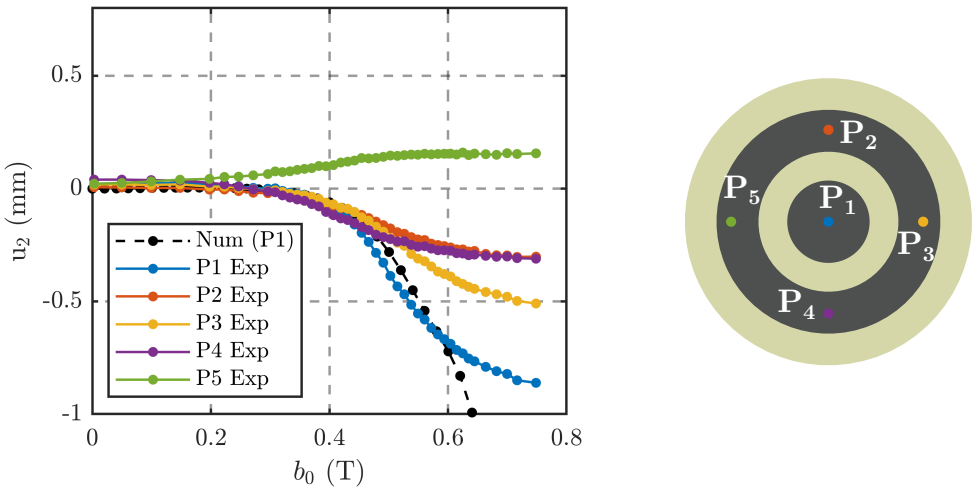


Figure 4.12: Thin-film experimental assessment for the cylindrical disc-annulus topology ($h_f = 0.7$ mm). Out-of-plane displacement $u_2$ as a function of the applied magnetic field $b_0$ measured at the disc center (P1) and at four locations on the annulus (P2-P5), compared to the numerical response extracted at the disc center. The inset shows the locations of the experimental points.

The experiment shows that the dominant deformation is concentrated at the central disc (pronounced downward deformation after the onset), whereas the annulus points remain noticeably

smaller in magnitude over the same field range, with one location showing a slight upward drift due to an upward undulation. The numerical curve measured at the disc center is able to capture both the response of the central disc and the onset of the instability, as well as the comparatively weaker deformation observed in the annular region, which destabilizes more slowly through surface undulations.

This qualitative agreement is directly evident in the contour comparison shown in Figure 4.13 plotted for $b_0 = 0.7$ T. The experiment exhibits a central downward deformation together with a circumferentially-modulated pattern in the annular region, consistent with the numerical prediction.

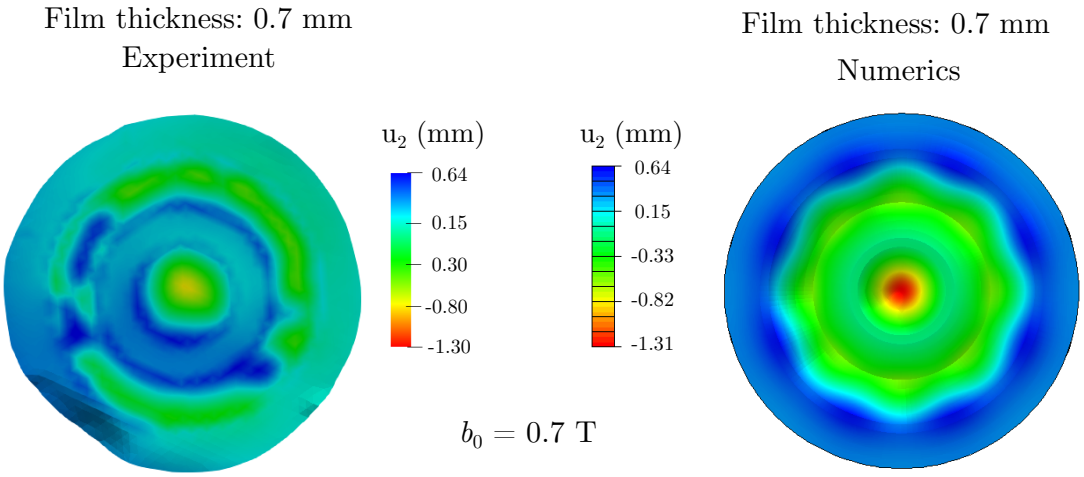


Figure 4.13: Out-of-plane displacement contours $u_2$ for the cylindrical disc-annulus topology at $h_f = 0.7$ mm for $b_0 = 0.7$ T: experiment (left) versus corresponding numerical prediction (right).

Overall, these thin-specimen experiments show that the numerical model is able to predict the instability mechanisms observed for the printed $h_f = 0.7$ mm configurations, namely a localized dip-like response at low fields followed by the formation of wrinkling-type modulations in slender topologies (strips and annulus) at higher fields, while post-bifurcation deformation amplitudes have variations due to the imperfection sensitivity.

## 4.2 Effect of geometrical parameters

### 4.2.1 Further insight into the effect of thickness

In the previous section, the influence of topology on magneto-mechanical instabilities was examined separately for thick and thin film regimes. Here, the role of film thickness is investigated more systematically by comparing the response of each topology across different thicknesses, while keeping all other parameters fixed. This approach directly helps to study the evolution of instability modes with film thickness. In the following, three main representative thicknesses, $h_f = 0.7$, 1.2 and 1.8 mm, are considered. These values are selected to provide an even distribution across the thickness range investigated and correspond to the practical print heights of single-, double- and triple-layer films.

Figure 4.14 compares the evolution of the out-of-plane displacement $u_2$ as a function of the applied magnetic field $b_0$ for the cubic four-disc topology at different film thicknesses. As the film thickness increases from $h_f = 0.7$ to 1.8 mm, the critical magnetic field associated with the onset of instability decreases. This trend is primarily attributed to the increased volume of magnetic particles in thicker films, which leads to a stronger magneto-mechanical coupling for a given applied field. For the thicknesses $h_f = 0.7$ and 1.2 mm, the response is dominated by a dip-like instability mode, characterized by a monotonic increase in downward displacement at the disc centers. In this regime, interactions between neighboring magnetic domains remain weak, and the deformation stays localized within each disc, consistent with the observations reported in subsection 4.1.3. In contrast, for the thickest film ($h_f = 1.8$ mm), the displacement curve exhibits a clear change in slope beyond a critical field, indicating a transition from a localized dip-like response to a more global deformation mode. This behavior reflects the increasing interaction between neighboring discs, which promotes long-wavelength, specimen-scale deformation, as discussed in subsection 4.1.2. To further assess the role of geometric slenderness, an additional simulation is performed for the cubic four-disc topology with a reduced film thickness of $h_f = 0.4$ mm, also shown in Figure 4.14. Although the magnetic domains remain confined, the increased slenderness of the discs relative to film thickness allows the development of a weak undulation pattern at higher fields. This behavior is evident in the observation of a positive out-of-plane displacement at large fields, indicating the formation of an undulated surface.

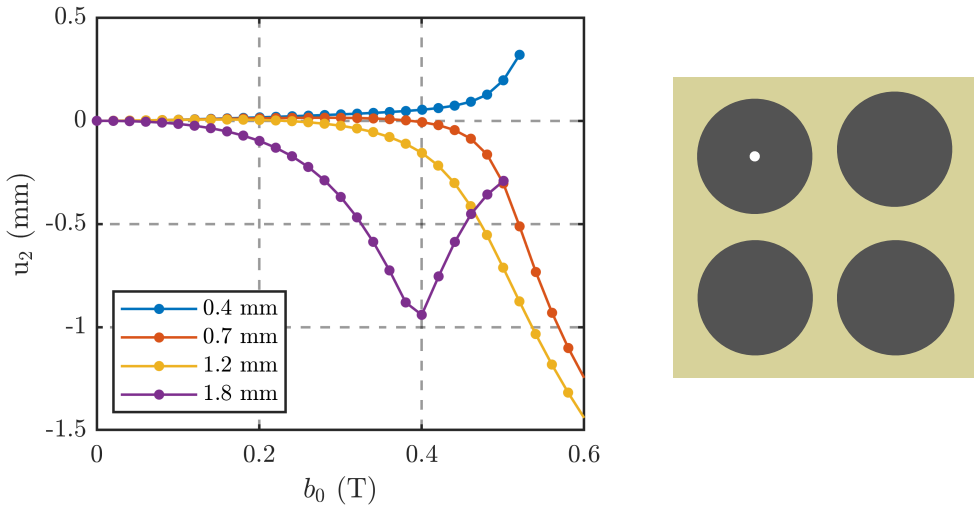


Figure 4.14: Out-of-plane displacement $u_2$ as a function of the applied magnetic field $b_0$ for the cubic four-disc topology at different film thicknesses measured at the point marked in the inset.

These thickness-dependent deformation modes are clearly reflected in the out-of-plane displacement contours shown in Figure 4.15, evaluated at $b_0 = 0.5$ T. For $h_f = 0.7$ and 1.2 mm, the deformation remains localized and dip-like, with downward displacement concentrated at the disc centers and minimal interaction between neighboring domains. For $h_f = 1.8$ mm, the contours show a global deformation across the entire solid surface, consistent with the emergence of a global mode driven by disc interactions. In contrast, for the thinnest film ($h_f = 0.4$ mm), the contours show the onset of a weak undulated surface profile despite the confined disc geometry.

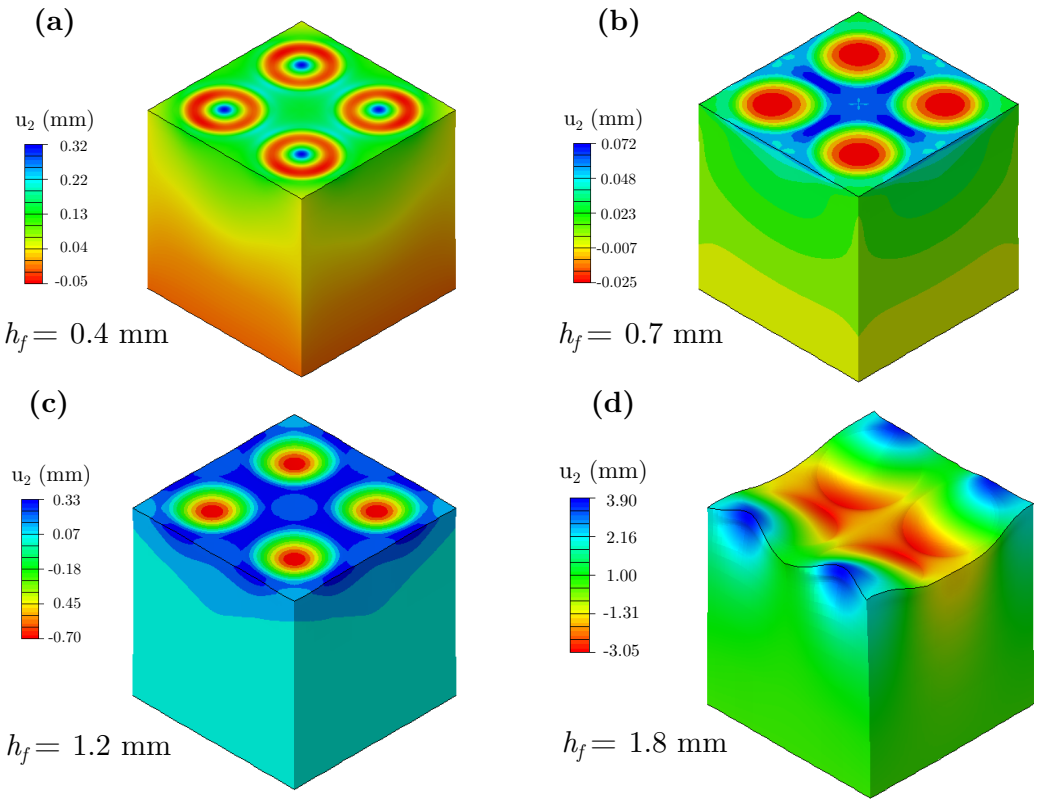


Figure 4.15: Three-dimensional out-of-plane displacement contours $u_2$ for the cubic four-disc topology evaluated at $b_0 = 0.5$ T, for a film thickness of (a) 0.4 mm, (b) 0.7 mm, (c) 1.2 mm and (d) 1.8 mm.

The corresponding in-plane displacement profiles extracted along the $X_1$ and $X_3$ directions at $b_0 = 0.5$ T are shown in Figure 4.16.

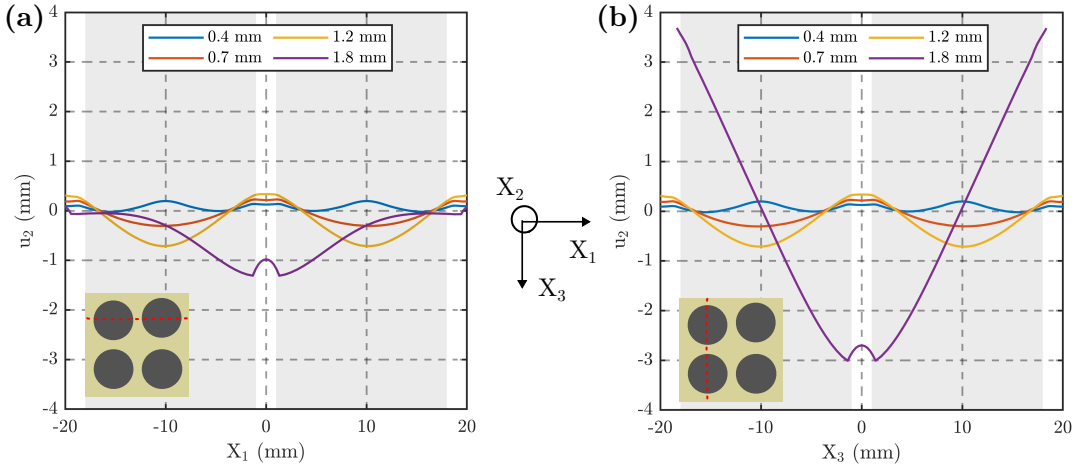


Figure 4.16: Out-of-plane displacement profiles $u_2$ extracted along the (a) $X_1$ and (b) $X_3$ directions for the cubic four-disc topology at different film thicknesses, evaluated at $b_0 = 0.5$ T.

For $h_f = 0.7$ and 1.2 mm, the profiles confirm a purely dip-like instability, with symmetric downward deformation localized at the disc positions and no evidence of periodic modulation between domains. For $h_f = 1.8$ mm, the profiles clearly capture the transition from local to global deformation, characterized by long-wavelength variations spanning the specimen width. By contrast, for the thinnest film ($h_f = 0.4$ mm), the profiles clearly show the development of

a weak wrinkling-type undulation at the center of the MRE domains. This result demonstrates that, even within a confined disc geometry, wrinkling-type deformations can emerge when the magnetic domains are sufficiently slender relative to the film thickness. Compared to the $h_f = 0.7$ and 1.2 mm cases, where the response remains purely dip-like, the $h_f = 0.4$ mm film exhibits surface undulations, highlighting the combined influence of domain geometry and film thickness on instability mode selection.

Next, the effect of film thickness on the instability behavior of the cubic three-strip topology is examined. The evolution of the out-of-plane displacement $u_2$ as a function of the applied magnetic field $b_0$ is shown in Figure 4.17. Owing to the geometric symmetry of the configuration, the displacement is extracted at the centers of the first and second strips. For the thinner films ($h_f = 0.7$ and 1.2 mm), the critical magnetic field associated with the onset of instability remains relatively close, reflecting the slender nature of the strip geometry, which promotes similar local destabilization mechanisms. For $h_f = 0.7$ mm, the response remains predominantly local, and a change in the slope is seen, showing the formation of small wrinkling undulation at the centre of the strip. For $h_f = 1.2$ mm, a change in the slope of the $u_2$–$b_0$ curve becomes apparent at higher magnetic fields, indicating the onset of interaction between neighboring strips. This interaction occurs at a higher critical field than in the thickest film, where the reduced thickness results in greater substrate confinement. For the thickest film ($h_f = 1.8$ mm), strip interaction and the associated transition toward a global deformation mode occur at a significantly lower magnetic field, around $b_0 \approx 0.36$ T, whereas for $h_f = 1.2$ mm this transition is delayed to approximately $b_0 \approx 0.54$ T. These observations confirm that reducing the film thickness shifts the local-to-global mode transition to higher magnetic fields, while the strip topology continues to promote interaction between magnetic domains once a sufficient loading level is reached.

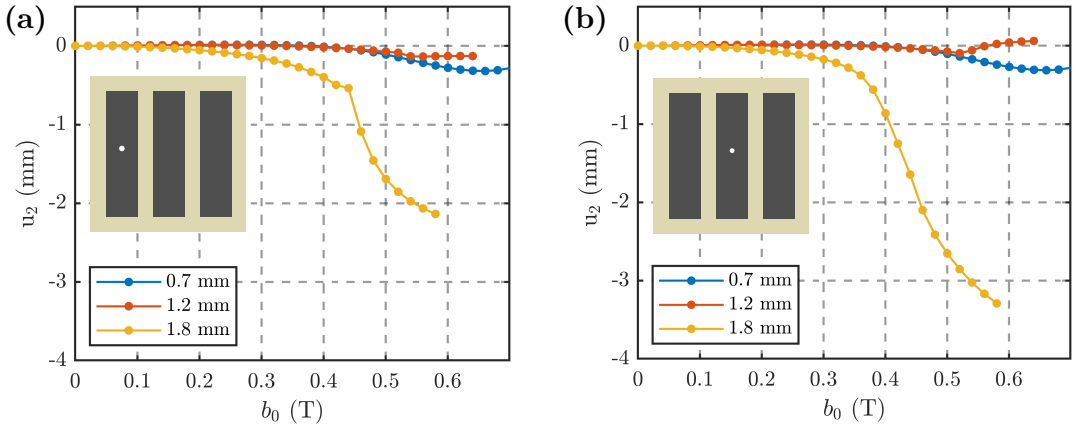


Figure 4.17: Out-of-plane displacement $u_2$ as a function of the applied magnetic field $b_0$ for the cubic three-strip topology at different film thicknesses. The displacement is measured at the centers of the (a) first and (b) second strips.

These thickness-dependent trends are clearly reflected in the three-dimensional out-of-plane displacement contours shown in Figure 4.18, evaluated at $b_0 = 0.58$ T. For $h_f = 0.7$ mm, the deformation remains localized within each strip, with a small undulation visible at the center of the strips. For $h_f = 1.2$ mm, the contours reveal the onset of interaction between the strips, accompanied by a partial reorganization of the surface deformation toward a specimen-scale

response. For the thickest film ($h_f = 1.8$ mm), the deformation clearly transitions to a global mode, with pronounced long-wavelength features spanning the entire specimen width.

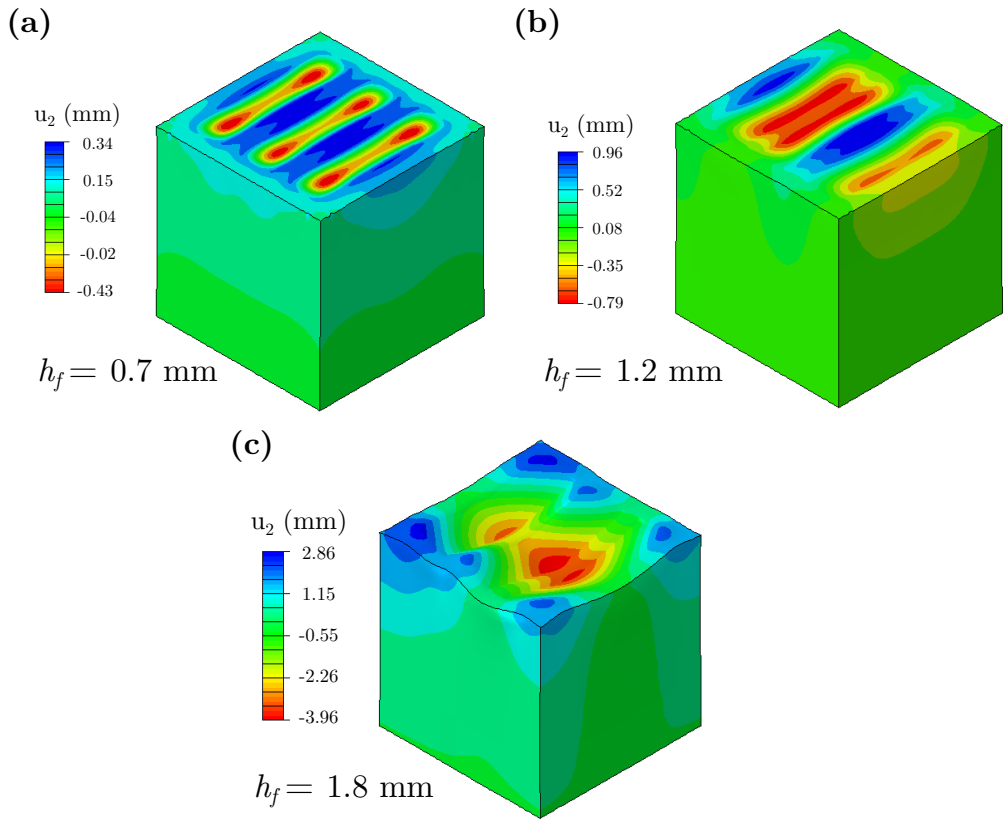


Figure 4.18: Three-dimensional out-of-plane displacement contours $u_2$ for the cubic three-strip topology evaluated at $b_0 = 0.58$ T, for a film thickness of (a) 0.7 mm, (b) 1.2 mm and (c) 1.8 mm.

Further insight into the thickness-controlled transition from local to global deformation modes is provided by the displacement profiles extracted along the $X_1$ and $X_3$ directions, shown in Figure 4.19. Along the $X_1$ direction, the profiles for $h_f = 0.7$ mm display localized downward dips aligned with the positions of the MRE strips, consistent with a purely local response. In contrast, for $h_f = 1.2$ and 1.8 mm, the profiles progressively evolve toward global deformation shapes. In particular, the $h_f = 1.2$ mm film exhibits a half-wavelength modulation across the specimen width, indicating an intermediate regime between local and global behavior, whereas the $h_f = 1.8$ mm film develops a fully global buckling mode spanning the entire width. Along the $X_3$ direction, the $h_f = 0.7$ mm profiles remain weakly modulated and localized, while increasing the film thickness leads to a pronounced amplification of long-wavelength deformation, with the thickest film clearly exhibiting a specimen-scale mode. In these profiles, solid lines denote measurements taken along the left-most strip, whereas dashed lines correspond to measurements taken along the central strip. As the film thickness increases, the responses of the different strips become increasingly different, indicating a growing interaction between neighboring magnetic domains. Together, these results demonstrate that, for the cubic three-strip topology, increasing the film thickness promotes earlier interaction between magnetic domains and facilitates the transition from local dip-like instabilities to global deformation modes.

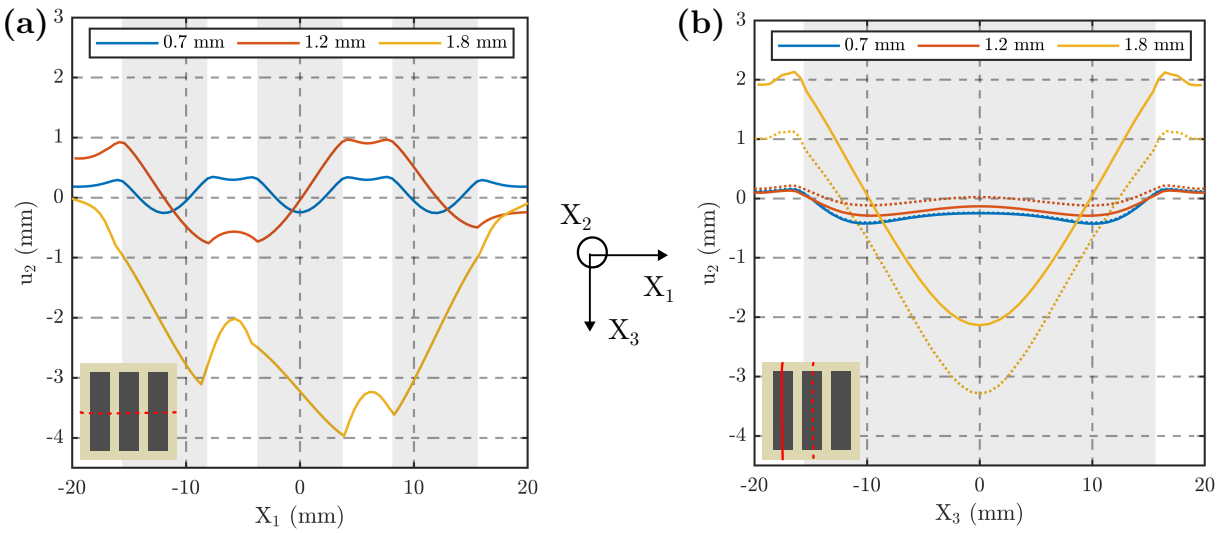


Figure 4.19: Out-of-plane displacement profiles $u_2$ extracted along the (a) $X_1$ and (b) $X_3$ directions for the cubic three-strip topology at different film thicknesses, evaluated at $b_0 = 0.58$ T (solid lines denote measurements taken along the left-most strip, while dashed lines denote measurements taken along the central strip for the $X_3$ measurement).

Finally, the influence of film thickness on the instability behavior of the cylindrical disc-annulus topology is studied. Figure 4.20 shows the evolution of the out-of-plane displacement $u_2$ as a function of the applied magnetic field $b_0$. The displacement is extracted at the center of the circular disc and at a point on the annular region, as shown in the inset illustration.

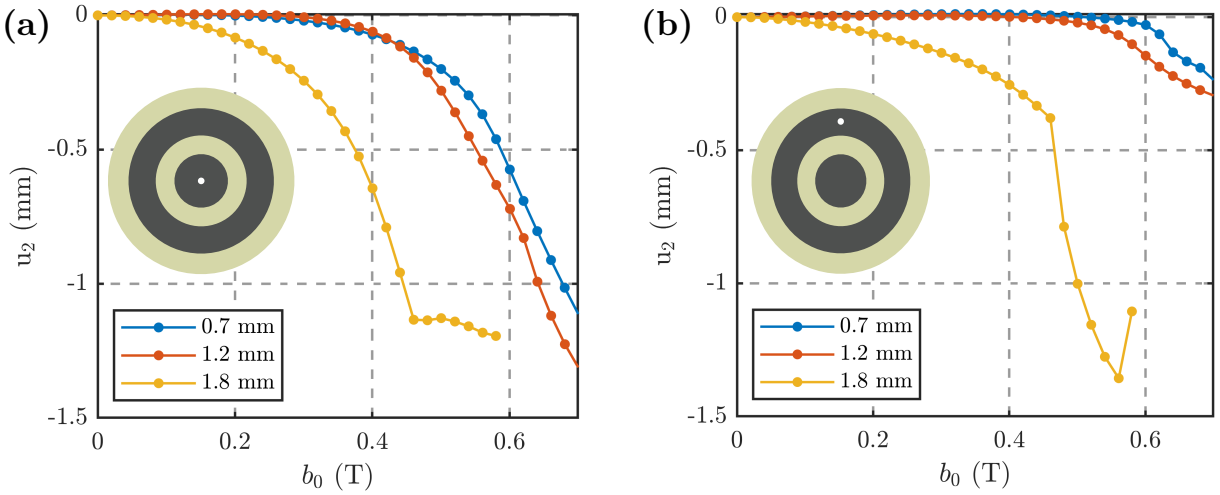


Figure 4.20: Out-of-plane displacement $u_2$ as a function of the applied magnetic field $b_0$ for the cylindrical disc-annulus topology at different film thicknesses. The displacement is measured (a) at the center of the disc and (b) at the marked point on the annular region.

For all thicknesses, the central disc destabilizes first, with an increased downward displacement at relatively low magnetic fields. This behavior reflects the ability of the circular disc to deform easily due to its geometric symmetry, as discussed in subsection 4.1.2. For the thinner film ($h_f = 0.7$ mm), the response remains predominantly local over a wide range of magnetic fields. After an initial dip-like deformation of the disc, the annular region remains weakly deformed, and only at higher fields does the response progressively transition toward a wrinkling-type deformation of the annulus. This transition is associated with the development of circumferential

undulations, consistent with the thin-film behavior described in subsection 4.1.3. For the intermediate thickness ($h_f$ = 1.2 mm), a similar dip-dominated response is observed, with the annular region largely following the deformation of the disc and no pronounced global mode developing within the field range considered. In contrast, for the thickest film ($h_f$ = 1.8 mm), the displacement curves reveal a clear transition from a localized response to a global deformation mode at higher magnetic fields. In this case, the interaction between the disc and the annular region becomes significantly stronger, leading to a deformation of the entire specimen. This local-to-global mode transition mirrors the behavior observed for other topologies in the thick-film regime and highlights the role of increased thickness in promoting long-range interaction between magnetic domains.

These thickness-dependent trends are clearly illustrated by the three-dimensional out-of-plane displacement contours shown in Figure 4.21. For the thinner and intermediate films ($h_f$ = 0.7 and 1.2 mm), the contours are evaluated at $b_0$ = 0.7 T and reveal the formation of circumferential wrinkling undulations localized along the annular region, while the central disc remains predominantly dip-like. For $h_f$ = 1.2 mm, the deformation remains largely localized, with a smooth, axisymmetric displacement profile and no clear global reorganization of the surface. In contrast, for the thickest film ($h_f$ = 1.8 mm), the contours are shown at a lower magnetic field of $b_0$ = 0.5 T and already exhibit a pronounced redistribution of deformation across the surface, with a clear departure from axisymmetry. This behavior is consistent with the emergence of a global deformation mode driven by strong interactions between the disc and the annular region.

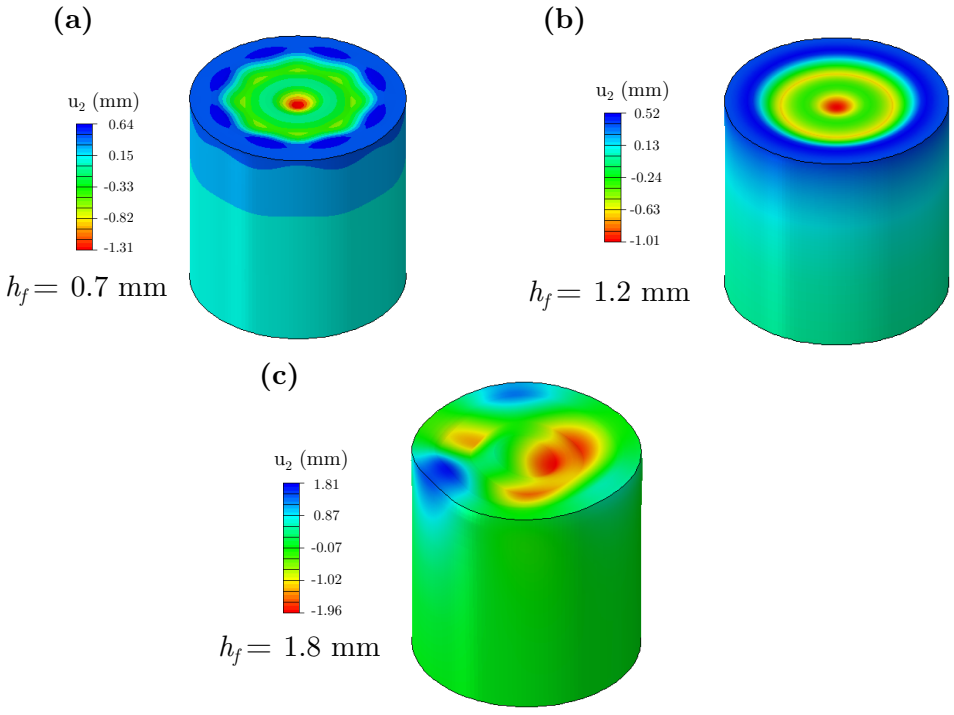


Figure 4.21: Three-dimensional out-of-plane displacement contours $u_2$ for the cylindrical disc-annulus topology. Results for (a) $h_f$ = 0.7 mm and (b) 1.2 mm are shown at $b_0$ = 0.7 T, while results for (c) $h_f$ = 1.8 mm are shown at $b_0$ = 0.5 T.

Further insight into the spatial organization of the deformation is obtained from the displacement profiles extracted along $X_1$ and $X_3$, as shown in Figure 4.22a-b. For $h_f = 0.7$ and 1.2 mm, the profiles are evaluated at $b_0 = 0.7$ T and remain nearly symmetric along both directions, reflecting the axisymmetric nature of the deformation under the dominance of local dip-like or circumferential wrinkling responses. In these cases, no clear symmetry breaking is observed, and the deformation remains confined to the magnetic regions. For $h_f = 1.8$ mm, the profiles are shown at $b_0 = 0.5$ T and clearly reveal symmetry breaking associated with the transition from a local to a global deformation mode. The displacement profiles exhibit long-wavelength variations spanning the specimen, indicating the onset of a specimen-scale buckling response that couples the disc and annular regions. In addition, Figure 4.22c presents the circumferential variation of $u_2$ extracted along the arc length of the annular region. For $h_f = 0.7$ and 1.2 mm, the profiles are evaluated at $b_0 = 0.7$ T. A well-defined periodic modulation is observed for $h_f = 0.7$ mm, confirming the presence of circumferential wrinkling, whereas for $h_f = 1.2$ mm the response remains nearly uniform along the circumference, consistent with a predominantly dip-like deformation of the annulus. For $h_f = 1.8$ mm, the circumferential profile shown at $b_0 = 0.5$ T departs from a simple periodic pattern, reflecting the influence of global buckling.

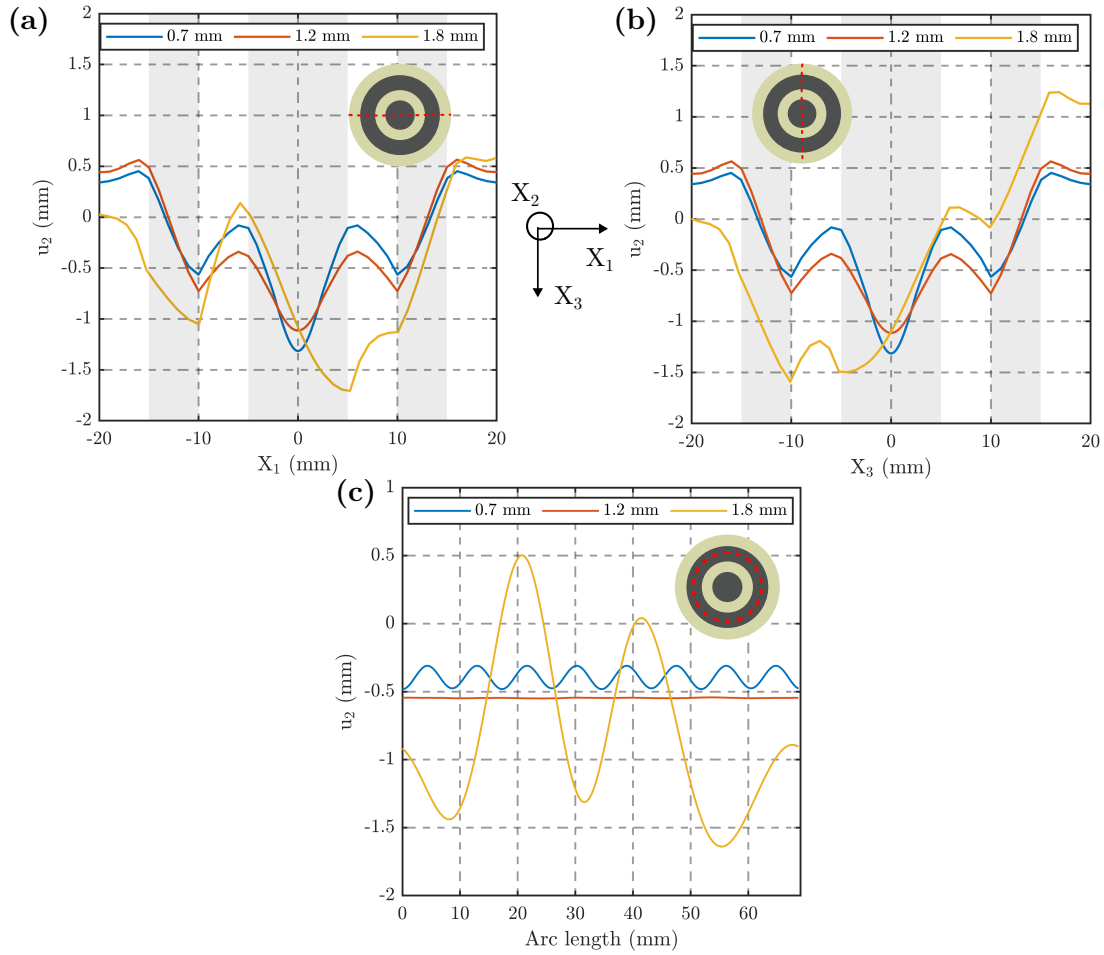


Figure 4.22: Out-of-plane displacement profiles $u_2$ for the cylindrical disc-annulus topology at different film thicknesses. (a, b) Profiles extracted along the $X_1$ and $X_3$ directions, respectively. (c) Circumferential displacement $u_2$ plotted along the arc length of the annular region. Results for $h_f = 0.7$ and 1.2 mm are evaluated at $b_0 = 0.7$ T, whereas results for $h_f = 1.8$ mm are evaluated at $b_0 = 0.5$ T.

### 4.2.2 Effect of pattern footprint: annulus width for the cylindrical sample

In this subsection, the influence of the magnetic pattern footprint is investigated by varying the outer width of the annular MRE region in the cylindrical disc-annulus topology. The annulus width is increased from 5 to 9 mm, while all other geometric, material and loading parameters are kept fixed. This study is carried out for two film thicknesses, $h_f = 1.2$ and 0.7 mm, in order to highlight the coupled effects of topology and thickness on the instability behavior.

The effect of annulus width for the intermediate thickness $h_f = 1.2$ mm is first examined through the evolution of the out-of-plane displacement $u_2$ as a function of the applied magnetic field $b_0$, shown in Figure 4.23. The displacement is extracted at the center of the circular disc (P1) and at a representative location along the annular region (P2).

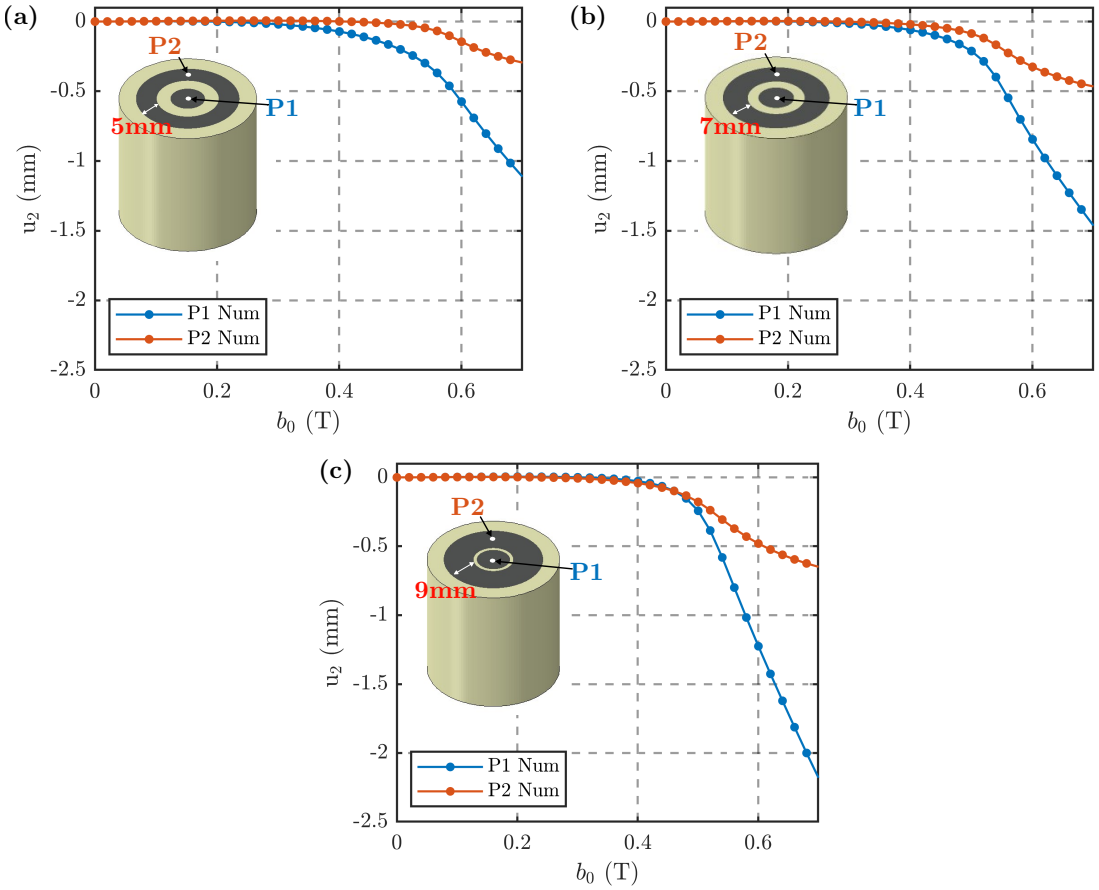


Figure 4.23: Out-of-plane displacement $u_2$ as a function of the applied magnetic field $b_0$ for the cylindrical disc-annulus topology at $h_f = 1.2$ mm. Results are shown for different annulus widths: (a) $w = 5$ mm, (b) $w = 7$ mm, and (c) $w = 9$ mm.

For all annulus widths considered, the response is dominated by a global dip-like deformation, with no clear wrinkling-type modulation developing in this thickness regime. As the annulus width increases from 5 to 9 mm, two main trends are observed. First, the delay between the destabilization of the central disc and that of the annular region progressively decreases. This indicates an enhanced interaction between the disc and the annulus, as the larger annular footprint increases the magnetic coupling between these two regions. Second, the downward displacement at the center of the disc evolves more rapidly with increasing magnetic field. This

behavior can be attributed to the increased magnetic area of the annular region, which promotes a stronger global deformation response.

When the film thickness is reduced to $h_f = 0.7$ mm, the influence of the annulus width becomes significantly more pronounced, and the deformation behavior transitions from a purely dip-like response to a wrinkling-dominated regime. This behavior is illustrated in Figure 4.24, where the circumferential variation of $u_2$ is extracted along the annular region, as indicated schematically in the inset. For the smallest annulus width (5 mm), a well-defined circumferential wrinkling pattern is observed, characterized by a relatively high wavenumber with approximately eight undulations around the circumference. As the annulus width is increased to 7 and 9 mm, the number of wrinkles decreases systematically to approximately six and four, respectively. This reduction in wavenumber is accompanied by a corresponding increase in the wrinkle amplitude for a given magnetic field. This trend can be interpreted as increasing the annulus width effectively increases the available length scale over which stresses can reorganize, favoring longer wavelengths and, consequently, a smaller number of wrinkles.

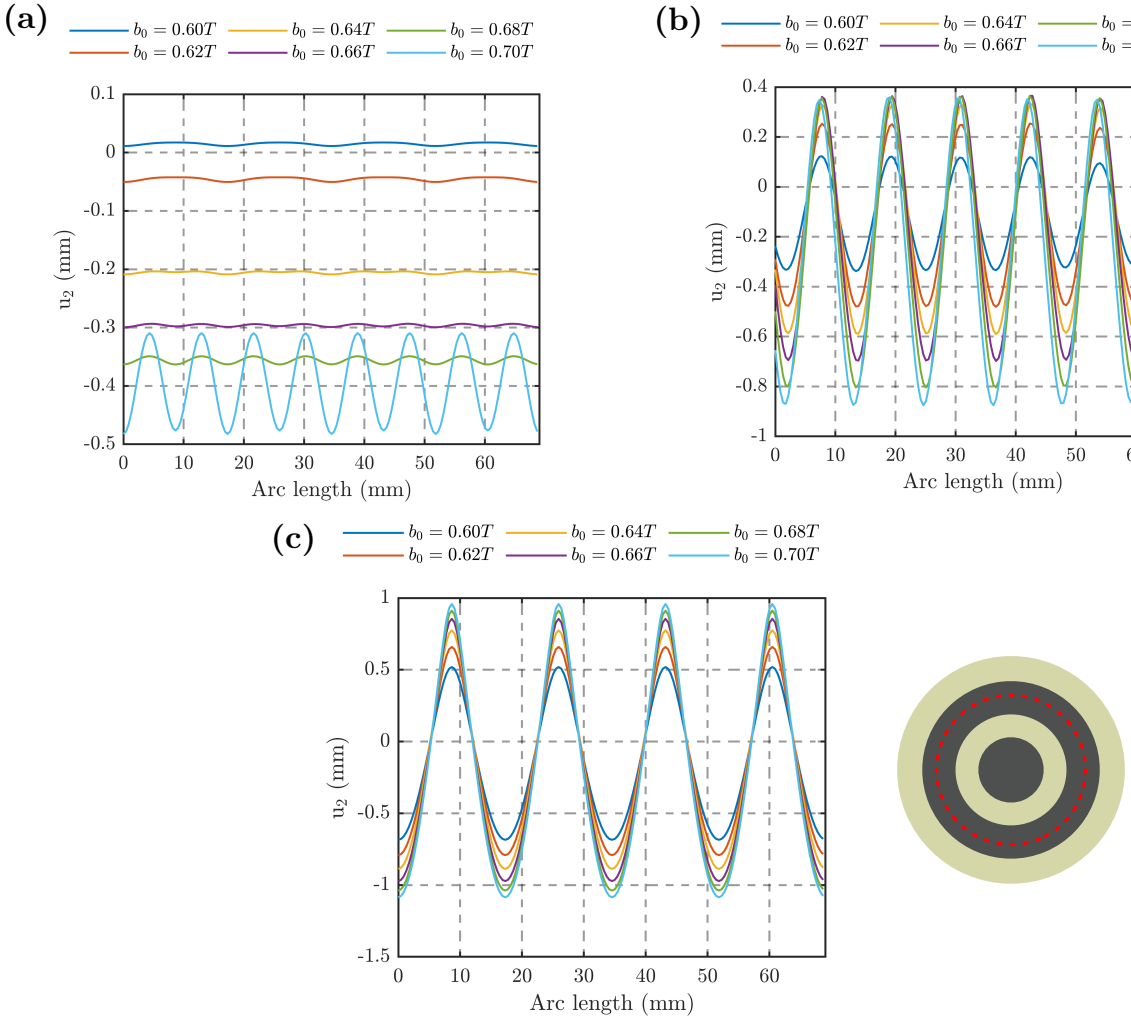


Figure 4.24: Circumferential out-of-plane displacement $u_2$ extracted along the annular region at $h_f = 0.7$ mm for increasing magnetic fields. Results are shown for different annulus widths: (a) $w = 5$ mm, (b) $w = 7$ mm, and (c) $w = 9$ mm. The inset illustrates the extraction path along the annulus.

The footprint-dependent wrinkling behavior shown in the circumferential displacement profiles is illustrated by the three-dimensional out-of-plane displacement contours shown in Figure 4.25. For the narrow annulus (5 mm), the surface deformation exhibits a higher number of closely spaced wrinkles. As the annulus width increases to 7 mm and 9 mm, the wrinkling pattern reorganizes into fewer, more widely spaced undulations with larger amplitudes. These three-dimensional deformation fields provide a direct visualization of how the annular footprint influences both the wavelength and amplitude of the wrinkling response in the thin-film regime.

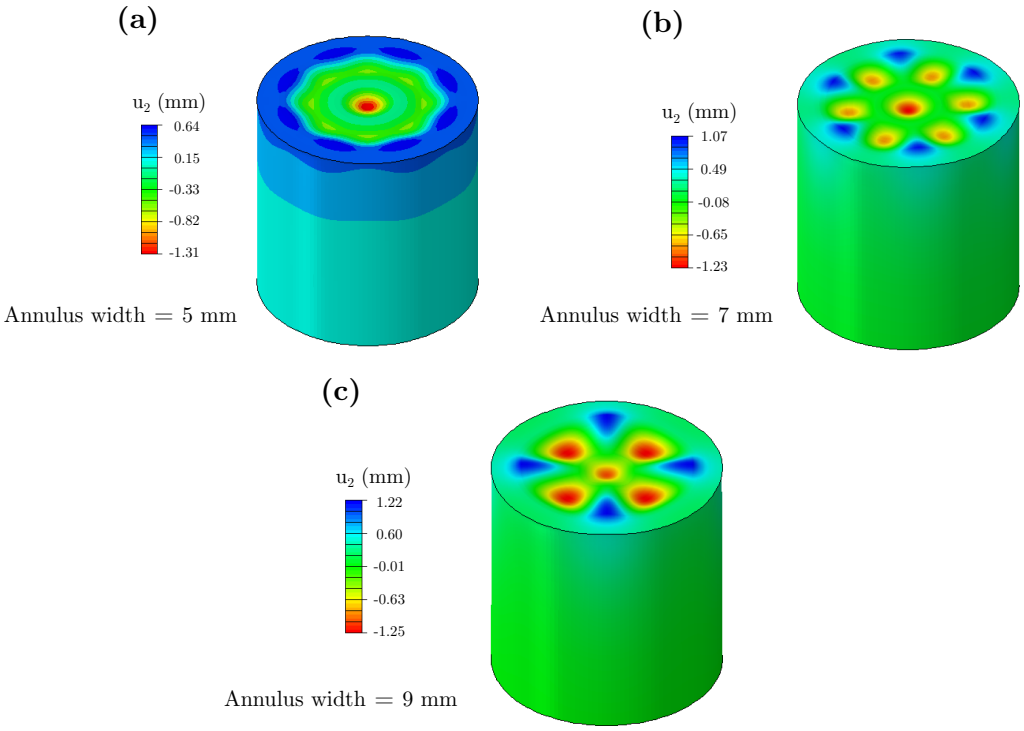


Figure 4.25: Three-dimensional out-of-plane displacement contours $u_2$ for the cylindrical disc-annulus topology for $h_f = 0.7$ mm at 0.7 T. Results are shown for different annulus widths: (a) $w = 5$ mm, (b) $w = 7$ mm, and (c) $w = 9$ mm.

### 4.2.3 Effect of pattern distribution: number of discs for the cubic sample

The results for the cubic four-disc topology in section 3.4 showed that, in thicker films ($h_f = 1.8$ mm), the post-bifurcation deformation changes from a local response to a more global, specimen-scale mode as magnetic interactions develop between nearby magneto-active regions. Here, we build on this by increasing the number of circular MRE inclusions in the cubic specimen to a denser $4 \times 4$ arrangement (sixteen discs), keeping the film thickness fixed at $h_f = 1.8$ mm. This allows us to study the effects of pattern distribution on the emergence and spatial global mode. The numerical study is performed using identical material parameters, boundary conditions and magnetic loadings as in the cubic four-disc topology study. The cubic specimen and the sixteen-disc distribution are shown in Figure 4.26. The overall cube dimensions are $40 \times 40 \times 40$ mm$^3$, and the top surface contains an embedded periodic $4 \times 4$ array of circular magneto-active domains (disc diameter $d = 6$ mm). The disc layout is characterized by a gap of 4 mm between neighboring discs and a clearance to the lateral boundaries of 2 mm.

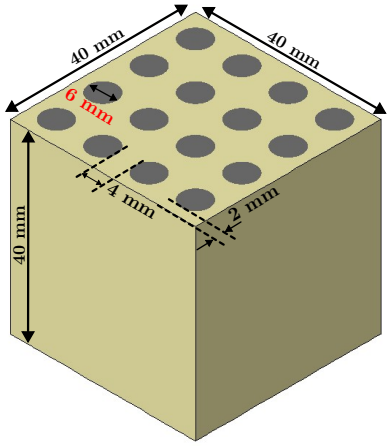


Figure 4.26: Cubic specimen with a $4 \times 4$ distribution of circular MRE domains used to study pattern-distribution effects. The cube has sixteen circular magneto-active domains (disc diameter $d = 6$ mm) with a film thickness of $h_f = 1.8$ mm.

The numerically-predicted three-dimensional out-of-plane displacement fields $u_2$ for the cubic sixteen-disc specimen are shown in Figure 4.27 for two representative magnetic fields. At the moderate field ($b_0 = 0.4$ T), the response remains predominantly local, where each disc exhibits a downward displacement at its center and an upward displacement near its edge, similar to the behavior reported for the cubic four-disc topology at low-to-intermediate fields. In this regime, the deformation is still largely confined to the magneto-active domains. As the magnetic field increases ($b_0 = 0.6$ T in Figure 4.27b), the deformation undergoes a transformation where the disc's deformation is no longer local, and the surface pattern transitions toward a more global response with long-wavelength modulations spanning across multiple inclusions. This is the same physical mechanism observed in the cubic four-disc specimen at higher fields ($b_0 \approx 0.48$ T), where disc-to-disc interactions trigger the emergence of a long-wavelength mode. However, in the cubic sixteen-disc topology, the interaction network is denser, leading to a richer post-bifurcation organization in which groups of discs collectively form larger-scale deformation.

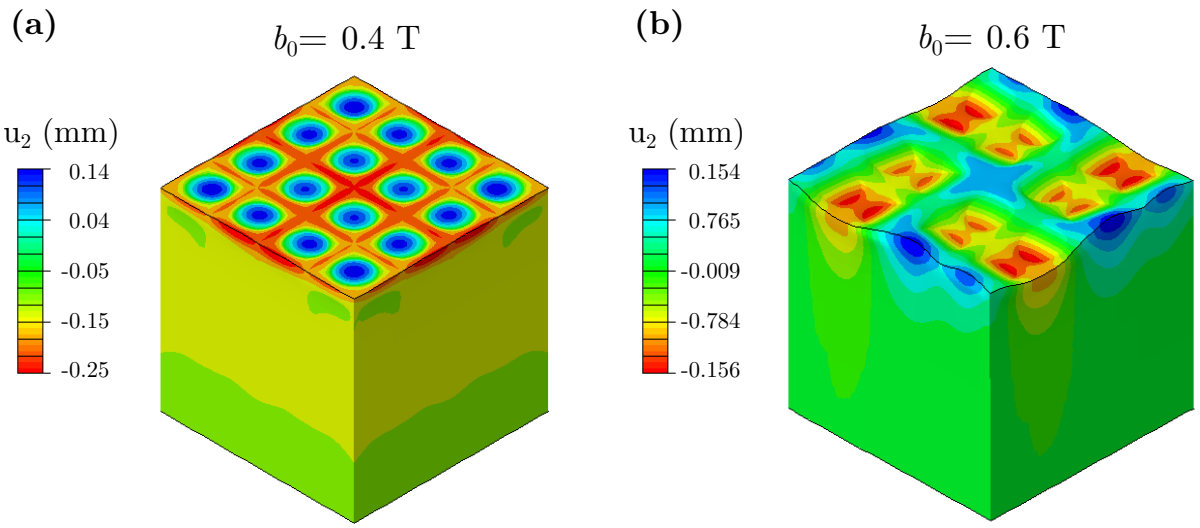


Figure 4.27: Three-dimensional out-of-plane displacement fields $u_2$ for the cubic sixteen-disc topology for $h_f = 1.8$ mm at (a) $b_0 = 0.4$ T and (b) $b_0 = 0.6$ T.

To quantify this transition, the out-of-plane displacement $u_2$ is extracted at the centers of all sixteen discs (P1-P16) and plotted as a function of $b_0$ in Figure 4.28. The global trend is consistent with the cubic four-disc topology, where the displacement evolves smoothly at low fields (smooth bifurcation response due to the imperfection as discussed section 3.4), then exhibits a distinct change in slope and branching behavior as disc-to-disc interactions become dominant. Across all discs (Figure 4.28a), a predominantly downward displacement is observed up to approximately $b_0 \simeq 0.46$ T, after which a sudden change in the curves marks the onset of the global mode formation. Beyond this point, the responses cluster into a small number of similar post-bifurcation branches, indicating that the system does not select a unique deformation amplitude for all discs. Instead, groups of inclusions follow similar branches depending on their positions within the array and their interaction environments.

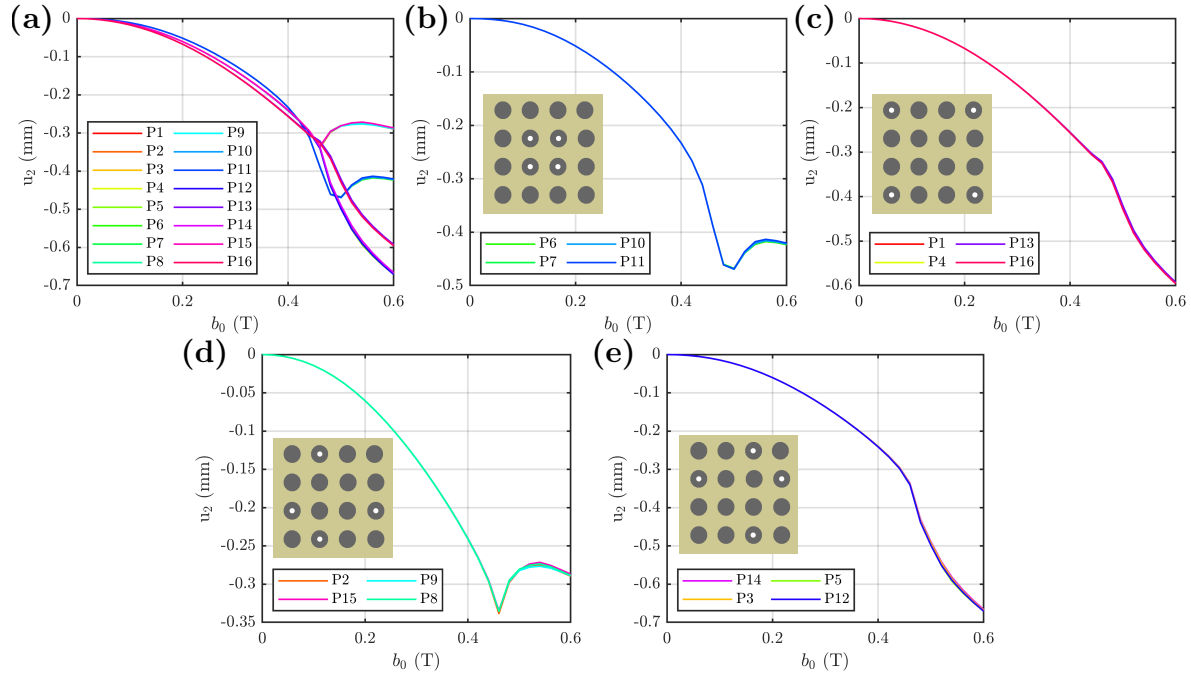


Figure 4.28: Out-of-plane displacement $u_2$ as a function of the applied magnetic field $b_0$ for the cubic sixteen-disc topology at $h_f = 1.8$ mm. Displacements at the centers of (a) all sixteen discs (P1–P16), (b) the four discs located in the middle of the array (central $2 \times 2$ subset), (c) the four corner discs, positioned at the specimen corners and adjacent to two free lateral boundaries, and (d, e) the edge discs, located along the specimen edges between the corner and central regions.

The subplots in Figure 4.28 explain how the spatial structure is associated with these branches. For the central discs forming the middle $2 \times 2$ subset (see inset of Figure 4.28b), the displacement curves exhibit a pronounced post-bifurcation change, which can be attributed to the strong mechanical and magnetic confinement imposed by neighboring discs on all sides. In contrast, the corner discs (Figure 4.28c) display significantly larger downward displacements at high magnetic fields. This enhanced response is due to their proximity to two free lateral boundaries of the specimen, where the reduced mechanical constraint facilitates larger out-of-plane motion and promotes stronger tilting or rotation of the local magnetic domains. The discs located along the edges of the array (Figure 4.28d,e) exhibit intermediate behaviors, reflecting an asymmetric constraint environment characterized by one free boundary and a more confined interior side. As in the cubic four-disc topology, the global mode selection at higher fields corresponds to a regime

where several long-wavelength patterns are nearly energetically equivalent. In such a regime, the post-bifurcation state becomes extremely sensitive to small perturbations, which selects a specific global mode. For the cubic sixteen-disc topology, this selection is expressed as an alternating deformation of neighboring discs rather than all discs dipping uniformly, some discs tilt preferentially along $X_1$ while adjacent ones tilt along $X_3$, consistent with the non-uniform reorganization visible in the 3D displacement fields (Figure 4.27b).

To have better insight into this, additional analysis is obtained from the in-plane displacement profiles shown in Figure 4.29, where $u_2$ is extracted along four representative lines crossing the disc rows/columns (lines 1-4) and along the specimen mid-plane (mid line). The profiles reveal two main features. First, along the individual row/column lines (solid curves), the response is strongly modulated by the local disc sequence, but the modulation is not identical from one line to another. Neighboring lines exhibit different peak/trough arrangements, reflecting the alternating post-bifurcation response discussed above. In particular, within a given row (or column), if one subset of discs tilts predominantly along $X_1$, the neighboring subset tends to tilt along $X_3$, producing out-of-phase extrema between lines. Second, the mid-plane profile (dashed curve) displays a smoother, longer-wavelength wrinkling-like mode that emerges from the combined deformation of multiple rows/columns. The mid-plane response reflects the overall, macroscopic behavior of the specimen, while the deformation remains locally governed by the periodic disc pattern. The alternating tilting of the discs produces a specimen-scale modulation resembling a global wrinkle. Compared to the cubic four-disc topology, in which the long-wavelength modulation spans the specimen in a single dominant organization, the cubic sixteen-disc topology effectively distributes the global mode across multiple interacting local places. In practice, this appears as a quadrantal organization of the deformation, in which a global mode exists at the specimen scale but is assembled from repeated local reorganizations across the denser inclusion network.

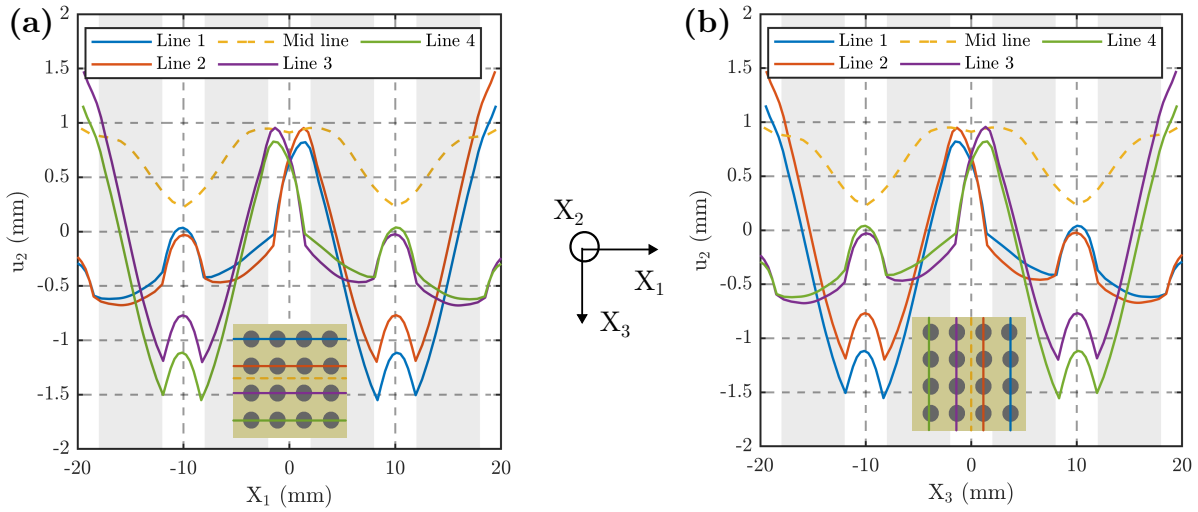


Figure 4.29: Out-of-plane displacement profiles $u_2$ extracted along representative in-plane directions for the cubic sixteen-disc topology. (a) Profiles along $X_1$ across four disc rows (lines 1-4 represented by solid lines) and along the specimen mid-plane (dashed). (b) Corresponding profiles along $X_3$ across four disc columns (lines 1-4 represented by solid lines) and the mid-plane (dashed line).

To study the mechanism governing the interaction of the discs the numerical Eulerian magnetic field and magnetization contours evaluated at $b_0 = 0.6$ T are shown in Figure E.3. As in the case of other topologies, the application of a vertical magnetic field promotes the rotation of the magneto-active domains toward aligning with the applied field, while the surrounding compliant substrate constrains this motion and generates internal magneto-mechanical stresses. The vertical components $b_2$ and $m_2$ dominate the response within each disc and remain relatively uniform over the disc interiors, confirming that the primary magnetic response is aligned with the loading direction. In contrast, the in-plane components $b_1$, $b_3$, $m_1$, and $m_3$ are strongly localized near the disc edges, where sharp magnetic field gradients arise due to geometric discontinuities. For the cubic sixteen-disc topology, owing to the dense disc distribution, these localized magnetic concentrations frequently overlap with neighboring inclusions, leading to enhanced magnetic interactions and asymmetric torque distributions. These regions coincide with areas of increased curvature in the out-of-plane displacement field and play a key role in triggering the alternating post-bifurcation deformation patterns observed in the sixteen-disc topology.

## 4.3 Effect of material property contrast

In addition to topology and geometry, the surface-morphing response of heterogeneous film-substrate systems can be tailored through material-property contrast. In magneto-active soft composites, changes in particle content and matrix stiffness modify the magnitude and localization of magnetic forces, as well as the mechanical resistance imposed by the surrounding soft substrate. As a result, material contrast provides an additional design leverage to tune instability modes and post-bifurcation amplitudes. The study is conducted using the cylindrical disc-annulus topology with a film thickness of $h_f = 0.7$ mm, where localized responses are prominent and the influence of material contrast can be more clearly studied.

### 4.3.1 Effect of particle content

Here, the particle content is varied to quantify its influence on the instability response. 70 *phr* and 140 *phr* particle contents are used for the comparison which are modeled through the particle volume fraction $c$, with $c = 0.087$ for 70 *phr* and $c = 0.16$ for 140 *phr*. In addition, a spatial imperfection is introduced by prescribing a 6% variation of $c$ across the film, as detailed in subsubsection 3.2.4.3. All other geometric parameters, boundary conditions and magnetic loading conditions are kept identical, so that the observed differences can be attributed only to the particle content contrast. Changing $c$ affects the response in two coupled ways. First, it increases the magnetic coupling by raising the amount of magnetizable material within the film. Second, it modifies the effective stiffness of the MRE film. Using the homogenized Lefèvre and Lopez-Pamies (2022) (LLP) model introduced in Eq. (3.4), the effective shear modulus of the film is $G_f = 0.058$ MPa for 70 *phr* and $G_f = 0.072$ MPa for 140 *phr* (printed MRE modulus). With a fixed substrate shear modulus $G_s = 0.0058$ MPa, this corresponds to stiffness ratios $G_s/G_f \approx 0.10$ (70 *phr*) and $G_s/G_f \approx 0.08$ (140 *phr*).

Figure 4.30 summarizes the changes in the out-of-plane displacement $u_2$. A common inset placed at the bottom right indicates the evaluation points used for extracting $u_2$ at the disc center (P1) and along the annulus (P2-P5). For the 70 *phr* case (Figure 4.30a), the response is dominated by a nearly rigid-body-like motion of the film, with the disc and annulus displacements evolving in a similar manner and no clear wrinkling-type modulation developing over the explored field range. In contrast, the 140 *phr* case (Figure 4.30b) shows a distinct transition toward a wrinkling response, with the annular points (P2-P5) exhibiting a rapid growth in displacement beyond $b_0 \approx 1$ T, consistent with the onset of circumferential modulation. Compared to the 210 *phr* reference case discussed in subsection 4.1.3, the modululation of the the 140 *phr* specimen gives rise to a slightly longer-wavelength pattern (about seven wrinkles) relative to the eight-wrinkle pattern observed at 210 phr (see Figure 4.9).

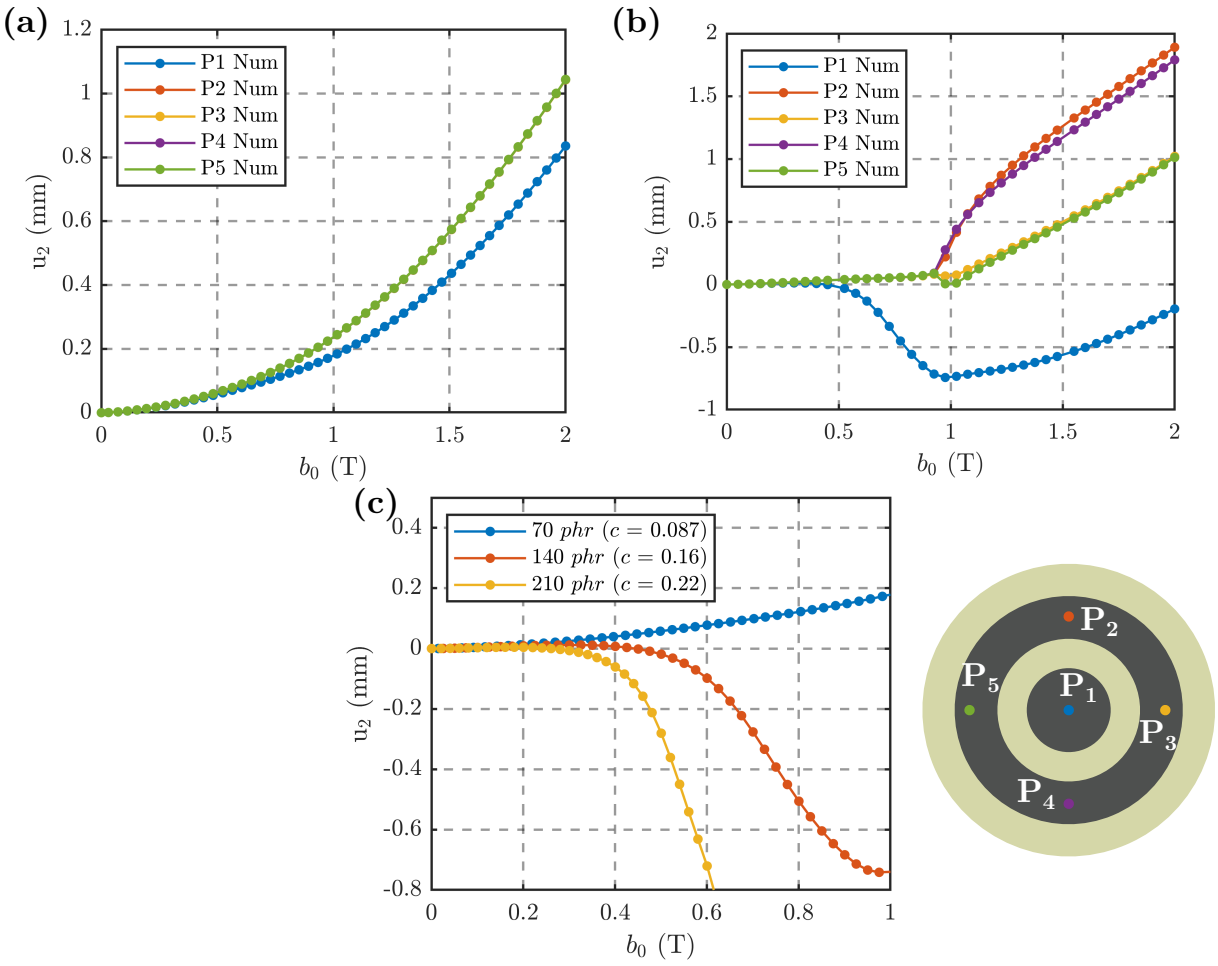


Figure 4.30: Effect of particle content on the cylindrical disc-annulus topology at $h_f = 0.7$ mm. Out-of-plane displacement $u_2$ as a function of the applied magnetic field $b_0$ extracted at the disc center (P1) and along the annulus (P2-P5) for (a) 70 *phr* and (b) 140 *phr*. (c) Disc-center $u_2$ displacement comparing all three particle content.

To further compare the effect of particle content the effect at the disc center, Figure 4.30c compares the disc-center displacement. The lower-particle case destabilizes at higher magnetic fields, consistent with the reduced magnetic coupling associated with fewer particles. Overall, increasing particle content enhances magnetic coupling and promotes the emergence of wrinkling-type instabilities in the annulus, while simultaneously changing the mechanical contrast through

$G_f$. These qualitative differences can be directly visualized by the 3D deformation fields in Figure 4.31, where the 70 *phr* configuration shows s aminimal rigid-body motion, whereas the 140 *phr* configuration exhibits a clearly modulated surface with circumferentially organized undulations along the annulus.

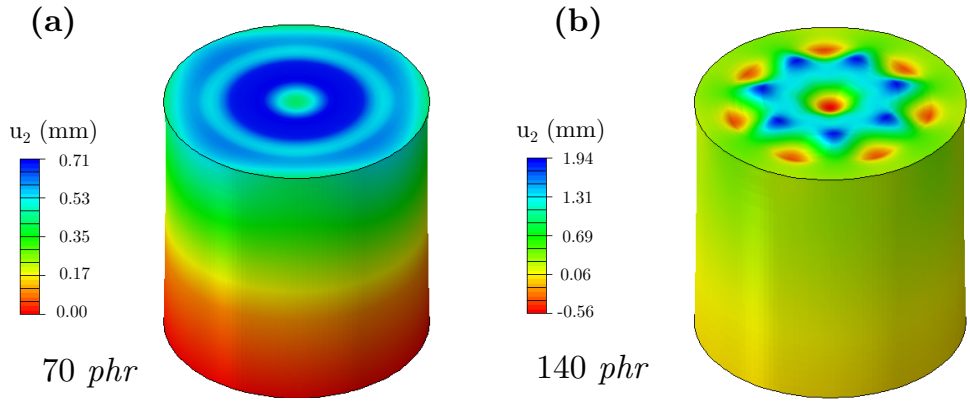


Figure 4.31: Three-dimensional out-of-plane displacement contours $u_2$ for the cylindrical disc-annulus topology at $h_f = 0.7$ mm for (a) 70 *phr* and (b) 140 *phr*.

### 4.3.2 Effect of the substrate softness

This subsection investigates the influence of substrate compliance on the instability behavior for the cylindrical disc-annulus topology at a fixed film thickness of $h_f = 0.7$ mm. In contrast to the previous subsection, where the material contrast was varied through the particle content of the MRE film, here the film properties are kept unchanged and the substrate stiffness is increased to assess how enhanced mechanical confinement alters the deformation response. For this study, the substrate shear modulus is set to $G_s = 0.015$ MPa, while the effective shear modulus of the MRE film remains $G_f = 0.087$ MPa for $c = 0.22$. This corresponds to a stiffness contrast of $G_s/G_f \approx 0.17$. All other geometric, material and loading parameters are kept identical, so that the observed differences can be directly attributed to the increased substrate stiffness.

Figure 4.32a shows the evolution of the out-of-plane displacement $u_2$ as a function of the applied magnetic field $b_0$, extracted at the disc center (P1) and at representative points along the annular region (P2-P5). Compared to the softer substrate cases discussed earlier, the displacement amplitudes are markedly reduced, and all monitored points follow nearly identical curves. This indicates that the deformation remains highly uniform and is dominated by a small-amplitude, global motion of the film rather than by localized or wrinkling-type instabilities. The response is characterized by a slight rigid-body-like motion of the whole specimen, with the disc and annular regions moving coherently. The corresponding three-dimensional out-of-plane displacement field shown in Figure 4.32b confirms this behavior. The deformation is smooth and nearly axisymmetric across the surface, and no circumferential wrinkling develops along the annular region. The stiffer substrate imposes a stronger mechanical constraint on the film, which suppresses curvature localization and penalizes out-of-plane gradients, thereby inhibiting the formation of wrinkling modes even in the presence of slender magnetic features and imposed material imperfections. Overall, these results show that increasing substrate stiffness

effectively suppresses surface pattern formation in thin MRE films. While the magnetic loading still induces out-of-plane motion, the response remains limited to a small, rigid-body-like deformation with no observable wrinkling. Substrate softness therefore plays a critical role in enabling instability-driven surface morphing in heterogeneous MRE film-substrate systems.

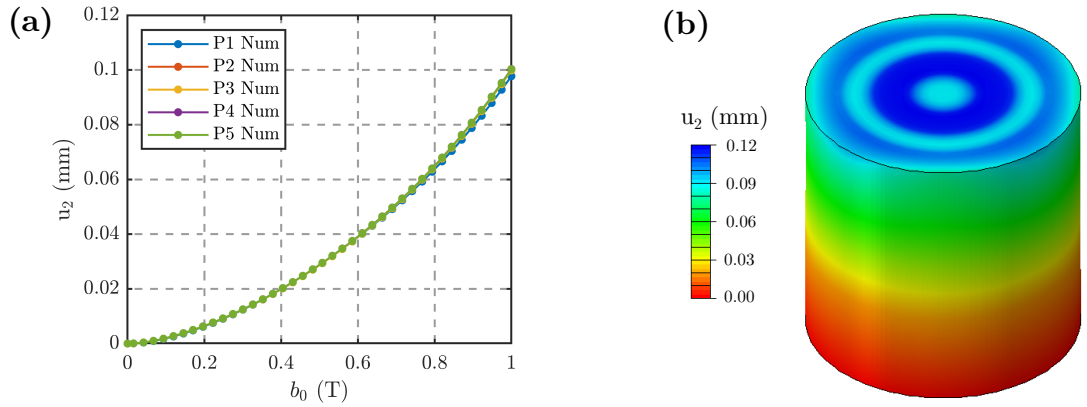


Figure 4.32: Effect of substrate stiffness for the cylindrical disc-annulus topology at $h_f = 0.7$ mm with $G_s/G_f \approx 0.17$. (a) Out-of-plane displacement $u_2$ as a function of the applied magnetic field $b_0$ measured at the disc center (P1) and along the annular region (P2-P5). (b) Corresponding three-dimensional out-of-plane displacement field $u_2$.

## 4.4 Concluding remarks

This chapter used numerical methods to study magneto-mechanically induced surface instabilities in heterogeneous MRE film-substrate systems and discussed how topology and geometry govern the onset of instability and the resulting post-bifurcation morphologies under an applied vertical magnetic field.

To study the effect of overall topology, three representative layouts were analyzed: a cubic four-disc topology, a cubic three-strip topology, and a cylindrical disc-annulus topology. In the thicker-film regime ($h_f = 1.8$ mm), all topologies exhibit an initially localized, domain-controlled dip-like deformation at low fields, followed by a transition toward specimen-scale, long-wavelength deformation at higher fields as magneto-active regions begin to interact. Although the onset fields remain comparable across topologies, the post-bifurcation response differs depending on the topologies. Compact disc-based topologies show a more rapid amplitude growth, whereas slender domains (strips and annulus) promote a more progressive deformation and have stronger sensitivity to the distance between magnetic domains connectivity and boundary proximity.

In the thinner-film regime ($h_f = 0.7$ mm), the response becomes strongly localized to the magneto-active regions and their immediate surroundings, and topology effects become more pronounced. Compact inclusions, such as the four discs, largely retain a dip-like response with reduced magnetic domain interaction, while slender geometries promote wrinkling-type modulations at high fields. In particular, the cylindrical disc-annulus configuration exhibits a clear two-stage response, with an early destabilization of the central disc followed by a circumferential

wrinkling of the annulus at higher fields. Overall, reducing film thickness suppresses specimen-scale global modes within the explored field range and favors localized wrinkling modes when the magnetic pattern provides a sufficiently extended (slender) length scale for wavelength growth.

The effect of geometric parameters was then investigated systematically. Varying the film thickness across $h_f = 0.7$, 1.2 and 1.8 mm demonstrated a clear thickness-controlled transition from localized dip-like modes toward global deformation modes as thickness increases, with the transition occurring at lower magnetic fields for thicker films due to the high magneto-mechanical coupling. For the cylindrical disc-annulus topology, the pattern footprint further controlled wavelength selection. Mainly in the thin-film regime, increasing the annulus width reduced the wrinkle wavenumber and promoted larger-amplitude with longer-wavelength circumferential undulations. Finally, increasing the pattern density in the cubic specimen (sixteen discs) revealed how a denser interaction network organizes the post-bifurcation state into multiple branches and alternating local tilts, which collectively assemble into a specimen-scale modulation resembling a global wrinkle.

The final section on the effect of material property contrast shows that, in addition to topology and geometry, material parameters provide an effective means to tune magneto-mechanical surface instabilities. Increasing the particle content enhances magnetic coupling and promotes the development of wrinkling-type modes, whereas lower particle content delays destabilization and leads to more rigid-body-like responses. Similarly, increasing substrate stiffness strongly suppresses wrinkling. These results show that the central role of the stiffness contrast, quantified by the ratio $G_s/G_f$, in governing instability onset and mode selections.

Overall, the results show that (i) topology primarily controls the type and spatial organization of post-bifurcation morphologies, especially in slender layouts, (ii) film thickness acts as a dominant control parameter that governs the transition between localized dip-like modes, localized wrinkling modes, and global specimen-scale deformation, and (iii) geometric footprint and pattern distribution provide practical design factors to tune wavelength selection, localization, and amplitude. In addition, the stiffness contrast between the film and substrate, quantified by the ratio $G_s/G_f$, plays a central role in enabling or suppressing surface instabilities. These findings offer clear guidelines for programmable surface morphing in heterogeneous MRE layers by combining controlled topology with thickness and footprint tuning.

# Conclusion and perspectives

This thesis investigated the design, fabrication, modeling and control of magnetically-induced surface instabilities in heterogeneous magnetorheological elastomer (MRE) film–substrate systems. By combining an active-mixing-assisted direct ink writing (DIW) process, a fully coupled three-dimensional numerical method and an experimental strategy to quantitatively measure the three-dimensional instability profile, an experimental–numerical frame work was established. This framework was then used in a systematic study of topology, geometry and material contrast to program complex magneto-responsive surface morphologies.

The first major contribution of this thesis is the development of a fabrication strategy for heterogeneous MRE films. An active-mixing-assisted DIW process was proposed and calibrated to overcome the limitations associated with the short pot life and evolving rheology of two-part silicone-based MRE inks. Rheological characterization demonstrated that a small amount of thixotropic agent is sufficient to transform Ecoflex™ 00-50 into a shear-thinning, yield-stress material required for DIW of MRE inks. A transparent, pigmented silicone system was used to experimentally determine the dynamic mixer speed, and a theoretical framework was used to predict the minimum rotational speed required for complete mixing of opaque MRE inks. These results led to the identification of an optimal operating range around 56.25 rpm, ensuring homogeneous mixing without inducing cavitation. Further extrusion and printing tests showed that nozzle geometry plays a critical role in stabilizing the flow of highly filled MRE inks. A short cylindrical nozzle with a 0.6 mm outlet diameter provided the best compromise among print resolution, stable extrusion and clogging prevention. Printing experiments allowed the extrusion speed to be determined for each particle content, enabling the deposition of equi-dimensional filaments over a wide range of printing conditions. Multi-layer tests highlighted a trade-off between geometric accuracy and porosity, leading to the choice of non-heated printing for thin films. Continuous-printing experiments finally quantified the practical printing windows of the inks, demonstrating that the active-mixing-assisted DIW platform provides a robust approach for fabricating heterogeneous MRE films with controlled geometry and rheology.

The second major contribution of this thesis is the development and validation of a fully coupled three-dimensional numerical framework to analyze magnetically-induced surface instabilities in heterogeneous film–substrate systems. A unified variational formulation based on the **F**–**B** framework was implemented using a dedicated Abaqus user-defined element, allowing mechanical displacements and magnetic vector potential to be solved consistently within the finite element discretization. Mechanical tests were performed and calibrated against constitutive models to identify the key material parameters required for modeling the substrate and MRE films used in the numerical model. A physically-motivated random imperfection in particle volume fraction

was introduced to break the symmetry and stabilize the post-bifurcation response, with an optimal imperfection level of $c_{\text{imp}} = 6\%$. Validation against a two-dimensional benchmark problem demonstrated good agreement in both critical field and post-bifurcation amplitude evolution. A second validation against full three-dimensional stereo-digital image correlation (stereo-DIC) measurements on a heterogeneous cubic four-disc topology confirmed that the model is able to capture both the onset of instability and the main deformation modes observed experimentally. These results establish the proposed three-dimensional **F**–**B** framework as a numerical method for predicting magnetically-induced instabilities in heterogeneous MRE systems.

The third major contribution of this thesis is the systematic investigation of surface morphing in heterogeneous MRE film–substrate systems and the determination of the effects of topology, geometry and material contrast on instability modes and post-bifurcation morphologies. Three representative topologies were analyzed: a cubic four-disc layout, a cubic three-strip layout and a cylindrical disc–annulus layout. In the thicker-film regime, all topologies exhibit a transition from localized dip-like deformation at low magnetic fields to a more global specimen-scale deformation at higher fields, as interactions between magnetic domains become dominant. Although the critical fields remain comparable across topologies, the post-bifurcation amplitude growth and deformation organization depend strongly on domain slenderness and boundary proximity. In the thinner-film regime, topology effects become much more pronounced. Compact inclusions, such as discs, largely retain localized dip-like modes, whereas slender geometries promote wrinkling-type instabilities. The cylindrical disc–annulus topology exhibits a clear two-stage response, with an early destabilization of the central disc followed by circumferential wrinkling of the annulus. Systematic parametric studies showed that film thickness is the dominant control parameter governing the transition between localized dip-like modes, localized wrinkling modes and global deformation modes. The geometric footprint study, by varying annulus width and the number of discs, directly controls wavelength selection, localization and amplitude. An increasing number of discs alters the post-bifurcation state, leading to interacting local domains that assemble into specimen-scale modulations. Finally, material contrast, quantified by the stiffness ratio $G_s/G_f$ and the particle content, provides an efficient means to control the instabilities and to tune the nature of the emerging modes similar to that of the uniform MRE film-substrate system as discussed in Rambausek et al. (2022).

Taken together, the results of this thesis demonstrate that programmable surface morphing in heterogeneous MRE layers can be achieved through a rational combination of controlled fabrication, robust three-dimensional modeling and systematic topological study. The active-mixing-assisted DIW process enables the reproducible fabrication of complex heterogeneous films, the three-dimensional **F**–**B** framework provides a predictive tool for instability and post-bifurcation behavior, and the parametric studies establish clear guidelines for designing magneto-responsive surfaces with targeted morphologies. In conclusion, this thesis provides a comprehensive experimental and numerical framework for understanding and designing magnetically-induced surface instabilities in heterogeneous MRE film–substrate systems and establishes a strong foundation for future developments in programmable magneto-responsive soft materials.

Several perspectives emerge from this work, spanning fabrication, modeling, experimental metrology, and inverse design. From a fabrication standpoint, a direct extension of the active-mixing-assisted DIW platform developed in this thesis can be used to enable multi-material, functionally graded heterogeneous films, in which magnetic and mechanical properties vary spatially within a single printed layer. Practically, this can be implemented by increasing the number of independently-controlled inlets feeding the mixing chamber (e.g., two or more syringes/extruders), while retaining the same helical mixing principle (see, for e.g. Rocha et al. (2020)). Another strategy to obtain a functionally graded heterogeneous film is to use two material streams that differ in particle volume fraction (e.g., a high-$c$ and a lower-$c$ MRE ink, or an MRE ink and a pure silicone ink). By prescribing time-dependent feed rates $Q_1(t)$ and $Q_2(t)$ for the two ink compounds, the effective composition at the nozzle outlet can be programmed continuously, yielding a controllable gradient along the printing path. In this context, the mixer rotational speed sets the homogenization quality for a given total flow rate, whereas the ratio $Q_1/(Q_1 + Q_2)$ directly prescribes the local effective particle content, and therefore the local magnetic coupling and stiffness.

A further fabrication perspective concerns the extruder hardware itself, in particular the torque capacity of the screw-driven extruder. In the present work, the maximum printable particle content and the achievable flow stability are partly limited by the available motor torque, especially for highly-filled MRE inks at 210 *phr*, where the apparent viscosity and yield stress become very large. An important extension would therefore be the development of a custom high-torque motor–gearbox assembly specifically designed for screw extruders. By increasing the available torque and maintaining precise low-speed control, such a system would enable reliable extrusion of inks with even higher particle volume fractions and more pronounced yield-stress behavior, without motor stalling. From a materials and instability-design perspective, this capability is particularly relevant. Increasing the particle content directly enhances the magnetic susceptibility and magneto-mechanical coupling of the film, which in turn reduces the critical magnetic field for instability onset and accelerates the development of post-bifurcation morphologies. Access to stable extrusion at higher particle fractions would therefore make it possible to fabricate films that are more responsive, activate at lower fields, and exhibit larger deformation amplitudes for a given magnetic loading.

From a modeling perspective, incorporating viscoelasticity is expected to significantly refine the predictive capability of instability simulations, especially when the time scales associated with polymer relaxation become comparable to the loading and pattern-formation time scales. In filled elastomers and silicone-based MREs, viscous dissipation introduces hysteresis and rate dependence under cyclic magnetic loading. These effects can be essential when comparing with experiments in which the magnetic field ramp rate and viscoelastic relaxation play a major role in determining both the apparent critical field and the post-bifurcation evolution. Beyond quasi-static loading, such extensions become particularly important for advanced morphing strategies based on rapid magnetic actuation. In applications involving fast on–off switching of the mag-

netic field or high-frequency modulation, the competition between magnetic driving, elastic restoring forces, and viscous relaxation is expected to govern the transient selection, growth, and decay of instability modes. Capturing these dynamics requires a constitutive framework that can predict not only equilibrium morphologies but also time-dependent instabilities under dynamic loading. A concrete implementation route is therefore to build on continuum magneto-viscoelastic formulations that couple nonlinear viscoelasticity with magneto-mechanical energy densities, such as the framework proposed by Danas et al. (2025).

A second major modeling perspective concerns the computational cost of explicitly meshing the surrounding air. While full-field three-dimensional air domains provide high fidelity, they dramatically increase the number of degrees of freedom. Established open-boundary strategies, such as open-boundary transformations and infinite elements (Gerdes 2000), offer efficient ways to represent the infinite exterior field without a massive airbox, thereby reducing computational cost while preserving accuracy. Beyond purely open configurations, an important extension is the treatment of a third medium in contact with the solid and the surrounding air, which can strongly influence both magnetic and mechanical boundary conditions. Recent developments in Third Medium Contact (TMC) modeling, such as the HuHu–LuLu regularization, show that curved contacts and snap-through behavior can be captured accurately on coarse meshes by selectively penalizing skew deformations while preserving bending modes (Frederiksen et al. 2025). Such approaches provide a promising route to incorporate contact and confinement effects into three-dimensional **F-B** simulations without the prohibitive cost of mesh refinement.

From an experimental standpoint, the stereo-DIC pipeline can be made more robust by tailoring the optical contrast at the specimen surface. As shown in Appendix D, introducing a black pigment in the substrate enables the use of an "inverted" speckle pattern, in which only a white speckle is applied without a preliminary white base coat. This reduces the thickness and invasiveness of the paint layer and avoids cracking during large deformations, while still providing sufficient grayscale contrast for correlation. The inverted speckle proposed in this work unfortunately introduces minor re-projection defects, but further work on tailoring the properties of the white ink to reduce tackiness and increase drying time are expected to solve this issue. Such an approach, when robust, would therefore offer a minimally invasive alternative for measuring large, highly localized deformations, which is particularly valuable in the present context where sharp curvature changes and strong displacement gradients are central to the identification of instability modes.

Finally, a major perspective is to move from forward simulation (given topology and material parameters, predict morphology) to inverse design (given a target morphology, identify a printable topology/material distribution and loading protocol). In this regard, further systematic numerical and experimental studies should be carried out to explore a wide range of topologies, geometries, material contrasts and process parameters, in order to build a sufficiently rich and representative design space. A practical strategy is then to construct a database of forward simulations spanning (i) topology parameters (layout, feature slenderness, spacing), (ii) geometry parameters (film thickness, footprint dimensions), (iii) material parameters (particle content,

$G_s/G_f$), and potentially (iv) process parameters (graded compositions achievable by multi-inlet active mixing). From this database, one can train surrogate models that map design variables to quantitative morphology modes (e.g., wrinkle wavelength, wavenumber, amplitude, localization metrics, bifurcation field). The inverse problem can then be solved to propose candidate designs matching a target response. In the long term, such ML-assisted inverse design could enable "reverse morphology estimation", where a desired 3D surface profile is translated directly into a set of printable heterogeneous film parameters (multi-material feed-rate schedules, mixer rpm, toolpath) together with the magnetic actuation protocol, thereby enabling truly programmable magneto-responsive surfaces for applications in soft robotics, adaptive optics, and haptics.

# Appendix A
# Mixer length selection

The length of the mixing tube plays an important role in determining the effective operating conditions of the active mixer, as it directly influences the rotational speed required for complete homogenization, residence time (both of which are discussed in subsubsection 2.4.1.2), and torque requirements during extrusion. While increasing the mixer length increases the effective mixing volume (see Figure A.1a) and can improve homogenization, it also introduces several limitations, particularly for two-part-based reactive silicone inks. The two main drawbacks to using longer mixing tubes are :

- **Higher extrusion torque and pressure demand:** A longer mixing tube increases the hydraulic resistance of the system, requiring higher inlet pressures to sustain a given flow rate. This effect is illustrated in Figure A.1b, which shows numerical predictions of the inlet pressure as a function of flow rate for different mixing tube lengths. For all cases, the pressure increases nearly linearly with flow rate, with longer mixers consistently demanding higher pressures. These results are obtained from steady-state flow simulations performed in COMSOL MULTIPHYSICS using the Polymer Flow Module, considering a needle length of 6.35 mm and material and flow parameters consistent with those described in subsubsection 2.4.2.2. For a screw-extruder-based system, this directly translates into increased torque requirements, pushing the system closer to its motor limits.

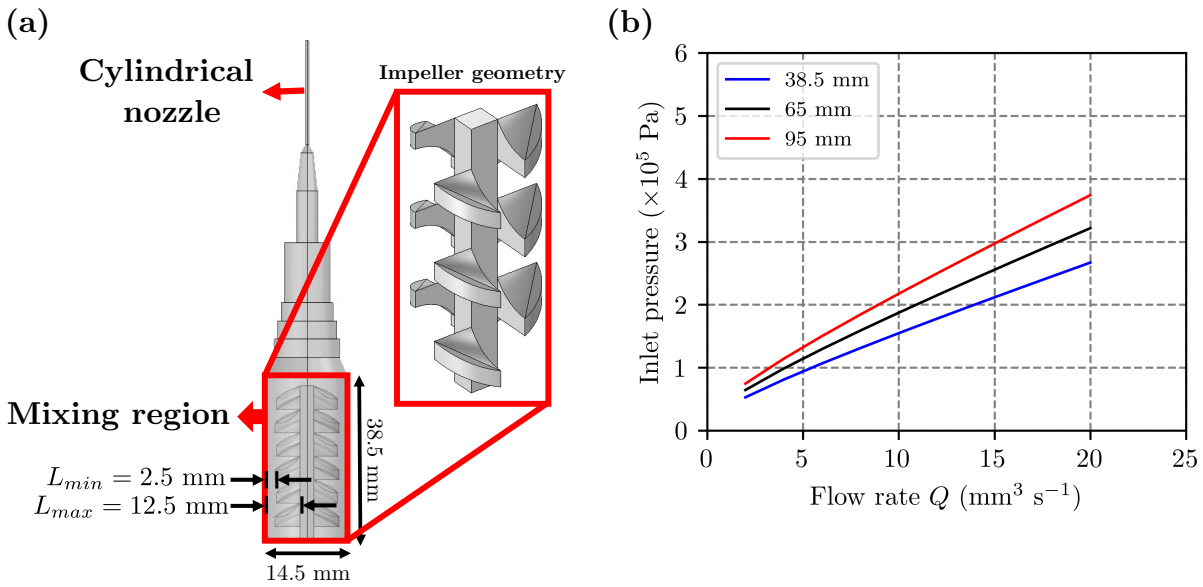


Figure A.1: (a) Schematic of the mixing region with a helical ribbon impeller equipped with a cylindrical nozzle. An enlarged view highlights the alternating ribbon elements that promote chaotic advection and efficient mixing of high-viscosity MRE inks. (b) Inlet pressure as a function of flow rate for different mixing tube lengths, showing that shorter mixers require significantly lower inlet pressures for the same volumetric flow rate.

- **Increased residence time and premature curing risk:** For reactive two-part silicone systems, parts A and B will start crosslinking once mixed in the active mixer, even if is it unclear at which point within the mixer the curing is triggered. Nevertheless, a longer mixer inherently increases the residence time of the material within the mixing tube, as more material is retained inside the channel for a given flow rate. This prolonged residence time raises the likelihood of curing or partial curing within the mixer, leading to viscosity buildup, further pressure increase, and ultimately flow blockage or motor stalling. Shorter mixers, in contrast, reduce both residence time and pressure buildup, thereby lowering the risk of curing-induced failure.

As a result, the mixing tube length must be carefully chosen to balance mixing efficiency with torque requirement while lowering the risk of residence-time-induced curing. Longer mixers may be advantageous for non-reactive or low-viscosity systems, but shorter mixing tubes are preferable for reactive silicone-based inks, as they minimize residence time and backpressure while maintaining sufficient mixing when paired with an efficient helical impeller design. Although the pressure penalty associated with longer mixers could be alleviated through pressure-driven extrusion systems, residence-time constraints remain a fundamental limitation for reactive materials. Based on these considerations, a mixing tube length of 38.5 mm is selected for the present study.

In subsubsection 2.4.1.2, theoretical residence times are calculated considering a printing speed of $V = 10$ mm s$^{-1}$. These are $\sim$ 16, 15, 13 and 12 min for the base base EcoflexTM 00-50 and the 70, 140 and 210 *phr* MRE inks, respectively, which remains below the pot life. One could thus expect an infinite printing time, only limited by the content of the syringes. Nevertheless, continuous-printing experiments reported in subsection 2.5.2 show that the 00-50 silicone can be printed continuously for 126 min (7 times the pot life, here nearly emptying both 60 mL syringes), and that the 210 *phr* MRE ink remains stable for approximately 45 min before curing-related effects become noticeable through filament irregularities. Despite a significant improvement in printing time compared to the state-of-the art of soft material printing, this suggest that fragments or pockets of curing ink remain in the mixer longer than the theoretically-calculated residence time, eventually disrupting the flow, and eventually blocking it. On this point, further insight could be obtained by performing 3D computer fluid dynamics (CFD) simulations, but this is beyond the scope of this thesis.

# Appendix B
# Rheological validation

In the context of the determination of most suitable nozzle geometry, numerical simulations are conducted using rheological data obtained from experiments. The objective of this appendix is to ensure that the parameters derived from rheological measurements are consistent and can be reliably used in the numerical simulations. The experimental data obtained from the parallel-disk rheometer is compared with both analytical model and numerical simulations performed in COMSOL MULTIPHYSICS.

To numerically model the rheometer, we use a 2D axis-symmetric model, as shown in Figure B.1. The upper plate rotates with an angular velocity $\Omega$ that is calculated from the plate rpm recorded by the rheometer using the equation:

$$\mathbf{\Omega} = rpm \times \frac{2\pi}{60}. \tag{B.1}$$

The lower plate remains stationary with a fixed wall condition.

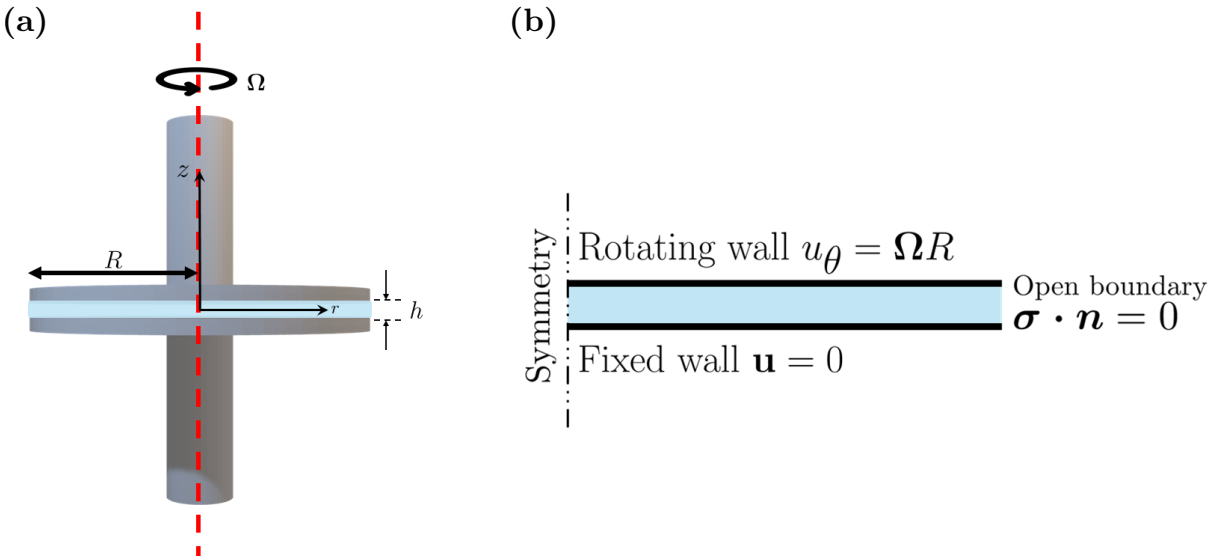


Figure B.1: (a) Cross-sectional view of the torsional parallel-disk rheometer used for viscosity measurement. (b) Corresponding 2-D axis-symmetric numerical boundary value problem.

## B.1 Constitutive equations

The fluid is governed by momentum and continuity equations:

$$\frac{\partial \rho}{\partial t} + \nabla \cdot (\rho \mathbf{u}) = 0, \tag{B.2}$$

where $\mathbf{u}$ is the velocity vector and $\rho$ is the fluid density.

For a fluid of constant density (an incompressible fluid), the continuity equation simplifies to:

$$\nabla \cdot \mathbf{u} = 0. \tag{B.3}$$

In cylindrical coordinates it is given as:

$$\frac{1}{r}\frac{\partial}{\partial r}(ru_r) + \frac{1}{r}\frac{\partial u_\theta}{\partial \theta} + \frac{\partial u_z}{\partial z} = 0. \tag{B.4}$$

The Navier-Stokes equation to describe the motion of a viscous fluid in 3D is given by:

$$\rho\frac{D\mathbf{u}}{Dt} = -\nabla p + \nabla \cdot \boldsymbol{\sigma} + \rho\mathbf{g}, \tag{B.5}$$

where $\mathbf{u}$ is the velocity field, $\frac{D\mathbf{u}}{Dt} = \frac{\partial \mathbf{u}}{\partial t} + \mathbf{u} \cdot \nabla\mathbf{u}$ is the material derivative, $\boldsymbol{\sigma}$ is the stress tensor, and $\rho\mathbf{g}$ represents body forces such as gravity.

The Cauchy stress tensor $\boldsymbol{\sigma}$ is given by:

$$\boldsymbol{\sigma} = -p\mathbf{I} + 2\eta\boldsymbol{\varepsilon}, \tag{B.6}$$

where $p$ is the pressure, $\mathbf{I}$ is the identity tensor, $\eta$ is the apparent viscosity, and $\boldsymbol{\varepsilon}$ is the strain rate tensor.

The strain rate tensor $\boldsymbol{\varepsilon}$ (also called the rate of deformation tensor) is defined as:

$$\boldsymbol{\varepsilon} = \frac{1}{2}\left(\nabla\mathbf{u} + (\nabla\mathbf{u})^T\right). \tag{B.7}$$

Substituting the expression for $\boldsymbol{\sigma}$ into the momentum equation:

$$\rho\frac{D\mathbf{u}}{Dt} = -\nabla p + \nabla \cdot (2\eta\boldsymbol{\varepsilon}) + \rho\mathbf{g}, \tag{B.8}$$

which expands to:

$$\rho\frac{D\mathbf{u}}{Dt} = -\nabla p + \nabla \cdot \left(\eta\left(\nabla\mathbf{u} + (\nabla\mathbf{u})^T\right)\right) + \rho\mathbf{g}. \tag{B.9}$$

The governing equations are implemented directly in the COMSOL Multiphysics commercial software to model the rheometer, allowing the evaluation of apparent viscosity as a function of shear rate. The COMSOL Polymer Flow Module is used to accurately capture the non-Newtonian behavior of the ink, utilizing the fitted rheological data based on the Casson–Papanastasiou model described in subsubsection 2.4.1.2.

## B.2 Simplified analytical rheometer model

To analytically model the rheometer, a 2D axisymmetric Couette flow assumption is used with a velocity $\mathbf{u} = (0, u_\theta(r, z), 0)$. The strain rate tensor then reduces to:

$$\boldsymbol{\varepsilon} = \frac{1}{2} \begin{bmatrix} 0 & \frac{\partial u_\theta}{\partial r} & 0 \\ \frac{\partial u_\theta}{\partial r} & 0 & \frac{\partial u_\theta}{\partial z} \\ 0 & \frac{\partial u_\theta}{\partial z} & 0 \end{bmatrix}. \tag{B.10}$$

Since $u_r = 0$ and $u_z = 0$, the momentum equation simplifies to:

$$\frac{\partial}{\partial z} \left( \eta \frac{\partial u_\theta}{\partial z} \right) = 0, \tag{B.11}$$

where the shear rate $\dot{\gamma}$ is:

$$\dot{\gamma} = \frac{\partial u_\theta}{\partial z}. \tag{B.12}$$

In a Couette flow setup, where the upper plate rotates at velocity $\boldsymbol{\Omega} R$ while the lower plate remains stationary, the velocity gradient is approximately linear across the gap height $h$. Thus, the shear rate is given by:

$$\dot{\gamma} = \frac{\partial u_\theta}{\partial z} \approx \frac{\boldsymbol{\Omega} R}{h}, \tag{B.13}$$

where $\boldsymbol{\Omega}$ is the angular velocity of the rotating upper plate, $R$ is the radius of the plate, and $h$ is the gap height between the plates. This shear rate $\dot{\gamma}$ is directly used in the Casson–Papanastasiou model to analytically estimate the apparent viscosity $\eta$.

Figure B.2a shows the comparison of apparent viscosity as a function of shear rate for different concentrations of CIP, where experimental, analytical and numerical results are plotted together. The corresponding error analysis between the methodologies is summarized in the table of Figure B.2b. A very good agreement is observed between the experimental rheometer data and both the analytical and numerical predictions. The percentage of error between the experimental and analytical data is consistently lower than that between the experimental and numerical data. This can be attributed to the fact that the analytical model is directly fitted to the experimental data and is based on a simplified Couette flow assumption with a velocity field $\mathbf{u} = (0, u_\theta(r, z), 0)$, thereby minimizing the deviation. In contrast, the numerical model in COMSOL solves the problem with the full velocity field and incorporates additional geometrical and discretization considerations, which can introduce numerical errors and increase the deviation from the experimental measurements.

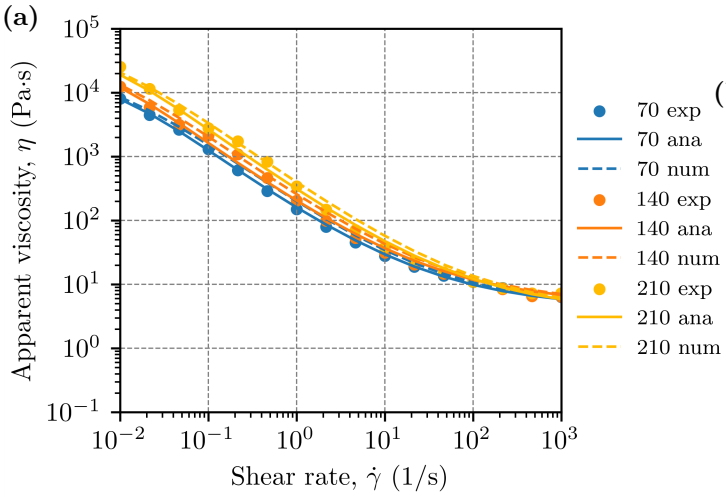


**(b)**

| CIP phr | Methodology | % error |
|---|---|---|
| 70 | Experiment - Analytical | 5.59 |
| | Experiment - Numerical | 16.87 |
| 140 | Experiment - Analytical | 12.31 |
| | Experiment - Numerical | 21.49 |
| 210 | Experiment - Analytical | 14.17 |
| | Experiment - Numerical | 22.23 |

Figure B.2: Comparison of experimental rheological data (dots) with analytical Casson–Papanastasiou model (solid lines) and COMSOL MULTIPHYSICS numerical simulations (dashed lines) for different CIP contents: apparent viscosity $\eta$ as a function of shear rate $\dot{\gamma}$ for different CIP contents (70, 140 and 210 *phr*). (b) Summary of error data between different analysis methods.

# Appendix C
# Material characterization of molded and printed samples

This appendix focuses on assessing the mechanical response of molded samples and of samples printed without and with a heated bed, as well as with various hatching strategies. The objective is to provide some insight into the impact of printing and of the printing strategy on the effective behavior of the obtained samples.

## C.1 Fabrication of dogbone specimens and mechanical testing

The corresponding dogbone geometry follows the ASTM D412 standard, as depicted in Figure 2.21a. Dogbone specimens are prepared using two different methods: traditional molding and active-mixing direct ink writing (DIW) using the experimental methodology presented in chapter 2. The molded specimens provide a baseline for bulk material properties, largely free from fabrication-related variations. In contrast, the printed specimens represent more closely the films used for the fabrication of the film-substrate system, which accounts for the effects of the interfilament interactions and the layer-by-layer deposition process.

For the molded MRE dogbone specimens, Ecoflex™ 00-50 (parts A and B) is first combined with the required amount of CIP particles, and the mixture is thoroughly mixed for 5 min using a drill mixer to ensure uniform particle dispersion. After mixing, the suspension is degassed in a vacuum chamber for 6 min to remove entrapped air. Next, the material is poured into precision-machined copper molds, whose inner surfaces are coated with Ease Release 200 before use, cured at 70 °C for 2 h, and left 2 h at room temperature before demolding.

The printed specimens are obtained using the processing parameters reported in Table 2.4. A printing speed of $V = 10$ mm s$^{-1}$ is employed, and the corresponding extruder speed $V_E$ is adjusted for each particle content (70, 140 and 210 *phr*) according to the calibration summarized in Table 2.4. As discussed in subsection 2.5.3, printed specimens produced without a heated bed exhibit lesser shape fidelity but improved filament coalescence and more homogeneous layer filling, owing to the longer available flow time before curing. In this case, the influence of printing orientation becomes negligible due to enhanced interlayer blending. Hence, only the cross hatching strategy is considered for these samples. Conversely, samples printed with a heated bed (set at 60°C), although they exhibit better shape retention, suffer from the formation of voids between layers, as illustrated in Figure 2.21d. In this latter case, where filaments are cured as they are deposited, different hatching strategies (similar to those used in FDM) are considered, namely longitudinal, transverse and cross (i.e., longitudinal and transverse directions alternate from one layer to the next), as sketched in Figure C.1. In all cases, four layers are printed, and each sample undergoes a final cure in an oven at 70°C for 2 h.

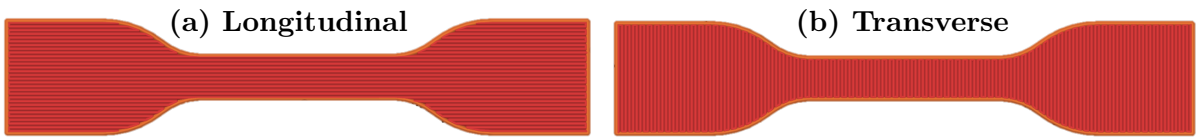


Figure C.1: Sketch of the hatching strategies employed in the printing of specimens with a heated bed using Slic3r software: (a) longitudinal and (b) transverse hatching. For cross hatching, longitudinal and transverse directions alternate from one layer to the next.

Cyclic uniaxial tensile tests are performed under displacement control at a rate of 0.25 mm $s^{-1}$, corresponding to a nominal strain rate of $5 \times 10^{-3}$ $s^{-1}$, and the unloading phase stops when the load reaches zero. Each specimen undergoes 10 consecutive loading–unloading cycles, and three specimens of each configuration are tested. The load applied to the sample and its longitudinal stretch (tracked by means of optical extensometry via white markers applied on the specimen gage area) are recorded simultaneously during the test.

Converting this data into a nominal stress–strain curve requires input of the sample cross-sectional area. For molded specimens, the gage section is measured with a caliper at three points across the width and thickness, and the average of these measurements is used to calculate the stress. Because the molding process is highly precise, the variation between measurements stays below 2%.

In contrast, the printed MRE specimens have variations in filament arrangement and interlayer compaction. Hence, their cross-sectional area cannot be assumed to be an idealized rectangular section, nor can they be measured precisely with a caliper. Instead, they are evaluated post-mortem by image processing as follows. After mechanical testing, each specimen is cut at three locations along its gage length—left, middle and right—to account for possible geometrical irregularities. The cross-sectional surfaces are imaged using a *VHX-5000* series Keyence digital microscope, as shown in Figure C.2a in the case of a sample printed without a heated bed. The captured images are then analyzed using the Python OpenCV library through a dedicated image-processing routine. Each image is first converted into an 8-bit grayscale format and binarized according to a selected threshold value ranging from 0 (black) to 255 (white) (Figure C.2b). Closed contours are then extracted from the binarized images, and small, noisy regions are filtered out to retain the largest connected contour corresponding to the specimen boundary. The threshold value is then adjusted until the identified contour accurately matches the true cross-sectional edge (Figure C.2c). Finally, the area enclosed by the largest contour is calculated based on the resolution of the image. This analysis is repeated for all three cut positions to compute the average cross-sectional area, which gives reliable data for stress computations in the printed MRE specimens. For specimens printed with a heated bed that show porosities as described in subsection 2.5.3, a similar image-processing method is used (Figure C.2d). First, the largest binarized contour is identified for the cross-section (Figure C.2e). Next, the porous regions inside this contour are found and subtracted from the total matrix area (Figure C.2f). The remaining matrix area is then used to calculate stress.

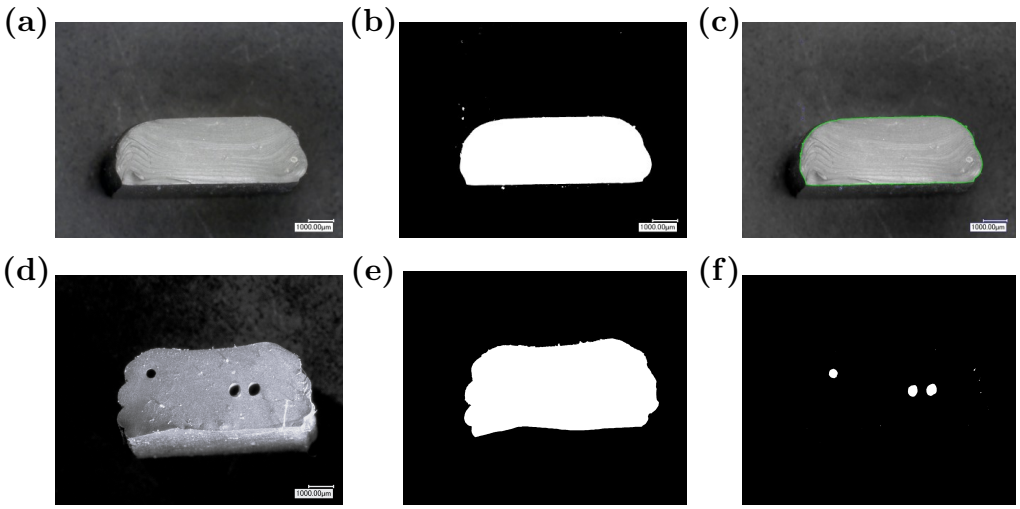


Figure C.2: Image analysis procedure for determining the cross-sectional area of printed MRE specimens. (a) Microscope image of the cross-section of a 70 *phr* MRE specimen printed without a heated bed. (b) Binarized image using a threshold value of 90. (c) Selected largest contour in green, matching the cross-section of the specimen. (d) Microscope image of the cross-section of a 70 *phr* MRE specimen longitudinally-printed with a heated bed. (e) Binarized image using a threshold value of 50. (e) The void area in white is subtracted from the previous cross-section.

## C.2 Effect of Thivex on the tensile response

First, we set to analyze the effect of THIVEX® on the response of MREs. This analysis is performed on molded samples for two reasons: i) molded specimens provide a better representation of bulk material properties without the effect of the printing included, and ii) specimen cannot be printed without THIVEX®. Figure C.3 shows the upload curves of the stabilized $10^{\text{th}}$ cycle of the stress–strain responses of molded MRE samples fabricated with and without THIVEX® at 70, 140 and 210 *phr*, where the lines correspond to the mean response and the shaded regions represent the variable range including the results of all three specimens tested in each case.

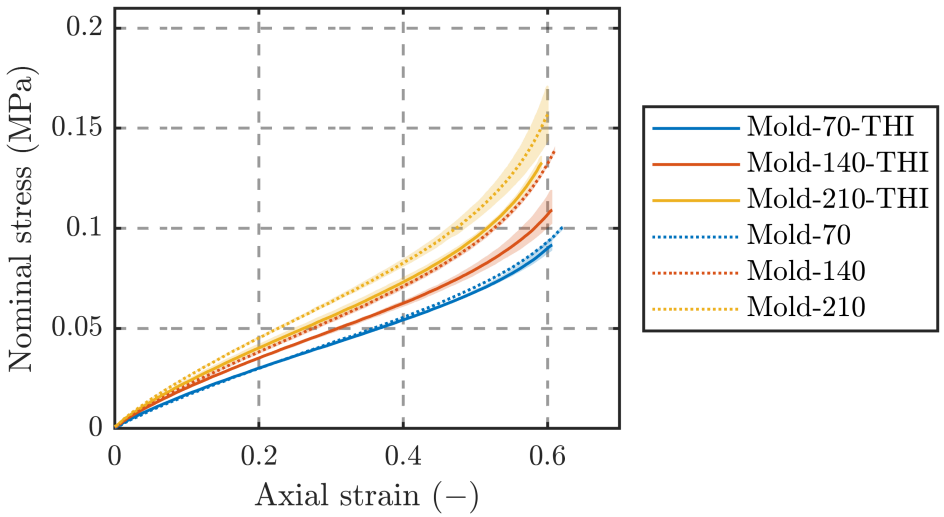


Figure C.3: Upload curves of the stabilized $10^{\text{th}}$ cycle of the stress–strain responses of molded MRE specimens fabricated with and without THIVEX® for CIP particle contents of 70, 140 and 210 *phr*.

For all particle contents, samples with THIVEX® have lower nominal stresses at the same strain than those without THIVEX®. This result shows that the additive consistently softens the material. Indeed, additives such as silicone oils or rheology modifiers like THIVEX® disrupt the full crosslinking of the polymers chains. Additionally, they affect the dispersion of the particles by altering the viscosity of the pre-cured polymer matrix. A reduction in viscosity increases particle mobility and improves the homogeneity of the suspension and, conversely, a more viscous medium restricts particle movement and can cause local clustering. At a low particle volume fraction (70 *phr*), the CIP particle network is not well developed and the particles are already fairly well dispersed in the matrix. As a result, the effect of THIVEX® on particle distribution due to viscosity is small, and the overall softening effect in the cured material stays limited. At higher particle contents (140 and 210 *phr*), the suspension becomes more crowded, and particle interactions and possible micro-agglomeration become important. Here, the increase in viscosity from THIVEX® has a stronger effect on the microstructure, resulting in less efficient packing and weaker particle networks in the cured state. This increases the overall softening effect seen in the experiments. In summary, while THIVEX® improves the flow and printability of the uncured ink, it also causes a noticeable reduction in stiffness in the cured material.

## C.3 Effect of particle content on tensile response

Figure C.4 shows the nominal stress–strain curves from cyclic uniaxial tensile tests on both molded and printed MRE specimens (without heated bed) at particle contents of 70, 140 and 210 *phr*, where one representative sample is considered in each case. Figure C.4a,c display the full 10-cycle stress–strain responses (which highlights the Mullins softening and hysteresis effects), while Figure C.4b,d show the stabilized $10^{\text{th}}$ cycles.

The full cyclic data in Figure C.4a,c show clear stress softening during the first few loading and unloading cycles before the mechanical response becomes stable. This drop in stress with repeated cycling is known as the Mullins effect, which happens when polymer and filler interactions break down and rearrange under strain. After several cycles, the curves settle into a stable pattern, as seen in the $10^{\text{th}}$-cycle data (Figure C.4b,d).

For both molded and printed specimens, increasing the particle content causes a clear rise in nominal stress at the same strain, showing that the material becomes stiffer as more particles are added. Molded specimens show this effect more strongly, with slightly higher stress values than printed ones at the same *phr*. This difference is likely due to the non-uniform strain distribution caused by the irregular cross-section of the printed specimens, as well as local variations in particle distribution resulting from the mixing and deposition process. In both cases, the hysteresis also gets larger as particle content increases, which means there is a stronger irreversible slip process between the fillers and the matrix (Miehe and Keck 2000).

Overall, these results confirm that both the stiffness and the dissipative behavior of the MREs increase with particle concentration. The molded and printed specimens show the same qualita-

tive trend, with the printed ones exhibiting slightly reduced stiffness due to differences in their layer-by-layer structure.

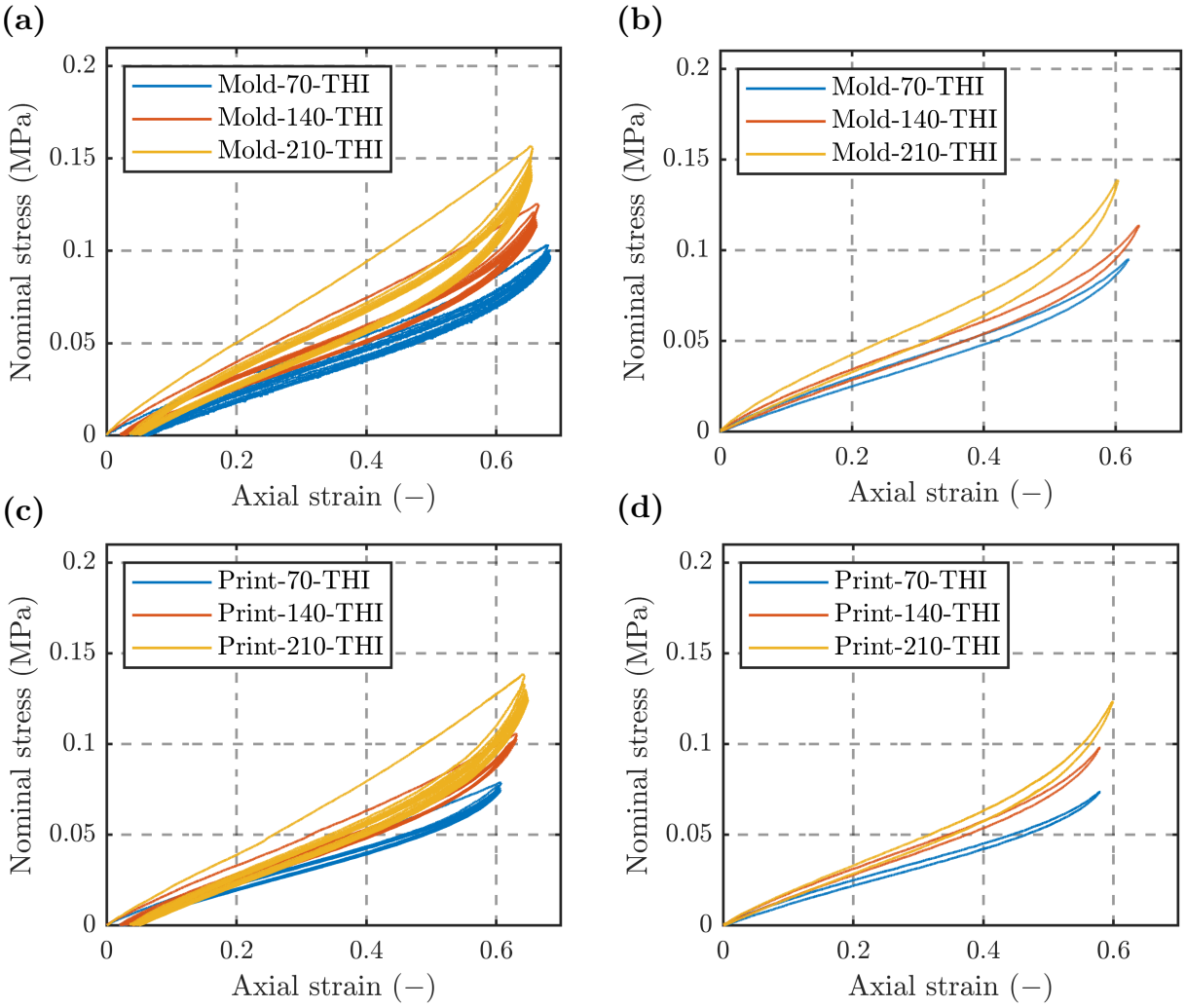


Figure C.4: Effect of particle content on the cyclic uniaxial tensile response of MREs. (a) Complete 10-cycle response of molded specimens for 70, 140 and 210 *phr*. (b) Stabilized $10^{\text{th}}$ cycle for the same specimens. (c) Complete 10-cycle response of printed specimens without heated bed for 70, 140 and 210 *phr*. (d) Stabilized $10^{\text{th}}$ cycle for the same printed specimens.

## C.4 Comparison of molded and printed specimens

We now focus more precisely on how the fabrication method affects the mechanical response by comparing, in the same plot, molded and printed specimens (without a heated bed), both made with THIVEX®. Figure C.5 presents the upload curves of the stabilized $10^{\text{th}}$ cycle of the stress–strain responses for samples obtained with both methods at CIP contents of 70, 140 and 210 *phr*, where the lines correspond to the mean response and the shaded regions represent the variable range including the results of all three specimens tested in each case.

For all particle contents, the curves for molded and printed specimens remain fairly similar, suggesting that the fabrication process has a limited effect on the material's overall stiffness (at least less marked that the contribution of THIVEX® reported in Figure C.3). The slight

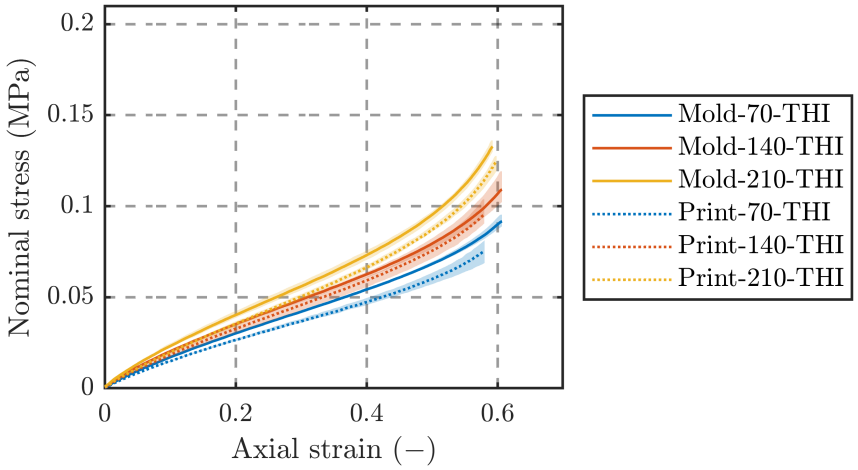


Figure C.5: Upload curves of the stabilized 10$^{\text{th}}$ cycle of the stress–strain responses of molded and printed (without heated bed) MRE specimens for CIP contents of 70, 140 and 210 *phr*.

softening observed in printed samples is mostly due to differences in how particles are arranged between the two fabrication methods. The inks for the molded specimens are prepared using a drill mixer, and the specimens cure in a static mold, which lets the suspension settle into a more even particle distribution. In contrast, the inks for the printed specimens go through the active mixer and experience shear during extrusion, which can slightly change how particles are distributed. These small changes in the microstructure likely explain the minor differences in the measured responses and are consistent with the observations reported in Figure C.6, where an FEI Quanta 650 FEG environmental scanning electron microscope (ESEM) was used to examine the specimens in high-vacuum mode at 8 kV beam voltage.

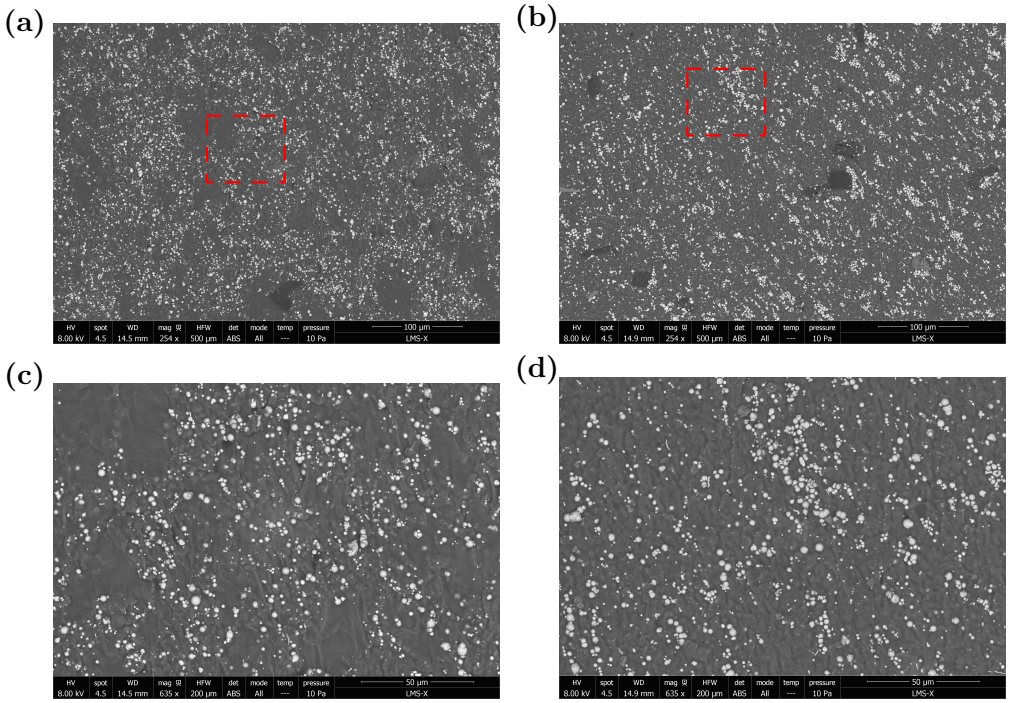


Figure C.6: SEM images of 210 *phr* MRE specimen made with THIVEX®: (a) molded, (b) printed without heated bed, (c–d) close-up views of the marked regions.

The SEM images show cross sections of 210 *phr* MRE specimen (made with THIVEX®) fabricated by molding (Figure C.6a) and printed without a heated bed (Figure C.6b). The molded specimen exhibits a more even particle spread, while the printed specimen has areas with denser and more irregular clusters. This is more evident at a closer scale shown in Figure C.6c-d. These differences likely account for the small variations in the measured macroscopic responses.

In summary, when both specimens have THIVEX® and printing is done without a heated bed, molded and printed MRE samples show rather similar mechanical behavior. The small differences can be explained by slight changes in how particles are spread during fabrication.

## C.5 Effect of the heated bed and printing orientation

To further probe how printing conditions may affect the mechanical response, cyclic tensile tests are carried out on specimens printed with and without a heated bed, using in both cases a cross hatching orientation. Figure C.7a shows the upload curves of the stabilized $10^{\text{th}}$ cycle of the stress–strain responses of specimen printed with and without a heated bed for CIP contents of 70, 140 and 210 *phr*. Here again, the lines correspond to the mean response, and the shaded regions represent the range of values for all three specimens tested for each case. As explained in section C.1, printed specimens do not have a perfect rectangular cross section because of variations in filament paths and voids. To find the actual cross-sectional area, all specimen are analyzed post-mortem using image processing in order to assess the average cross-sectional area to be used in the nominal stress calculation and thus enable a fair comparison between the two printing conditions. The results indicate that the overall mechanical behavior is very similar whether or not a heated bed is used after compensating for the voids and cross-sectional changes.

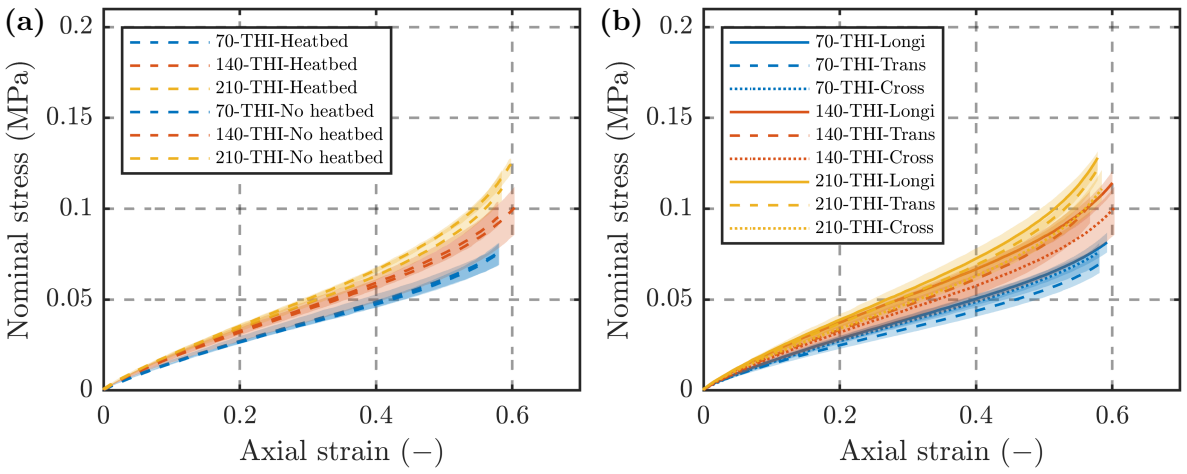


Figure C.7: (a) Upload curves of the stabilized $10^{\text{th}}$ cycle of the stress–strain responses comparing MRE specimens printed with and without a heated bed for 70, 140 and 210 *phr*. (b) Influence of printing orientation (longitudinal, transverse and cross, with a heated bed) on the stabilized tensile response for the same particle contents.

Figure C.7b examines how printing orientation affects results by comparing longitudinal, transverse and cross patterns, all printed with a heated bed. There are small differences in stiffness,

mainly because the filaments line up differently with the loading direction. In particular, in nearly all cases, the stiffest response is obtained when the filaments are aligned with the loading direction and the softest response when the filaments are transverse to the loading direction, while the samples printed with the cross-hatching strategy exhibit an intermediate stiffness. However, these differences are much smaller than what is usually seen in FDM-printed thermoplastics (Khan et al. 2022). This is because the DIW process allows filaments to spread and merge more easily than in FDM, which reduces anisotropy and creates a more uniform microstructure (Yirmibesoglu et al. 2021). As a result, within the fabrication variability highlighted by the shaded regions, the tensile response remains similar across all three orientations.

Overall, after accounting for cross-sectional area changes and voids, the tensile behavior of printed MRE samples is only slightly affected by using a heated bed or by the printing orientation. This shows that the DIW process, especially without a heated bed, produces samples with comparable mechanical properties at the macroscopic level, with only small differences due to filament deposition patterns.

# Appendix D
# Stereo digital image correlation (stereo-DIC)

In order to perform DIC, the surface of the sample needs to be covered by a speckle pattern exhibiting a wide distribution of gray levels (Jones and Iadicola 2018). Since the system is very soft and submitted to rather large strains and displacements, several routes have been tested to obtain a speckle pattern that does not crack during the test, is suitable for DIC, and does not modify the response of the sample. In what follows, all patterns are printed with the 210 *phr* ink and the substrate is fully made of Ecoflex™ 00-10, except in Figure D.1 where the pattern is first surrounded by Ecoflex™ 00-50 before pouring the substrate.

Unless the sample already exhibits naturally a speckled aspect, standard practice consists in first covering the sample with a layer of white paint before applying a black paint speckle, either with an airbrush or with a spray can. The former technique usually yields much thinner paint layers as well as finer speckle marks. However, in our case, paint applied with the airbrush does not sustain large displacements and starts cracking during the test, as shown in Figure D.1. Note that all samples are tested within minutes of applying the speckle patterns.

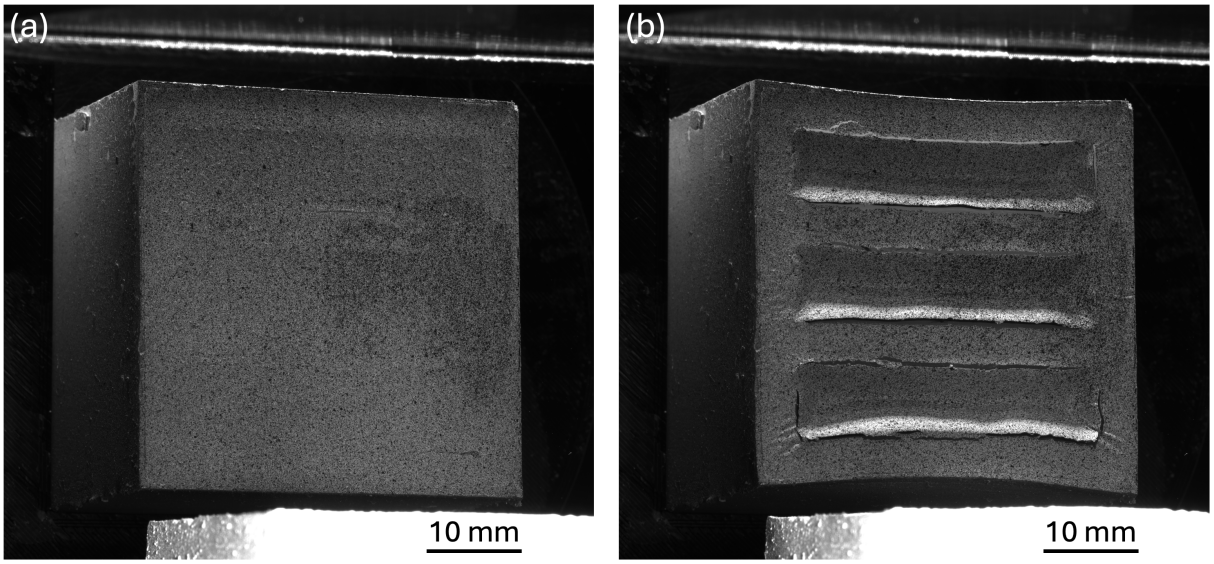


Figure D.1: Cubic three-strip sample (with one printed layer surrounded by Ecoflex™ 00-50 to minimize displacements) covered with a white paint layer and a black paint speckle, both applied with an airbrush, here shown (a) at rest and (b) at an applied field of 0.78 T.

On the other hand, a speckle pattern applied entirely with spray cans yields a paint layer that does not crack during the test, as evidenced in Figure D.2. Unfortunately, the black speckles are too large and too heterogeneous in size to permit systematic and correct pattern recognition, thereby leading the software to fail in properly re-projecting the defined zone of interest on

the views of both cameras (see Figure D.3a). It is very likely than in some elements of the correlation mesh (of size 80 pixels), marks are too large, thereby not providing enough contrasts in the elements.

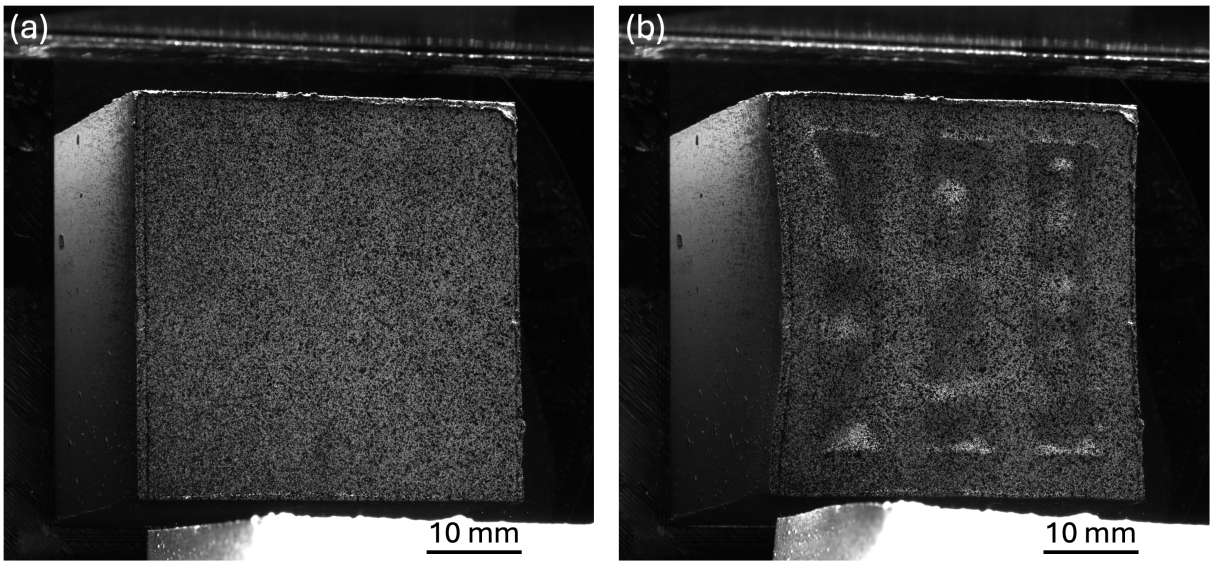


Figure D.2: Cubic three-strip sample (with one printed layer) covered with a white layer and a black speckle, both applied with a spray can, here shown (a) at rest and (b) at an applied field of 0.78 T.

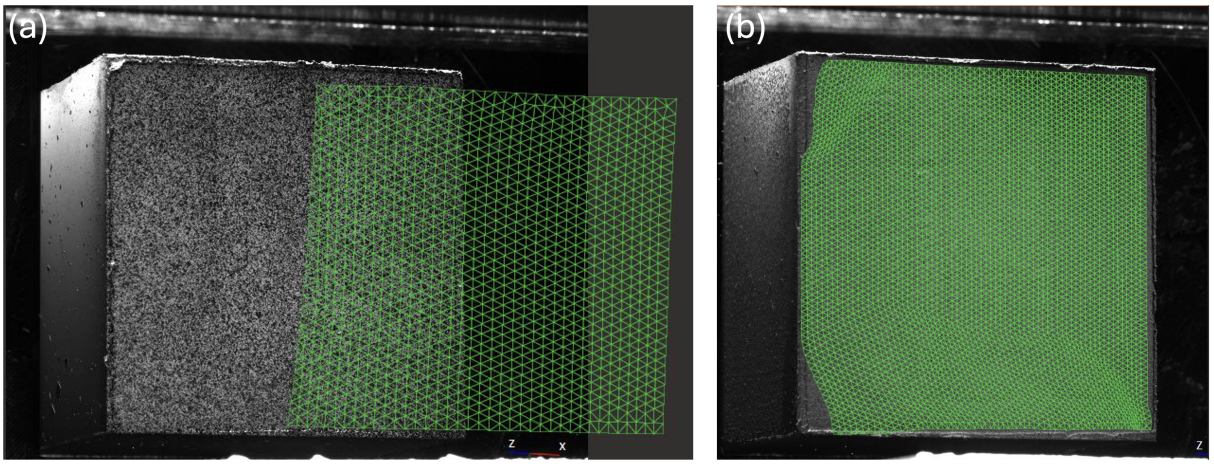


Figure D.3: Re-projection error of the defined zone of interest in the case of a speckle pattern where the white layer is applied with a spray can and the black speckle is applied with (a) a spray can, or (b) an airbrush.

If one applies the white layer with a spray can and the black speckle with an airbrush, the resulting speckle pattern still sustains the large displacements during the test, as seen in Figure D.4. However, despite a much narrower size distribution, the reconstruction still suffers large errors (see Figure D.3b, top and bottom left corners), probably here because the speckle is too fine and some marks are not resolved by three to five pixels, as typically recommended.

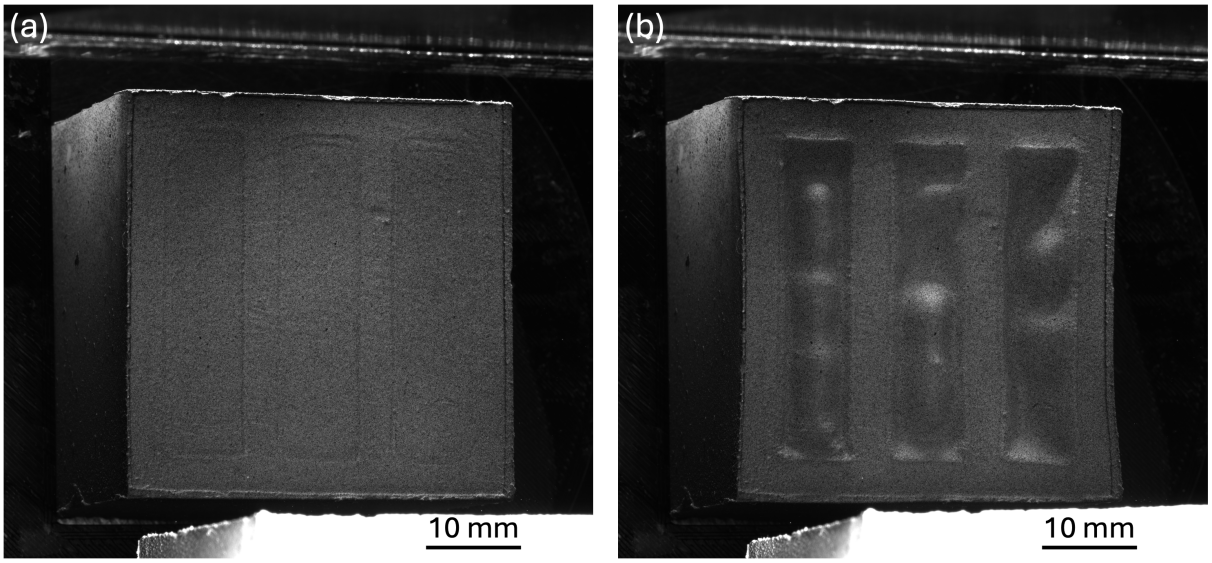


Figure D.4: Cubic three-strip sample (with one printed layer) covered with a white layer applied with a spray can and a black speckle aplied with an airbrush, here shown (a) at rest and (b) at an applied field of 0.78 T.

Ideally, one should have a black speckle finer than the one obtained with the spray can but larger than the one obtained with the airbrush, while exhibiting a rather tight size distribution. A very good compromise is to use the stamp system developed by Diani et al. 2026 and shown in Figure D.5. The black speckle is definitely reproducible in terms of size distribution and is even fixed in mark sizes, since the stamp bears 100 µm-diameter small posts randomly distributed in space, obtained by casting an elastomer in a 3D-printed mold.

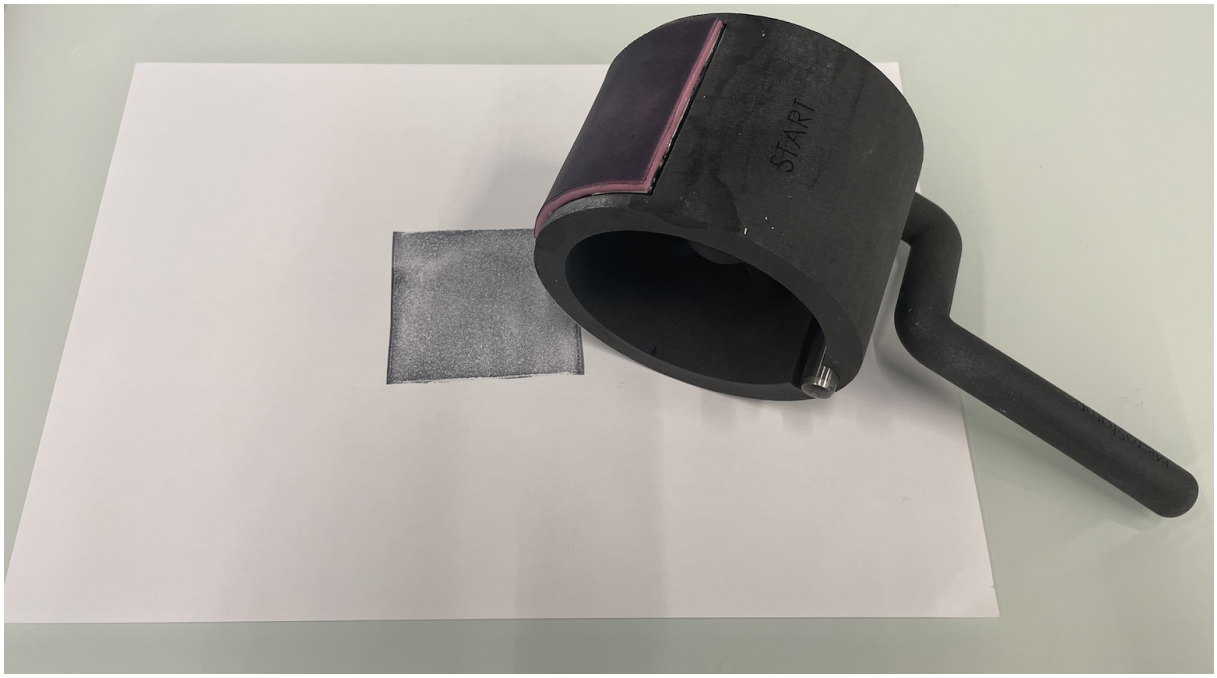


Figure D.5: Stamp system developed by Diani et al. 2026.

Since the samples are rather soft, two application modes are explored after the stamp has been

rolled on a black inkpad. The first one (Figure D.6a) consists in affixing the stamp to the upper plate of an Instron machine and lowering the crosshead so as to apply a 15 N force on the sample. The second one (Figure D.6b) uses directly the roller developed by Diani et al. 2026, along with a 3D-printed support from which the samples emerges by 1 mm, in order to help sustaining a constant pressure throughout the rolling movement. This second technique proves more successful in obtaining dots of the same black intensity, as can be seen by comparing the two speckles in Figure D.6.

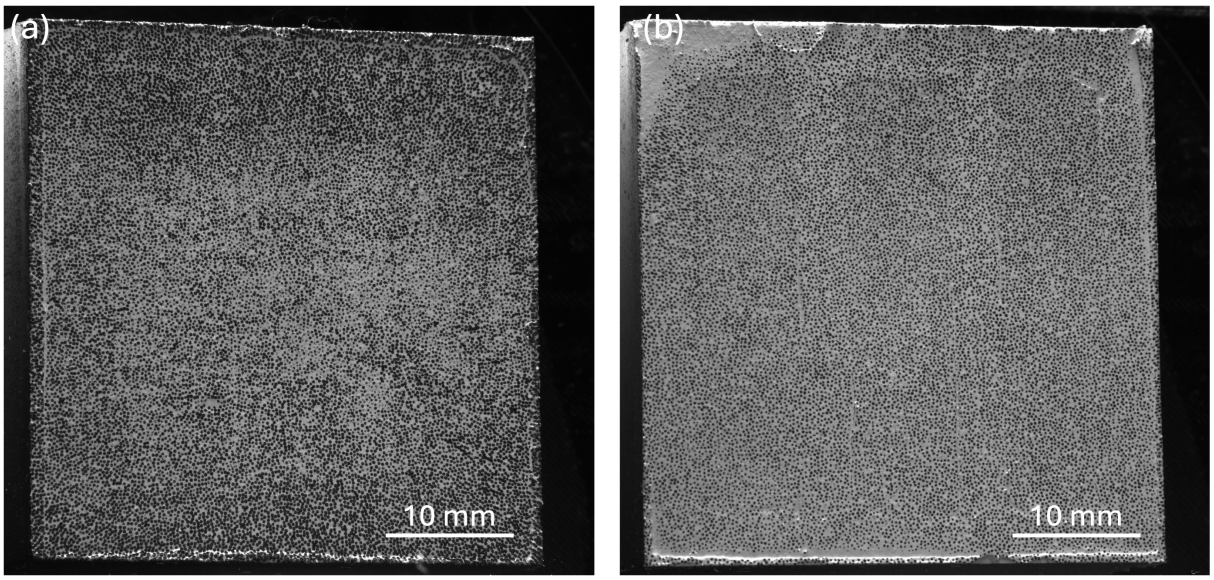


Figure D.6: Cubic three-strip sample (with one printed layer) covered with a white layer applied with a spray can and a black speckle applied with the stamp developed by Diani et al. 2026. (a) Stamp impressed on the surface using an Instron machine to limit the applied pressure to 15 N, and (b) stamp applied with the roller developed by Diani et al. 2026, using a 3D-printed support.

Though a slight drawback is that the minimum marker size available is 100 µm, thereby limiting the achievable spatial resolution, one has to note that this speckle pattern consistently permits proper re-projection of the defined zone of interest on the views of both cameras.

Finally, it is important to assess whether the applied speckle pattern modifies the response of the specimen, notably here because we deal with very soft materials. For this purpose, a cubic four-disc sample (with one printed layer) is fabricated with a substrate containing black pigment. The fact that the sample is very dark permits to use that "darkness" as a black background (thereby necessitating no application of paint) and to apply only a white speckle by replacing the black inkpad with a white one. The obtained "inverted" speckle, using the above-mentioned rolling method, is shown in Figure D.7a. It is difficult however to systematically obtain an homogeneous application (several trials are sometimes necessary) due to the fact that the white ink is more tacky and dries very rapidly on the stamp. Even when the application is somewhat successful, some dots remain more lightly impressed than others and the mesh re-projection exhibits some minor defects as discussed later in the context of Figure D.9a.

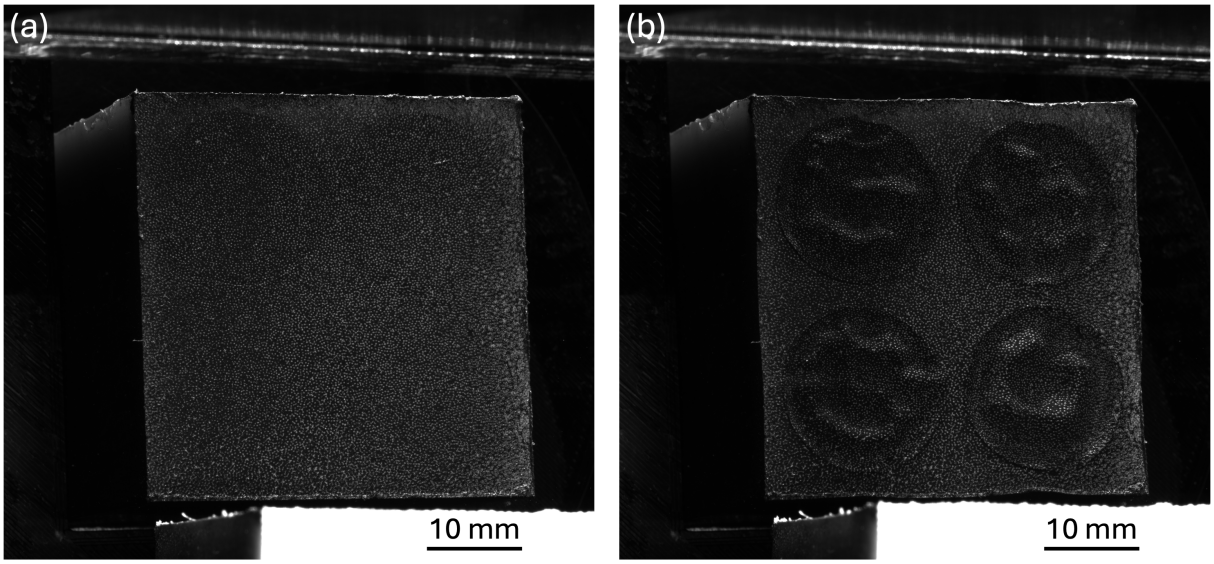


Figure D.7: Cubic four-disc sample (with one printed layer) with substrate containing black pigment covered with a white speckle applied with the stamp, here shown (a) at rest and (b) at an applied field of 0.78 T.

For comparison the same sample is subsequently washed and covered with a white layer applied with a spray can and a black speckle applied with the stamp (Figure D.8a). A preliminary visual comparison of the deformed images of the same sample bearing either a minimally-invasive speckle pattern (Figure D.7b) or a fully-covering speckle pattern (Figure D.8b) does not reveal significant differences in the obtained patterns.

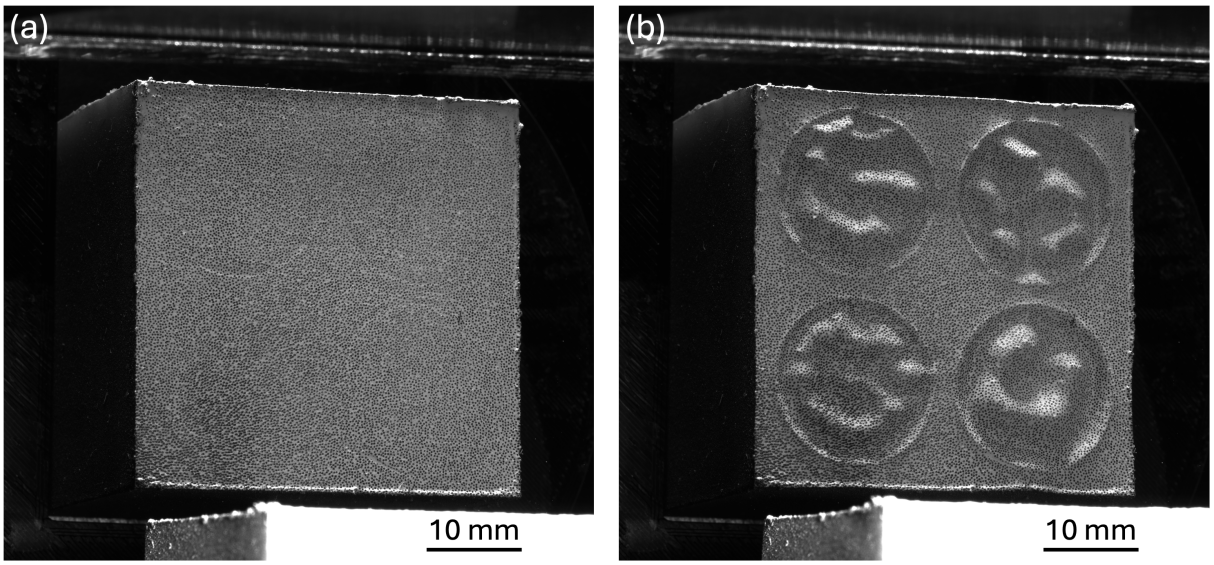


Figure D.8: Cubic four-disc sample (with one printed layer) with substrate containing black pigment covered with a white layer applied with a spray can and a black speckle applied with the stamp, here shown (a) at rest and (b) at an applied field of 0.78 T.

Despite the minor defects in the mesh re-projection observed in the case of the white speckle, the stereo-DIC process somehow still proceeds—even though it is unclear how to assess properly the errors incurred by this re-projection error. Nevertheless, the vertical displacement fields obtained

by stereo-DIC at the maximum applied field of 0.78 T are reported in Figure D.9 for the two speckles. The distributions of the obtained vertical displacement fields are very similar, thus confirming that the white layer does not affect the general pattern of the instability. One note however a respective difference of 26 µm and 47 µm between the maximum and minimum values obtained with the two different speckles. These values are moderately larger than the noise-floor of the DIC computations (see later discussion), here estimated (conservatively) at 7 µm and 11 µm. It thus seems that if the white layer does not change the geometric distribution of the instability pattern, it may reduce the amplitude of the extremum displacements. Note however that this effect remains below a 7% error on the maximum amplitude that is $\sim$ 550 µm in the present case, when some cases see maximum amplitudes above 1 mm.

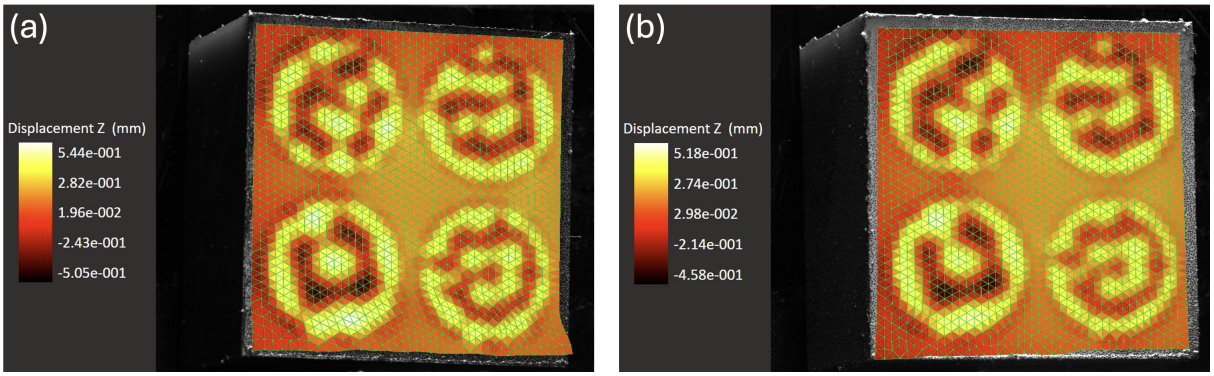


Figure D.9: Stereo-DIC vertical displacement fields obtained for an applied field of 0.78 T on the cubic four-disc sample (with one printed layer) with substrate containing black pigment when (a) covered with a white speckle applied with the stamp, and (b) covered with a white layer applied with a spray can and a black speckle applied with the stamp.

As a compromise between an unknown and unpredictable error due to mesh re-projection issues and a slight underestimation of the maximum amplitudes, the white layer-black speckle pattern method (applied with a spray can and the stamp, respectively) is retained. Guided by the speckle size and spatial distribution, the mesh size is fixed at 80 pixels, ensuring that between three and four marks can be found within each element, as typically recommended for the technique (Jones and Iadicola 2018). Such a mesh provides displacement values with a spacing of 1 mm.

Variance and bias errors are evaluated for the stereo-DIC setup and processing parameters by analyzing 20 static images of a sample bearing the selected speckle. As recommended by Jones and Iadicola 2018, the variance is obtained by averaging the spatial standard deviation of the static images, and the bias by taking the mean displacement of the static images (that should be zero). The obtained values are 5.4 µm and 6.4 µm, respectively for the validation test presented in chapter 3. This yields an average of 6 µm, representative of the noise-floor. Note that this does not (and cannot) include variance errors present during the actual test and linked to possible electromagnetically-induced noise and reflections at the surface of the sample.

A final point concerns the height of the sample, which has been reduced to 38 mm for the experiments versus the nominal 40 mm of the numerical model. As discussed in chapter 4, thick films trigger global instability modes across the whole sample, thereby yielding very large

displacements of the sample's surface. In this case, two problems arise: 1) the sample can touch and degrade the gold coating of the mirror, and 2) the sample's vertical movement impinges on the reflection of its surface by the mirror. In this latter case, stereo-DIC fails as soon as the image no longer contains the entirety of the zone of interest defined in the initial image of the sample's surface (see Figure D.10).

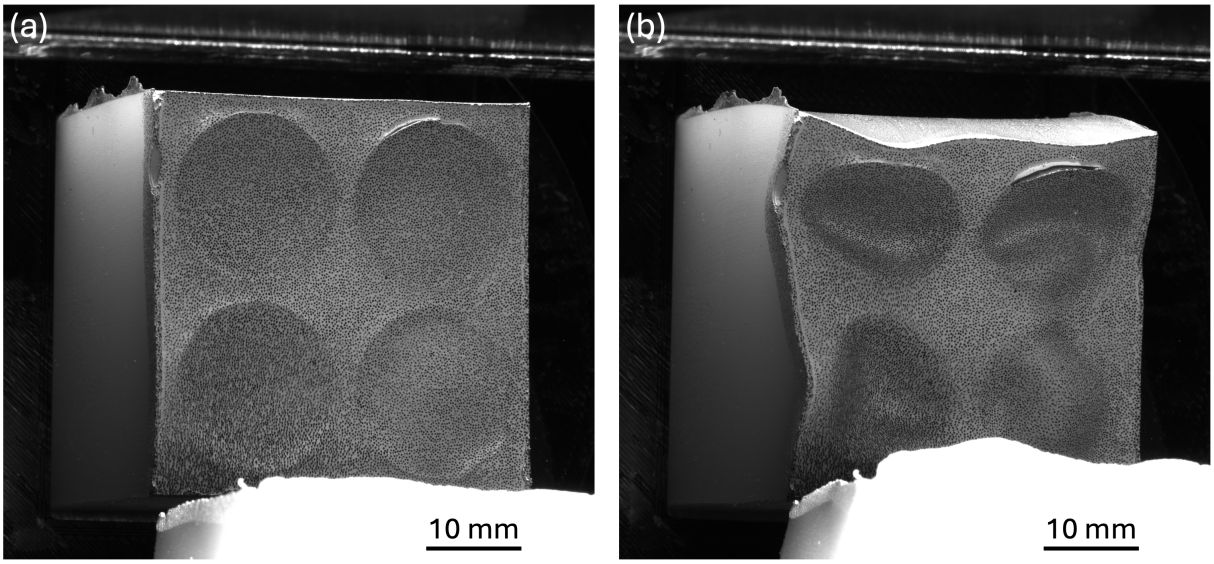


Figure D.10: Cubic four-disc sample (with two printed layers and a height of 40 mm), here shown at an applied field of (a) 0.39 T and (b) 0.78 T.

# Appendix E
# 3D magnetic profile contour maps

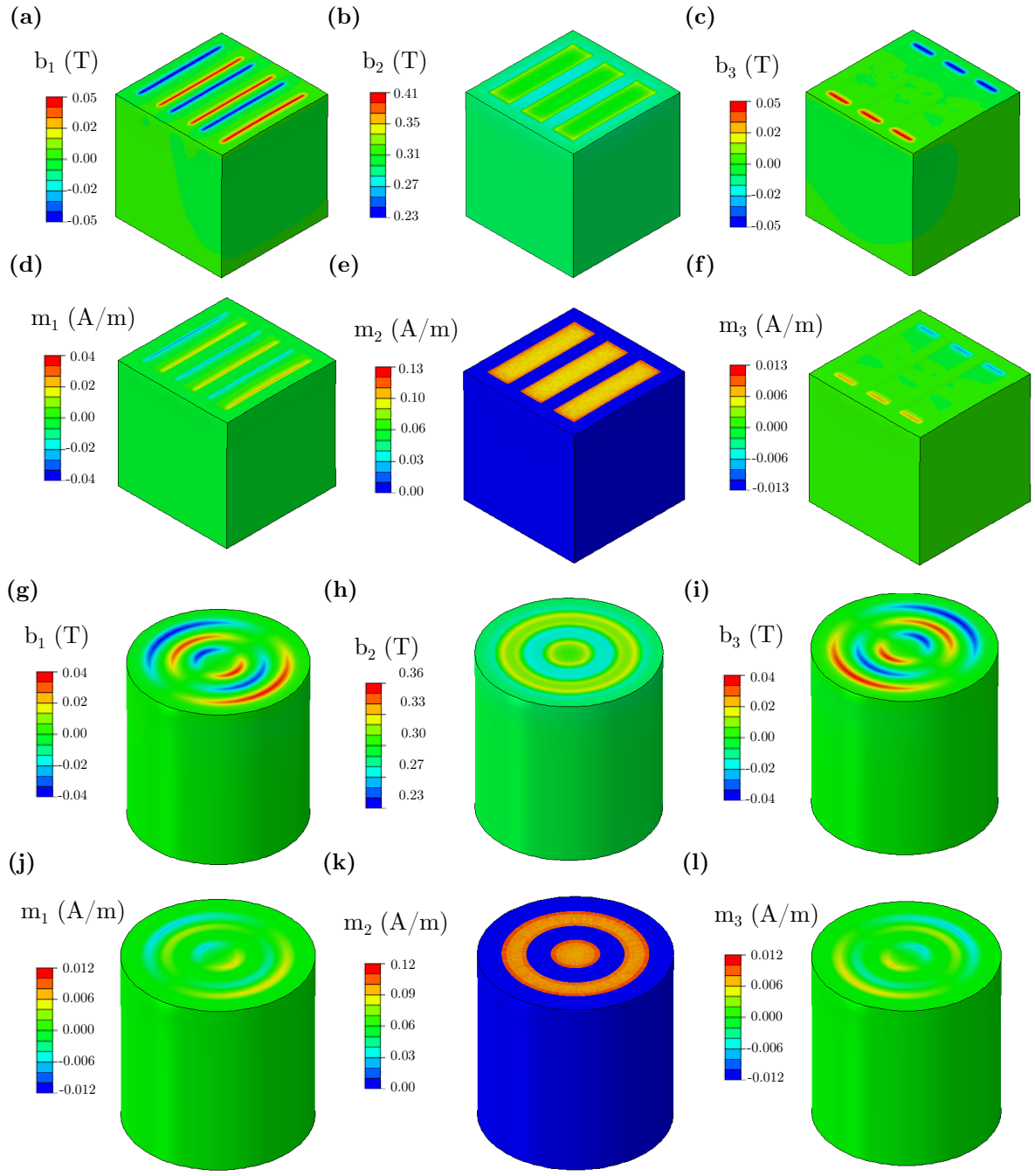


Figure E.1: Numerical Eulerian magnetic field components $(b_1, b_2, b_3)$ and magnetization components $(m_1, m_2, m_3)$ evaluated at $b_0 = 0.3$ T for (a-f) the cubic three-strip topology, and (g-l) the cylindrical disc-annulus topology .

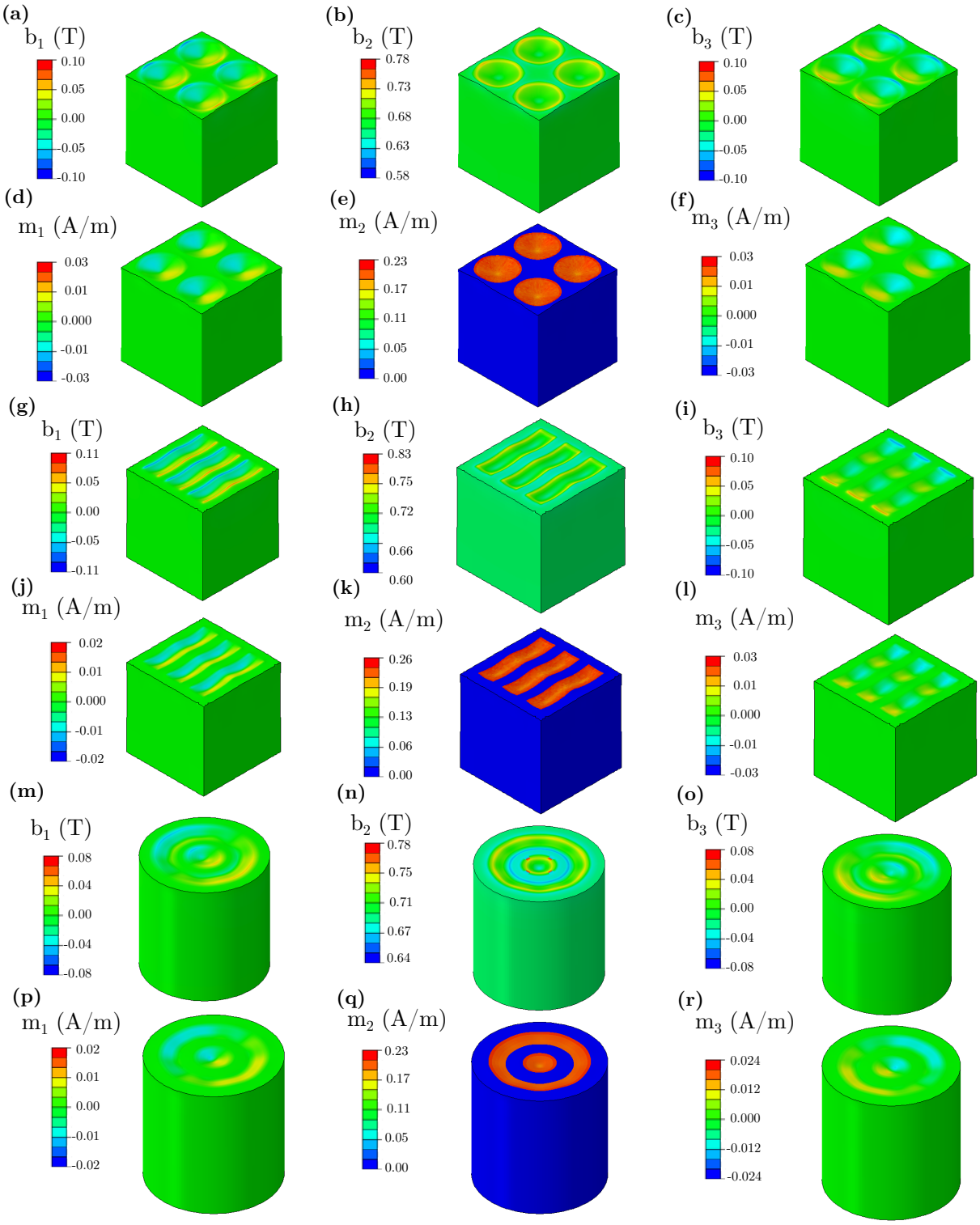


Figure E.2: Numerical Eulerian magnetic field components $(b_1, b_2, b_3)$ and magnetization components $(m_1, m_2, m_3)$ evaluated for $h_f = 0.7$ mm at high magnetic field (post-wrinkling state). Panels are grouped by topology: (a-f) cubic four-discs topology, (g-l) cubic three-strip topology, and (m-r) cylindrical disc-annulus topology.

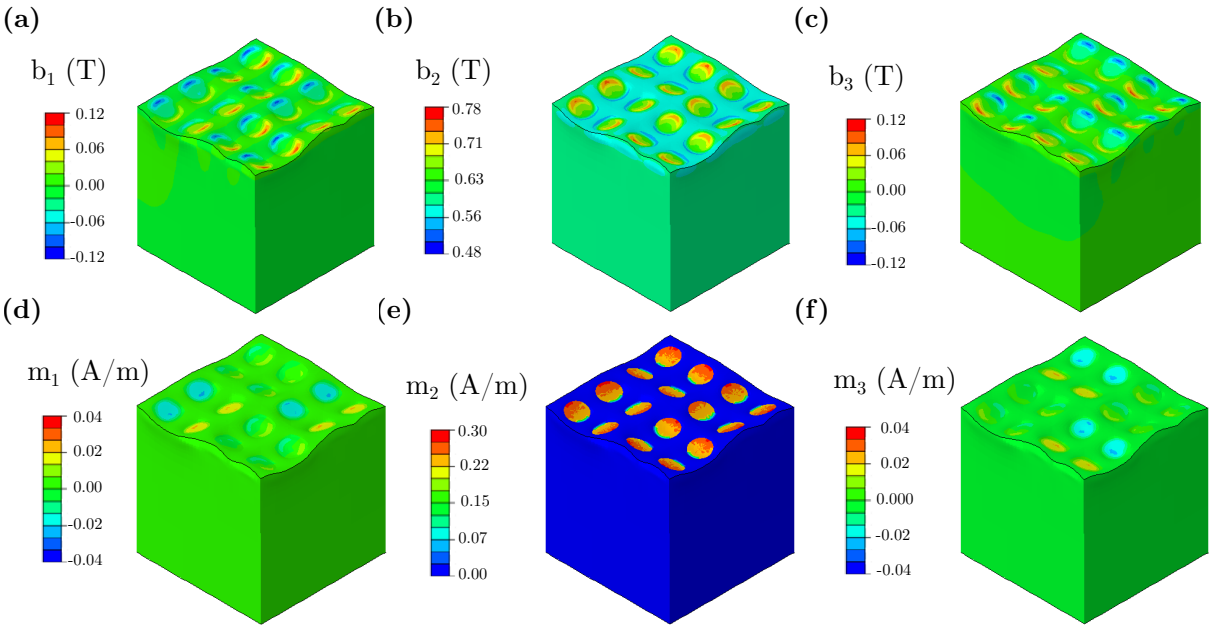


Figure E.3: Numerical Eulerian magnetic field components $(\mathrm{b}_1, \mathrm{b}_2, \mathrm{b}_3)$ and magnetization components $(\mathrm{m}_1, \mathrm{m}_2, \mathrm{m}_3)$ evaluated for the cubic sixteen-disc topology at $b_0 = 0.6$ T.

# Bibliography


Abbasi, A., Chen, T., Aymon, B. F., & Reis, P. M. (2024). Leveraging the Snap Buckling of Bistable Magnetic Shells to Design a Refreshable Braille Dot. *Advanced Materials Technologies*, *9*(3), 2301344. https://doi.org/10.1002/admt.202301344

Alamán, J., Alicante, R., Peña, J. I., & Sánchez-Somolinos, C. (2016). Inkjet printing of functional materials for optical and photonic applications. *Materials*, *9*(11), 910. https://doi.org/10.3390/ma9110910

Alapan, Y., Karacakol, A. C., Guzelhan, S. N., Isik, I., & Sitti, M. (2020). Reprogrammable shape morphing of magnetic soft machines. *Science Advances*, *6*(38), eabc6414. https://doi.org/10.1126/sciadv.abc6414

Alkhalaf, A., Hooshiar, A., & Dargahi, J. (2020). Composite magnetorheological elastomers for tactile displays: Enhanced MR-effect through bi-layer composition. *Composites Part B: Engineering*, *190*, 107888. https://doi.org/10.1016/j.compositesb.2020.107888

Allen, H. G., & Feng, Z. (1998). Classification of Structural Sandwich Panel Behaviour. In A. Vautrin (Ed.), *Mechanics of Sandwich Structures* (pp. 1–12). Springer Netherlands. https://doi.org/10.1007/978-94-015-9091-4_1

And, N. S., & De Kee, D. (2001). Simple shear, hysteresis and yield stress in biofluids. *The Canadian Journal of Chemical Engineering*, *79*(1), 36–41. https://doi.org/10.1002/cjce.5450790107

Audoly, B., & Boudaoud, A. (2008a). Buckling of a stiff film bound to a compliant substrate—Part I: Formulation, linear stability of cylindrical patterns, secondary bifurcations. *Journal of the Mechanics and Physics of Solids*, *56*(7), 2401–2421. https://doi.org/10.1016/j.jmps.2008.03.003

Audoly, B., & Boudaoud, A. (2008b). Buckling of a stiff film bound to a compliant substrate—Part II: A global scenario for the formation of herringbone pattern. *Journal of the Mechanics and Physics of Solids*, *56*(7), 2422–2443. https://doi.org/10.1016/j.jmps.2008.03.002

Audoly, B., & Boudaoud, A. (2008c). Buckling of a stiff film bound to a compliant substrate—Part III: Herringbone solutions at large buckling parameter. *Journal of the Mechanics and Physics of Solids*, *56*(7), 2444–2458. https://doi.org/10.1016/j.jmps.2008.03.001

Ausanio, G., Hison, C. L., Iannotti, V., Lanotte, L., & Lanotte, L. (2011). Magneto-piezoresistance in elastomagnetic composites. *Journal of Applied Physics*, *110*(6). https://doi.org/10.1063/1.3634120

Aziz, S. A., Mazlan, S. A., Ismail, N. N., Choi, S.-B., & Yunus, N. A. (2017). An enhancement of mechanical and rheological properties of magnetorheological elastomer with multiwall carbon nanotubes. *J. Intell. Mater. Syst. Struct.*, *28*(20), 3127–3138. https://doi.org/10.1177/1045389X17705211

Bahl, S., Nagar, H., Singh, I., & Sehgal, S. (2020). Smart materials types, properties and applications: A review. *Materials Today: Proceedings*, *28*, 1302–1306. https://doi.org/10.1016/j.matpr.2020.04.505

Bandyopadhyay, A., & Heer, B. (2018). Additive manufacturing of multi-material structures. *Materials Science and Engineering: R: Reports*, *129*, 1–16. https://doi.org/10.1016/j.mser.2018.04.001

Bastola, A., Paudel, M., & Li, L. (2018). Development of hybrid magnetorheological elastomers by 3D printing. *Polymer*, *149*, 213–228. https://doi.org/10.1016/j.polymer.2018.06.076

Bastola, A., Paudel, M., & Li, L. (2020). Line-patterned hybrid magnetorheological elastomer developed by 3D printing. *Journal of Intelligent Material Systems and Structures*, *31*(3), 377–388. https://doi.org/10.1177/1045389X19891557

Bastola, A., He, Y., Im, J., Rivers, G., Wang, F., Worsley, R., Austin, J. S., Nelson-Dummett, O., Wildman, R. D., & Hague, R. (2023). Formulation of functional materials for inkjet printing: A pathway towards fully 3D printed electronics. *Materials Today Electronics*, *6*, 100058. https://doi.org/10.1016/j.mtelec.2023.100058

Bastola, A. K., & Hossain, M. (2021). The shape – morphing performance of magnetoactive soft materials. *Materials & Design*, *211*, 110172. https://doi.org/10.1016/j.matdes.2021.110172

Bauman, J. T. (2008). Fatigue, stress, and strain of rubber components. A guide for design engineers Hanser Publishers.

Bellan, C., & Bossis, G. (2012). Field dependence of viscoelastic properties of MR elastomers. *International Journal of Modern Physics B*. https://doi.org/10.1142/S0217979202012499

Biot, M. A. (1963). Surface instability of rubber in compression. *Applied Scientific Research*, *12*(2), 168–182. https://doi.org/10.1007/BF03184638

Boczkowska, A., & Awietj, S. (2012). Microstructure and Properties of Magnetorheological Elastomers. In A. Boczkowska (Ed.), *Advanced Elastomers - Technology, Properties and Applications*. InTech. https://doi.org/10.5772/50430

Bodelot, L., Voropaieff, J.-P., & Pössinger, T. (2018). Experimental investigation of the coupled magneto-mechanical response in magnetorheological elastomers. *Experimental Mechanics*, *58*(2), 207–221. https://doi.org/10.1007/s11340-017-0334-7

Borin, D., Stepanov, G., & Dohmen, E. (2019). On anisotropic mechanical properties of heterogeneous magnetic polymeric composites. *Philosophical Transactions of the Royal Society A: Mathematical, Physical and Engineering Sciences*, *377*(2143), 20180212. https://doi.org/10.1098/rsta.2018.0212

Bowden, N., Brittain, S., Evans, A. G., Hutchinson, J. W., & Whitesides, G. M. (1998). Spontaneous formation of ordered structures in thin films of metals supported on an elastomeric polymer. *Nature*, *393*(6681), 146–149. https://doi.org/10.1038/30193

Bratek-Skicki, A. (2021). Towards a new class of stimuli-responsive polymer-based materials – Recent advances and challenges. *Applied Surface Science Advances*, *4*, 100068. https://doi.org/10.1016/j.apsadv.2021.100068

Breid, D., & Crosby, A. J. (2011). Effect of stress state on wrinkle morphology. *Soft Matter*, *7*(9), 4490–4496. https://doi.org/10.1039/C1SM05152K

Brown, W. F. (1966). The Energy Method. In W. F. Brown (Ed.), *Magnetoelastic Interactions* (pp. 71–107). Springer. https://doi.org/10.1007/978-3-642-87396-6_3

Brusa Da Costa Linn, L., Danas, K., & Bodelot, L. (2022). Towards 4D Printing of Very Soft Heterogeneous Magnetoactive Layers for Morphing Surface Applications via Liquid Additive Manufacturing. *Polymers*, *14*(9), 1684. https://doi.org/10.3390/polym14091684

Bustamante, R., Dorfmann, A., & Ogden, R. (2008). On variational formulations in nonlinear magnetoelastostatics. *Mathematics and Mechanics of Solids*, *13*(8), 725–745. https://doi.org/10.1177/1081286507079832

Cai, S., Breid, D., Crosby, A., Suo, Z., & Hutchinson, J. (2011). Periodic patterns and energy states of buckled films on compliant substrates. *Journal of the Mechanics and Physics of Solids*, *59*(5), 1094–1114. https://doi.org/10.1016/j.jmps.2011.02.001

Calais, T., Sebastian Joseph, V., Jain, S., Stalin, T., & Valdivia Y Alvarado, P. (2022). Mechanical characterization of 3D-printed silicone/epoxy hybrids. *Materials Today: Proceedings*, *70*, 218–223. https://doi.org/10.1016/j.matpr.2022.09.024

Calvo-Correas, T., Shirole, A., Alonso-Varona, A., Palomares, T., Weder, C., Corcuera, M. A., & Eceiza, A. (2020). Impact of the Combined Use of Magnetite Nanoparticles and Cellulose Nanocrystals on the Shape-Memory Behavior of Hybrid Polyurethane Bionanocomposites. *Biomacromolecules*, *21*(6), 2032–2042. https://doi.org/10.1021/acs.biomac.9b01764

Cao, C., Chan, H. F., Zang, J., Leong, K. W., & Zhao, X. (2014). Harnessing localized ridges for high-aspect-ratio hierarchical patterns with dynamic tunability and multifunctionality. *Advanced Materials*, *26*(11), 1763–1770. https://doi.org/10.1002/adma.201304589

Cao, X., Xuan, S., Sun, S., Xu, Z., Li, J., & Gong, X. (2021). 3D Printing Magnetic Actuators for Biomimetic Applications. *ACS Applied Materials & Interfaces*, *13*(25), 30127–30136. https://doi.org/10.1021/acsami.1c08252

Cao, Y., & Hutchinson, J. W. (2012a). From wrinkles to creases in elastomers: The instability and imperfection-sensitivity of wrinkling. *Proceedings of the Royal Society A: Mathematical, Physical and Engineering Sciences*, *468*(2137), 94–115. https://doi.org/10.1098/rspa.2011.0384

Cao, Y., & Hutchinson, J. W. (2012b). Wrinkling Phenomena in Neo-Hookean Film/Substrate Bilayers. *Journal of Applied Mechanics*, *79*(3), 031019. https://doi.org/10.1115/1.4005960

Carlson, J. D., & Jolly, M. R. (2000). MR fluid, foam and elastomer devices. *mechatronics*, *10*(4–5), 555–569. https://doi.org/10.1016/S0957-4158(99)00064-1

Carlson, J. D., & Spencer, B. F. (2021). Magnetorheological Fluid Dampers for Seismic Control. https://doi.org/10.1115/DETC97/VIB-4124

Cerda, E., & Mahadevan, L. (2003). Geometry and Physics of Wrinkling. *Physical Review Letters*, *90*(7), 074302. https://doi.org/10.1103/PhysRevLett.90.074302

Cerda, E., Ravi-Chandar, K., & Mahadevan, L. (2002). Wrinkling of an elastic sheet under tension. *Nature*, *419*(6907), 579–580. https://doi.org/10.1038/419579b

Cesarano, J., & Calvert, P. D. (2000). *Freeforming objects with low-binder slurry* (U.S. pat. No. 6027326A). https://patents.google.com/patent/US6027326A/en

Chan, E. P., & Crosby, A. J. (2006). Fabricating Microlens Arrays by Surface Wrinkling. *Advanced Materials*, *18*(24), 3238–3242. https://doi.org/10.1002/adma.200601595

Chan, E. P., Smith, E. J., Hayward, R. C., & Crosby, A. J. (2008). Surface wrinkles for smart adhesion. *Advanced materials*, *20*(4), 711–716. https://doi.org/10.1002/adma.200701530

Chandra, D., Yang, S., & Lin, P.-C. (2007). Strain responsive concave and convex microlens arrays. *Applied Physics Letters*, *91*(25). https://doi.org/10.1063/1.2827185

Chater, E., & Hutchinson, J. W. (1984). On the propagation of bulges and buckles. https://doi.org/10.1115/1.3167611

Chen, H., Wang, X., Xue, F., Huang, Y., Zhou, K., & Zhang, D. (2018). 3D printing of SiC ceramic: Direct ink writing with a solution of preceramic polymers. *Journal of the European Ceramic Society*, *38*(16), 5294–5300. https://doi.org/10.1016/j.jeurceramsoc.2018.08.009

Chen, V. W., Arora, N., Goshkoderia, A., Willey, C. L., Turgut, Z., Buskohl, P. R., Rudykh, S., & Juhl, A. T. (2023). Mechanical instability tuning of a magnetorheological elastomer composite laminate. *Composites Part B: Engineering*, *251*, 110472. https://doi.org/10.1016/j.compositesb.2022.110472

Chen, X., & Hutchinson, J. W. (2004). Herringbone buckling patterns of compressed thin films on compliant substrates. *J. Appl. Mech.*, *71*(5), 597–603. https://doi.org/10.1115/1.1756141

Chen, Z., Zhao, D., Liu, B., Nian, G., Li, X., Yin, J., Qu, S., & Yang, W. (2019). 3D Printing of Multifunctional Hydrogels. *Advanced Functional Materials*, *29*(20), 1900971. https://doi.org/10.1002/adfm.201900971

Chhabra, R. P., & Richardson, J. F. (2011). *Non-Newtonian flow and applied rheology: Engineering applications*. Butterworth-Heinemann. https://doi.org/10.1016/B978-0-7506-8532-0.X0001-7

Chiu, W.-T., Watanabe, Y., Tahara, M., Inamura, T., & Hosoda, H. (2023). Investigations of Shape Deformation Behaviors of the Ferromagnetic Ni–Mn–Ga Alloy/Porous Silicone Rubber Composite towards Actuator Applications. *Micromachines*, *14*(8), 1604. https://doi.org/10.3390/mi14081604

Christie, M. D., Fredericksen, T., & Li, W. (2023). Development of a Magnetorheological Elastomer Actuator for a Mixed Reality Haptic Glove. *2023 IEEE/ASME International Conference on Advanced Intelligent Mechatronics (AIM)*, 507–510. https://doi.org/10.1109/AIM46323.2023.10196291

Chung, J. Y., Youngblood, J. P., & Stafford, C. M. (2007). Anisotropic wetting on tunable micro-wrinkled surfaces. *Soft Matter*, *3*(9), 1163–1169. https://doi.org/10.1039/B705112C

Coulomb, J.-L. (1981). Finite elements three dimensional magnetic field computation. *IEEE Transactions on Magnetics*, *17*(6), 3241–3246. https://doi.org/10.1109/TMAG.1981.1061587

Danas, K. (2017). Effective response of classical, auxetic and chiral magnetoelastic materials by use of a new variational principle. *Journal of the Mechanics and Physics of Solids*, *105*, 25–53. https://doi.org/10.1016/j.jmps.2017.04.016

Danas, K., Kankanala, S., & Triantafyllidis, N. (2012). Experiments and modeling of iron-particle-filled magnetorheological elastomers. *Journal of the Mechanics and Physics of Solids*, *60*(1), 120–138. https://doi.org/10.1016/j.jmps.2011.09.006

Danas, K., & Triantafyllidis, N. (2014). Instability of a magnetoelastic layer resting on a non-magnetic substrate. *Journal of the Mechanics and Physics of Solids*, *69*, 67–83. https://doi.org/10.1016/j.jmps.2014.04.003

Danas, K., Nakano, M., & Sebald, G. (2025). A continuum magneto-viscoelastic model for isotropic soft magnetorheological elastomers: Experiments, theory and numerical implementation. *Mechanics of Materials*, *200*, 105187. https://doi.org/10.1016/j.mechmat.2024.105187

Dargazany, R., Khiêm, V. N., & Itskov, M. (2014). A generalized network decomposition model for the quasi-static inelastic behavior of filled elastomers. *International Journal of Plasticity*, *63*, 94–109. https://doi.org/10.1016/j.ijplas.2013.12.004

De Pedro, S., Cadarso, V., Muñoz-Berbel, X., Plaza, J., Sort, J., Brugger, J., Büttgenbach, S., & Llobera, A. (2014). PDMS-based, magnetically actuated variable optical attenuators obtained by soft lithography and inkjet printing technologies. *Sensors and Actuators A: Physical*, *215*, 30–35. https://doi.org/10.1016/j.sna.2014.01.021

Deng, X., Liu, Z., Yu, H., Xiao, Z., & Zhang, G. (2015). Isotropic and anisotropic nanocrystalline NdFeB bulk magnets prepared by binder-free high-velocity compaction tech-

nique. *Journal of Magnetism and Magnetic Materials*, *390*, 26–30. https://doi.org/10.1016/j.jmmm.2015.04.075

Derby, B. (2010). Inkjet Printing of Functional and Structural Materials: Fluid Property Requirements, Feature Stability, and Resolution. *Annual Review of Materials Research*, *40*(1), 395–414. https://doi.org/10.1146/annurev-matsci-070909-104502

Dhiman, N. K., Salodkar, S. M., Gagandeep, & Susheel, C. (2024). Advances in Modeling and Control of Magnetorheological Elastomers for Engineering Applications. *Archives of Computational Methods in Engineering*, *31*(3), 1823–1865. https://doi.org/10.1007/s11831-023-10031-0

Diani, J., Geraud, G., Coq, A., & Kuzyara, V. (2026). Stamps for pattern applications for digital image correlation and marker tracking [Under revision]. *Experimental Techniques*.

Diani, J., Fayolle, B., & Gilormini, P. (2009). A review on the Mullins effect. *European Polymer Journal*, *45*(3), 601–612. https://doi.org/10.1016/j.eurpolymj.2008.11.017

Dorfmann, A., & Ogden, R. (2003). Magnetoelastic modelling of elastomers. *European Journal of Mechanics-A/Solids*, *22*(4), 497–507. https://doi.org/10.1016/s0997-7538(03)00067-6

Dorfmann, A., & Ogden, R. (2004). Nonlinear magnetoelastic deformations of elastomers. *Acta Mechanica*, *167*(1–2), 13–28. https://doi.org/10.1007/s00707-003-0061-2

Dorfmann, A., & Ogden, R. (2005). Some problems in nonlinear magnetoelasticity. *Zeitschrift für angewandte Mathematik und Physik ZAMP*, *56*(4), 718–745. https://doi.org/10.1007/s00033-004-4066-z

Dorn, C., Bodelot, L., & Danas, K. (2021). Experiments and Numerical Implementation of a Boundary Value Problem Involving a Magnetorheological Elastomer Layer Subjected to a Nonuniform Magnetic Field. *Journal of Applied Mechanics*, *88*(7), 071004. https://doi.org/10.1115/1.4050534

Duenas, T. A., & Carman, G. P. (2000). Large magnetostrictive response of Terfenol-D resin composites. *Journal of Applied Physics*, *87*(9), 4696–4701. https://doi.org/10.1063/1.373133

Duncan, B., Weeks, R. D., Barclay, B., Beck, D., Bluem, P., Rojas, R., Plaut, M., Russo, J., Uzel, S. G. M., Lewis, J. A., & Fedynyshyn, T. (2023). Low-Loss Graded Dielectrics via Active Mixing of Nanocomposite Inks during 3D Printing. *Advanced Materials Technologies*, *8*(3), 2201496. https://doi.org/10.1063/1.373133

Duty, C., Ajinjeru, C., Kishore, V., Compton, B., Hmeidat, N., Chen, X., Liu, P., Hassen, A. A., Lindahl, J., & Kunc, V. (2018). What makes a material printable? A viscoelastic model for extrusion-based 3D printing of polymers. *Journal of Manufacturing Processes*, *35*, 526–537. https://doi.org/10.1016/j.jmapro.2018.08.008

Efimenko, K., Rackaitis, M., Manias, E., Vaziri, A., Mahadevan, L., & Genzer, J. (2005). Nested self-similar wrinkling patterns in skins. *Nature materials*, *4*(4), 293–297. https://doi.org/10.1038/nmat1342

Einstein, A. (1905). *Eine neue bestimmung der molekü̈ldimensionen* [Doctoral dissertation, ETH Zurich]. https://doi.org/10.3929/ethz-a-000565688

Euler, L. (1744). Methodus inveniendi lineas curvas maximi minimive proprietate gaudentes, sive solutio problematis isoperimetrici lattissimo sensu accepti. *Lausanne Geneva: Marcum-Michaelem Bousquet*, 1–322. https://scholarlycommons.pacific.edu/euler-works/65

Euler, L. (1759). Sur la force des colonnes. *Mémoires de l'académie des sciences de Berlin*, 252–282. https://scholarlycommons.pacific.edu/euler-works/238

Falahati, M., Ahmadvand, P., Safaee, S., Chang, Y.-C., Lyu, Z., Chen, R., Li, L., & Lin, Y. (2020). Smart polymers and nanocomposites for 3D and 4D printing. *Materials Today*, *40*, 215–245. https://doi.org/10.1016/j.mattod.2020.06.001

Fang, F. F., Choi, H. J., & Seo, Y. (2010). Sequential Coating of Magnetic Carbonyliron Particles with Polystyrene and Multiwalled Carbon Nanotubes and Its Effect on Their Magnetorheology. *ACS Applied Materials & Interfaces*, *2*(1), 54–60. https://doi.org/10.1021/am900577w

Ferry, J. D. (1948). Viscoelastic properties of polymer solutions. *J. Res. Natl. Bur. Stand*, *41*(1), 53–62. https://doi.org/10.1149/1.2428174

Ferry, J. D., & Myers, H. S. (1961). Viscoelastic properties of polymers. *Journal of The Electrochemical Society*, *108*(7), 142C. https://doi.org/10.1149/1.2428174

Frederiksen, A. H., Dalklint, A., Sigmund, O., & Poulios, K. (2025). Improved third medium formulation for 3D topology optimization with contact. *Computer Methods in Applied Mechanics and Engineering*, *436*, 117595. https://doi.org/10.1016/j.cma.2024.117595

Freundlich, H., & Bircumshaw, L. L. (1926). Ueber das thixotrope Verhalten von Aluminiumhydroxydgelen. *Kolloid-Zeitschrift*, *40*(1), 19–22. https://doi.org/10.1007/BF01422279

Galipeau, E., & Ponte Castañeda, P. (2013). A finite-strain constitutive model for magnetorheological elastomers: Magnetic torques and fiber rotations. *Journal of the Mechanics and Physics of Solids*, *61*(4), 1065–1090. https://doi.org/10.1016/j.jmps.2012.11.007

Gebhart, P., & Wallmersperger, T. (2024). On some energy-based variational principles in non-dissipative magneto-mechanics using a vector potential approach. *International Journal for Numerical Methods in Engineering*, *125*(24), e7593. https://doi.org/10.1002/nme.7593

Gent, A. N., & Cho, I. S. (1999). Surface Instabilities in Compressed or Bent Rubber Blocks. *Rubber Chemistry and Technology*, *72*(2), 253–262. https://doi.org/10.5254/1.3538798

Gent, A. N. (2011). Engineering with Rubber. In *Engineering with Rubber* (pp. I–XVIII). Carl Hanser Verlag GmbH & Co. KG. https://doi.org/10.3139/9783446428713.fm

Gerdes, K. (2000). A review of infinite element methods for exterior helmholtz problems. *Journal of Computational Acoustics*, *08*(01), 43–62. https://doi.org/10.1142/S0218396X00000042

Ghosh, A., Sinha, S., Dharmadhikari, J. A., Roy, S., Dharmadhikari, A. K., Samuel, J., Sharma, S., & Mathur, D. (2006). Euler buckling-induced folding and rotation of red blood cells in an optical trap. *Physical Biology*, *3*(1), 67. https://doi.org/10.1088/1478-3975/3/1/007

Ginder, J., Davis, L., & Elie, L. (1996). Rheology of magnetorheological fluids: Models and measurements. *International Journal of Modern Physics B*, *10*, 3293–3303. https://doi.org/10.1142/S0217979296001744

Ginder, J. M. (1998). Behavior of Magnetorheological Fluids. *MRS Bulletin*, *23*(8), 26–29. https://doi.org/10.1557/S0883769400030785

Ginder, J. M., Nichols, M. E., Elie, L. D., & Clark, S. M. (2000). Controllable-stiffness components based on magnetorheological elastomers. In N. M. Wereley (Ed.). https://doi.org/10.1117/12.388844

Ginder, J. M., Nichols, M. E., Elie, L. D., & Tardiff, J. L. (1999). Magnetorheological elastomers: Properties and applications. In M. R. Wuttig (Ed.). https://doi.org/10.1117/12.352787

Golobic, A. M., Durban, M. D., Fisher, S. E., Grapes, M. D., Ortega, J. M., Spadaccini, C. M., Duoss, E. B., Gash, A. E., & Sullivan, K. T. (2019). Active Mixing of Reactive Materials for 3D Printing. *Advanced Engineering Materials*, *21*(8), 1900147. https://doi.org/10.1002/adem.201900147

Gong, X. L., Zhang, X. Z., & Zhang, P. Q. (2005). Fabrication and characterization of isotropic magnetorheological elastomers. *Polymer testing*, *24*(5), 669–676. https://doi.org/10.1016/j.polymertesting.2005.03.015

Goriely, A., Vandiver, R., & Destrade, M. (2008). Nonlinear Euler buckling. *Proceedings of the Royal Society A: Mathematical, Physical and Engineering Sciences*, *464*(2099), 3003–3019. https://doi.org/10.1098/rspa.2008.0184

Gorodkin, S. R., James, R. O., & Kordonski, W. I. (2009). Magnetic properties of carbonyl iron particles in magnetorheological fluids. *Journal of Physics: Conference Series*, *149*(1), 012051. https://doi.org/10.1088/1742-6596/149/1/012051

Guan, R., Zheng, H., Liu, Q., Ou, K., Li, D.-s., Fan, J., Fu, Q., & Sun, Y. (2022). DIW 3D printing of hybrid magnetorheological materials for application in soft robotic grippers. *Composites Science and Technology*, *223*, 109409. https://doi.org/10.1016/j.compscitech.2022.109409

Hamers, R. J. (2001). Flexible electronic futures. *Nature*, *412*(6846), 489–490. https://doi.org/10.1038/35087682

Hannezo, E., Prost, J., & Joanny, J.-F. (2011). Instabilities of Monolayered Epithelia: Shape and Structure of Villi and Crypts. *Physical Review Letters*, *107*(7), 078104. https://doi.org/10.1103/PhysRevLett.107.078104

Hardin, J. O., Ober, T. J., Valentine, A. D., & Lewis, J. A. (2015). Microfluidic Printheads for Multimaterial 3D Printing of Viscoelastic Inks. *Advanced Materials*, *27*(21), 3279–3284. https://doi.org/10.1002/adma.201500222

Hashin, Z., & Shtrikman, S. (1961). Note on a variational approach to the theory of composite elastic materials. *Journal of the Franklin Institute*, *271*(4), 336–341. https://doi.org/10.1016/0016-0032(61)90032-1

Hassan, I., & Selvaganapathy, P. R. (2022). Microfluidic Printheads for Highly Switchable Multimaterial 3D Printing of Soft Materials. *Advanced Materials Technologies*, *7*(9), 2101709. https://doi.org/10.1002/admt.202101709

Haynes, W. M. (2016). *CRC handbook of chemistry and physics*. CRC press.

Hoffman, R. D., & Myers, R. R. (1960). Flow down an inclined plane. *Transactions of the Society of Rheology*, *4*(1), 119–130. https://doi.org/10.1122/1.548877

Hohlfeld, E., & Mahadevan, L. (2011). Unfolding the Sulcus. *Physical Review Letters*, *106*(10), 105702. https://doi.org/10.1103/PhysRevLett.106.105702

Houwink, R. (1956). Slipping of molecules during the deformation of reinforced rubber. *Rubber Chemistry and Technology*, *29*(3), 888–893. https://doi.org/10.5254/1.3542602

Hu, Y., Hiltner, A., & Baer, E. (2004). Buckling in elastomer/plastic/elastomer 3-layer films. *Polymer Composites*, *25*(6), 653–661. https://doi.org/10.1002/pc.20060

Huang, S., Pessot, G., Cremer, P., Weeber, R., Holm, C., Nowak, J., Odenbach, S., Menzel, A. M., & Auernhammer, G. K. (2015). Buckling of paramagnetic chains in soft gels. *Soft Matter*, *12*(1), 228–237. https://doi.org/10.1039/C5SM01814E

Huck, W. T., Bowden, N., Onck, P., Pardoen, T., Hutchinson, J. W., & Whitesides, G. M. (2000). Ordering of spontaneously formed buckles on planar surfaces. *Langmuir : the ACS journal of surfaces and colloids*, *16*(7), 3497–3501. https://doi.org/10.1021/la991302l

Jang, S., Boddorff, A., Jang, D. J., Lloyd, J., Wagner, K., Thadhani, N., & Brettmann, B. (2021). Effect of material extrusion process parameters on filament geometry and inter-filament voids in as-fabricated high solids loaded polymer composites. *Additive Manufacturing*, *47*, 102313. https://doi.org/10.1016/j.addma.2021.102313

Javili, A., Chatzigeorgiou, G., & Steinmann, P. (2013). Computational homogenization in magneto-mechanics. *International Journal of Solids and Structures*, *50*(25–26), 4197–4216. https://doi.org/10.1016/j.ijsolstr.2013.08.024

Jiang, H., Khang, D.-Y., Song, J., Sun, Y., Huang, Y., & Rogers, J. A. (2007). Finite deformation mechanics in buckled thin films on compliant supports. *Proceedings of the National Academy of Sciences*, *104*(40), 15607–15612. https://doi.org/10.1073/pnas.0702927104

Jiang, W.-Q., Yao, J.-J., Gong, X.-L., & Chen, L. (2008). Enhancement in magnetorheological effect of magnetorheological elastomers by surface modification of iron particles. *Chinese Journal of Chemical Physics*, *21*(1), 87. https://doi.org/10.1088/1674-0068/21/01/87-92

Jin, L., Takei, A., & Hutchinson, J. W. (2015). Mechanics of wrinkle/ridge transitions in thin film/substrate systems. *Journal of the Mechanics and Physics of Solids*, *81*, 22–40. https://doi.org/10.1016/j.jmps.2015.04.016

Jing, X., Chen, H., Zhang, L., Zhao, S., Wang, Y., Wang, Z., & Zhou, Y. (2023). Accurate Magneto-Driven Multi-Dimensional Droplet Manipulation. *Advanced Functional Materials*, *33*(9), 2210883. https://doi.org/10.1002/adfm.202210883

Johnston, M. T., & Ewoldt, R. H. (2013). Precision rheometry: Surface tension effects on low-torque measurements in rotational rheometers. *Journal of Rheology*, *57*(6), 1515–1532. https://doi.org/10.1122/1.4819914

Jolly, M. R., Carlson, J. D., Muñoz, B. C., & Bullions, T. A. (1996). The Magnetoviscoelastic Response of Elastomer Composites Consisting of Ferrous Particles Embedded in a Polymer Matrix. *Journal of Intelligent Material Systems and Structures*, *7*(6), 613–622. https://doi.org/10.1177/1045389X9600700601

Jones, E. M. C., & Iadicola, M. A. (Eds.). (2018). *A good practices guide for digital image correlation*. International Digital Image Correlation Society. https://doi.org/10.32720/idics/gpg.ed1/print.format

Kalina, K. A., Metsch, P., & Kästner, M. (2016). Microscale modeling and simulation of magnetorheological elastomers at finite strains: A study on the influence of mechanical preloads. *International Journal of Solids and Structures*, *102–103*, 286–296. https://doi.org/10.1016/j.ijsolstr.2016.10.019

Kang, S., Choi, K., Nam, J.-D., & Choi, H. (2020). Magnetorheological Elastomers: Fabrication, Characteristics, and Applications. *Materials*, *13*(20), 4597. https://doi.org/10.3390/ma13204597

Kankanala, S. (2004). On finitely strained magnetorheological elastomers. *Journal of the Mechanics and Physics of Solids*, *52*(12), 2869–2908. https://doi.org/10.1016/j.jmps.2004.04.007

Kankanala, S., & Triantafyllidis, N. (2008). Magnetoelastic buckling of a rectangular block in plane strain. *Journal of the Mechanics and Physics of Solids*, *56*(4), 1147–1169. https://doi.org/10.1016/j.jmps.2007.10.008

Keip, M.-A., & Rambausek, M. (2016). A multiscale approach to the computational characterization of magnetorheological elastomers. *International Journal for Numerical Methods in Engineering*, *107*(4), 338–360. https://doi.org/10.1002/nme.5178

Keip, M.-A., & Rambausek, M. (2017). Computational and analytical investigations of shape effects in the experimental characterization of magnetorheological elastomers. *International Journal of Solids and Structures*, *121*, 1–20. https://doi.org/10.1016/j.ijsolstr.2017.04.012

Khairi, M. H. A., Noor, E. E. M., Ubaidillah, U., Aziz, S. A. A., Mazlan, S. A., Tarmizi, S. M. A., & Nordin, N. A. (2022). Enhancement of Magneto-Induced Modulus by the Combination of Filler and Plasticizer Additives-Based Magnetorheological Elastomer. *Materials*, *15*(18), 6396. https://doi.org/10.3390/ma15186396

Khan, S., Joshi, K., & Deshmukh, S. (2022). A comprehensive review on effect of printing parameters on mechanical properties of FDM printed parts. *Materials Today: Proceedings*, *50*, 2119–2127. https://doi.org/10.1016/j.matpr.2021.09.433

Khang, D.-Y., Jiang, H., Huang, Y., & Rogers, J. A. (2006). A Stretchable Form of Single-Crystal Silicon for High-Performance Electronics on Rubber Substrates. *Science*, *311*(5758), 208–212. https://doi.org/10.1126/science.1121401

Khare, K., Zhou, J., & Yang, S. (2009). Tunable Open-Channel Microfluidics on Soft Poly(dimethylsiloxane) (PDMS) Substrates with Sinusoidal Grooves. *Langmuir*, *25*(21), 12794–12799. https://doi.org/10.1021/la901736n

Kim, D.-H., Ahn, J.-H., Choi, W. M., Kim, H.-S., Kim, T.-H., Song, J., Huang, Y. Y., Liu, Z., Lu, C., & Rogers, J. A. (2008). Stretchable and Foldable Silicon Integrated Circuits. *Science*, *320*(5875), 507–511. https://doi.org/10.1126/science.1154367

Kim, J., Chung, S. E., Choi, S.-E., Lee, H., Kim, J., & Kwon, S. (2011a). Programming magnetic anisotropy in polymeric microactuators. *Nature Materials*, *10*(10), 747–752. https://doi.org/10.1038/nmat3090

Kim, Y., Parada, G. A., Liu, S., & Zhao, X. (2019). Ferromagnetic soft continuum robots. *Science Robotics*, *4*(33), eaax7329. https://doi.org/10.1126/scirobotics.aax7329

Kim, Y., Yuk, H., Zhao, R., Chester, S. A., & Zhao, X. (2018). Printing ferromagnetic domains for untethered fast-transforming soft materials. *Nature*, *558*(7709), 274–279. https://doi.org/10.1038/s41586-018-0185-0

Kim, Y.-K., Koo, J.-H., Kim, K.-S., & Kim, S. (2011b). Developing a real time controlled adaptive MRE-based tunable vibration absorber system for a linear cryogenic cooler. *2011 IEEE/ASME International Conference on Advanced Intelligent Mechatronics (AIM)*, 287–290. https://doi.org/10.1109/AIM.2011.6026978

Kolchanov, D. S., Slabov, V., Keller, K., Sergeeva, E., Zhukov, M. V., Drozdov, A. S., & Vinogradov, A. V. (2019). Sol–gel magnetite inks for inkjet printing. *Journal of Materials Chemistry C*, *7*(21), 6426–6432. https://doi.org/10.1039/C9TC00311H

Koo, W. H., Jeong, S. M., Araoka, F., Ishikawa, K., Nishimura, S., Toyooka, T., & Takezoe, H. (2010). Light extraction from organic light-emitting diodes enhanced by spontaneously formed buckles. *Nature Photonics*, *4*(4), 222–226. https://doi.org/10.1038/nphoton.2010.7

Kovetz, A. (2000). *Electromagnetic theory* (Vol. 975). Oxford University Press Oxford. https://doi.org/10.1093/oso/9780198506041.001.0001

Krieger, I. M., & Dougherty, T. J. (1959). A mechanism for non-Newtonian flow in suspensions of rigid spheres. *Trans. Soc. Rheol*, *3*(1), 137–152. https://doi.org/10.1122/1.548848

Kücken, M., & Newell, A. C. (2004). A model for fingerprint formation. *Europhysics Letters*, *68*(1), 141. https://doi.org/10.1209/epl/i2004-10161-2

Kukla, C., Duretek, I., Gonzalez-Gutierrez, J., & Holzer, C. (2018). Rheology of Highly Filled Polymers. In J. L. Rivera-Armenta & B. A. S. Cruz (Eds.), *Polymer Rheology*. InTech. https://doi.org/10.5772/intechopen.75656

Kusakawa, T., & Otani, T. (1964). Properties of Various Pure Irons Study on pure iron-I. *Tetsu-to-Hagane*, *50*(1), 42–47. https://doi.org/10.2355/tetsutohagane1955.50.1_42

Lagrange, J.-L. A. (1867). *Oeuvres de Lagrange. T. 2 / publiées par les soins de M. J.-A. Serret [et G. Darboux] ; [précédé d'une notice sur la vie et les ouvrages de J.-L. Lagrange, par M. Delambre].*

Lantean, S., Barrera, G., Pirri, C. F., Tiberto, P., Sangermano, M., Roppolo, I., & Rizza, G. (2019). 3D printing of magnetoresponsive polymeric materials with tunable mechanical and magnetic properties by digital light processing. *Advanced Materials Technologies*, *4*(11), 1900505. https://doi.org/10.1002/admt.201900505

Lantean, S., Roppolo, I., Sangermano, M., Hayoun, M., Dammak, H., Barrera, G., Tiberto, P., Pirri, C. F., Bodelot, L., & Rizza, G. (2022). Magnetoresponsive Devices with Programmable Behavior Using a Customized Commercial Stereolithographic 3D Printer. *Advanced Materials Technologies*, *7*(11), 2200288. https://doi.org/10.1002/admt.202200288

Lee, J.-Y., An, J., & Chua, C. K. (2017). Fundamentals and applications of 3D printing for novel materials. *Applied Materials Today*, *7*, 120–133. https://doi.org/10.1016/j.apmt.2017.02.004

Lee, S. G., Lee, D. Y., Lim, H. S., Lee, D. H., Lee, S., & Cho, K. (2010). Switchable transparency and wetting of elastomeric smart windows. *Advanced materials*, *22*(44), 5013–5017. https://doi.org/10.1002/adma.201002320

Lefèvre, V., Danas, K., & Lopez-Pamies, O. (2017). A general result for the magnetoelastic response of isotropic suspensions of iron and ferrofluid particles in rubber, with applications to spherical and cylindrical specimens. *Journal of the Mechanics and Physics of Solids*, *107*, 343–364. https://doi.org/10.1016/j.jmps.2017.06.017

Lefèvre, V., Danas, K., & Lopez-Pamies, O. (2019). Two families of explicit models constructed from a homogenization solution for the magnetoelastic response of MREs containing iron and ferrofluid particles. *International Journal of Non-Linear Mechanics*. https://doi.org/10.1016/j.ijnonlinmec.2019.103362

Lefèvre, V., & Lopez-Pamies, O. (2022). The effective shear modulus of a random isotropic suspension of monodisperse rigid n-spheres: From the dilute limit to the percolation threshold. *Extreme Mechanics Letters*, *55*, 101818. https://doi.org/10.1016/j.eml.2022.101818

Lewis, J. A. (2006). Direct Ink Writing of 3D Functional Materials. *Advanced Functional Materials*, *16*(17), 2193–2204. https://doi.org/10.1002/adfm.200600434

Li, B., Cao, Y.-P., Feng, X.-Q., & Gao, H. (2012). Mechanics of morphological instabilities and surface wrinkling in soft materials: A review. *Soft Matter*, *8*(21), 5728–5745. https://doi.org/10.1039/C2SM00011C

Li, B., Huang, S.-Q., & Feng, X.-Q. (2010). Buckling and postbuckling of a compressed thin film bonded on a soft elastic layer: A three-dimensional analysis. *Archive of Applied Mechanics*, *80*(2), 175–188. https://doi.org/10.1007/s00419-009-0313-2

Li, S.-R., & Batra, R. C. (2007). Thermal Buckling and Postbuckling of Euler-Bernoulli Beams Supported on Nonlinear Elastic Foundations. *AIAA Journal*, *45*(3), 712–720. https://doi.org/10.2514/1.24720

Li, W. H., Zhang, X. Z., & Du, H. (2013). Magnetorheological Elastomers and Their Applications. In P. M. Visakh, S. Thomas, A. K. Chandra, & A. P. Mathew (Eds.), *Advances in Elastomers I: Blends and Interpenetrating Networks* (pp. 357–374). Springer. https://doi.org/10.1007/978-3-642-20925-3_12

Li, W., Armani, A., Martin, A., Kroehler, B., Henderson, A., Huang, T., Watts, J., Hilmas, G., & Leu, M. (2021). Extrusion-based additive manufacturing of functionally graded ceramics. *Journal of the European Ceramic Society*, *41*(3), 2049–2057. https://doi.org/10.1016/j.jeurceramsoc.2020.10.029

Li, Y., Li, J., Li, W., & Du, H. (2014). A state-of-the-art review on magnetorheological elastomer devices. *Smart Materials and Structures*, *23*(12), 123001. https://doi.org/10.1088/0964-1726/23/12/123001

Li, Z., Li, D., Chen, Y., Guo, Y., & Zhang, Z. (2019). Thixotropic yielding behaviors of ferrofluids. *Journal of Magnetism and Magnetic Materials*, *486*, 165277. https://doi.org/10.1016/j.jmmm.2019.165277

Liao, Z., Hossain, M., & Yao, X. (2020). Ecoflex polymer of different Shore hardnesses: Experimental investigations and constitutive modelling. *Mechanics of Materials*, *144*, 103366. Retrieved November 12, 2025, from 10.1016/j.mechmat.2020.103366

Liu, T., & Xu, Y. (2019). *Magnetorheological elastomers: Materials and applications* (Vol. 5). IntechOpen London, UK. https://doi.org/10.5772/intechopen.85083

Liu, Z., Li, M., Dong, X., Ren, Z., Hu, W., & Sitti, M. (2022). Creating three-dimensional magnetic functional microdevices via molding-integrated direct laser writing. *Nature Communications*, *13*(1), 2016. https://doi.org/10.1038/s41467-022-29645-2

Lokander, M., & Stenberg, B. (2003). Performance of isotropic magnetorheological rubber materials. *Polymer Testing*, *22*(3), 245–251. https://doi.org/10.1016/s0142-9418(02)00043-0

Lopez-Donaire, M. L., de Aranda-Izuzquiza, G., Garzon-Hernandez, S., Crespo-Miguel, J., Fernandez-de la Torre, M., Velasco, D., & Garcia-Gonzalez, D. (2023). Computationally Guided DIW Technology to Enable Robust Printing of Inks with Evolving Rheological Properties. *Advanced Materials Technologies*, *8*(3), 2370012. https://doi.org/10.1002/admt.202201707

Lopez-Pamies, O. (2010). A new I1-based hyperelastic model for rubber elastic materials. *Comptes Rendus Mecanique*, *338*(1), 3–11. https://doi.org/10.1016/j.crme.2009.12.007

Martin, J. E., Venturini, E., Gulley, G. L., & Williamson, J. (2004). Using triaxial magnetic fields to create high susceptibility particle composites. *Physical Review E*, *69*(2), 021508. https://doi.org/10.1103/PhysRevE.69.021508

Maugin, G. A., & Eringen, A. C. (1972a). Deformable magnetically saturated media. I. Field equations. *Journal of Mathematical Physics*, *13*(2), 143–155. https://doi.org/10.1063/1.1665947

Maugin, G. A., & Eringen, A. C. (1972b). Deformable magnetically saturated media. II. Constitutive theory. *Journal of Mathematical Physics*, *13*(9), 1334–1347. https://doi.org/10.1063/1.1666143

Mei, H., Landis, C. M., & Huang, R. (2011). Concomitant wrinkling and buckle-delamination of elastic thin films on compliant substrates. *Mechanics of Materials*, *43*(11), 627–642. https://doi.org/10.1016/j.mechmat.2011.08.003

Meza, L. R., Das, S., & Greer, J. R. (2014). Strong, lightweight, and recoverable three-dimensional ceramic nanolattices. *Science*, *345*(6202), 1322–1326. https://doi.org/10.1126/science.1255908

Mezger, T. (2020). *The Rheology Handbook: For users of rotational and oscillatory rheometers*. Vincentz Network. https://doi.org/10.1515/9783748603702

Miehe, C., & Keck, J. (2000). Superimposed finite elastic–viscoelastic–plastoelastic stress response with damage in filled rubbery polymers. Experiments, modelling and algorithmic implementation. *Journal of the Mechanics and Physics of Solids*, *48*(2), 323–365. https://doi.org/10.1016/S0022-5096(99)00017-4

Miya, K., Hara, K., & Someya, K. (1978). Experimental and Theoretical Study on Magnetoelastic Buckling of a Ferromagnetic Cantilevered Beam-Plate. *Journal of Applied Mechanics*, *45*(2), 355–360. https://doi.org/10.1115/1.3424301

Miya, K., Takagi, T., & Ando, Y. (1980). Finite-Element Analysis of Magnetoelastic Buckling of Ferromagnetic Beam Plate. *Journal of Applied Mechanics*, *47*(2), 377–382. https://doi.org/10.1115/1.3153672

Moon, F. C., & Pao, Y.-H. (1968). Magnetoelastic Buckling of a Thin Plate. *Journal of Applied Mechanics*, *35*(1), 53–58. https://doi.org/10.1115/1.3601173

Moreno-Mateos, M. A., Gonzalez-Rico, J., Nunez-Sardinha, E., Gomez-Cruz, C., Lopez-Donaire, M. L., Lucarini, S., Arias, A., Muñoz-Barrutia, A., Velasco, D., & Garcia-Gonzalez, D. (2022). Magneto-mechanical system to reproduce and quantify complex strain patterns in biological materials. *Applied Materials Today*, *27*, 101437. https://doi.org/10.1016/j.apmt.2022.101437

Morrison, F. A. (2001). *Understanding rheology*. Oxford University Press. https://doi.org/10.1515/arh-2002-0030

Mukherjee, D. (2020). Theoretical and numerical modeling of magnetorheological elastomers comprising magnetically soft and hard particles. *PhD Thesis*.

Mukherjee, D., & Danas, K. (2022). A unified dual modeling framework for soft and hard magnetorheological elastomers. *International Journal of Solids and Structures*, *257*, 111513. https://doi.org/10.1016/j.ijsolstr.2022.111513

Mukherjee, D., Rambausek, M., & Danas, K. (2021). An explicit dissipative model for isotropic hard magnetorheological elastomers. *Journal of the Mechanics and Physics of Solids*, *151*, 104361. https://doi.org/10.1016/j.jmps.2021.104361

Mullins, L. (1949). Permanent set in vulcanized rubber. *Rubber Chemistry and Technology*, *22*(4), 1036–1044. https://doi.org/10.5254/1.3543010

Mullins, L. (1969). Softening of rubber by deformation. *Rubber chemistry and technology*, *42*(1), 339–362. https://doi.org/10.5254/1.3539210

Myers, R. R., Brookfield, D. R., Eirich, F. R., Ferry, J. D., Stoloff, L., & Traxler, R. N. (1959). Communication Problems in Industrial Rheology: Committee Recommendations for Describing Flow Phenomena. *Transactions of the Society of Rheology*, *3*(1), 205–206. https://doi.org/10.1122/1.548852

Nagarajan, B., Mertiny, P., & Qureshi, A. J. (2020). Magnetically loaded polymer composites using stereolithography—Material processing and characterization. *Materials Today Communications*, *25*, 101520. https://doi.org/10.1016/j.mtcomm.2020.101520

Nikravesh, S., & Shen, Y.-L. (2022). Evolution of thin-film wrinkle patterns on a soft substrate: Direct simulations and the effects of the deformation history. *Nanomaterials*, *12*(19), 3505. https://doi.org/10.3390/nano12193505

Ober, T. J., Foresti, D., & Lewis, J. A. (2015). Active mixing of complex fluids at the microscale. *Proceedings of the National Academy of Sciences*, *112*(40), 12293–12298. https://doi.org/10.1073/pnas.1509224112

Ogden, R. W. (1997). *Non-linear elastic deformations*. Courier Corporation. https://doi.org/10.1002/zamm.19850650903

Ohzono, T., & Monobe, H. (2010). Morphological Transformation of a Liquid Micropattern on Dynamically Tunable Microwrinkles. *Langmuir*, *26*(9), 6127–6132. https://doi.org/10.1021/la1006204

Otténio, M., Destrade, M., & Ogden, R. W. (2008). Incremental Magnetoelastic Deformations, with Application to Surface Instability. *Journal of Elasticity*, *90*(1), 19–42. https://doi.org/10.1007/s10659-007-9120-6

Pao, Y.-H., & Hutter, K. (1975). Electrodynamics for moving elastic solids and viscous fluids. *Proceedings of the IEEE*, *63*(7), 1011–1021. https://doi.org/10.1109/proc.1975.9878

Peach, M. O., Christopherson, N. S., Dalrymple, J. M., & Viegelahn, G. L. (1988). Magnetoelastic buckling: Why theory and experiment disagree. *Experimental Mechanics*, *28*(1), 65–69. https://doi.org/10.1007/BF02328998

Pelteret, J.-P., & Steinmann, P. (2019). *Magneto-Active Polymers: Fabrication, characterisation, modelling and simulation at the micro-and macro-scale*. Walter de Gruyter GmbH & Co KG. https://doi.org/10.1515/9783110418576

Perales-Martínez, I. A., Palacios-Pineda, L. M., Lozano-Sánchez, L. M., Martínez-Romero, O., Puente-Cordova, J. G., & Elías-Zúñiga, A. (2017). Enhancement of a magnetorheological PDMS elastomer with carbonyl iron particles. *Polymer Testing*, *57*, 78–86. https://doi.org/10.1016/j.polymertesting.2016.10.029

Perrinet, C., Courtial, E.-J., Colly, A., Marquette, C., & Fulchiron, R. (2020). An emulsion approach to resolve the paradox of 3D printing of very soft silicones. *Advanced Materials Technologies*, *5*(6), 1901080. https://doi.org/10.1002/admt.201901080

Pham, T. V., & Mitsoulis, E. (1994). Entry and exit flows of casson fluids. *The Canadian Journal of Chemical Engineering*, *72*(6), 1080–1084. https://doi.org/10.1002/cjce.5450720619

Podstawczyk, D., Nizioł, M., Szymczyk, P., Wiśniewski, P., & Guiseppi-Elie, A. (2020). 3D printed stimuli-responsive magnetic nanoparticle embedded alginate-methylcellulose hydrogel actuators. *Additive Manufacturing*, *34*, 101275. https://doi.org/10.1016/j.addma.2020.101275

Ponte Castañeda, P., & Galipeau, E. (2011). Homogenization-based constitutive models for magnetorheological elastomers at finite strain. *Journal of the Mechanics and Physics of Solids*, *59*(2), 194–215. https://doi.org/10.1016/j.jmps.2010.11.004

Poojary, U. R., Hegde, S., & Gangadharan, K. V. (2018). Experimental investigation on the effect of carbon nanotube additive on the field-induced viscoelastic properties of magnetorheological elastomer. *Journal of Materials Science*, *53*(6), 4229–4241. https://doi.org/10.1007/s10853-017-1883-y

Popelar, C. H. (1972). Postbuckling Analysis of a Magnetoelastic Beam. *Journal of Applied Mechanics*, *39*(1), 207–211. https://doi.org/10.1115/1.3422614

Pössinger, T., Bolzmacher, C., Bodelot, L., & Triantafyllidis, N. (2014). Influence of interfacial adhesion on the mechanical response of magneto-rheological elastomers at high strain. *Microsystem technologies*, *20*, 803–814. https://doi.org/10.1007/s00542-013-2036-0

Psarra, E., Bodelot, L., & Danas, K. (2019). Wrinkling to crinkling transitions and curvature localization in a magnetoelastic film bonded to a non-magnetic substrate. *Journal of the Mechanics and Physics of Solids*, *133*, 103734. https://doi.org/10.1016/j.jmps.2019.103734

Psarra, E., Bodelot, L., & Danas, K. (2017). Two-field surface pattern control via marginally stable magnetorheological elastomers. *Soft Matter*, *13*(37), 6576–6584. https://doi.org/10.1039/C7SM00996H

Qi, S., Fu, J., Xie, Y., Li, Y., Gan, R., & Yu, M. (2019). Versatile magnetorheological plastomer with 3D printability, switchable mechanics, shape memory, and self-

healing capacity. *Composites Science and Technology*, *183*, 107817. https://doi.org/10.1016/j.compscitech.2019.107817

Quanjin, M., Rejab, M. R. M., Idris, M. S., Kumar, N. M., Abdullah, M. H., & Reddy, G. R. (2020). Recent 3D and 4D intelligent printing technologies: A comparative review and future perspective. *Procedia Computer Science*, *167*, 1210–1219. https://doi.org/10.1016/j.procs.2020.03.434

Rabinow, J. (1948). The magnetic fluid clutch. *Electrical Engineering*, *67*(12), 1167–1167. https://doi.org/10.1109/EE.1948.6444497

Rambausek, M., & Danas, K. (2021). Bifurcation of magnetorheological film–substrate elastomers subjected to biaxial pre-compression and transverse magnetic fields. *International Journal of Non-Linear Mechanics*, *128*, 103608. https://doi.org/10.1016/j.ijnonlinmec.2020.103608

Rambausek, M., & Keip, M.-A. (2018). Analytical estimation of non-local deformation-mediated magneto-electric coupling in soft composites. *Proceedings of the Royal Society A*, *474*(2216), 20170803. https://doi.org/10.1098/rspa.2017.0803

Rambausek, M., Mukherjee, D., & Danas, K. (2022). A computational framework for magnetically hard and soft viscoelastic magnetorheological elastomers. *Computer Methods in Applied Mechanics and Engineering*, *391*, 114500. https://doi.org/10.1016/j.cma.2021.114500

Razzaq, M. Y., Behl, M., & Lendlein, A. (2012). Memory-effects of magnetic nanocomposites. *Nanoscale*, *4*(20), 6181–6195. https://doi.org/10.1039/C2NR31332D

Ren, Z., Hu, W., Dong, X., & Sitti, M. (2019). Multi-functional soft-bodied jellyfish-like swimming. *Nature Communications*, *10*(1). https://doi.org/10.1038/s41467-019-10549-7

Richman, D. P., Stewart, R. M., Hutchinson, J., & Caviness, V. S. (1975). Mechanical Model of Brain Convolutional Development: Pathologic and experimental data suggest a model based on differential growth within the cerebral cortex. *Science*, *189*(4196), 18–21. https://doi.org/10.1126/science.1135626

Rigbi, Z., & Jilken, L. (1983). The response of an elastomer filled with soft ferrite to mechanical and magnetic influences. *Journal of magnetism and magnetic materials*, *37*(3), 267–276. https://doi.org/10.1016/0304-8853(83)90055-0

Rocha, V. G., Saiz, E., Tirichenko, I. S., & García-Tuñón, E. (2020). Direct ink writing advances in multi-material structures for a sustainable future. *Journal of Materials Chemistry A*, *8*(31), 15646–15657. https://doi.org/10.1039/D0TA04181E

Rudykh, S., & Bertoldi, K. (2013). Stability of anisotropic magnetorheological elastomers in finite deformations: A micromechanical approach. *Journal of the Mechanics and Physics of Solids*, *61*(4), 949–967. https://doi.org/10.1016/j.jmps.2012.12.008

Schubert, G. (2014). *Manufacture, characterisation and modelling of magneto-rheological elastomers* [Doctoral dissertation, University of Glasgow]. https://doi.org/https://theses.gla.ac.uk/id/eprint/5475

Schümann, M., Borin, D., Huang, S., Auernhammer, G., Müller, R., & Odenbach, S. (2017). A characterisation of the magnetically induced movement of NdFeB-particles in magnetorheological elastomers. *Smart Materials and Structures*, *26*(9), 095018. https://doi.org/10.1088/1361-665x/aa788a

Shanley, F. R. (1947). Inelastic Column Theory. *Journal of the Aeronautical Sciences*, *14*(5), 261–268. https://doi.org/10.2514/8.1346

Shao, K., Jiang, S., Hu, Y., Zhang, Y., Li, C., Zhang, Y., Li, J., Wu, D., & Chu, J. (2022). Bioinspired Lubricated Slippery Magnetic Responsive Microplate Array for High Performance Multi-Substance Transport. *Advanced Functional Materials*, *32*(40), 2205831. https://doi.org/10.1002/adfm.202205831

Sharma, G., Wu, W., & Dalal, E. N. (2005). The CIEDE2000 color-difference formula: Implementation notes, supplementary test data, and mathematical observations. *Color Research & Application*, *30*(1), 21–30. https://doi.org/10.1002/col.20070

Shtarkman, E. M. (1991). *Fluid responsive to a magnetic field* (pat.). Google Patents. Retrieved April 27, 2025, from https://patents.google.com/patent/US4992190A/en

Sirringhaus, H., & Shimoda, T. (2003). Inkjet Printing of Functional Materials. *MRS Bulletin*, *28*(11), 802–806. https://doi.org/10.1557/mrs2003.228

Skylar-Scott, M. A., Mueller, J., Visser, C. W., & Lewis, J. A. (2019). Voxelated soft matter via multimaterial multinozzle 3D printing. *Nature*, *575*(7782), 330–335. https://doi.org/10.1038/s41586-019-1736-8

Soledad Antonel, P., Jorge, G., Perez, O. E., Butera, A., Gabriela Leyva, A., & Martín Negri, R. (2011). Magnetic and elastic properties of $CoFe_2O_4$-polydimethylsiloxane magnetically oriented elastomer nanocomposites. *Journal of Applied Physics*, *110*(4). https://doi.org/10.1063/1.3624602

Song, H., Spencer, J., Jander, A., Nielsen, J., Stasiak, J., Kasperchik, V., & Dhagat, P. (2014). Inkjet printing of magnetic materials with aligned anisotropy. *Journal of Applied Physics*, *115*(17). https://doi.org/10.1063/1.4863168

Song, J., Jiang, H., Liu, Z. J., Khang, D. Y., Huang, Y., Rogers, J. A., Lu, C., & Koh, C. (2008). Buckling of a stiff thin film on a compliant substrate in large deformation. *International Journal of Solids and Structures*, *45*(10), 3107–3121. https://doi.org/10.1016/j.ijsolstr.2008.01.023

Soto, G. D., Meiorin, C., Actis, D. G., Mendoza Zélis, P., Moscoso Londoño, O., Muraca, D., Mosiewicki, M. A., & Marcovich, N. E. (2018). Magnetic nanocomposites based on shape memory polyurethanes. *European Polymer Journal*, *109*, 8–15. https://doi.org/10.1016/j.eurpolymj.2018.08.046

Steigmann, D. J. (2010). Applications of polyconvexity and strong ellipticity to nonlinear elasticity and elastic plate theory. In *CISM international centre for mechanical sciences* (pp. 265–299). Springer Vienna. https://doi.org/10.1007/978-3-7091-0174-2_8

Sugawa, Y., Ishidate, K., Sonehara, M., & Sato, T. (2013). Carbonyl-Iron/Epoxy Composite Magnetic Core for Planar Power Inductor Used in Package-Level Power Grid. *IEEE Transactions on Magnetics*, *49*(7), 4172–4175. https://doi.org/10.1109/TMAG.2013.2250925

Sun, J., Phan-Thien, N., & Tanner, R. I. (1996). Extrudate swell through an orifice die. *Rheologica Acta*, *35*(1), 1–12. https://doi.org/10.1007/BF00366548

Sun, T. L., Gong, X. L., Jiang, W. Q., Li, J. F., Xu, Z. B., & Li, W. H. (2008). Study on the damping properties of magnetorheological elastomers based on cis-polybutadiene rubber. *Polymer Testing*, *27*(4), 520–526. https://doi.org/10.1016/j.polymertesting.2008.02.008

Takagi, T. (1990). A Concept of Intelligent Materials. *Journal of Intelligent Material Systems and Structures*, *1*(2), 149–156. https://doi.org/10.1177/1045389X9000100201

Tan, C. O., Ogata, S., Yap, H. J., Nakamoto, I., Usop, Z., Fauthan, M. '., Liew, S. J., & Ng, S.-C. (2025). Insights into a new overclustering technique using machine learning for a self-selecting bin-restricted colour sorting setup for light red meranti (Rubroshorea spp.) *European Journal of Wood and Wood Products*, *83*(4), 131. https://doi.org/10.1007/s00107-025-02280-6

Tang, J., Sun, B., Yin, Q., Yang, M., Hu, J., & Wang, T. (2021). 3D printable, tough, magnetic hydrogels with programmed magnetization for fast actuation. *Journal of Materials Chemistry B*, *9*(44), 9183–9190. https://doi.org/10.1039/D1TB01694F

Te, L., Jianhui, D., Lili, L., Haibo, L., Boyao, C., Qi, L., & Yongqing, W. (2022). Three-Dimensional Printing Ink Preparation and Process Analysis of Magnetorheological Elastomer With Complex Structure. *Journal of Manufacturing Science and Engineering*, *144*(9), 091005. https://doi.org/10.1115/1.4054179

Teves, S., Biermann, T., Ziebehl, A., Eckert, J. G., Hill, O., Xia, P., Wollweber, M., Ripken, T., Bigall, N. C., & Lachmayer, R. (2024). Active-mixing printhead for on-the-fly composition adjustment of multi component materials in Direct Ink Writing. *Additive Manufacturing Letters*, *10*, 100217. https://doi.org/10.1016/j.addlet.2024.100217

Thomas, J. D., & Triantafyllidis, N. (2009). On electromagnetic forming processes in finitely strained solids: Theory and examples. *Journal of the Mechanics and Physics of Solids*, *57*(8), 1391–1416. https://doi.org/10.1016/j.jmps.2009.04.004

Tibbits, S. (2014). 4D Printing: Multi-Material Shape Change. *Architectural Design*, *84*(1), 116–121. https://doi.org/10.1002/ad.1710

Timoshenko, S. P., & Gere, J. M. (2012). *Theory of elastic stability*. Courier Corporation. https://doi.org/10.1115/1.3636481

Treloar, L. R. G. (1975). *The Physics of Rubber Elasticity*. OUP Oxford. https://doi.org/10.1002/pi.4980080107

Truesdell, C., & Toupin, R. (1960). The Classical Field Theories. In S. Flügge (Ed.), *Principles of Classical Mechanics and Field Theory / Prinzipien der Klassischen*

*Mechanik und Feldtheorie* (pp. 226–858, Vol. 2 / 3 / 1). Springer Berlin Heidelberg. https://doi.org/10.1007/978-3-642-45943-6_2

Vandeparre, H., Gabriele, S., Brau, F., Gay, C., Parker, K. K., & Damman, P. (2010). Hierarchical wrinkling patterns. *Soft Matter*, *6*(22), 5751–5756. https://doi.org/10.1039/C0SM00394H

Vidal-Verdu, F., & Hafez, M. (2007). Graphical Tactile Displays for Visually-Impaired People. *IEEE Transactions on Neural Systems and Rehabilitation Engineering*, *15*(1), 119–130. https://doi.org/10.1109/TNSRE.2007.891375

Wagner, N. J., & Brady, J. F. (2009). Shear thickening in colloidal dispersions. *Physics Today*, *62*(10), 27–32. https://doi.org/10.1063/1.3248476

Wallerstein, D. V., & Peach, M. O. (1972). Magnetoelastic buckling of beams and thin plates of magnetically soft material. Retrieved May 5, 2025, from 10.1115/1.3422699

Wang, Q., & Zhao, X. (2015). A three-dimensional phase diagram of growth-induced surface instabilities. *Scientific reports*, *5*(1), 8887. https://doi.org/10.1038/srep08887

Wang, T., Ren, Z., Hu, W., Li, M., & Sitti, M. (2021a). Effect of body stiffness distribution on larval fish–like efficient undulatory swimming. *Science Advances*, *7*(19), eabf7364. https://doi.org/10.1126/sciadv.abf7364

Wang, T., Yang, Y., & Xu, F. (2022). Mechanics of tension-induced film wrinkling and restabilization: A review. *Proceedings of the Royal Society A: Mathematical, Physical and Engineering Sciences*, *478*(2263), 20220149. https://doi.org/10.1098/rspa.2022.0149

Wang, X.-X., Yu, G.-F., Zhang, J., Yu, M., Ramakrishna, S., & Long, Y.-Z. (2021b). Conductive polymer ultrafine fibers via electrospinning: Preparation, physical properties and applications. *Progress in Materials Science*, *115*, 100704. https://doi.org/10.1016/j.pmatsci.2020.100704

Wang, Y., Hu, Y., Chen, L., Gong, X., Jiang, W., Zhang, P., & Chen, Z. (2006). Effects of rubber/magnetic particle interactions on the performance of magnetorheological elastomers. *Polymer testing*, *25*(2), 262–267. https://doi.org/10.1016/j.polymertesting.2005.10.002

Wickramasinghe, S., Do, T., & Tran, P. (2020). FDM-Based 3D Printing of Polymer and Associated Composite: A Review on Mechanical Properties, Defects and Treatments. *Polymers*, *12*(7), 1529. https://doi.org/10.3390/polym12071529

Winslow, W. M. (1949). Induced fibration of suspensions. *Journal of applied physics*, *20*(12), 1137–1140. https://doi.org/10.1063/1.1698285

Xia, X., Spadaccini, C. M., & Greer, J. R. (2022). Responsive materials architected in space and time. *Nature Reviews Materials*, *7*(9), 683–701. https://doi.org/10.1038/s41578-022-00450-z

Xie, H., Sun, M., Fan, X., Lin, Z., Chen, W., Wang, L., Dong, L., & He, Q. (2019). Reconfigurable magnetic microrobot swarm: Multimode transformation, locomotion, and manipulation. *Science Robotics*, *4*(28), eaav8006. https://doi.org/10.1126/scirobotics.aav8006

Xu, T., Zhang, J., Salehizadeh, M., Onaizah, O., & Diller, E. (2019). Millimeter-scale flexible robots with programmable three-dimensional magnetization and motions. *Science Robotics*, *4*(29), eaav4494. https://doi.org/10.1126/scirobotics.aav4494

Yarali, E., Baniasadi, M., Zolfagharian, A., Chavoshi, M., Arefi, F., Hossain, M., Bastola, A., Ansari, M., Foyouzat, A., Dabbagh, A., Ebrahimi, M., Mirzaali, M. J., & Bodaghi, M. (2022). Magneto-/ electro-responsive polymers toward manufacturing, characterization, and biomedical/ soft robotic applications. *Applied Materials Today*, *26*, 101306. https://doi.org/10.1016/j.apmt.2021.101306

Yin, J., Han, X., Cao, Y., & Lu, C. (2014). Surface wrinkling on polydimethylsiloxane microspheres via wet surface chemical oxidation. *Scientific reports*, *4*(1), 5710. https://doi.org/10.1038/srep05710

Yirmibesoglu, O. D., Simonsen, L. E., Manson, R., Davidson, J., Healy, K., Menguc, Y., & Wallin, T. (2021). Multi-material direct ink writing of photocurable elastomeric foams. *Communications Materials*, *2*(1), 82. https://doi.org/10.1038/s43246-021-00186-3

Yuk, H., Lu, B., Lin, S., Qu, K., Xu, J., Luo, J., & Zhao, X. (2020). 3D printing of conducting polymers. *Nature Communications*, *11*(1), 1604. https://doi.org/10.1038/s41467-020-15316-7

Yuk, H., & Zhao, X. (2018). A new 3D printing strategy by harnessing deformation, instability, and fracture of viscoelastic inks. *Advanced Materials*, *30*(6), 1704028. https://doi.org/10.1002/adma.201704028

Zang, J., Zhao, X., Cao, Y., & Hutchinson, J. W. (2012). Localized ridge wrinkling of stiff films on compliant substrates. *Journal of the Mechanics and Physics of Solids*, *60*(7), 1265–1279. https://doi.org/10.1016/j.jmps.2012.03.009

Zhang, C., Li, X., Jiang, L., Tang, D., Xu, H., Zhao, P., Fu, J., Zhou, Q., & Chen, Y. (2021). 3D Printing of Functional Magnetic Materials: From Design to Applications. *Advanced Functional Materials*, *31*(34), 2102777. https://doi.org/10.1002/adfm.202102777

Zhang, C., Song, J., & Yang, Q. (2014). Periodic buckling patterns of graphene/hexagonal boron nitride heterostructure. *Nanotechnology*, *25*(44), 445401. https://doi.org/10.1088/0957-4484/25/44/445401

Zhang, F., Wang, L., Zheng, Z., Liu, Y., & Leng, J. (2019). Magnetic programming of 4D printed shape memory composite structures. *Elsevier*. https://doi.org/10.1016/j.compositesa.2019.105571

Zhao, W., Zhang, F., Leng, J., & Liu, Y. (2019). Personalized 4D printing of bioinspired tracheal scaffold concept based on magnetic stimulated shape memory composites.

*Composites Science and Technology*, *184*, 107866. https://doi.org/10.1016/j.compscitech.2019.107866

Zhao, Y., Han, X., Li, G., Lu, C., Cao, Y., Feng, X.-Q., & Gao, H. (2015). Effect of lateral dimension on the surface wrinkling of a thin film on compliant substrate induced by differential growth/swelling. *Journal of the Mechanics and Physics of Solids*, *83*, 129–145. https://doi.org/10.1016/j.jmps.2015.06.003

Zheng, Q., Xie, B., Xu, Z., & Wu, H. (2023). A systematic printability study of direct ink writing towards high-resolution rapid manufacturing. *International Journal of Extreme Manufacturing*, *5*(3), 035002. https://doi.org/10.1088/2631-7990/acd090

Zhou, J. Z. Q., Uhlherr, P. H. T., & Luo, F. T. (1995). Yield stress and maximum packing fraction of concentrated suspensions. *Rheologica Acta*, *34*(6), 544–561. https://doi.org/10.1007/BF00712315

Zhou, L.-y., Gao, Q., Fu, J.-z., Chen, Q.-y., Zhu, J.-p., Sun, Y., & He, Y. (2019). Multimaterial 3D Printing of Highly Stretchable Silicone Elastomers. *ACS Applied Materials & Interfaces*, *11*(26), 23573–23583. https://doi.org/10.1021/acsami.9b04873

Zhou, Q., Ji, B., Hu, F., Dai, Z., Ding, S., Yang, H., Zhong, J., Qiao, Y., Zhou, J., Luo, J., & Zhou, B. (2022). Magnetized Microcilia Array-Based Self-Powered Electronic Skin for Micro-Scaled 3D Morphology Recognition and High-capacity Communication. *Advanced Functional Materials*, *32*(46), 2208120. https://doi.org/10.1002/adfm.202208120

**ECOLE DOCTORALE**

**Titre :** Contrôle de la formation de motifs par champ magnétique à la surface de structures élastomères magnétoactives

**Mots clés :** élastomères magnéto-actifs, instabilités, motifs de surface, impression 3D, simulations numériques couplées

**Résumé :** Les élastomères magnétorhéologiques (EMR) sont des matériaux composites intelligents composés de particules magnétisables incorporées dans une matrice élastomère. Ils réagissent rapidement et de manière réversible aux champs magnétiques appliqués au travers de déformations magnéto-induites ou d'instabilités de surface provoquées par des contraintes magnéto-mécaniques couplées et des interactions magnétiques. Dans les systèmes film EMR-substrat, ces instabilités peuvent être déclenchées par des charges mécaniques, magnétiques ou combinées, conduisant à des morphologies de surface allant d'ondulations périodiques à des motifs de plissement plus complexes. Malgré d'importants efforts expérimentaux et numériques, ces phénomènes ont jusqu'à présent été principalement limités aux films uniformes, donnant lieu à des motifs 2,5D avec une capacité d'ajustement restreinte. Cependant, l'obtention de morphologies de surface entièrement tridimensionnelles dans des films uniformes nécessite des champs magnétiques importants, tandis que l'instabilité est souvent confinée à des plages étroites de charges mécaniques. Ce travail vise à surmonter ces limites en permettant l'obtention de motifs de surface tridimensionnels contrôlables et ciblés grâce à l'introduction de propriétés magnéto-mécaniques hétérogènes dans les films EMR, rendue possible par des techniques de fabrication avancées. Pour atteindre ces objectifs, une méthode de mélange actif pour les encres EMR est développée et mise en œuvre dans un processus de "direct ink writing" à l'aide d'un mélangeur hélicoïdal dynamique. Il s'agit de la première application de mélange actif aux EMRs. Cette approche intégrée offre une façon fiable et reproductible d'imprimer des films EMR hétérogènes présentant une géométrie, une uniformité et des propriétés rhéologiques bien contrôlées. Parallèlement, un modèle numérique tridimensionnel est établi pour capturer avec précision l'évolution des motifs de surface sous l'effet de champs magnétiques. Ce modèle utilise un cadre capable de reproduire la magnétisation, la magnétostriction et le comportement mécanique sur un large spectre de champs magnétiques. Les propriétés des matériaux sont identifiées expérimentalement et les profils de surface tridimensionnels sont mesurés par stéréo corrélation d'images numériques, ce qui permet de valider le modèle numérique. Grâce à cette approche expérimentale et numérique intégrée, ce travail examine de manière systématique l'évolution des motifs de surface dans les systèmes film EMR hétérogène-substrat. L'influence de l'hétérogénéité du film sur l'apparition et la transformation des motifs de surface est examinée, révélant de nouvelles stratégies pour contrôler des morphologies tridimensionnelles complexes à l'aide de champs magnétiques. Dans l'ensemble, les résultats démontrent que la combinaison d'une conception de film hétérogène, de fabrication additive et d'une modélisation avancée élargit considérablement la gamme des transformations de forme réalisables dans les systèmes basés sur les EMR, ouvrant ainsi de nouvelles perspectives pour les surfaces adaptatives et les dispositifs souples reconfigurables.

**Title :** Controlling pattern formation via magnetic field at the surface of magneto-active elastomer structures

**Keywords :** magneto-active elastomers, instabilities, surface patterns, 3D printing, coupled numerical modeling

**Abstract :** Magnetorheological elastomers (MREs) are smart composite materials composed of magnetizable particles embedded in an elastomeric matrix. They respond readily and reversibly to applied magnetic fields through magneto-induced deformations or surface instabilities driven by coupled magneto-mechanical stresses and magnetic interactions. In layered MRE film–substrate systems, such instabilities can be triggered by mechanical, magnetic, or combined loading, leading to surface morphologies ranging from periodic wrinkling to more complex crinkling patterns. Despite extensive experimental and numerical efforts, these phenomena have so far been mostly limited to uniform films, resulting in 2.5D patterns with restricted tunability. However, achieving fully three-dimensional surface morphologies in uniform films requires large magnetic fields, while instability is often confined to narrow ranges of mechanical loading. This work aims to overcome these limitations by enabling controllable, targeted three-dimensional surface patterns through the introduction of heterogeneous magneto-mechanical properties in MRE films, made possible by advanced fabrication techniques. To achieve these objectives, an active mixing method for MRE inks is developed and implemented in a direct ink writing process using a dynamic helical mixer. This represents the first application of active mixing to MREs. This integrated approach provides a reliable and repeatable route to print heterogeneous MRE films with well-controlled geometry, uniformity, and rheological properties. Concurrently, a three-dimensional numerical model is established to accurately capture surface pattern evolution under magnetic fields. This model employs a framework capable of reproducing magnetization, magnetostriction, and mechanical behavior across a broad spectrum of magnetic fields. Material properties are identified experimentally, and three-dimensional surface profiles are measured using stereo digital image correlation, enabling validation of the numerical model. Using this integrated experimental and numerical approach, this study systematically investigates surface pattern evolution in heterogeneous MRE film–substrate systems. The influence of film heterogeneity on the onset and transformation of surface patterns is examined, revealing new strategies for controlling complex three-dimensional morphologies via magnetic fields. Overall, the findings demonstrate that the combination of heterogeneous film design, additive manufacturing, and advanced modeling substantially expands the range of achievable shape transformations in MRE-based systems, thereby enabling new opportunities for adaptive surfaces and reconfigurable soft devices.

**Institut Polytechnique de Paris**
91120 Palaiseau, France